

Microstructured Optical Fibre Sensors for Extreme Environments

A thesis submitted for the degree of Doctor of Philosophy

Tongyu Liu

St Catherine's College



Supervised by Dr. Julian Fells and Prof. Martin Booth

Department of Engineering Science

May 2026

Abstract

Optical fibre sensors offer numerous advantages, including immunity to electromagnetic interference, the ability to operate under extreme temperature and pressure conditions, compact form factor, and high sensitivity. As a result, they find wide-ranging applications in structural health monitoring of bridges, wind turbines, and other civil infrastructure, with growing deployment anticipated in battery systems, nuclear facilities, and aero engines. By employing two complementary femtosecond-laser processing techniques, namely (i) femtosecond-laser-assisted selective chemical etching to realise complex three-dimensional (3D) microstructures and (ii) direct femtosecond-laser-induced refractive-index modification to inscribe gratings and waveguides, I fabricated sensor elements with more complex and customisable 3D architectures in both silica and sapphire fibres, enabling pressure or temperature sensing in extreme environments.

Pressure sensors based on fibre Bragg gratings (FBGs) in side-hole silica optical fibre enable remote monitoring of pressure at multiple locations in environments that would otherwise be inaccessible. However, preform drawn side hole designs impose material and geometric constraints and introduce a trade off between sensitivity and splice loss due to mode mismatch. To address these limitations, complex 3D architectures were numerically optimised and realised directly within commercial step-index fibres using femtosecond laser irradiation followed by selective chemical etching, producing precisely defined cladding voids while avoiding the splice loss associated with joining a separately drawn side-hole fibre to a standard fibre.

This work further presents the first sapphire photonic crystal fibre temperature sensor fabricated using femtosecond laser induced refractive index modification. Compared with established depressed cladding approaches, the attainable device length is increased by nearly a factor of two, markedly expanding the application space of sapphire fibre sensors. Overall, the results provide a new route for femtosecond laser processing of microstructured fibre sensors.

Publications

Liu, T., Song, Z., Reeves, R. J., Wang, M., Doyle, C. T., Booth, M. J., & Fells, J. A. (2024). 3D structured optical fiber pressure sensors. Journal of Lightwave Technology, 42(18), 6375-6380.

Liu, T., Song, Z., Wang, M., Doyle, C. T., Booth, M. J., & Fells, J. A. (2023, November). 3D Structured Optical Fiber Pressure Sensors Based on Femtosecond Laser Fabrication. In Optical Fiber Sensors (pp. W4-61). Optica Publishing Group.

Song, Z., Wang, M., Payne, F. P., Salter, P. S., Liu, T., Elston, S. J., ... & Fells, J. A. (2025). Fiber Bragg Gratings with Micro-Engineered Temperature Coefficients. Advanced Optical Materials, 13(8), 2402726..

Wang, M., Salter, P. S., Payne, F. P., Liu, T., Booth, M. J., & Fells, J. A. (2024). Laser-written scalable sapphire integrated photonics platform. Optics Express, 32(26), 45600-45612.

Wang, M., Salter, P. S., Payne, F. P., Liu, T., Shipley, A., Song, Z., ... & Fells, J. A. (2024). Optimization of single-mode sapphire waveguide Bragg gratings. Journal of Lightwave Technology, 42(16), 5629-5638.

Wang, M., Salter, P. S., Payne, F. P., Shipley, A., Dyson, I. N., Liu, T., ... & Fells, J. A. (2024). Single-mode sapphire fiber temperature sensor. Journal of Lightwave Technology.

Song, Z., Wang, M., Salter, P. S., Liu, T., Elston, S. J., Booth, M. J., ... & Fells, J. A. (2023, November). Fiber Bragg grating sensors with ultrahigh or ultralow temperature sensitivity. In Optical Fiber Sensors (pp. W2-2). Optica Publishing Group.

Acknowledgements

I am deeply grateful to Dr Julian Fells and Professor Martin Booth for giving me the opportunity to come to Oxford and pursue research on optical fibre sensors. I owe particular thanks to Julian, an outstanding supervisor whose guidance was always exactly what I needed: timely and practical when I was uncertain, yet never intrusive or prescriptive. He preserved a generous degree of freedom for me to shape the direction of the project, while steadily encouraging me to grow into an independent and mature scholar. I have learned a great deal from him: not only technical knowledge but also how to think clearly, communicate rigorously, and take ownership of my work.

I would also like to thank my research group colleagues, Dr Mohan Wang and Dr Zipei Song. Over the four years of my DPhil, they generously shared their expertise and experimental skills, and they were invariably ready to help whenever I encountered difficulties in the lab. Their openness, patience, and high standards improved the quality of my research and strongly influenced my approach to collaborative work.

Finally, I am indebted to my parents for their unwavering support. They provided me with a wonderful education and have stood behind every major decision I have made. Without their encouragement and belief in me, this research would not have been possible.

Table of Contents

Publications **i**

Acknowledgements **ii**

1 Introduction **1**

1.1 Research Motivation 1

1.2 The history of FBG 5

1.3 Research progress on FBG sensors 8

1.4 Research progress on sapphire optical fibre sensors 13

1.5 Thesis Outline 19

2 Background **29**

2.1 Coupled-Mode Theory of FBG 29

2.2 Principles of Sensing 36

2.3 Birefringence in Optical fibre 38

2.3.1 Intrinsic birefringence 38

2.3.2 Induced birefringence 39

2.4 Stress-Optic Effect 41

2.5 Thermo-Optic Effect and Thermal Expansion 44

2.5.1 Thermo-optic effect 44

2.5.2 Thermal expansion 45

3 Design and Simulation of Pressure Sensors 49

3.1 Simulation of Stress-Optic Effect 49

3.2 Simulation of FBG 54

3.3 Sensor Structure Optimization and Parameter Sweep 57

4 Fabrication and Characterisation of Sensors 66

4.1 Laser inscription 66

4.1.1 Laser focusing method 66

4.1.2 Principles of laser modified optical materials 68

4.1.3 Laser fabrication systems 70

4.1.4 Fabrication process 71

4.1.4.1 Fibre Bragg grating inscription 72

4.2 Wet etching of fused silica 73

4.3 Sensor Sealing 77

5 Pressure and Temperature Testing 82

5.1 Initial FBG testing 82

5.2 Hydraulic Testing at Halliburton 84

5.3 Build of a Hydraulic Test System 86

5.4 Hydraulic Pressure Testing 87

5.5 Thermal Stability Testing 90

5.6 Analysis of the results 91

5.7 Summary 93

6 Photonic crystal tip temperature sensor based on sapphire optical fibre 95

6.1 Background 95

6.2 Sensor Simulation 101

6.3 Sensor fabrication 103

6.4 Summary and transition 104

7 Sapphire Photonic Crystal Fibre Sensors 108

7.1 Background 108

7.2 Simulation Design 113

8 Fabrication and Test of Sapphire Photonic Crystal Fibre Sensors 121

8.1 Sensor fabrication 121

8.2 Sensor Testing 130

8.3 Summary 144

9 Conclusions and Outlook 147

List of Figures

1.1 The development history of key battery sensing technology [12]. 2

1.2 Schematic diagram of the FBG sensor grid in the aircraft [15]. 3

1.3 Phase mask method [33]. 7

1.4 Femtosecond laser writing method [44]. 7

1.5 Schematic diagram for two superimposed FBG [47]. 8

1.6 Fibre Bragg Grating written in germanosilicate and boron-codoped germanosilicate fibres [53]. 10

1.7 Schematic diagram for FBG and LPG sensor system [55]. 10

1.8 Schematic of pressure-testing setup and cross-section photo [56]. 11

1.9 Response of FBG sensor to external pressure at room temperature [56]. 11

1.10 The cross-section photo and fusion splice photo [57]. 12

1.11 Reflectance spectra and cross-sectional electron micrographs of sensor sample [58]. . 12

1.12 Microscope cross-section image and FEA results [59]. 13

1.13 Schematic diagram of a radiometric temperature sensing system [62]. 14

1.14 Schematic diagram of a FP sensor in sapphire fibre [63]. 14

1.15 Adhesive free FP sensor fabrication process [67]. 15

1.16 Fibre Bragg Grating reflection spectrum and sensor microscopic image [68]. 16

1.17 (a) Schematic diagram of fusion splicing with tapered fibre tip [68]. (b) Microscopic image of sapphire fibre after wet etching [70]. (c) Schematic diagram of the refractive index distribution change due to nuclear radiation [71]. 17

1.18 (a) Schematic diagram of point-by-point writing method to produce FBG in sapphire fibre [72]. (b) Schematic diagram of helical scanning approach to produce FBG in sapphire fibre [73]. 18

1.19 (a) Schematic diagram of adaptive optics-based femtosecond laser fabrication system [75]. (b) Microscopic image of a sapphire single-mode fibre [75]. (c) Mode profile of the sapphire single-mode fibre at 1550 nm [75]. 19

2.1 (a) Preform of polarization-maintaining fibre [9]. (b) Microscopic image of the polarization-maintaining fibre cross-section [9]. 39

2.2 (a) Microscopic image of the photonic crystal fibre cross-section [10]. (b) Simulation design of the fibre cross-section [10]. 40

2.3 Schematic diagram of the induced birefringence created by femto-second laser and microscopic image of the fibre cross section [12]. 40

2.4 Relationship between the induced birefringence and laser-irradiated stress track [12]. 41

2.5 The relationship of the thermo-optic coefficient with temperature [16]. 45

3.1 Schematic diagram of grid refinement(from: www.comsol.com/multiphysics). 50

3.2 (a) Fibre cross section using a sparse mesh division. (b) Stress distribution using sparse mesh division. (c) Fibre cross section using a finer mesh division. (d) Stress distribution using finer mesh division. 51

3.3 Stress distribution in the side-hole fibre cross-section. 52

3.4 Distribution of the changes in the refractive index component along the x-direction $N_x - N$. 53

3.5 Distribution of the changes in the refractive index component along the y-direction $N_y - N$. 53

3.6 Distribution of the difference between the refractive index components in the x and y directions $N_x - N_y$. 53

3.7 Use of the eigenmode expansion method in FIMMPROP to calculate light propagation in microstructured fibres. The specific microstructured fibre geometry shown here is included as an illustrative example of the modelling workflow and is explored in detail in Section 3.3. 54

3.8 Stress-induced change in the refractive-index component along the x-direction, $N_x - N$, obtained directly from the COMSOL stress-optic simulation of the side-hole fibre under applied external pressure. The data are shown before curve fitting and resampling for import into FIMMPROP. 55

3.9 Stress-induced change in the refractive-index component along the y-direction, $N_y - N$, obtained directly from the COMSOL stress-optic simulation of the side-hole fibre under applied external pressure. The data are shown before curve fitting and resampling for import into FIMMPROP. 55

3.10 Resampled distribution of $N_x - N$ after curve fitting and interpolation in MATLAB. The processed refractive-index data are converted onto the regular grid required for subsequent FIMMPROP simulations. 56

3.11 Resampled distribution of $N_y - N$ after curve fitting and interpolation in MATLAB. The processed refractive-index data are converted onto the regular grid required for subsequent FIMMPROP simulations. 56

3.12 Anisotropic refractive index profile example from FIMMWAVE manual. 56

3.13 Simulated transmission spectra of the side-hole fibre sensor using a 1000-period second-order FBG with a grating pitch of $\Lambda = 1.073\ \mu\mathrm{m}$ and a refractive-index modulation of $\Delta n = 0.001$. The spectra compare the two orthogonal polarisation modes before and after the application of external pressure. 57

3.14 Layout of the sector-shaped air holes in a 220 μm diameter silica fibre. The sector regions represent air voids introduced into the cladding, while the remaining cross-section corresponds to the silica step-index fibre. 58

3.15 Simulated distribution of $N_x - N_y$ for sector-shaped air holes with different opening angles in a 220 μm diameter silica fibre. The sector opening angle was varied from 40° to 90° in 5° increments under an external pressure of 124 bar. 58

3.16 Parameter sweep for the sector angle for a 220 $\mu\mathrm{m}$ diameter fibre at an external pressure of 124 bar. 59

3.17 $N_x - N_y$ distribution simulation of sector holes with different radius between 10 $\mu\mathrm{m}$ to 90 $\mu\mathrm{m}$ in the 220 $\mu\mathrm{m}$ diameter fibre. 60

3.18 Under an external pressure of 124 bar, a sweep of the fibre's inner sector radius was performed to obtain the average $N_x - N_y$ in the core region variation trend. 61

3.19 simulation of cross-sectional refractive index components difference distribution in sector holes with elliptical micro-holes. 61

3.20 Fibre Bragg Grating transmissivity in two polarization directions at different pressure. 62

3.21 Relation between peak wavelength separation and pressure change for a 220 $\mu\mathrm{m}$ diameter fibre. 63

3.22 Transmission spectrum of TE modes at different temperature. 64

3.23 Transmission spectrum of TM modes at different temperature. 64

3.24 Simulation of peak separation at different temperatures and pressures for a 220 μm diameter fibre. 65

4.1 Schematic diagram of focusing light exactly on the centre of a fibre. 66

4.2 Laser focusing aberration at the fibre core. 67

4.3 Simulation of laser focusing in the fibre periphery. 67

4.4 Non-linear optical absorption. (a) Quantum tunnelling (b) Multiphoton absorption (c) Avalanche ionization [3]. 69

4.5 SEM images of nano-gratings parallel and perpendicular to the laser direct writing direction [9]. 70

4.6 SEM images of the laser direct writing voided cavity [12]. 70

4.7 A simplified schematic diagram of the femtosecond laser fabrication system. 71

4.8 Meshing diagram of holes in COMSOL and micrograph of a sample cross section. . 72

4.9 Heatmaps of the etching selectivity of laser-modified silica in 8 mol/L KOH and 5% HF solution [17]. 73

4.10 Micrographs of samples etched using the entry channel. 74

4.11 Schematic diagram of the access channel. 75

4.12 Microscope image of the samples. (a),(b) Side views of the inscribed and uninscribed areas of the 125 μm SMF before and after etching. (c),(d) Side views of the inscribed and uninscribed areas of the 250 μm large diameter fibre before and after etching. . . 76

4.13 Cross-sectional view of the 250 μm fibre inscription area. 77

4.14 The sample was sealed using the adhesive. 78

4.15 The sample was sealed by fusion splicer. 78

5.1 Schematic diagram of the measurement system. 82

5.2 (a) Effect of stress introduced by femtosecond laser irradiation on fibre birefringence in the literature[1] (b) Fibre Bragg Grating reflection spectra of my un-etched sample. 83

5.3 Fibre Bragg Grating reflection spectra of the etched sample. 83

5.4 Preliminary pressure test result of the sample sealed using the fusion splicer. 84

5.5 Preliminary pressure test result of the sample sealed using the ceramic adhesive. . . . 85

5.6 Schematic diagram of the hydraulic pressure-testing system for FBG sensors. 86

5.7 Photograph of the hydraulic pressure-testing system for FBG sensors. 87

5.8 Normalised pressure test results of the sector holes with elliptical micro-holes sample. 88

5.9 Pressure test results before and after thermal stability test, with a linear fit. 89

5.10 Thermal stability test results for the sector holes with elliptical micro-holes sample. . 90

5.11 Simulation of refractive index change of micro-structured sensors in PM fibres. . . . 92

5.12 Schematic of induced birefringence created by femtosecond laser inside an optical fibre [2]. 92

5.13 Micro graphs of stress rod created by femtosecond laser [2]. 93

6.1 FDTD simulation of Fano resonance spectra in photonic crystal structure [2]. 96

6.2 (a), (b) Scanning electron micrograph of the meta surface (c) Simulation of transmission and reflection spectra of the meta surface (d) Experimentally measured transmission and reflection spectra of the meta surface [3]. 98

6.3 (a), (b) Scanning electron micrograph of the bilayer photonic crystal (c) Simulated and measured reflection spectra of the bilayer photonic crystal (d) Partial zoom in view of the spectra [9]. 98

6.4 (a) Scanning electron micrograph of the photonic crystal slab (b) Scanning electron micrograph of the fibre tip sensor (c) Measured reflection spectra of the fibre tip sensor (d) Peak wavelength shift of the fibre tip sensor [13]. 99

6.5 (a) Schematic diagram of the fibre tip sensor (b) SEM of the fibre tip sensor (c) Average reflection spectra of the fibre tip sensor [15]. 100

6.6 Schematic diagram of the photonic crystal fibre tip. 101

6.7 Simulated reflection and transmission spectra of the photonic crystal fibre tip. 102

6.8 Simulated temperature response of the photonic crystal fibre tip. 102

6.9 SEM of the photonic crystal on a silicon on sapphire wafer. 103

7.1 SEM of the first photonic crystal fibre [1]. 109

7.2 Various photonic crystal fibres made at the University of Bath. [2]. 110

7.3 SEM of the PCF cross section before and after laser irradiation [8]. 110

7.4 Three patterns of liquid crystal molecule arrangement in PCF cavities. [10]. 110

7.5 The end face of the sintered sapphire photonic crystal fibre [11]. 111

7.6 Photonic crystal waveguides fabricated using the EFG method [13]. 112

7.7 Top view and cross-section microscopy images of the sapphire photonic crystal waveguide [14]. 112

7.8 Finite element simulation of the air-hole sapphire photonic crystal fibre mode. 113

7.9 Finite element simulation of the solid-hole sapphire photonic crystal fibre mode. . . . 114

7.10 Finite element simulation of the PCF modes at different layers. 116

7.11 (a) Confinement loss for different PCF layers (b) Confinement loss using a logarithmic coordinate axis. 116

7.12 Finite element simulation of the PCF modes in different lattice pitches. 118

8.1 Optical micrograph of the sapphire photonic crystal structure cross section in slab. . . 122

8.2 SEM of the sapphire photonic crystal structure cross section in slab. 122

8.3 Schematic diagram of the focal positions of two different refractive index matching oils. 123

8.4 Schematic Diagram of Optical Path Difference. 124

8.5 Phase maps of $\psi_R(\rho), \psi_{DP}(\rho), \psi'_R(\rho)$. 126

8.6 SLM phase mask required for the final compensation. 126

8.7 Corrected and uncorrected cross sectional micrographs of laser-modified regions. . . 127

8.8 AO corrected cross sectional micrographs of photonic crystal structure in sapphire slab. 128

8.9 Micrographs of cracks in the laser-modified region as power increases in sapphire slab. 128

8.10 Micrographs of the 3 tracks per cell photonic crystal laser-modified region in sapphire slab. 129

8.11 SEM of the 3 tracks per cell photonic crystal laser-modified region in sapphire fibre. . 129

8.12 Micrographs of the photonic crystal waveguide with different rings in sapphire slab. . 131

8.13 Micrographs of the photonic crystal waveguide with different rings. 131

8.14 Mode field of the waveguide and X Y cross-sectional profiles (the image has been noise-reduced and smoothed). 132

8.15 Micrographs of the sapphire photonic-crystal fibre cross section. 133

8.16 Mode field of the sapphire photonic-crystal fibre and X Y cross-sectional profiles (the image has been noise-reduced and smoothed). 134

8.17 Micrographs of the two orthogonal polarisation modes input after propagation in sapphire PCF. (a) adjust the polarisation to minimise the mode field (b) adjust the polarisation to maximise the mode field. 135

8.18 Cross-sectional micrographs of sapphire-slab photonic crystal waveguides incorporating Bragg gratings. The two structures compare PCW unit cells formed from a single laser-written track and from three adjacent laser-written tracks, respectively. The Bragg grating was written along the waveguide propagation direction by periodically modulating the femtosecond-laser exposure. 136

8.19 (a) Reflectivity spectrum of 3 tracks per cell PCW (b) Reflectivity spectrum of 1 track per cell PCW. 137

8.20 (a) PCW in the sapphire slab (b) PCW in the sapphire fibre. 138

8.21 Simulation of the mode field for a PCW with the innermost ring removed. 138

8.22 Normalised reflectivity spectra of the 7 cm sapphire photonic-crystal fibre Bragg grating sample for two orthogonal polarisation states before fusion splicing to SMF-28e. 139

8.23 Schematic of the sapphire photonic crystal FBG temperature sensor fusion splicing setup. 139

8.24 (a) The alignment screen for the two fibres before fusion splicing (b) Photo of the joint after fusion splicing. 140

8.25 Reflectivity spectrum of the 7 cm sapphire FBG sample after fusion splicing. 140

8.26 Spectra of the 7 cm sapphire FBG sensor at different temperatures between 100 °C to 700 °C. 141

8.27 Characterization curve of the 7 cm sapphire FBG sensor at different temperatures. . . 142

8.28 Spectra of the 4 cm sapphire FBG sensor at different temperatures between 25 °C to 1200 °C. 143

8.29 Characterization curve of the 4 cm sapphire FBG sensor at different temperatures. . . 143

List of Abbreviations

3D . . . . . Three-dimensional

FBG . . . . . Fibre Bragg Grating

IEA . . . . . International Energy Agency

OSA . . . . . Optical Spectrum Analyzer

LPG . . . . . Long-Period fibre Grating

MSF . . . . . Micro-Structured fibre

FEA . . . . . Finite-Element Analysis

SMF . . . . . Single-Mode fibre

PM . . . . . Polarization-Maintaining

EV . . . . . Electric Vehicle

BMM . . . . . Battery Monitoring and Management

SHM . . . . . Structural Health Monitoring

FP . . . . . Fabry-Perot

SVEA . . . . . Slowly varying envelope approximation

LCF . . . . . Large cladding fibre

FDTD . . . . . Finite-difference time-domain

SEM . . . . . Scanning electron micrograph

PCF . . . . . Photonic crystal fibre

1 | Introduction

1.1 Research Motivation

Optical fibre sensors are now widely deployed across industrial processes, structural and geotechnical health monitoring, oil and gas operations, geothermal reservoirs, nuclear facilities and aerospace, leveraging both point sensing (e.g., fibre Bragg gratings) and distributed modalities such as distributed temperature and acoustic sensing [1, 2]. Against this broad backdrop, in recent years, several major economies, including the United States, China, Norway, the Netherlands, Germany, and the United Kingdom, have defined timetables for phasing out internal-combustion-engine vehicles, reflecting recognition of the transport sector's significant share of carbon emissions [3]. By 2023, nearly 14 million electric vehicles were sold globally, representing 18% of all cars sold and a 35% increase over 2022 [4]. With forecasts from the International Energy Agency (IEA) suggesting electric cars could represent up to two-thirds of global sales in 2035, thereby cutting oil consumption by as much as 12 million barrels per day. Nevertheless, battery safety and longevity remain significant obstacles to the broader adoption of electric vehicles. In particular, thermal runaway incidents can trigger fires of considerable intensity that are difficult to suppress, thereby posing a serious threat to public safety [5]. As a consequence, the need for advanced battery monitoring and management systems (BMM) has correspondingly increased. BMM systems play a pivotal role in optimizing battery performance, ensuring health monitoring, and safeguarding overall safety [6, 7]. They rely on the precise measurement of parameters such as voltage, current, temperature, and pressure, which are then processed via monitoring algorithms to achieve these essential functions [8].

In earlier implementations, temperature sensors were frequently constructed using thermocouples or thermistors, whereas pressure sensors predominantly relied on capacitive, Hall-effect, or piezoelectric materials [9, 10]. These sensors are prone to diverse forms of electromagnetic inter-

ference and chemical corrosion, and similar placement constraints arise in many harsh industrial environments, preventing their effective placement in critical areas within the battery. As a result, the BMM system is confined to using data from externally positioned sensors to infer the internal parameters of the battery [10, 11]. Under these circumstances, employing a more conservative battery design becomes necessary to ensure adequate safety.

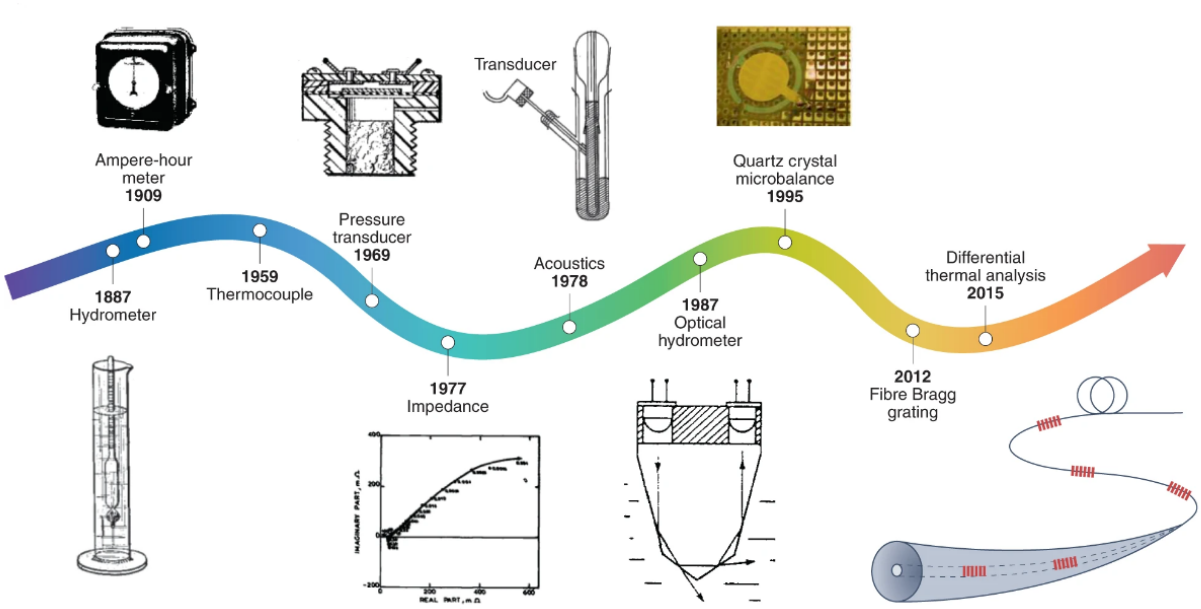


Figure 1.1: The development history of key battery sensing technology [12].

In order to design more advanced, high-performance batteries, it is essential to identify sensors that can be positioned within the battery itself. Compared to conventional electronic sensors, optical fibre sensors possess several attributes that render them especially suitable for this role. Their insensitivity to electromagnetic interference and inherent electrical insulation enable them to operate effectively in complex electromagnetic environments. Moreover, the external polyimide coating on the fibre helps guard against chemical corrosion. An additional advantage is the fibre's compact size, light weight, and low cost; even when placed inside the battery, it does not significantly affect the overall dimensions or mass of the system. These benefits are difficult to achieve with traditional electronic sensors, highlighting the importance of developing optical fibre sensors for operation under extreme conditions. Beyond batteries, these same attributes underpin robust monitoring in subsurface

and high-temperature settings.

Optical fibre sensors also hold substantial promise in the realm of structural health monitoring (SHM) for both infrastructure and aircraft. Over time, various types of infrastructure such as bridges, railways, and skyscrapers undergo aging processes that can compromise their integrity. To avert catastrophic failures, it is prudent to deploy sensor networks that enable continuous monitoring of structural health [13]. Aircraft impose the most stringent requirements on structural safety, making fibre-optic-based SHM broadly suitable for both airframe structures and engines. As aircraft are highly sensitive to weight and size, optical fibre sensors present significant advantages over traditional electronic sensors in these respects. There is also technology available that enables the embedding of optical fibre sensors into the composite materials used in aircraft manufacturing [14]. Moreover, optical fibre sensors offer multi-point monitoring capabilities. For instance, fibre Bragg grating sensors occupy only a narrow operational bandwidth, allowing multiple sensors to be incorporated into a single fibre for measuring different points [15]. In the future, cascading FBG sensor networks to simultaneously assess parameters such as temperature, pressure, strain, and vibration holds substantial promise for advanced monitoring applications [16].

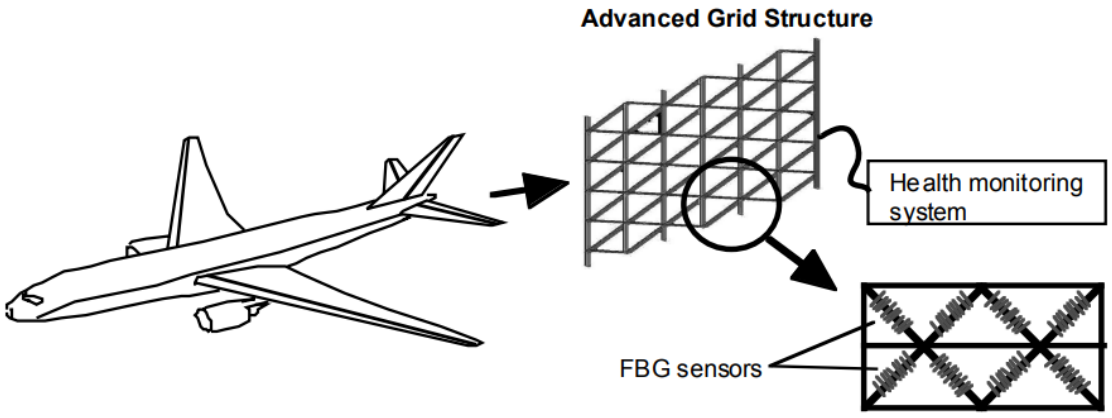


Figure 1.2: Schematic diagram of the FBG sensor grid in the aircraft [15].

In addition to their roles in battery health monitoring and infrastructure diagnostics, fibre Bragg grating sensors are also in high demand within the clean energy sector, particularly for operations

under extreme conditions. Nuclear energy constitutes a vital source of clean power, accounting for over 10% of global electricity generation according to the IEA. In the United Kingdom, policy signals point to sustained expansion: the Civil Nuclear Roadmap sets an ambition of up to 24 gigawatts by 2050, Great British Nuclear continues the small modular reactor technology selection process, and in July 2025 the government confirmed a final investment decision for Sizewell C. To attain the goal of net-zero carbon emissions by 2050, investments in nuclear power will need to expand by at least twofold. Optical fibre sensors enable temperature and strain measurements in high-radiation, high-temperature environments; moreover, their compact footprint, intrinsic electrical insulation, and inherent multiplexing capability confer indispensable advantages. Developing advanced nuclear reactors necessitates new sensors capable of enduring temperatures exceeding 1,000°C and exposure to extreme nuclear radiation. Compared with fused silica fibres, single-crystal sapphire fibre sensors have demonstrated significant promise in meeting these demanding requirements [17]. On the one hand, sapphire possesses a melting point of approximately 2050°C, whereas fused silica optical fibre begins to soften at around 1400°C. On the other hand, the amorphous structure of fused silica can be severely compromised by intense radiation exposure, leading to significant performance degradation, whereas the single-crystal structure of sapphire exhibits greater resilience under such conditions [17, 18].

Beyond batteries, nuclear facilities and general infrastructure, geothermal applications increasingly employ fibre optic sensing under high temperature and pressure. In wells and heat exchange fields, distributed temperature sensing provides continuous, depth resolved thermal profiles for reservoir characterisation and thermal response testing, while distributed acoustic sensing assists seismic surveillance and flow zone identification [19, 20, 21]. Recent deployments document routine use from boreholes to urban geothermal projects. Policy support has strengthened: in August 2025 the UK Department for Energy Security and Net Zero published the UK Geothermal Energy Review and Cost Estimations with updated levelised costs for heat and power. Global geothermal power capacity

reached about 15.1 gigawatts at the end of 2024, indicating growing demand for resilient in well and surface fibre sensing.

Research on optical fibre sensors offers substantial benefits across a variety of critical applications, including next-generation battery systems, structural health monitoring, and the clean energy sector. The research on micro-structured optical fibre sensors for extreme environments presented in this thesis is expected to further advance the application of optical fibre sensing technologies in these domains.

1.2 The history of FBG

Over the past 47 years, fibre-optic sensing has experienced rapid technological development, largely attributable to its immunity to electromagnetic interference, robust reliability, absence of an internal power supply requirement, remote and multiplexed operational capabilities, compact size, light weight, high sensitivity, and resilience to elevated temperatures and pressures [22, 23, 24, 25]. In 1977, K. Hill and his research group at the Canadian Communications Research Centre achieved a significant milestone by producing the first FBG. This was accomplished by exposing germanium-doped silica fibres to standing waves generated by an argon ion laser [26, 27]. Due to two-photon absorption, the periodic fringes formed by the standing wave yielded a corresponding periodic change in refractive index within the fibre, thus creating the FBG structure.

This early standing-wave-based method is straightforward to implement but relies on Ge-doped silica single mode fibre and a single-frequency laser whose operating wavelength must fall within the photosensitive region. Consequently, the final Bragg wavelength produced is equal to that of the laser source, thereby introducing substantial constraints. Despite its initial promise, progress in this field remained slow for nearly a decade, until G. Meltz and W. Morey, among others, successfully demonstrated a transverse holographic inscription technique in which the core of a germanosilicate

fibre is exposed from the side to a two-beam UV interference pattern (244 or 257 nm), thereby forming a Bragg grating in 1989. Following this breakthrough, research on FBG expanded rapidly, leading to the development of multiple fabrication techniques [28]. Because the refractive index modulation is nonlinear, once a certain threshold is reached during the exposure process, further increases in exposure time no longer result in additional changes to the refractive index [29]. Consequently, higher-order reflections may occur.

Another widely utilized method for fabricating FBG is the phase-mask technique. While this approach facilitates large-scale production, it still necessitates high-pressure H_2 loading to achieve ultrahigh ultraviolet photosensitivity in standard optical fibres [30]. Additionally, Ge-B-doped optical fibres may serve as alternatives to hydrogenated fibres [31]. By substituting a femtosecond laser for the ultraviolet laser source, it becomes feasible to inscribe FBG in non-photosensitive fibres [32]. By contrast, fibre Bragg gratings fabricated via the standing-wave method or UV-laser transverse holographic/phase-mask side-writing are susceptible to high-temperature degradation, whereas femtosecond-laser inscription yields gratings with exceptional thermal stability.

In 1996, K. M. Davis and colleagues discovered that focusing femtosecond laser pulses within glass could be used to fabricate waveguides [34, 35]. While no precise physical model currently provides a quantitative explanation for this phenomenon, it is well established that the extremely high peak power and ultrashort pulse duration of femtosecond lasers induce complex nonlinear optical interactions in the material, leading to permanent modifications of its refractive index and microstructure [36, 37]. This technology can be employed not only for the fabrication of optical waveguides but also for FBGs. Femtosecond laser irradiation enhances the refractive index modulation in FBGs, making them more pronounced and eliminating the need for photosensitive fibre or hydrogen loading, thus simplifying the fabrication process [38, 39]. Fibre Bragg Grating fabricated using ultraviolet interference methods tend to degrade at temperatures around 700°C. By contrast, the work of D. Grobnic and colleagues demonstrates that FBGs produced in silica optical fibres through a combination

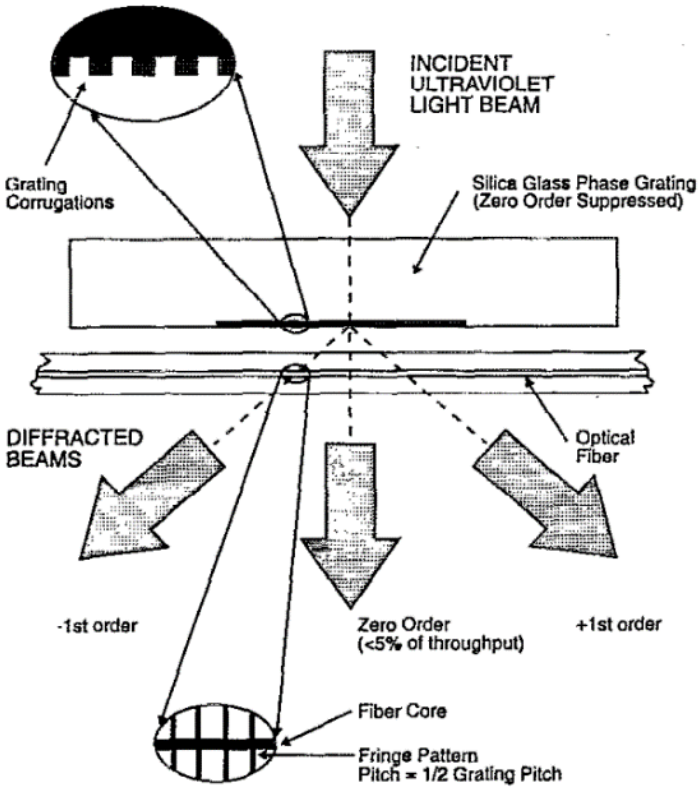


Figure 1.3: Phase mask method [33].

of femtosecond laser exposure and a phase mask can remain stable at 1000°C [40]. Even in the absence of a phase mask, FBGs can be fabricated by tightly focusing a femtosecond laser into the fibre core and translating the fibre axially with high-precision stages in a point-by-point manner [41, 42]. The refractive index modification in this process is driven by multi-photon absorption and avalanche ionization, making this approach especially suitable for the fabrication of long-period fibre gratings [43]. A long-period fibre grating is a periodic modulation (with period much larger than for FBG) that couples the core mode to forward-propagating cladding modes, creating wavelength-dependent attenuation in transmission.

This image has been removed from the dissemination version for copyright reasons. For the original figure, please see: Jörg Burgmeier et al. "Point-by-point inscription of phase-shifted fibre Bragg gratings with electro-optic amplitude modulated femtosecond laser pulses". In: Optics letters 39.3 (2014), pp. 540–543.

Figure 1.4: Femtosecond laser writing method [44].

A primary constraint of this technique arises from aberrations introduced by the fibre's cylindrical geometry during laser focusing, which compromise both the beam's precision and the resulting FBG quality. Employing an oil-immersion objective whose refractive index matches that of the fibre can address these distortions; however, the viscosity of the oil may cause slight misalignments when the fibre is in motion [45]. An alternative is to enclose the fibre within a sleeve made from a material of similar refractive index, featuring a planar interface capable of achieving a comparable corrective effect. More recently, adaptive optics have been employed to rectify aberrations induced by the fibre itself, ensuring accurate beam focusing after its entry into the fibre and eliminating the need for index-matching oils [46].

1.3 Research progress on FBG sensors

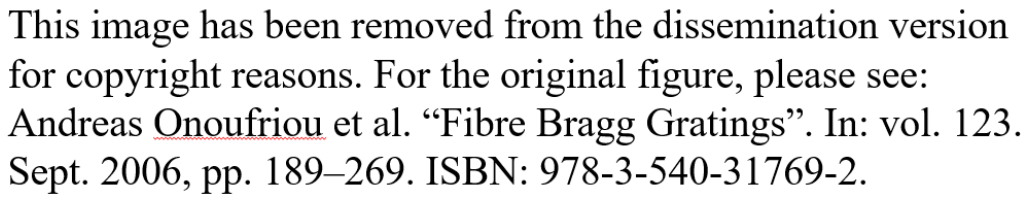


Figure 1.5: Schematic diagram for two superimposed FBG [47].

Since the late twentieth century, researchers have investigated the feasibility of employing FBGs as sensors. Their high sensitivity to temperature, pressure, vibration, strain, and acceleration makes FBGs suitable for measuring multiple parameters. However, the capacity to detect various factors simultaneously has both benefits and drawbacks: on one hand, FBGs function as versatile, multifunctional sensors; On the other, these different variables can interfere with one another. One potential solution involves using two distinct FBGs to measure temperature and pressure concurrently, followed by a matrix-based computation to resolve each parameter independently and thereby mitigate the cross-sensitivity between temperature and pressure. Building on this principle, Xu et al. utilized two superimposed FBGs with different wavelengths (850 nm and 1300 nm) to measure tempera-

ture and pressure simultaneously [48]. In practical engineering applications, such as measuring the strain on aircraft engine components, FBGs may be attached directly to engine structures. Given the inevitable fluctuations in internal engine temperature, employing a dual-FBG approach effectively addresses this challenge by enabling accurate strain measurements while mitigating the influence of temperature variations [49]. However, discrimination in some reported implementations is modest, especially under large temperature spans or in harsh environments, suggesting that additional techniques or higher contrast in sensitivity may be required[50].

Alternatively, G. P. Brady and colleagues achieved similar results using the first- and second-order diffraction wavelengths of a single FBG [51]. According to coupled mode theory, the diffraction equation for first-order diffraction is $\lambda_B = 2n_{eff}\Lambda$, while for second-order diffraction it is $\lambda_B = n_{eff}\Lambda$, where n_{eff} is the refractive index and Λ is the grating period. Consequently, the second-order wavelength is precisely half the first-order wavelength, effectively functioning as two distinct FBGs. By applying the matrix-based solution, one can analyze these resonances simultaneously, thereby simplifying the sensing system in comparison to using two physically separate FBGs. However, in practice the discrimination is not perfect. Because n_{eff} is wavelength-dependent and the thermo-optical coefficient dn/dT can differ slightly between wavelengths, the sensitivity contrast is limited, leading to residual cross-sensitivity and modest separation performance under realistic conditions. In a separate approach, S. W. James and collaborators experimented with joining FBG of different diameters for dual measurement of temperature and pressure, attaining a maximum error of $\pm 1^{\circ}$ within a 120°C range [52]. Beyond variations in diameter, researchers also fused fibres with different dopant elements. Because the two fibres possess distinct parameters, their temperature sensitivities differ even though their pressure sensitivities remain identical, allowing them to measure both temperature and pressure simultaneously [53].

Research conducted by H. J. Patrick and colleagues demonstrates that integrating a long-period fibre grating (LPG) with a FBG provides another viable approach. An LPG is characterized by a

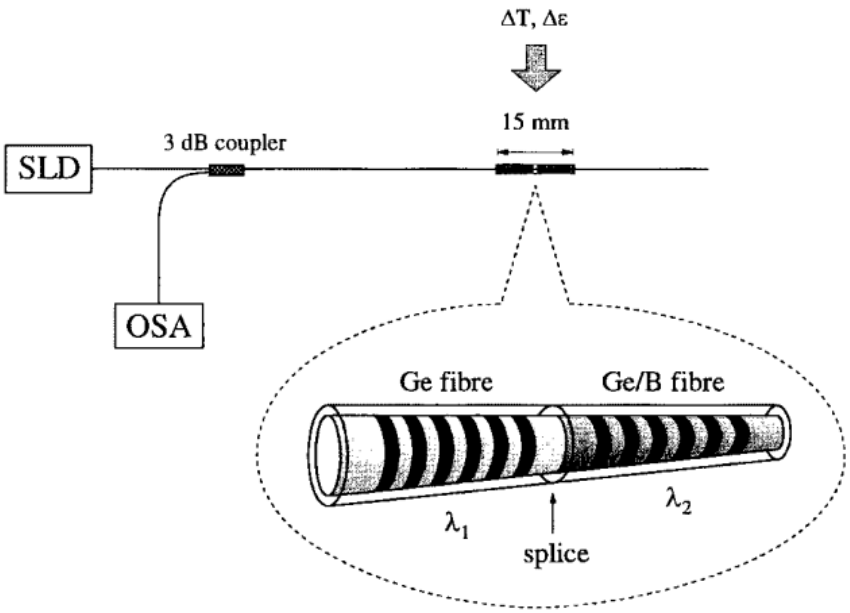


Figure 1.6: Fibre Bragg Grating written in germanosilicate and boron-codoped germanosilicate fibres [53].

substantially larger grating period relative to its operating wavelength, causing its guided mode to couple into the cladding mode [54]. Because the selected LPG exhibits markedly different temperature and pressure sensitivities compared to an FBG, employing two FBGs together with one LPG enables comprehensive multi-parameter measurement [55].

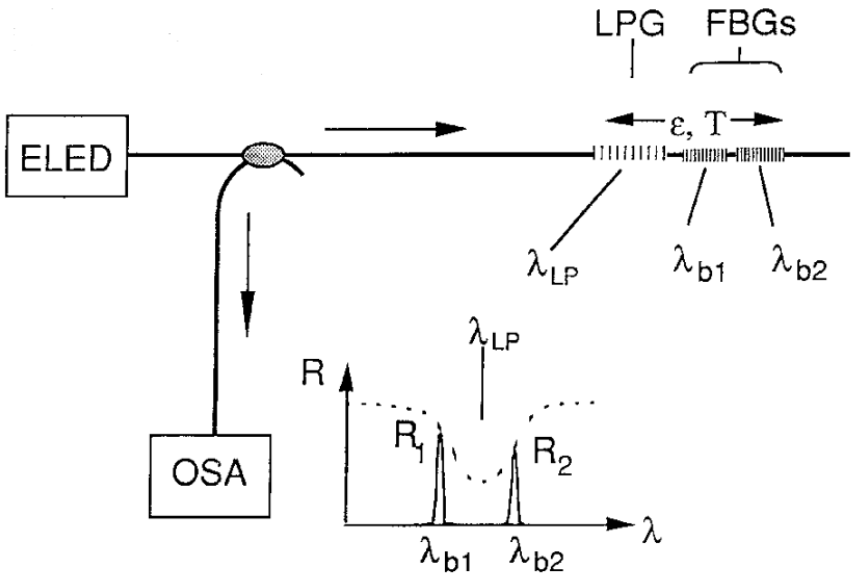


Figure 1.7: Schematic diagram for FBG and LPG sensor system [55].

Incorporating microstructures and air holes into the optical fibre offers an alternative approach

that enables a single device to measure both temperature and pressure in parallel. This design relies on embedded features that induce a non-uniform stress distribution within the fibre when subjected to external pressure. According to the stress-optic effect, the presence of uneven stresses in the fibre causes the refractive index to become anisotropic, so that each orthogonal polarisation mode experiences a different effective refractive index n_{eff}. By the Bragg relation, a change in n_{eff} for each mode produces a corresponding shift in its Bragg wavelength, giving rise to a splitting of the reflection peak into two distinct resonances. Importantly, because pressure tends to enhance anisotropy, an increase in external pressure further magnifies the difference between the two n_{eff} values, thereby increasing the separation between the two Bragg peaks. In contrast, temperature changes induce isotropic refractive index variations that shift both modes equally and do not alter the peak separation.

Jewart C. M. and colleagues employed a femtosecond laser to inscribe FBG on a 220 μm diameter optical fibre containing two air holes, each measuring 90 μm in diameter [56]. Their sensors exhibited stable performance at temperatures up to 800°C and were capable of measuring external pressures ranging from 15 to 2000 psi. Figures 1.8 and 1.9 illustrate the testing apparatus and the experimental results, respectively.

This image has been removed from the dissemination version for copyright reasons. For the original figure, please se
Charles M Jewart et al. "Ultrafast femtosecond-laser-in
fibre Bragg gratings in air-hole microstructured fibres f
temperature pressure sensing". In: Optics letters 35.9 (2
pp. 1443–1445.

Figure 1.8: Schematic of pressure-testing setup and cross-section photo [56].

This image has been removed from the dissemination version for copyright reasons. For the original figure, please see:
Charles M Jewart et al. "Ultrafast femtosecond-laser-induced fibre Bragg gratings in air-hole microstructured fibres for high-temperature pressure sensing". In: Optics letters 35.9 (2010), pp. 1443–1445.

Figure 1.9: Response of FBG sensor to external pressure at room temperature [56].

The same technique was utilized by T. Chen and colleagues to fabricate a pressure sensor. They also fused the 220 μm diameter fibre to a standard 125 μm diameter fibre for ease of testing [57]. One limitation of this method is that, under relatively low external pressures, the separation of the reflection peaks is not readily discernible, making it difficult to measure small pressure variations. Beyond using fibres with two circular holes, researchers have additionally explored photonic crystal

fibres containing numerous micro-scale holes.

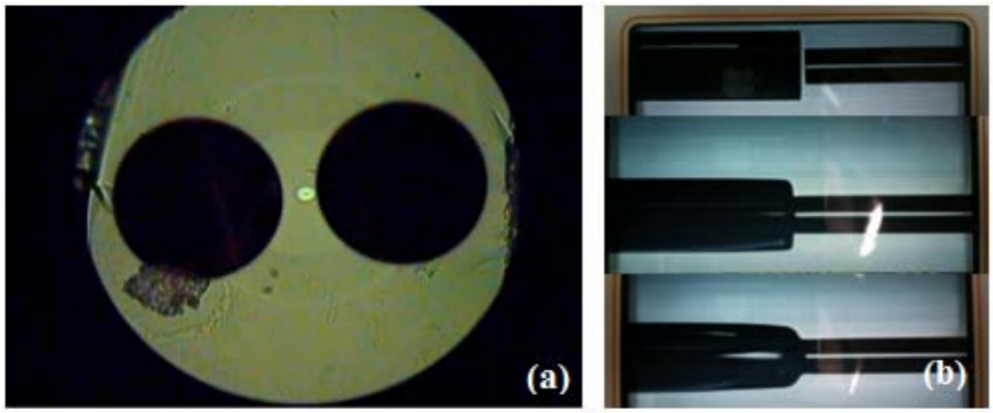


Figure 1.10: The cross-section photo and fusion splice photo [57].

J. Y. Huang and colleagues employed a butterfly-shaped micro-structured fibre to construct a pressure sensor. By inscribing the fibre Bragg grating within this micro-structured fibre (MSF), they achieved a pressure sensitivity of 3.30 pm/bar. Furthermore, after seven days of operation at 280°C, the standard deviation of the measured pressure was only 0.42 bar [58]. Figure 1.11 depicts the cross-sectional profile of the MSF they used, as well as the reflection peak separation attributable to intrinsic birefringence in the absence of external pressure.

This image has been removed from the dissemination version for copyright reasons. For the original figure, please see: Ji-Ying Huang et al. "FBGs written in specialty fibre for high pressure/high temperature measurement". In: Optics express 25.15 (2017), pp. 17936–17947.

Figure 1.11: Reflectance spectra and cross-sectional electron micrographs of sensor sample [58].

They employed a fibre fusion splicer to join the MSF with a standard fibre, resulting in a 12 dB insertion loss due to factors such as partial endface mismatch and the collapse of micro-holes. When multiple FBGs are connected in series to form a distributed sensor, these losses must be carefully considered. Moreover, only a limited number of facilities can customize this specialized fibre, and its production cost remains relatively high.

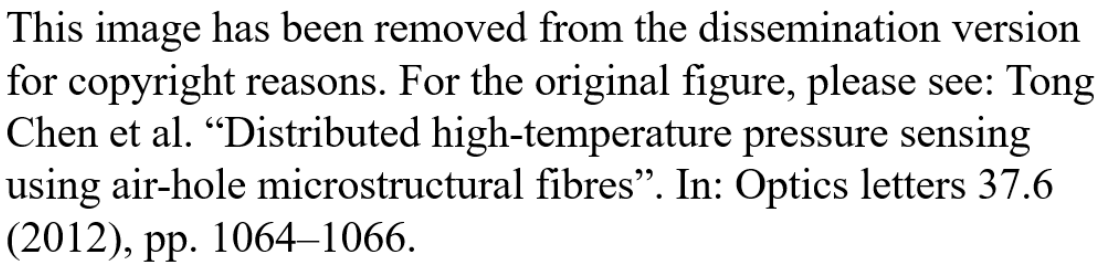


Figure 1.12: Microscope cross-section image and FEA results [59].

T. Chen et al. further employed finite-element analysis (FEA) to calculate the sensitivity of an additional MSF sensor and an air-hole fibre sensor. Rather than inscribing an FBG within this MSF, they utilized spatially resolved Rayleigh scattering to measure pressure [59]. Their simulation results indicate that the pressure sensitivity of the fibre labeled (b) in Figure 1.12 is approximately four to five times higher than that of the fibre labeled (a). These findings also underscore the value of using simulation to guide and optimize sensor design.

1.4 Research progress on sapphire optical fibre sensors

In addition to mitigating cross-sensitivity challenges, expanding the operational range of these sensors has become a significant research focus. Numerous high-temperature applications in the clean energy and aerospace sectors cannot be effectively addressed by silica optical fibres, which are limited to temperatures below approximately 900°C. Consequently, researchers have turned their attention to single-crystal sapphire fibre sensors as a more suitable alternative under extreme conditions. Compared with conventional core-clad silica fibres, sapphire fibres offer greater resistance to high-temperature softening and radiation-induced degradation, but are typically available in shorter lengths and lack a well-defined core-cladding structure. As a result, unmodified sapphire fibres support multiple propagation modes, making additional mode-control or microstructuring strategies necessary for high-resolution sensing. Sapphire fibre-based temperature sensors can be broadly categorized into three main types: radiometric sensors, Fabry-Perot (FP) sensors, and FBG sensors [60]. Radiometric

sensing relies on blackbody radiation principles, where a layer of material is attached to the terminus of the sapphire fibre to approximate a cylindrical blackbody cavity. By measuring the radiance spectrum emitted from this structure, the temperature can be determined [61].

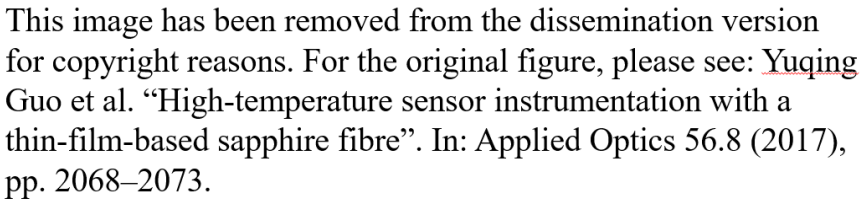


Figure 1.13: Schematic diagram of a radiometric temperature sensing system [62].

A common approach involves sputtering a metallic layer, such as iridium or molybdenum, onto the tip of the sapphire fibre (Figure 1.13), followed by an alumina film to protect against oxidation under high-temperature conditions [61, 62]. This design typically facilitates temperature measurements in the range of approximately 600°C to 2000°C. However, it cannot effectively measure below 500°C, and the sensor often exhibits a relatively slow response time. Additionally, post-processing of the spectral data is required to calculate the temperature. Moreover, the metallic coating at the fibre tip typically consists of high-temperature-resistant precious metals, increasing both manufacturing complexity and cost.

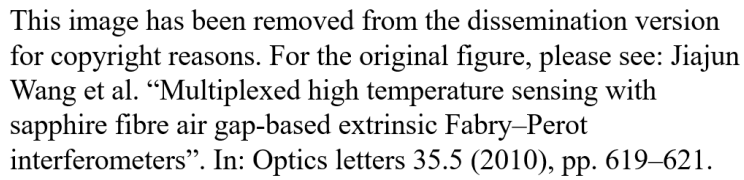


Figure 1.14: Schematic diagram of a FP sensor in sapphire fibre [63].

The fundamental principle of FP sensors is based on optical interference. As shown in Figure 1.14, by employing sapphire fibres in conjunction with other supporting materials, an FP cavity is constructed. When the ambient temperature varies, thermal expansion and the thermo-optic effect induce changes in both the cavity's dimensions and the refractive index of the fibre, which in turn alter the reflected spectrum. In 2003, Anbo Wang and colleagues developed the FP sensor based on

sapphire fibre by aligning two polished sapphire fibre endfaces at a fixed distance on a ceramic plate [64]. Subsequent studies experimented with various methods, such as bonding two sapphire fibres within a ceramic sleeve or adhering a sapphire fibre at one end of the sleeve and a sapphire wafer at the other [63, 65, 66]. However, these designs do not fully exploit the high-temperature capabilities of sapphire, as they all depend on adhesives. Consequently, operational temperatures generally cannot exceed 1600°C, and the stability and lifespan of adhesives at elevated temperatures impose additional constraints. Moreover, adhesive-bonded assemblies are difficult to manufacture and align, and they are not well suited to multipoint configurations.

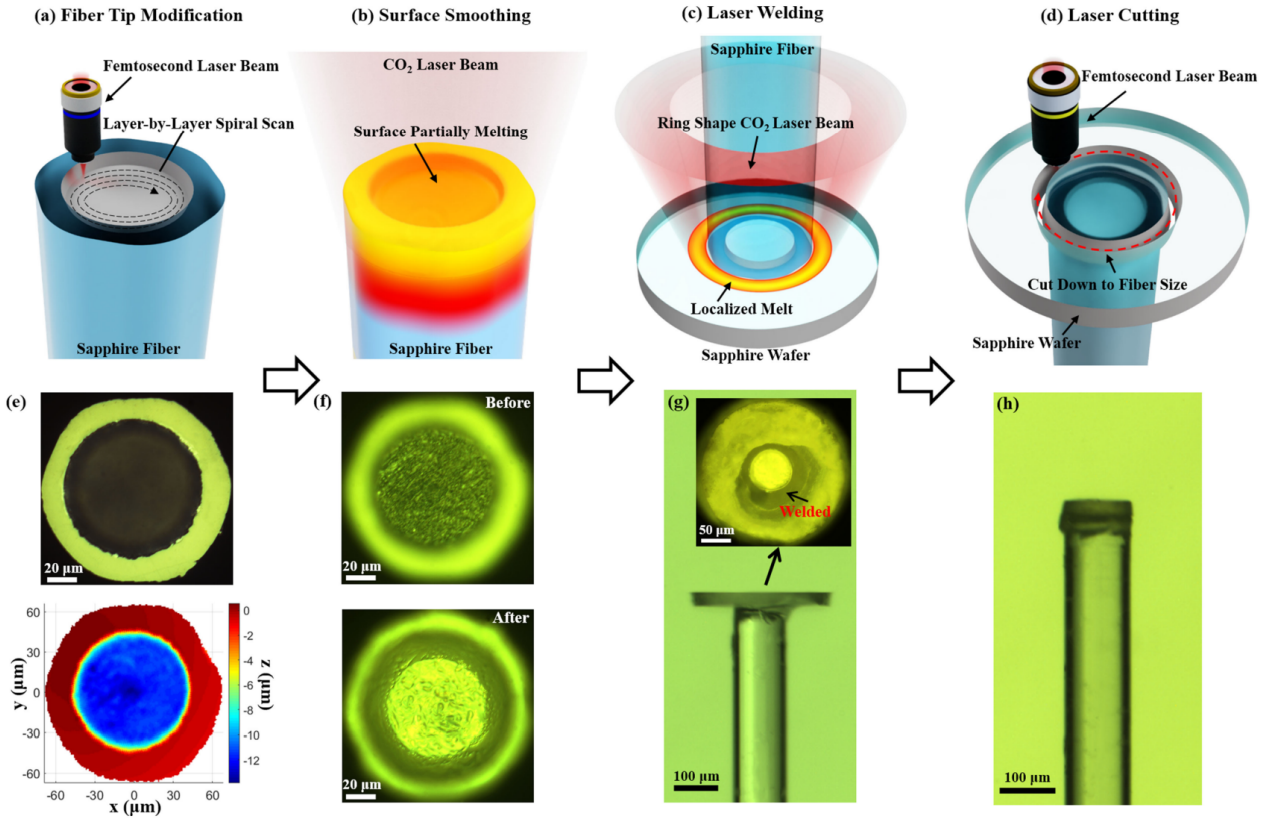


Figure 1.15: Adhesive free FP sensor fabrication process [67].

In order to circumvent the stability issues associated with adhesives, Shuo Yang et al. employed femtosecond laser irradiation combined with hydrofluoric acid wet etching to sculpt a cylindrical recess in the endface of a sapphire fibre [67]. Subsequently, they polished the recess bottom with a focused CO_2 laser and then laser-welded a sapphire wafer onto the top of the recess to form a FP cavity. This approach eliminates the need for adhesives and sleeves, resulting in a more compact

device. However, the manufacturing process (Figure 1.15) is exceptionally intricate and requires extremely precise laser welding. Overall, although the operational principle of sapphire fibre-based FP sensors is relatively straightforward, they place high demands on the precision of the cavity's endface. Any surface irregularities, dust particles, or misalignment can substantially degrade the signal-to-noise ratio. Moreover, most existing designs depend on adhesives, which undermines sensor reliability at high temperatures. Incorporating ceramic sleeves or wafer structures onto the fibre also negates much of the size advantage that optical fibre sensors typically afford.

The operating principle of FBG sensors does not differ from that of FBG sensors in silica fibres. However, because sapphire fibres lack the core, light propagates in multi-mode, each mode has a different n_{eff}, resulting in a broad FBG reflection spectrum that decreases the sensor's temperature resolution. In 2004, D. Grobnic and colleagues employed a femtosecond laser and a phase mask to fabricate the first FBG in a 150 μm-diameter sapphire fibre [68]. Their sensors can operate in 1500°C environments and have a sensitivity of 25 pm/°C at 1200°C. The figure below presents the reflection spectrum of their sensor and a corresponding microscopic image.

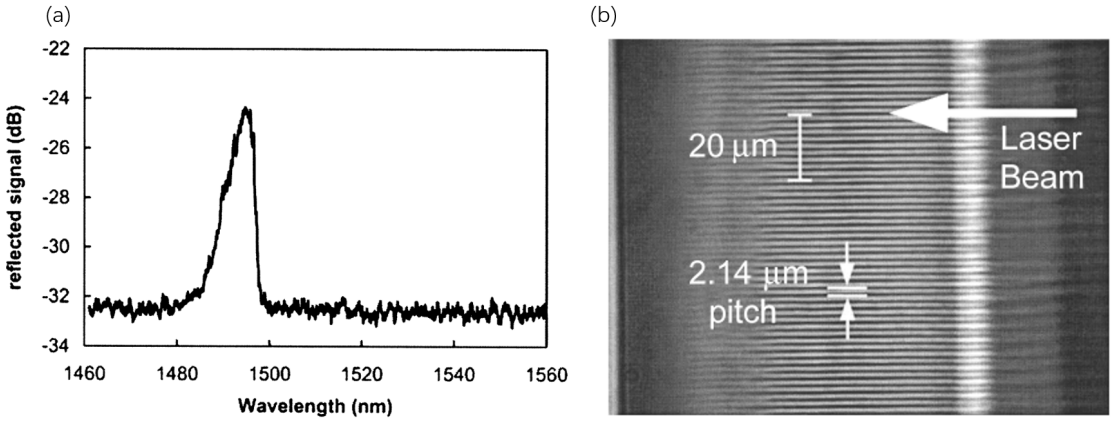


Figure 1.16: Fibre Bragg Grating reflection spectrum and sensor microscopic image [68].

In an effort to enhance the sensor's resolution, D. Grobnic et al. proposed a method wherein a 125 μm-diameter single-mode fibre is fusion spliced, through a tapered tip, to a thinner sapphire fibre with a diameter of 60 μm [69]. This design more effectively couples the modes from the single-mode

fibre into the sapphire fibre, thereby producing a relatively narrow FBG reflection peak. Nonetheless, the low mechanical strength at the fusion splice and the complexity of the fabrication process present significant challenges.

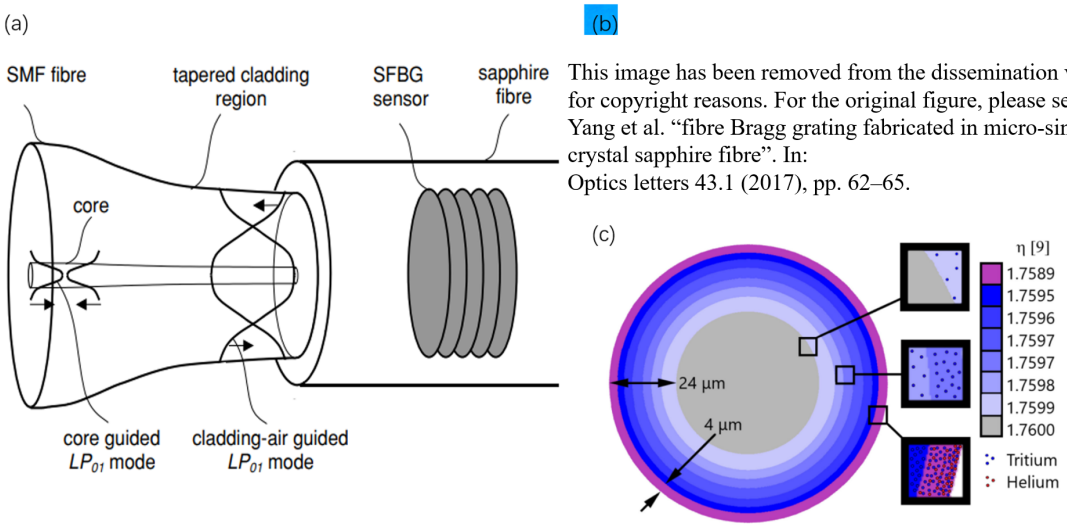


Figure 1.17: (a) Schematic diagram of fusion splicing with tapered fibre tip [68]. (b) Microscopic image of sapphire fibre after wet etching [70]. (c) Schematic diagram of the refractive index distribution change due to nuclear radiation [71].

Beyond this approach, Shuo Yang et al. employed wet etching using sulfuric and phosphoric acids to reduce the diameter of the sapphire fibre to 9.6 μm [70]. As shown in Figure 1.17b, although this dimension matches the typical core diameter of a conventional single-mode fibre, the large refractive-index contrast precludes strictly single-mode guidance and yields multiple peaks in the reflection spectrum. A similar concept involves placing the sapphire fibre in a reactor (Figure 1.17c), where high-energy alpha and tritium particles bombard the outer layer, inducing nanoscale structural damage and thus reducing the refractive index of the outer portion [71]. This procedure seeks to form a core-cladding structure akin to that of a traditional fibre. However, the manufacturing process is prohibitively complex, and it remains inaccessible to produce a genuinely single-mode fibre.

In recent years, notable advancements have been made in fabricating FBGs in sapphire fibres via femtosecond laser inscription. In 2017, Y. Shuo and colleagues employed a 780 nm infrared femtosec-

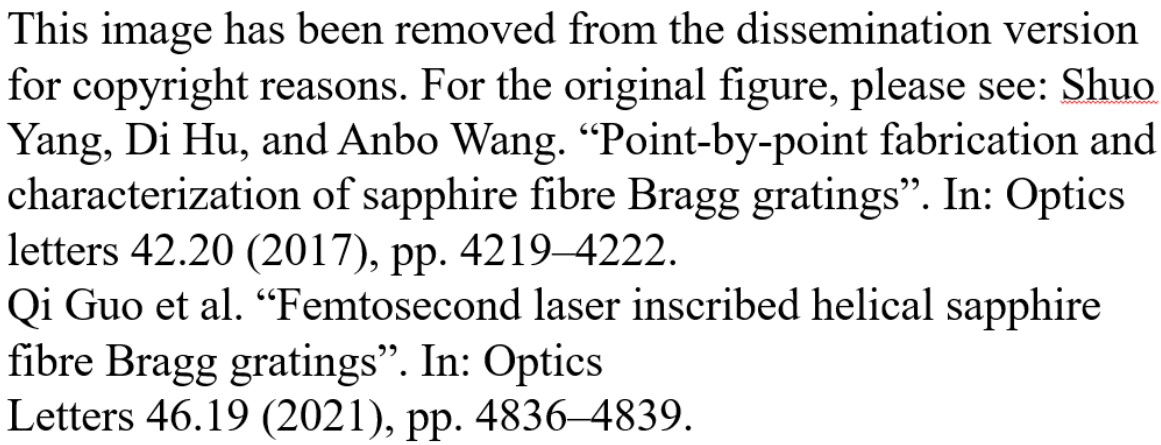


Figure 1.18: (a) Schematic diagram of point-by-point writing method to produce FBG in sapphire fibre [72]. (b) Schematic diagram of helical scanning approach to produce FBG in sapphire fibre [73].

ond laser and a point-by-point writing method (Figure 1.18a) to produce a FBG with a reflectivity of 0.6% [72]. Subsequently, in 2021, Q. Guo and collaborators utilized a 515 nm femtosecond laser with a helical scanning approach (Figure 1.18b) to create an FBG featuring a larger refractive index modulation region, achieving a reflectivity of 40% and a higher-quality reflection spectrum [73].

Femtosecond laser irradiation in silica fibres induces structural modifications that increase the refractive index, while in sapphire, these same processes lead to a decrease in refractive index. Exploiting this property, it becomes possible to employ femtosecond lasers to create precisely engineered cladding structures in sapphire that enable single-mode propagation. In 2019, researchers fabricated waveguides on sapphire slabs capable of single-mode transmission at a mid-infrared wavelength of 2850 nm [74]. Subsequently, Mohan Wang and colleagues developed waveguides in sapphire fibres supporting single-mode transmission at the more commonly used wavelength of 1550 nm [75]. They utilized a 515 nm femtosecond laser and adopted adaptive optics rather than refractive index matching oils to correct the aberrations introduced by the sapphire fibre geometry during the fabrication process. Figure 1.19a presents a schematic diagram of the manufacturing system they employed. To accommodate the hexagonal fibre geometry, they characterised the curvature-induced aberration and applied real-time compensation via a spatial light modulator, enabling cladding-by-cladding in-

scription of concentric rings that lower the refractive index around an unmodified core. Additionally, the team inscribed an FBG within this structure, achieving a narrow bandwidth of 0.3 nm, a crucial improvement to enhance temperature resolution in sensing applications.

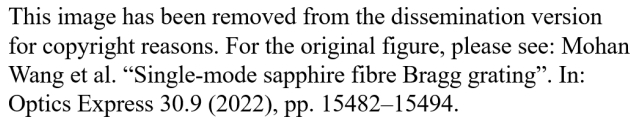


Figure 1.19: (a) Schematic diagram of adaptive optics-based femtosecond laser fabrication system [75]. (b) Microscopic image of a sapphire single-mode fibre [75]. (c) Mode profile of the sapphire single-mode fibre at 1550 nm [75].

Although single-mode sapphire FBGs produced via femtosecond laser inscription exhibit strong temperature resolution, structural defects that often arise during fabrication lead to elevated transmission losses, making it challenging to create sufficiently long single-mode fibres for broader applications. In summary, the various technological approaches to sapphire fibre sensors demonstrate considerable potential for use under extreme conditions; however, additional research is required to address existing shortcomings before these methods can be widely adopted in industrial settings.

1.5 Thesis Outline

This thesis is organised into nine chapters. Chapter 1, the Introduction, outlines the motivation for the study and reviews recent advances in fibre optic sensing. Chapter 2 presents the theoretical framework employed throughout the work, covering coupled-mode theory as applied to FBG, the sensing principles of FBG, birefringence in optical fibre, the stress-optic Effect, and the thermo-optic effect. Chapter 3 describes the numerical design of micro-structured fibre FBG sensors, while Chapter 4 details their fabrication by femtosecond-laser inscription combined with wet chemical etching. Chapter 5 reports pressure and thermal-stability tests of the resulting devices. Chapter 6 introduces preliminary simulations and prototype fabrication of sapphire photonic crystal fibre tip sensors. Chapter 7 explains the operating principles of sapphire fibre sensors and proposes an optimised design. Chap-

ter 8 presents experimental characterisation of the sapphire photonic crystal fibre sensors. Finally, Chapter 9 summarises the findings and offers a critical analysis of the contributions made by the study.

References

[1] Mattia Francesco Bado and Joan R Casas. "A review of recent distributed optical fiber sensors applications for civil engineering structural health monitoring". In: *Sensors* 21.5 (2021), p. 1818.

[2] Mohamed Elsherif et al. "Optical fiber sensors: Working principle, applications, and limitations". In: *Advanced Photonics Research* 3.11 (2022), p. 2100371.

[3] Vera O'Riordan et al. "How and why we travel–mobility demand and emissions from passenger transport". In: *Transportation Research Part D: Transport and Environment* 104 (2022), p. 103195.

[4] IEA. *Global EV Outlook 2024*. Tech. rep. Licence: CC BY 4.0. Paris: IEA, 2024. URL: https://www.iea.org/reports/global-ev-outlook-2024.

[5] Da Li et al. "Battery safety issue detection in real-world electric vehicles by integrated modeling and voltage abnormality". In: *Energy* 284 (2023), p. 128438.

[6] Hossam A Gabbar, Ahmed M Othman, and Muhammad R Abdussami. "Review of battery management systems (BMS) development and industrial standards". In: *Technologies* 9.2 (2021), p. 28.

[7] Matteo Dotoli et al. "A Review of Mechanical and Chemical Sensors for Automotive Li-Ion Battery Systems". In: *Sensors* 22.5 (2022), p. 1763.

[8] Gregory L Plett. *Battery management systems, Volume I: Battery modeling*. Artech House, 2015.

[9] Zhe Li et al. "Examining temporal and spatial variations of internal temperature in large-format laminated battery with embedded thermocouples". In: *Journal of Power Sources* 241 (2013), pp. 536–553.

[10] Yang-Duan Su et al. "fibre optic sensing technologies for battery management systems and energy storage applications". In: *Sensors* 21.4 (2021), p. 1397.

[11] Nassim A Samad et al. "Influence of battery downsizing and SOC operating window on battery pack performance in a hybrid electric vehicle". In: *2015 IEEE Vehicle Power and Propulsion Conference (VPPC)*. IEEE. 2015, pp. 1–6.

[12] Jiaqiang Huang, Steven T Boles, and Jean-Marie Tarascon. "Sensing as the key to battery lifetime and sustainability". In: *Nature Sustainability* 5.3 (2022), pp. 194–204.

[13] Yang Zhao et al. "A laser-based fibre Bragg grating ultrasonic sensing system for structural health monitoring". In: *IEEE Photonics Technology Letters* 28.22 (2016), pp. 2573–2576.

[14] Gayan C Kahandawa et al. "Use of FBG sensors for SHM in aerospace structures". In: *Photonic Sensors* 2.3 (2012), pp. 203–214.

[15] H Takeya, T Ozaki, and N Takeda. "Structural health monitoring of advanced grid structure using multipoint FBG sensors". In: *Smart Structures and Materials 2005: Industrial and Commercial Applications of Smart Structures Technologies*. Vol. 5762. SPIE. 2005, pp. 204–211.

[16] Iker García et al. "Optical fibre sensors for aircraft structural health monitoring". In: *Sensors* 15.7 (2015), pp. 15494–15519.

[17] Pattrick Calderoni et al. "Innovative sensing technologies for nuclear instrumentation". In: *2019 IEEE International Instrumentation and Measurement Technology Conference (I2MTC)*. 2019, pp. 1–6.

[18] Guy Cheymol et al. "High level gamma and neutron irradiation of silica optical fibres in CEA OSIRIS nuclear reactor". In: *2007 9th European Conference on Radiation and Its Effects on Components and Systems*. 2007, pp. 1–5.

[19] Anna Carmela Violante et al. "Use of distributed temperature sensing (DTS) coupled to ground source heat exchangers for geological thermo-stratigraphic correlation". In: *Renewable Energy* 225 (2024), p. 120242.

[20] Jérôme Azzola, Katja Thiemann, and Emmanuel Gaucher. "Integration of distributed acoustic sensing for real-time seismic monitoring of a geothermal field". In: *Geothermal Energy* 11.1 (2023), p. 30.

[21] Michael Iten et al. "Distributed fiber-optic temperature monitoring in boreholes of a seasonal geothermal energy storage". In: *Procedia Structural Integrity* 64 (2024), pp. 1642–1648.

[22] Byoungho Lee. "Review of the present status of optical fibre sensors". In: *Optical fibre technology* 9.2 (2003), pp. 57–79.

[23] Bo Dong et al. "High extinction-ratio dual thin-taper fibre interferometer fabricated by arc-discharge and its performance as sensors". In: *Optics Communications* 355 (2015), pp. 225–229.

[24] Xuewen Shu et al. "Dependence of temperature and strain coefficients on fibre grating type and its application to simultaneous temperature and strain measurement". In: *Optics letters* 27.9 (2002), pp. 701–703.

[25] Y-J Rao. "fibre Bragg grating sensors: principles and applications". In: *Optical fibre sensor technology*. Springer, 1998, pp. 355–379.

[26] Kenneth O Hill et al. "Photosensitivity in optical fibre waveguides: Application to reflection filter fabrication". In: *Applied physics letters* 32.10 (1978), pp. 647–649.

[27] Brian S Kawasaki et al. "Narrow-band Bragg reflectors in optical fibres". In: *Optics Letters* 3.2 (1978), pp. 66–68.

[28] Gerald Meltz, William W Morey, and William H Glenn. "Formation of Bragg gratings in optical fibres by a transverse holographic method". In: *Optics letters* 14.15 (1989), pp. 823–825.

[29] Sema Kurtaran and M Selami Kılıçkaya. "The modelling of fibre Bragg grating". In: *Optical and quantum electronics* 39.8 (2007), pp. 643–650.

[30] P Lemaire et al. "μHigh pressure H2 loading as a technique for achieving ultrahigh UV photosensitivity and thermal sensitivity in GeO2 doped optical fibres". In: *OHFWURQLFV/HWWHUV* 29 (1993), 1191^{2}1193.

[31] Dan Grobnic et al. "Ultrafast IR laser writing of strong Bragg gratings through the coating of high Ge-doped optical fibres". In: *IEEE Photonics Technology Letters* 20.12 (2008), pp. 973–975.

[32] J Thomas et al. "Inscription of fibre Bragg gratings with femtosecond pulses using a phase mask scanning technique". In: *Applied Physics A* 86.2 (2007), pp. 153–157.

[33] Kenneth O Hill et al. "Bragg gratings fabricated in monomode photosensitive optical fibre by UV exposure through a phase mask". In: *Applied Physics Letters* 62.10 (1993), pp. 1035–1037.

[34] K. M. Davis et al. "Writing waveguides in glass with a femtosecond laser". In: *Opt. Lett.* 21.21 (1996), pp. 1729–1731.

[35] K. Miura et al. "Photowritten optical waveguides in various glasses with ultrashort pulse laser". In: *Applied Physics Letters* 71.23 (1997), pp. 3329–3331.

[36] Kiyotaka Miura et al. "Space-selective growth of frequency-conversion crystals in glasses with ultrashort infrared laser pulses". In: *Opt. Lett.* 25.6 (2000), pp. 408–410.

[37] Jianrong Qiu et al. "Permanent photoreduction of Sm3+ to Sm2+ inside a sodium aluminoborate glass by an infrared femtosecond pulsed laser". In: *Applied Physics Letters* 74.1 (1999), pp. 10–12. ISSN: 0003-6951.

[38] K Arai et al. "Two-photon processes in defect formation by excimer lasers in synthetic silica glass". In: *Applied physics letters* 53.20 (1988), pp. 1891–1893.

[39] Adrian Dragomir et al. "Inscription of fibre Bragg gratings by ultraviolet femtosecond radiation". In: *Opt. Lett.* 28.22 (2003), pp. 2171–2173.

[40] D Grobnic et al. "Long-term thermal stability tests at 1000 °C of silica fibre Bragg gratings made with ultrafast laser radiation". In: *Measurement Science and Technology* 17.5 (2006), p. 1009.

[41] A. Martinez et al. "Direct writing of fibre Bragg gratings by femtosecond laser". In: *Electronics Letters* 40 (19 2004), pp. 1170–1172.

[42] Nemanja Jovanovic et al. "100 W CW Yb3+-Doped Silica fibre Laser Utilizing an Active-Core Inscribed Point-by-Point Bragg Grating". In: *Bragg Gratings, Photosensitivity, and Poling in Glass Waveguides*. Optica Publishing Group. 2007, BWB7.

[43] Yuki Kondo et al. "Fabrication of long-period fibre gratings by focused irradiation of infrared femtosecond laser pulses". In: *Opt. Lett.* 24.10 (1999), pp. 646–648.

[44] Jörg Burgmeier et al. "Point-by-point inscription of phase-shifted fibre Bragg gratings with electro-optic amplitude modulated femtosecond laser pulses". In: *Optics letters* 39.3 (2014), pp. 540–543.

[45] Lin Chen et al. "High-quality fibre Bragg grating inscribed in ZBLAN fibre using femtosecond laser point-by-point technology". In: *Optics Letters* 47.14 (2022), pp. 3435–3438.

[46] Patrick S Salter et al. "Femtosecond fibre Bragg grating fabrication with adaptive optics aberration compensation". In: *Optics Letters* 43.24 (2018), pp. 5993–5996.

[47] Andreas Onoufriou et al. "Fibre Bragg Gratings". In: vol. 123. Sept. 2006, pp. 189–269. ISBN: 978-3-540-31769-2.

[48] MG Xu et al. "Discrimination between strain and temperature effects using dual-wavelength fibre grating sensors". In: *Electronics letters* 30.13 (1994), pp. 1085–1087.

[49] Eric J. Ruggiero et al. "Decoupled temperature and strain measurements using fibre Bragg grating sensors". In: *Photonic fibre and Crystal Devices: Advances in Materials and Innovations in Device Applications II*. Ed. by Shizhuo Yin and Ruyan Guo. Vol. 7056. International Society for Optics and Photonics. SPIE, 2008, 70561Y.

[50] Guanghui Chen et al. "Simultaneous strain and temperature measurements with fiber Bragg grating written in novel Hi-Bi optical fiber". In: *IEEE Photonics Technology Letters* 16.1 (2004), pp. 221–223.

[51] G.P. Brady et al. "Simultaneous measurement of strain and temperature using the first- and second-order diffraction wavelengths of Bragg gratings". English. In: *IEE Proceedings Optoelectronics* 144.3 (1997), pp. 156–161. ISSN: 1350-2433.

[52] SW James, ML Dockney, and RP Tatam. "Simultaneous independent temperature and strain measurement using in-fibre Bragg grating sensors". In: *Electronics Letters* 32.12 (1996), pp. 1133–1134.

[53] PM Cavaleiro et al. "Simultaneous measurement of strain and temperature using Bragg gratings written in germanosilicate and boron-codoped germanosilicate fibres". In: *IEEE Photonics Technology Letters* 11.12 (1999), pp. 1635–1637.

[54] Turan Erdogan. "Cladding-mode resonances in short-and long-period fibre grating filters". In: *JOSA A* 14.8 (1997), pp. 1760–1773.

[55] HJ Patrick et al. "Hybrid fibre Bragg grating/long period fibre grating sensor for strain/temperature discrimination". In: *IEEE Photonics Technology Letters* 8.9 (1996), pp. 1223–1225.

[56] Charles M Jewart et al. "Ultrafast femtosecond-laser-induced fibre Bragg gratings in air-hole microstructured fibres for high-temperature pressure sensing". In: *Optics letters* 35.9 (2010), pp. 1443–1445.

[57] Tong Chen et al. "Thermally regenerated fibre Bragg gratings in twin-air-hole microstructured fibres for high temperature pressure sensing". In: *fibre Optic Sensors and Applications VIII*. Vol. 8028. SPIE. 2011, pp. 32–39.

[58] Ji-Ying Huang et al. "FBGs written in specialty fibre for high pressure/high temperature measurement". In: *Optics express* 25.15 (2017), pp. 17936–17947.

[59] Tong Chen et al. "Distributed high-temperature pressure sensing using air-hole microstructural fibres". In: *Optics letters* 37.6 (2012), pp. 1064–1066.

[60] Botao Wang et al. "Review of high temperature measurement technology based on sapphire optical fibre". In: *Measurement* 184 (2021), p. 109868. ISSN: 0263-2241.

[61] RR Dils. "High-temperature optical fibre thermometer". In: *Journal of applied Physics* 54.3 (1983), pp. 1198–1201.

[62] Yuqing Guo et al. "High-temperature sensor instrumentation with a thin-film-based sapphire fibre". In: *Applied Optics* 56.8 (2017), pp. 2068–2073.

[63] Jiajun Wang et al. "Multiplexed high temperature sensing with sapphire fibre air gap-based extrinsic Fabry–Perot interferometers". In: *Optics letters* 35.5 (2010), pp. 619–621.

[64] Hai Xiao et al. "Single-crystal sapphire fibre-based strain sensor for high-temperature applications". In: *Journal of lightwave technology* 21.10 (2003), p. 2276.

[65] Yizheng Zhu et al. "Sapphire-fibre-based white-light interferometric sensor for high-temperature measurements". In: *Optics letters* 30.7 (2005), pp. 711–713.

[66] Yizheng Zhu and Anbo Wang. "Surface-mount sapphire interferometric temperature sensor". In: *Applied optics* 45.24 (2006), pp. 6071–6076.

[67] Shuo Yang et al. "All-sapphire miniature optical fibre tip sensor for high temperature measurement". In: *Journal of Lightwave Technology* 38.7 (2019), pp. 1988–1997.

[68] Dan Grobnic et al. "Sapphire fibre Bragg grating sensor made using femtosecond laser radiation for ultrahigh temperature applications". In: *IEEE Photonics Technology Letters* 16.11 (2004), pp. 2505–2507.

[69] Dan Grobnic et al. "Single and low order mode interrogation of a multimode sapphire fibre Bragg grating sensor with tapered fibres". In: *Measurement Science and Technology* 17.5 (2006), p. 980.

[70] Shuo Yang et al. "fibre Bragg grating fabricated in micro-single-crystal sapphire fibre". In: *Optics letters* 43.1 (2017), pp. 62–65.

[71] Joshua T Jones et al. "Light propagation considerations for internally clad sapphire optical fibre using the 6Li (n, α) 3H reaction". In: *Journal of Lightwave Technology* 40.4 (2022), pp. 1181–1187.

[72] Shuo Yang, Di Hu, and Anbo Wang. "Point-by-point fabrication and characterization of sapphire fibre Bragg gratings". In: *Optics letters* 42.20 (2017), pp. 4219–4222.

[73] Qi Guo et al. "Femtosecond laser inscribed helical sapphire fibre Bragg gratings". In: *Optics Letters* 46.19 (2021), pp. 4836–4839.

[74] Jean-Philippe Bérubé et al. "Femtosecond laser inscription of depressed cladding single-mode mid-infrared waveguides in sapphire". In: *Optics Letters* 44.1 (2018), pp. 37–40.

[75] Mohan Wang et al. "Single-mode sapphire fibre Bragg grating". In: *Optics Express* 30.9 (2022), pp. 15482–15494.

2 | Background

This chapter primarily presents the theoretical foundations relevant to this thesis. It includes the coupled-mode theory used to explain the operating principles of FBGs, the sensing mechanisms of FBGs, birefringence in micro-structured optical fibre, as well as the stress-optic effect, thermal expansion, and thermo-optic effect.

2.1 Coupled-Mode Theory of FBG

Coupled mode theory was introduced in the 1950s by scholars across multiple fields, including S. E. Miller, who applied it to elucidate coupled transmission lines; J. R. Pierce, who utilized it to describe space charge waves; and R. W. Gould, who employed it in formulating the theory of backward-wave oscillators [1, 2, 3]. More than two decades later, a series of researchers began applying coupled mode theory to planar waveguides and optical fibres [4]. For instance, A. W. Snyder employed it to describe modal propagation in both uniform and slightly perturbed cylindrical fibres, while D. Marcuse used it to analyze mode propagation in fibres containing defects [5, 6]. In 1999, Raman Kashyap provided a detailed exposition on interpreting FBG through coupled mode theory [7]. This paper briefly introduces Raman's coupled-mode theory in optical fibres.

The propagation of light in optical fibre follows Maxwell's equations.

$$\begin{aligned} \nabla \times \vec{H} &= \vec{J} + \frac{\partial \vec{D}}{\partial t} \\ \nabla \times \vec{E} &= -\frac{\partial \vec{B}}{\partial t} \\ \nabla \cdot \vec{B} &= 0 \\ \nabla \cdot \vec{D} &= \rho_f \end{aligned} \tag{2.1}$$

Since there is no free current density in the optical fibre so $\vec{J} = 0$, combining the Ampere's law equation and Faraday's law equation in 2.1, constitutive relations in materials $\vec{D} = \varepsilon_0\vec{E} + \vec{P}$ and $\vec{B} = \mu_0\vec{H}$, we get

$$\nabla^2\vec{E} = \mu_0\varepsilon_0\frac{\partial^2\vec{E}}{\partial t^2} + \mu_0\frac{\partial^2\vec{P}}{\partial t^2}. \tag{2.2}$$

Because the FBG consists of a periodically varying refractive index within the optical fibre core, and the absolute difference in refractive index remains small, this variation can be regarded as a perturbation. Under these circumstances, the total polarization response can be represented as the sum of an intrinsic component and a perturbation component:

$$\vec{P} = \vec{P_0} + \vec{P_g} \tag{2.3}$$

where

$$\vec{P_0} = \varepsilon_0\chi_e\vec{E} = \varepsilon_0(\varepsilon_r - 1)\vec{E} \tag{2.4}$$

thus equation 2.2 becomes,

$$\nabla^2\vec{E} = \mu_0\varepsilon_0\varepsilon_r\frac{\partial^2\vec{E}}{\partial t^2} + \mu_0\frac{\partial^2\vec{P_g}}{\partial t^2} \tag{2.5}$$

where μ_0 and ε_0 are the permeability and permittivity of free space, respectively, ε_r is the relative permittivity of the unperturbed fibre material, $\vec{P_0}$ is the intrinsic polarisation of the unperturbed fibre material, $\vec{P_{\mathrm{g}}}$ is the grating-induced perturbation to the material polarisation, and χ_e is the electric susceptibility. Equation 2.5 can also be written in terms of its Cartesian field components, E_x, E_y, and E_z. The modes of an optical fibre consist of a collection of guided modes and radiation modes. Guided modes remain confined to the fibre core, whereas radiation modes leak into the cladding.

Consequently, the coupling into radiation modes can be disregarded. Under this assumption, the modes equation takes the form,

$$E(r,t) = \frac{1}{2}\sum_{m} A_m(z)\zeta^{(m)}(x)e^{i(\omega t-\beta_m z)} + c.c. \tag{2.6}$$

where m represents the mode number and c.c. indicates the complex conjugate. Using equation 2.6 in equation 2.5 gives the following results,

$$\begin{aligned}\nabla^2 &\left[\frac{1}{2}\sum_{m} A_m(z)\zeta^{(m)}(x)e^{i(\omega t-\beta_m z)} + c.c.\right] \\ = \mu_0\varepsilon_0\varepsilon_r &\frac{\partial^2}{\partial t^2}\left[\frac{1}{2}\sum_{m} A_m(z)\zeta^{(m)}(x)e^{i(\omega t-\beta_m z)} + c.c.\right] + \mu_0\frac{\partial^2 P_g}{\partial t^2}.\end{aligned} \tag{2.7}$$

Typically, the complex amplitude of modes in an FBG exhibits gradual variations over wavelength scale. Consequently, the slowly varying envelope approximation (SVEA) can be applied to simplify the governing equations, wherein higher-order derivatives are neglected in the differentiation process,

$$\left|\frac{\partial^2 A_m}{\partial z^2}\right| << \beta_m \left|\frac{\partial A_m}{\partial z}\right| \tag{2.8}$$

so $\nabla^2 E$ can be simplified to

$$\nabla^2 E = \frac{1}{2}\sum_{m}\left[-2i\beta_m\frac{\partial A_m}{\partial z}\zeta^{(m)}(x)e^{i(\omega t-\beta_m z)} - \beta_m^2 A_m\zeta^{(m)}(x)e^{i(\omega t-\beta_m z)} + c.c.\right]. \tag{2.9}$$

Taking equation 2.9 into equation 2.7 and using $\mu_0\varepsilon_0\varepsilon_r\omega^2 = \beta_m^2$ leads to

$$\sum_m \left[-i\beta_m \frac{\partial A_m}{\partial z}\zeta^{(m)}(x)e^{i(\omega t-\beta_m z)} + c.c. \right] = \mu_0 \frac{\partial^2 P_g}{\partial t^2}. \tag{2.10}$$

Multiplying both sides of the equation by complex conjugation $\zeta^{(m)}(x)^*$ and then integrating over the fibre cross section and applying the orthogonality relation gives

$$\sum_m \left[-2i\omega\mu_0 \frac{\partial A_m}{\partial z}e^{i(\omega t-\beta_m z)} + c.c. \right] = \int_{-\infty}^{+\infty}\int_{-\infty}^{+\infty} \mu_0 \frac{\partial^2 P_g}{\partial t^2}\zeta^{(m)}(x)^*\,dx\,dy. \tag{2.11}$$

Equation 2.1 illustrates the wave equation under perturbation, with the slowly varying envelope approximation (SVEA) applied. In an ideal fibre with no perturbations, the modes remain uncoupled. The equation demonstrates that refractive index modulation within the fibre core is what induces mode coupling. By analogy to conventional methods for handling wave equations, the solution can be represented as the superposition of forward- and backward-propagating waves.

$$\begin{aligned} &\left[\frac{\partial A_m}{\partial z}e^{i(\omega t-\beta_m z)} + c.c. \right] - \left[\frac{\partial B_n}{\partial z}e^{i(\omega t+\beta_n z)} + c.c. \right] \\ &= \frac{i}{2\omega}\int_{-\infty}^{+\infty}\int_{-\infty}^{+\infty} \frac{\partial^2 P_g}{\partial t^2}\zeta^{(mn)}(x)^*\,dx\,dy \end{aligned} \tag{2.12}$$

P_g is the perturbation term, which can be modelled as $P_g = \delta n(x,z)\varepsilon_0 E$. The δn represents the periodic refractive index modulation pattern. Ideally, in an FBG, the refractive index modulation within the fibre core is sinusoidal (yielding a single dominant Bragg wavelength). In actual fabrication, UV interference/phase-mask inscription approximates this sinusoidal profile, whereas femtosecond point-by-point writing produces discrete, relatively abrupt index perturbations; a perfectly abrupt transition between high and low refractive indices cannot be achieved. Instead, there is always a gradual tran-

sition between these regions. Consequently, the refractive index modulation for different fabrication techniques can be modelled by superimposing multiple harmonic components onto the average refractive index, and non-sinusoidal profiles (e.g., point-by-point) introduce higher spatial harmonics that can lead to additional spectral features and higher-order Bragg reflections. Therefore, $\delta n(x,z)$ can be given by

$$\delta n(x,z) = 2n \left[\overline{\Delta n} + \frac{\Delta n}{2} \left(e^{i[(2\pi N/\Lambda)z + \phi(z)]} + cc \right) \right] \tag{2.13}$$

where $\overline{\Delta n}$ is the average value of the refractive index change within one period, $\phi(z)$ is a phase function that varies with position and Λ is the length of grating period. Next, by substituting P_g into the equation 2.12, one must ensure that the driving field and the generated field in the fibre remain in phase; in other words, they must satisfy the phase-matching condition for proper light propagation. Phase matching must fulfill the requirements specified by equation ($\Delta\beta = \beta_m + \beta_n - \frac{2\pi N}{\Lambda}$). Considering the simplest scenario involving coupling between two guided modes propagating in forward and backward directions, the following equations can be derived,

$$\begin{aligned} \frac{\partial B_n}{\partial z} e^{i(\omega t + \beta_n z)} + c.c. &= in\omega\varepsilon_0 B_n \int_{-\infty}^{+\infty} \int_{-\infty}^{+\infty} \overline{\Delta n} \zeta^{(mn)}(x) \zeta^{(mn)}(x)^* e^{i(\omega t + \beta_n z)}\, dx\, dy \\ &+ in\omega\varepsilon_0 A_m \int_{-\infty}^{+\infty} \int_{-\infty}^{+\infty} \frac{\Delta n}{2} e^{i[(2\pi N/\Lambda)z + \phi(z)]} \zeta^{(mn)}(x) \zeta^{(mn)}(x)^* e^{i(\omega t - \beta_m z)}\, dx\, dy + c.c. \end{aligned} \tag{2.14}$$

and simplifying the equation to give

$$\begin{aligned} \frac{\partial B_n}{\partial z} &= in\omega\varepsilon_0 B_n \int_{-\infty}^{+\infty} \int_{-\infty}^{+\infty} \overline{\Delta n} \zeta^{(mn)}(x) \zeta^{(mn)}(x)^*\, dx\, dy \\ &+ in\omega\varepsilon_0 A_m \int_{-\infty}^{+\infty} \int_{-\infty}^{+\infty} \frac{\Delta n}{2} e^{i[(2\pi N/\Lambda - \beta_m - \beta_n)z + \phi(z)]} \zeta^{(mn)}(x) \zeta^{(mn)}(x)^*\, dx\, dy. \end{aligned} \tag{2.15}$$

To enhance the clarity and readability of the equations, two coupling constants,κ_1 and κ_2 can be introduced to rewrite the expressions as follows,

$$\frac{\partial B_n}{\partial z} = i\kappa_1 B_n + i\kappa_2 A_m e^{-i[\Delta\beta z - \phi(z)]} \tag{2.16}$$

where

$$\kappa_1 = n\omega\varepsilon_0 \int_{-\infty}^{+\infty}\int_{-\infty}^{+\infty} \overline{\Delta n}\zeta^{(mn)}(x)\zeta^{(mn)}(x)^* \, dx\, dy \tag{2.17}$$

$$\kappa_2 = n\omega\varepsilon_0 \int_{-\infty}^{+\infty}\int_{-\infty}^{+\infty} \frac{\Delta n}{2}\zeta^{(mn)}(x)\zeta^{(mn)}(x)^* \, dx\, dy. \tag{2.18}$$

Similarly, the equation for driving mode can be derived using a same approach.

$$\frac{\partial A_m}{\partial z} = -i\kappa_1 A_m - i\kappa_2^* B_n e^{i[\Delta\beta z - \phi(z)]} \tag{2.19}$$

Equation 2.19 and Equation 2.16 are both known as coupled-mode equation and κ_1, κ_2 are called coupling coefficients. To further simplify the solution process, two parameters can be introduced to replace the exponential terms in the equations [8].

$$\begin{aligned} R &= A_m e^{-(i/2)[\Delta\beta z - \phi(z)]} \\ S &= B_n e^{(i/2)[\Delta\beta z - \phi(z)]} \end{aligned} \tag{2.20}$$

Taking them into equation 2.16 and 2.19 leads to

$$\begin{aligned} \frac{dR}{dz} + i\left[\kappa_1 + \frac{1}{2}\left(\Delta\beta - \frac{d\phi(z)}{dz}\right)\right] R &= -i\kappa_2^* s \\ \frac{dS}{dz} - i\left[\kappa_1 + \frac{1}{2}\left(\Delta\beta - \frac{d\phi(z)}{dz}\right)\right] S &= i\kappa_2 R \end{aligned} \tag{2.21}$$

The equation can be expressed in matrix form and subsequently solved via the eigenvalue method. When α is real, the resulting power reflectivity is

$$|\Upsilon|^2 = \frac{\kappa_2^2 sinh^2(\alpha L)}{\delta^2 sinh^2(\alpha L) + \alpha^2 cosh^2(\alpha L)} \tag{2.22}$$

where

$$\delta = \kappa_1 + \frac{1}{2}\left(\Delta\beta - \frac{d\phi(z)}{dz}\right) \tag{2.23}$$

and

$$\alpha = \sqrt{|\kappa_2|^2 - \delta^2}. \tag{2.24}$$

Ideally, for the uniform grating $\dfrac{d\phi(z)}{dz} = 0$ and its reflection peak occurs at $\delta = 0$, the power reflectivity equation simplifies to $|\Upsilon|^2 = tanh^2(\kappa_2 L)$, so the centre wavelength is

$$\lambda_B = 2n_{neff}\Lambda. \tag{2.25}$$

2.2 Principles of Sensing

From Bragg equation 2.25, it can be seen that any change in the effective refractive index n_{eff} of the mode or in the grating period Λ will shift the central reflection wavelength. Because external factors such as temperature, strain and pressure influence both n_{eff} and Λ, fibre Bragg gratings can be employed to measure these parameters. Differentiating Eq. 2.25 leads to ,

$$\begin{aligned} \frac{d\lambda_B}{dX} &= 2\Lambda\frac{dn_{eff}}{dX} + 2n_{eff}\frac{d\Lambda}{dX} \\ \Delta\lambda_B = \frac{d\lambda_B}{dX}\Delta X &= \lambda_B(\frac{1}{n_{eff}}\frac{dn_{eff}}{dX} + \frac{1}{\Lambda}\frac{d\Lambda}{dX})\Delta X \end{aligned} \tag{2.26}$$

where X could be any physical quantity that can affect n_{eff} and Λ. When the FBG of a conventional optical fibre is subjected to strain $\varepsilon = \Delta L/L$, its central wavelength shifts according to

$$\frac{\Delta\lambda_B}{\lambda_B} = (1 - P_e)\varepsilon \tag{2.27}$$

where P_e denotes the effective stress-optic coefficient. This parameter depends on n_{eff}, the stress-optic coefficients P_{12} and P_{11}, as well as the material's Poisson ratio υ. When only the temperature changes, the central wavelength of the FBG shifts according to

$$\frac{\Delta\lambda_B}{\lambda_B} = (\alpha + \zeta)\Delta T \tag{2.28}$$

which arises from both thermal expansion and the thermo-optical effect. Here, $\alpha = \frac{1}{L}\frac{dL}{dT}$ is the thermal expansion coefficient of the fibre, and $\zeta = \frac{1}{n}\frac{dn}{dT}$ is the thermo-optical coefficient. By contrast,

a change in external pressure produces a similar influence on the FBG:

$$\frac{\Delta\lambda_B}{\lambda_B} = (\frac{1}{\Lambda}\frac{\partial\Lambda}{\partial P} + \frac{1}{n}\frac{\partial n}{\partial P})\Delta P \tag{2.29}$$

where

$$\begin{aligned} \frac{1}{\Lambda}\frac{\partial\Lambda}{\partial P} &= -\frac{1-2\upsilon}{E} \\ \frac{\partial n}{\partial P} &= \frac{n^2}{2E}(1-2\upsilon)(2P_{12}+P_{11}) \end{aligned} \tag{2.30}$$

In these expressions, E denotes the Young's modulus, and P_{11}, P_{12} are the stress-optic coefficients. Although the central reflection wavelength of an FBG is sensitive to variations in temperature, strain, or pressure, it cannot differentiate among these effects. For instance, when both strain and temperature change simultaneously, the centre wavelength is given by

$$\frac{\Delta\lambda_B}{\lambda_B} = (1-P_e)\varepsilon + (\alpha+\zeta)\Delta T = \kappa_\varepsilon\varepsilon + \kappa_\tau\Delta T \tag{2.31}$$

where κ_ε is a constant that depends solely on the Poisson ratio, the stress-optic coefficient, and the effective refractive index, while κ_τ is a constant determined by the thermo-optical coefficient and the thermal expansion coefficient.

A well-established strategy for decoupling strain and temperature involves employing two FBG systems with different sensitivities to both temperature and strain to perform simultaneous measurements. Their wavelength shifts can be expressed through the following matrix relationship:

$$\begin{pmatrix} \Delta\lambda_1 \\ \\ \Delta\lambda_2 \end{pmatrix} = \begin{pmatrix} \kappa_{\varepsilon 1} & \kappa_{\tau 1} \\ \\ \kappa_{\varepsilon 2} & \kappa_{\tau 2} \end{pmatrix} \begin{pmatrix} \Delta\varepsilon \\ \\ \Delta T \end{pmatrix} \tag{2.32}$$

For this strategy to function properly, it is necessary that $\frac{\kappa_{\varepsilon 1}}{\kappa_{\varepsilon 2}} \neq \frac{\kappa_{\tau 1}}{\kappa_{\tau 2}}$, which is the standard identifiability condition for two-parameter decoupling. One way to obtain sufficiently distinct coefficient pairs is to adopt a dual-wavelength scheme-i.e., use two gratings with widely separated Bragg wavelengths-to improve the conditioning of the sensitivity matrix, although this is not universally required. Dual-wavelength schemes, whether implemented with two gratings in the same fibre, with dissimilar grating types, or in different fibres, typically require at least two gratings (or equivalently, two sub-gratings), whereas a birefringence-based approach can operate with a single grating. Consequently, birefringence-based approaches are particularly effective for pressure or transverse-load sensing, where polarization-mode splitting is pronounced; for strain/temperature discrimination, however, the differential coefficients between the two polarization modes are typically modest, so the conditioning improvement is limited.

2.3 Birefringence in Optical fibre

2.3.1 Intrinsic birefringence

In optical fibres, birefringence can be divided into two categories: intrinsic birefringence and induced birefringence. Intrinsic birefringence arises from factors such as the manufacturing process, geometry, and material composition. Ideally, a single-mode fibre possesses a perfectly circular cross-section. Due to this circular symmetry, two orthogonal modes (X, Y) would, in principle, share the same propagation constant β. In practice, however, slight ellipticity in the fibre cross-section or thermal stresses from manufacturing processes lead to intrinsic birefringence. This phenomenon can be characterized by defining the normalized birefringence as the difference in effective refractive index between the

two orthogonal modes,

$$B = n_{eff}^{X} - n_{eff}^{Y}. \tag{2.33}$$

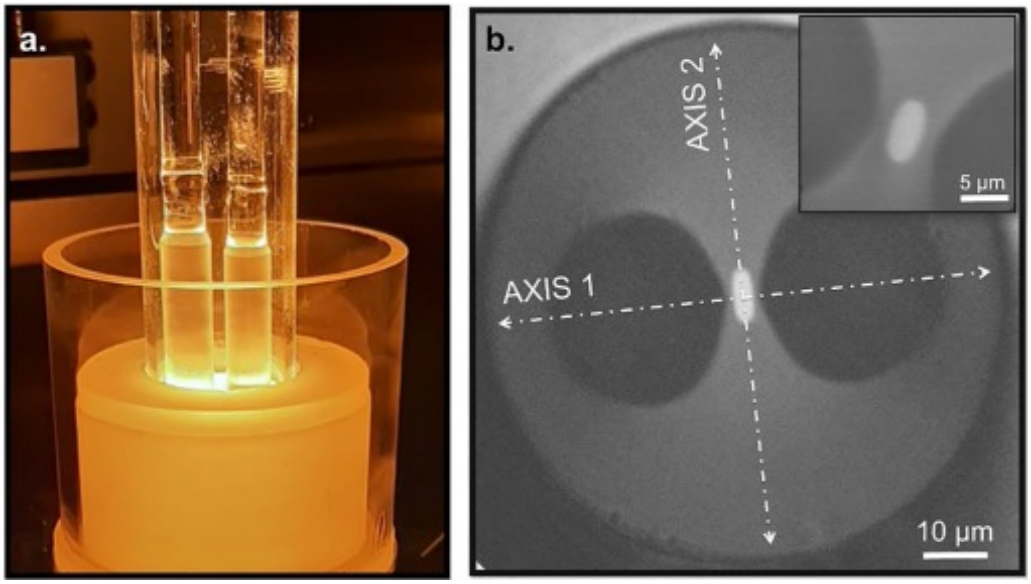


Figure 2.1: (a) Preform of polarization-maintaining fibre [9]. (b) Microscopic image of the polarization-maintaining fibre cross-section [9].

Based on this characteristic, high-birefringence fibres can be deliberately engineered to ensure that linearly polarized light maintains its initial polarization state during propagation. Such fibres are commonly referred to as polarization-maintaining fibres. Their production involves placing different materials in the fibre preform; during the drawing process, stress arises between these materials, modifying the refractive index distribution in the fibre cross-section and leading to a high level of birefringence. High birefringence fibres can also be created by introducing asymmetric design features into photonic crystal fibres.

2.3.2 Induced birefringence

The inherent stability of silica optical fibre makes it challenging to alter the core geometry once the fibre has been fabricated. However, external stress or deformation can modify the material's refractive

This image has been removed from the dissemination version for copyright reasons. For the original figure, please see: A Ortigosa-Blanch et al. "Highly birefringent photonic crystal fibres". In: Optics letters 25.18 (2000), pp. 1325–1327.

Figure 2.2: (a) Microscopic image of the photonic crystal fibre cross-section [10]. (b) Simulation design of the fibre cross-section [10].

index, owing to the stress-optic effect. For instance, when an optical fibre is bent, the resulting stress and shear forces alter the refractive index distribution within the fibre, thereby introducing birefringence known as induced birefringence. Femtosecond laser irradiation can also induce birefringence by altering the physical characteristics of the material in the focal region through complex nonlinear optical effects. These changes create stress differentials relative to the unexposed areas, which, in turn, modify the refractive index distribution [11]. Peter R. Herman and his research team have undertaken a comprehensive investigation into the birefringence induced by direct laser writing in silica optical fibres. Their findings reveal that variables such as the size of the laser-irradiated region, the laser's polarization direction, and the distance between the irradiated region and the fibre core all influence the extent of the induced birefringence [12].

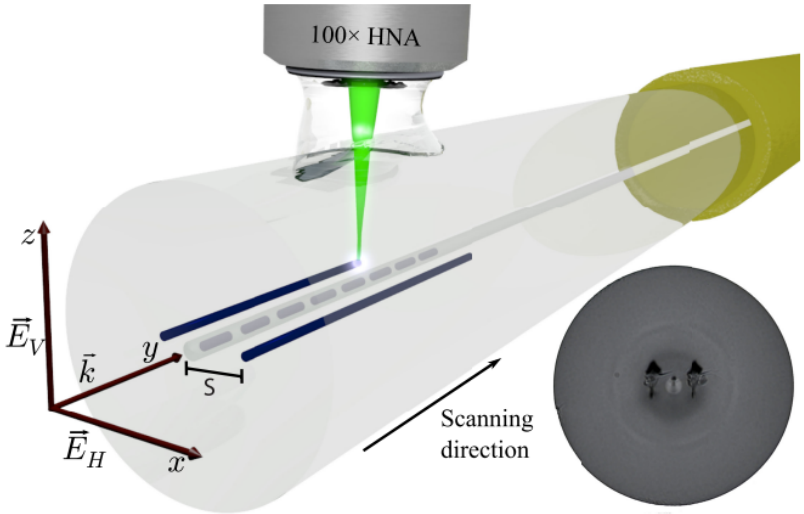


Figure 2.3: Schematic diagram of the induced birefringence created by femto-second laser and microscopic image of the fibre cross section [12].

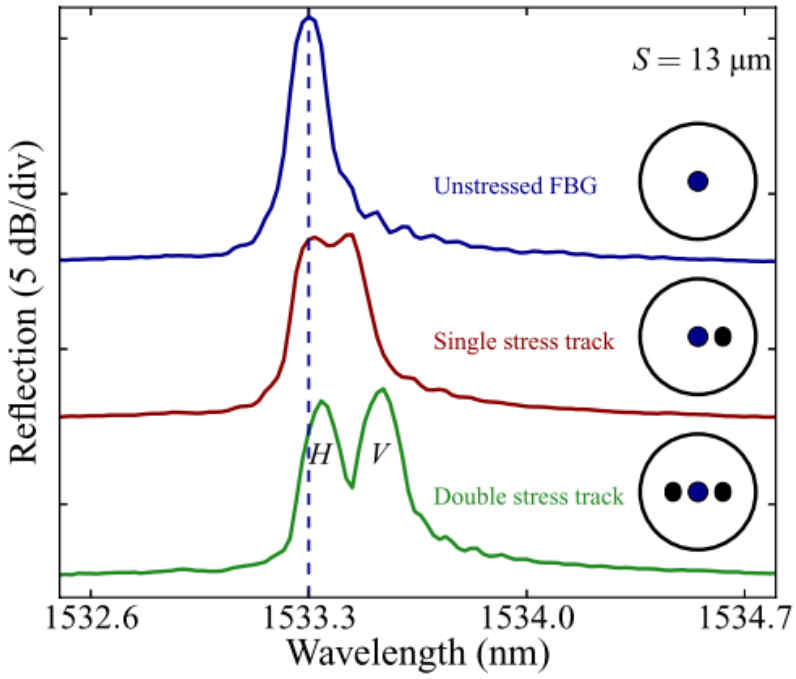


Figure 2.4: Relationship between the induced birefringence and laser-irradiated stress track [12].

2.4 Stress-Optic Effect

The stress-optic effect characterizes the change in refractive index when a waveguide is subjected to stress. In certain isotropic crystals, stress may transform them into anisotropic materials, thereby inducing birefringence [13, 14, 15]. This phenomenon can be represented by introducing the variation of the inverse permittivity tensor ΔB_{ij}:

$$\Delta B_{ij} = P_{ijkl} S_{kl} \tag{2.34}$$

where $B_{ij} = (1/n^2)_{ij}$, P_{ijkl} is fourth order stress-optic tensor and S_{kl} is the second order strain tensor [15]. The radial length of the refractive index ellipsoid denotes the index component along the direction of the light's oscillation. It must satisfy the following conditions.

$$\begin{aligned} B_{ij} = X_i X_j = 1 \\ [B_{ij}(0) + \Delta B_{ij}] X_i X_j = 1 \end{aligned} \tag{2.35}$$

Considering that ΔB_{ij} and S_{kl} are symmetric tensors, the number of independent parameters in the equation 2.35 can be reduced. Expanding equation 2.35 gives the following form,

$$\begin{bmatrix} \Delta B_1 \\ \Delta B_2 \\ \Delta B_3 \\ \Delta B_4 \\ \Delta B_5 \\ \Delta B_6 \end{bmatrix} = \begin{bmatrix} P_{11} & P_{12} & P_{13} & P_{14} & P_{15} & P_{16} \\ P_{21} & P_{22} & P_{23} & P_{24} & P_{25} & P_{26} \\ P_{31} & P_{32} & P_{33} & P_{34} & P_{35} & P_{36} \\ P_{41} & P_{42} & P_{43} & P_{44} & P_{45} & P_{46} \\ P_{51} & P_{52} & P_{53} & P_{54} & P_{55} & P_{56} \\ P_{61} & P_{62} & P_{63} & P_{64} & P_{65} & P_{66} \end{bmatrix} \begin{bmatrix} \varepsilon_x \\ \varepsilon_y \\ \varepsilon_z \\ 2\tau_{yz} \\ 2\tau_{xz} \\ 2\tau_{xy} \end{bmatrix} \tag{2.36}$$

For triclinic crystals lacking symmetry axes or planes, 36 stress-optic coefficients are needed to characterize the stress-optic effect. As the symmetry of a material increases, the number of required stress-optic coefficients decreases. In the case of silica optical fibres, only two independent stress-optic coefficients are necessary. Under the assumption that the fibre is isotropic in the absence of external pressure, the following equation applies:

$$\begin{bmatrix} \Delta B_1 \\ \Delta B_2 \\ \Delta B_3 \\ \Delta B_4 \\ \Delta B_5 \\ \Delta B_6 \end{bmatrix} = \begin{bmatrix} P_{11} & P_{12} & P_{12} & 0 & 0 & 0 \\ P_{12} & P_{11} & P_{12} & 0 & 0 & 0 \\ P_{12} & P_{12} & P_{11} & 0 & 0 & 0 \\ 0 & 0 & 0 & m & 0 & 0 \\ 0 & 0 & 0 & 0 & m & 0 \\ 0 & 0 & 0 & 0 & 0 & m \end{bmatrix} \begin{bmatrix} \varepsilon_x \\ \varepsilon_y \\ \varepsilon_z \\ 0 \\ 0 \\ 0 \end{bmatrix} \tag{2.37}$$

where $m = 1/2(P_{11} - P_{12})$. Simplifying equation 2.37 gives

$$\begin{aligned} \Delta B_1 &= P_{11}\varepsilon_x + P_{12}\varepsilon_y + P_{12}\varepsilon_z \\ \Delta B_2 &= P_{12}\varepsilon_x + P_{11}\varepsilon_y + P_{12}\varepsilon_z \\ \Delta B_3 &= P_{12}\varepsilon_x + P_{12}\varepsilon_y + P_{11}\varepsilon_z. \end{aligned} \tag{2.38}$$

Substituting the outcome into the refractive index ellipsoid equation,

$$\frac{x^2}{n_x^2} + \frac{y^2}{n_y^2} + \frac{z^2}{n_z^2} = 1 \tag{2.39}$$

Typically, the refractive index variation induced by the stress-optic effect is extremely small compared to the fibre's original refractive index. Consequently, the following approximate equation can be used:

$$\frac{1}{(n + \Delta n)^2} = \frac{1}{n^2} - \frac{2\Delta n}{n^3} \tag{2.40}$$

leads to

$$\begin{aligned} n_1 &= n_0 - \frac{1}{2}n_0^3(P_{11}\varepsilon_x + P_{12}\varepsilon_y + P_{12}\varepsilon_z) \\ n_2 &= n_0 - \frac{1}{2}n_0^3(P_{12}\varepsilon_x + P_{11}\varepsilon_y + P_{12}\varepsilon_z) \\ n_3 &= n_0 - \frac{1}{2}n_0^3(P_{12}\varepsilon_x + P_{12}\varepsilon_y + P_{11}\varepsilon_z). \end{aligned} \tag{2.41}$$

This expression represents the refractive index variation arising from the stress-optic effect, obtained by substituting the stress values into equation 2.41.

2.5 Thermo-Optic Effect and Thermal Expansion

2.5.1 Thermo-optic effect

The thermo-optic effect describes the phenomenon by which temperature variations alter a crystal or liquid crystal's molecular structure, thus changing its optical properties. As the refractive index shifts with temperature, it influences mode propagation in the fibre and modifies the effective refractive index. Although the refractive index typically increases with rising temperature, the relationship is not strictly linear. The dependence of the effective refractive index on temperature can be expressed as follows:

$$n_{eff} = n_0(1 + \alpha_1 T + \alpha_2 T^2 + \alpha_3 T^3 + \cdots) \tag{2.42}$$

where n_0 is the effective refractive index at $0°C$ [16]. $\alpha_1\alpha_2\alpha_3$ are the first-, second-, and third-order thermo-optic coefficients, which are defined as,

$$\alpha_1 = \frac{1}{n_0}\left(\frac{\partial n_{eff}}{\partial T}\right)_{T=0}, \alpha_2 = \frac{1}{2!}\frac{1}{n_0}\left(\frac{\partial^2 n_{eff}}{\partial T^2}\right)_{T=0}, \alpha_3 = \frac{1}{3!}\frac{1}{n_0}\left(\frac{\partial^3 n_{eff}}{\partial T^3}\right)_{T=0} \tag{2.43}$$

In certain situations, equation 2.42 may be simplified to include only the first-order term. Moreover, the thermo-optic coefficient of optical fibres also varies with temperature [16]. Figure 2.5 presents the measurement results reported by Wenyuan Wang and colleagues.

Below 400°C, a linear approximation provides sufficiently accurate results. The change in the reflective centre wavelength as a function of temperature can be determined according to the Bragg equation.

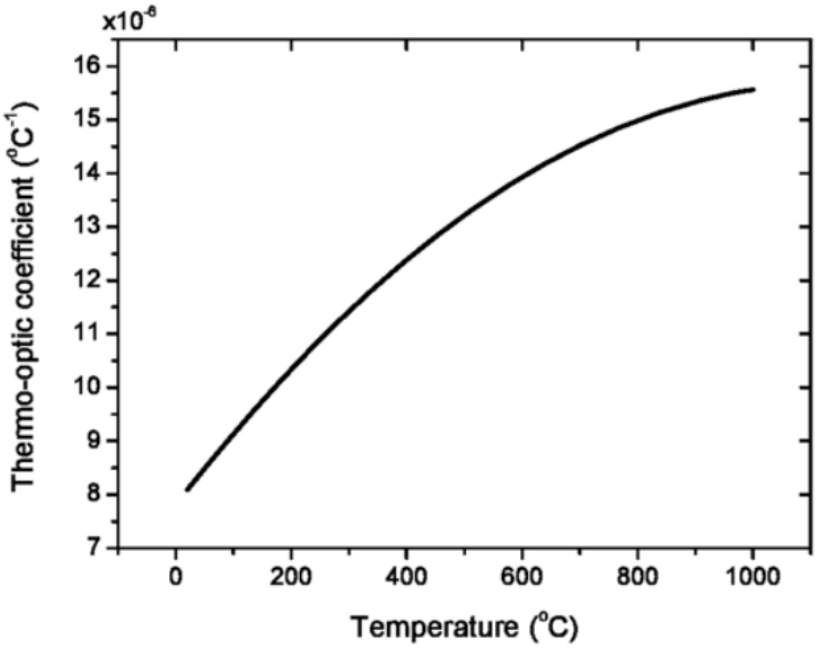


Figure 2.5: The relationship of the thermo-optic coefficient with temperature [16].

2.5.2 Thermal expansion

Temperature variations also cause thermal expansion, which alters the grating period Λ. According to the Bragg equation, any change in the grating period shifts the reflective centre wavelength. The relationship between fibre length and temperature can be expressed as follows:

$$L = L_0(1 + \beta_1 T + \beta_2 T^2 + \beta_3 T^3 + \cdots) \tag{2.44}$$

where L_0 denotes the fibre length at $0°C$ [16]. $\beta_1, \beta_2, \beta_3$ are the first-, second- and third-order thermal expansion coefficients, which are defined as,

$$\beta_1 = \frac{1}{L_0}\left(\frac{\partial L}{\partial T}\right)_{T=0}, \beta_2 = \frac{1}{2!}\frac{1}{L_0}\left(\frac{\partial^2 L}{\partial T^2}\right)_{T=0}, \beta_3 = \frac{1}{3!}\frac{1}{L_0}\left(\frac{\partial^3 L}{\partial T^3}\right)_{T=0} \tag{2.45}$$

Given the minimal cross-sectional area of the fibre, thermal equilibrium is rapidly established, allowing the assumption that temperature is uniformly distributed across the fibre's cross-section. Conse-

quently, a linear expansion model is typically adequate, and in most practical scenarios, only first-order thermal expansion needs to be considered.

References

[1] Stewart E Miller. "Coupled wave theory and waveguide applications". In: *Bell System Technical Journal* 33.3 (1954), pp. 661–719.

[2] John Robinson Pierce. "Coupling of modes of propagation". In: *Journal of Applied Physics* 25.2 (1954), pp. 179–183.

[3] RW Gould. "A coupled mode description of the backward–wave oscillator and the Kompfner dip condition". In: *IRE Transactions on Electron Devices* 2.4 (1955), pp. 37–42.

[4] Amnon Yariv. "Coupled-mode theory for guided-wave optics". In: *IEEE Journal of Quantum Electronics* 9.9 (2003), pp. 919–933.

[5] Allan W Snyder. "Coupled-mode theory for optical fibres". In: *Journal of the optical society of America* 62.11 (1972), pp. 1267–1277.

[6] D Marcuse. "Coupled mode theory of round optical fibres". In: *Bell System Technical Journal* 52.6 (1973), pp. 817–842.

[7] Raman Kashyap. *Chapter 4 - Theory of fibre Bragg Gratings*. Ed. by Raman Kashyap. Second Edition. Academic Press, 2010, pp. 119–187. ISBN: 978-0-12-372579-0.

[8] Herwig Kogelnik. "Coupled wave theory for thick hologram gratings". In: *Bell System Technical Journal* 48.9 (1969), pp. 2909–2947.

[9] Ali Karatutlu et al. "Fabrication of biaxial polarization-maintaining optical fibre with ultra-low bending-dependent polarization extinction ratio deterioration". In: *Optical fibre Technology* 69 (2022), p. 102836.

[10] A Ortigosa-Blanch et al. "Highly birefringent photonic crystal fibres". In: *Optics letters* 25.18 (2000), pp. 1325–1327.

[11] Luís A Fernandes et al. "Stress induced birefringence tuning in femtosecond laser fabricated waveguides in fused silica". In: *Optics express* 20.22 (2012), pp. 24103–24114.

[12] Luís A Fernandes et al. "Strong birefringence tuning of optical waveguides with femtosecond laser irradiation of bulk fused silica and single mode fibres". In: *Journal of lightwave technology* 31.22 (2013), pp. 3563–3569.

[13] A Barlow and D Payne. "The stress-optic effect in optical fibres". In: *IEEE Journal of Quantum Electronics* 19.5 (1983), pp. 834–839.

[14] Pericles S Theocaris and Emmanuel E Gdoutos. *Matrix theory of photoelasticity*. Vol. 11. Springer, 2013.

[15] Robert E Newnham. *Properties of materials: anisotropy, symmetry, structure*. OUP Oxford, 2004.

[16] Wenyuan Wang et al. "Measurements of thermo-optic coefficient of standard single mode fibre in large temperature range". In: *2015 International Conference on Optical Instruments and Technology: Optical Sensors and Applications*. Vol. 9620. SPIE. 2015, pp. 234–239.

3 | Design and Simulation of Pressure Sensors

This chapter provides a comprehensive overview of the design, modeling, and simulation processes of the microstructured optical fibre pressure sensor. It encompasses simulations related to the stress-optic effect, thermo-optic effect, and thermal expansion, as well as the optimization of structural parameters of the optical fibre.

3.1 Simulation of Stress-Optic Effect

The initial phase involves modeling the sensor and optimizing its structural configuration. The operating principle of the FBG pressure sensor based on air-hole fibres relies on birefringence and the stress-optic effect, both of which were theoretically analyzed in Chapter 2. However, beyond the simplest configurations, analytical solutions become increasingly difficult to obtain due to the complexity of the fibre structure. In a pioneering effort, H.M. Xie and his colleagues proposed a model for calculating birefringence in dual-hole fibres. By approximating the cross-sectional geometry of the fibre and the circular air holes as square shapes, they were able to derive an approximate analytical solution to this otherwise complex problem [1].

However, for more complex scenarios, such approximation methods become inadequate. In such cases, the finite element method (FEM) offers a powerful and effective solution. Finite element method was first introduced in the 1940s by A. Hrennikoff and Richard Courant to address problems in physics and engineering [2, 3]. Most physical phenomena, including the stress distribution within optical fibres under external pressure, can be described by partial differential equations. Due to the complexity of these structures, analytical solutions to such equations are often unattainable. Finite element method addresses this challenge by discretizing the object of study-dividing the domain into a large number of smaller subregions known as finite elements. Within each of these elements, sim-

plified approximate equations are applied to obtain numerical solutions. The finer the mesh used in this discretization process, the closer the numerical solution approaches the actual physical behavior. Figure 3.1 illustrates the progressive refinement of the mesh.

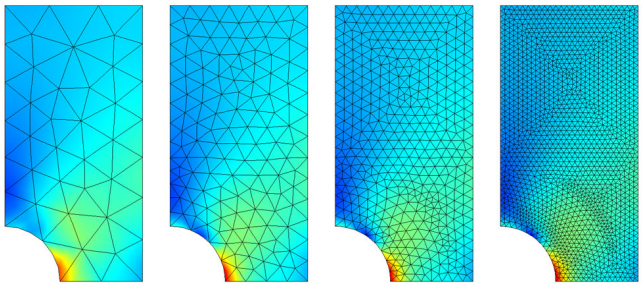


Figure 3.1: Schematic diagram of grid refinement(from: www.comsol.com/multiphysics).

The finite element simulation software used in this thesis is COMSOL Multiphysics. Within this platform, the Solid Mechanics module is utilized to compute stress distributions based on two fundamental equations. Equation 3.1 represents the differential form of the momentum balance equation, while Equation 3.2 corresponds to Hooke's law. In these equations, σ denotes the stress tensor, f_v represents the force per deformed volume, u is the displacement field, E is the Young's modulus, and ϵ denotes the strain tensor.

$$\nabla_x \cdot \sigma + f_v = \rho \frac{\partial^2 u}{\partial t^2} \tag{3.1}$$

$$\sigma = E\epsilon \tag{3.2}$$

The subsequent analysis starts with calculating the internal stress distribution within a single mode silica optical fibre, with a diameter of 125 μm, subjected to a uniformly applied external pressure. From a theoretical standpoint, an ideal SMF, free of manufacturing defects and residual thermal stresses, should exhibit a uniform stress distribution across its cross section when subjected to a uniformly applied normal pressure on its outer surface. The simulation presented in Fig.3.2b confirms

this expectation over most of the fibre's interior; however, it also reveals localized irregularities at the periphery. These edge anomalies arise because once the circular cross section is discretized, the fibre boundary is represented by discontinuous finite elements whose mechanical response deviates slightly from that of a perfect circle. When a finer mesh is employed (Fig.3.2c), the magnitude of these peripheral irregularities is markedly reduced. By weighing the simulation runtime against computational resources, one can thus establish an appropriate meshing strategy tailored to the fibre's dimensions.

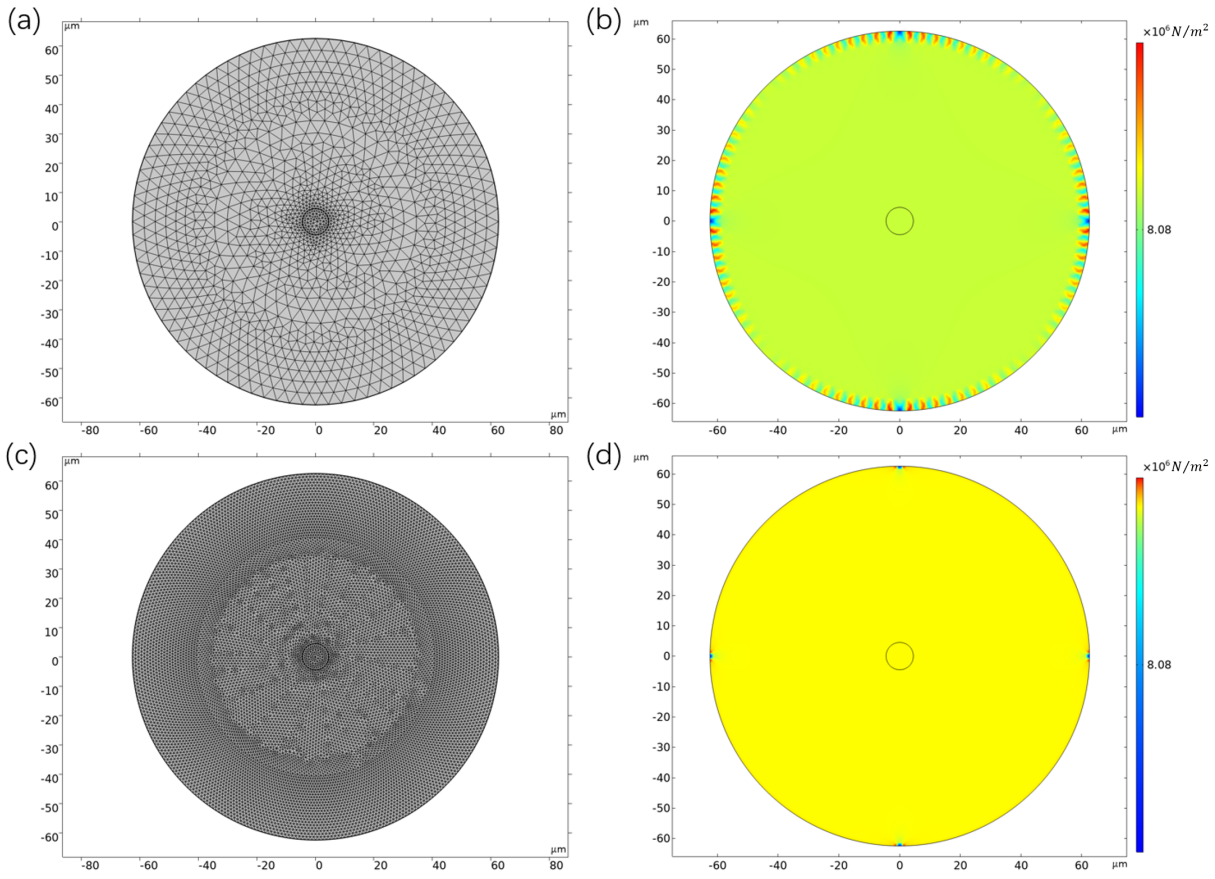


Figure 3.2: (a) Fibre cross section using a sparse mesh division. (b) Stress distribution using sparse mesh division. (c) Fibre cross section using a finer mesh division. (d) Stress distribution using finer mesh division.

The next simulation examines the cross-sectional stress distribution of a typical side-hole fibre subjected to a uniform external load. The fibre has an outer diameter of 220 μm, and two circular air-filled holes, each 90 μm in diameter, which are symmetrically placed on either side of the core. As illustrated in Fig.3.3, these cavities concentrate the internal stress within the core region. Conse-

quently, in light of the stress-optic effect, the associated refractive index variation is predicted to be most pronounced in the core.

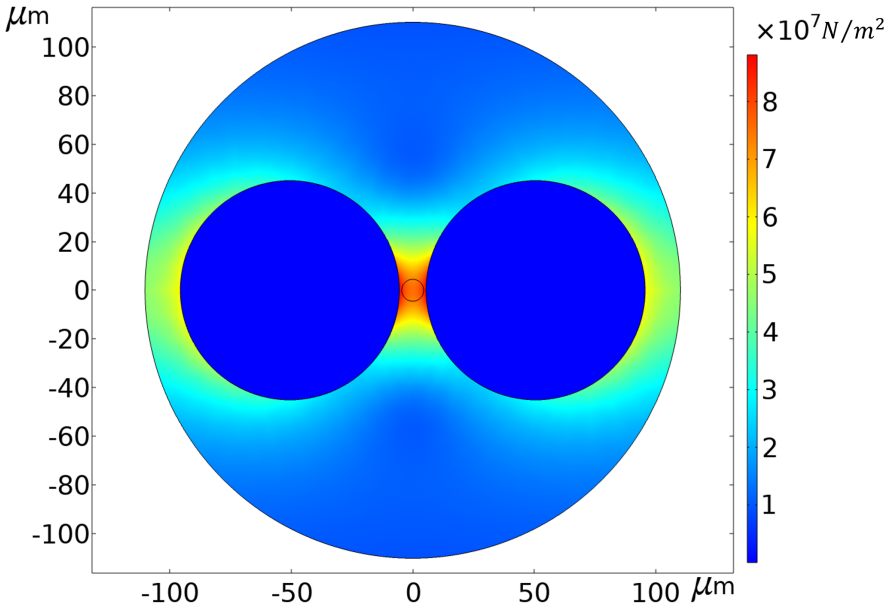


Figure 3.3: Stress distribution in the side-hole fibre cross-section.

After determining the stress distribution across the fibre cross section, these data can be substituted into the stress optic equation 2.41 to evaluate the resulting refractive index variations, a calculation that can be performed directly in COMSOL. Usually, the pressure sensor is used in scenarios where a transverse load is applied to the fibre and the components of axial stress can be neglected. Here, N denotes the refractive index of the unstressed isotropic silica fibre, while N_x and N_y denote the refractive-index components experienced by optical fields polarised along the x- and y-directions, respectively.

Figures 3.4 and 3.5 show that the refractive index components along the x and y directions are no longer identical under the applied stress. This divergence converts the originally isotropic fused silica material into an anisotropic one, thereby inducing birefringence within the fibre. Figure 3.6 further depicts how the refractive index difference between the x and y axes is distributed across the fibre cross section. Consistent with the stress distribution findings, the core region displays the most pronounced differences between the two refractive index components.

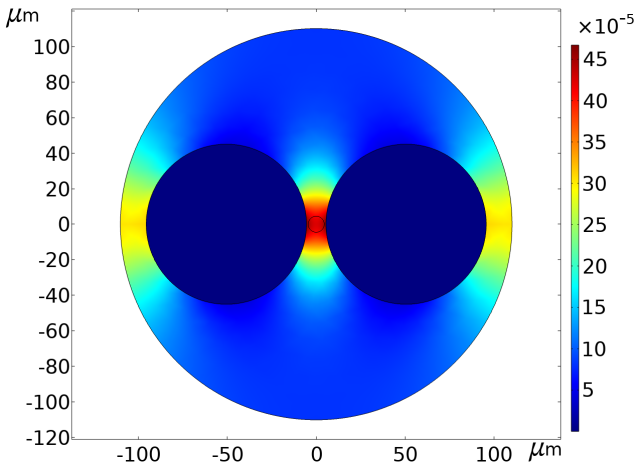


Figure 3.4: Distribution of the changes in the refractive index component along the x-direction $N_x - N$.

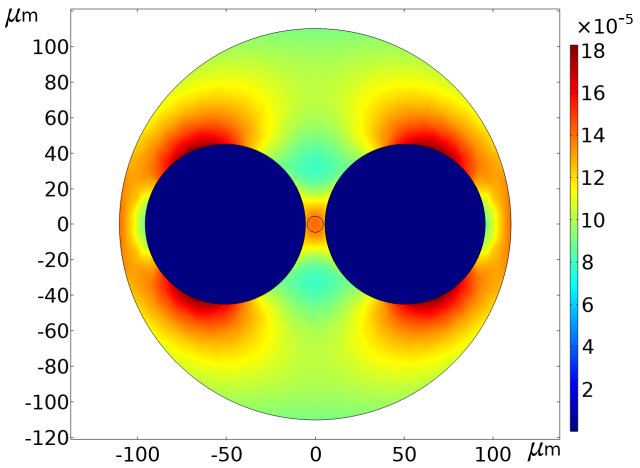


Figure 3.5: Distribution of the changes in the refractive index component along the y-direction $N_y - N$.

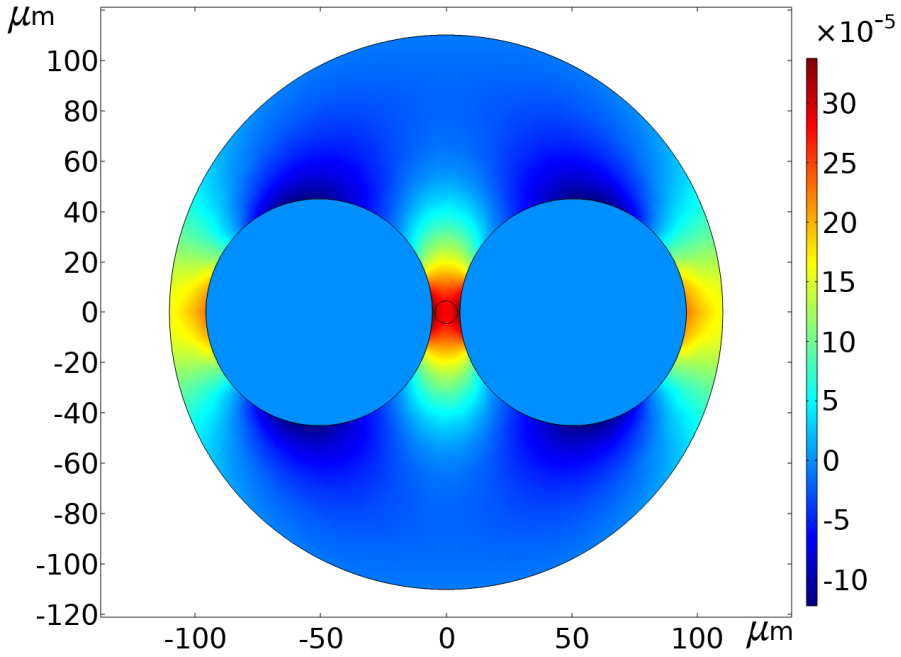


Figure 3.6: Distribution of the difference between the refractive index components in the x and y directions $N_x - N_y$.

In summary, the stress optic effect of side hole fibres has been successfully simulated with the finite element platform COMSOL. This methodology is equally applicable to micro-structured fibres containing holes of arbitrary shape and number, thereby greatly streamlining subsequent design-optimization efforts.

3.2 Simulation of FBG

In selecting an appropriate numerical technique for simulating FBGs, three candidates were evaluated: the finite-difference time-domain (FDTD) method, the finite-element method (FEM), and the eigenmode expansion (EME). The FDTD method discretises the computational domain into a Cartesian grid and solves Maxwell's equations at each cell through successive time stepping, thereby providing a full time-resolved electromagnetic response. However, when the simulated structure is elongated along the fibre axis, the required computational time and memory grow prohibitively, rendering FDTD impractical for large-scale fibre models. The finite-element method, which likewise necessitates meshing the entire geometry, faces similar scalability constraints; moreover, because the stress-optic effect alters the refractive-index distribution across the fibre cross section, a fully three-dimensional model is indispensable.

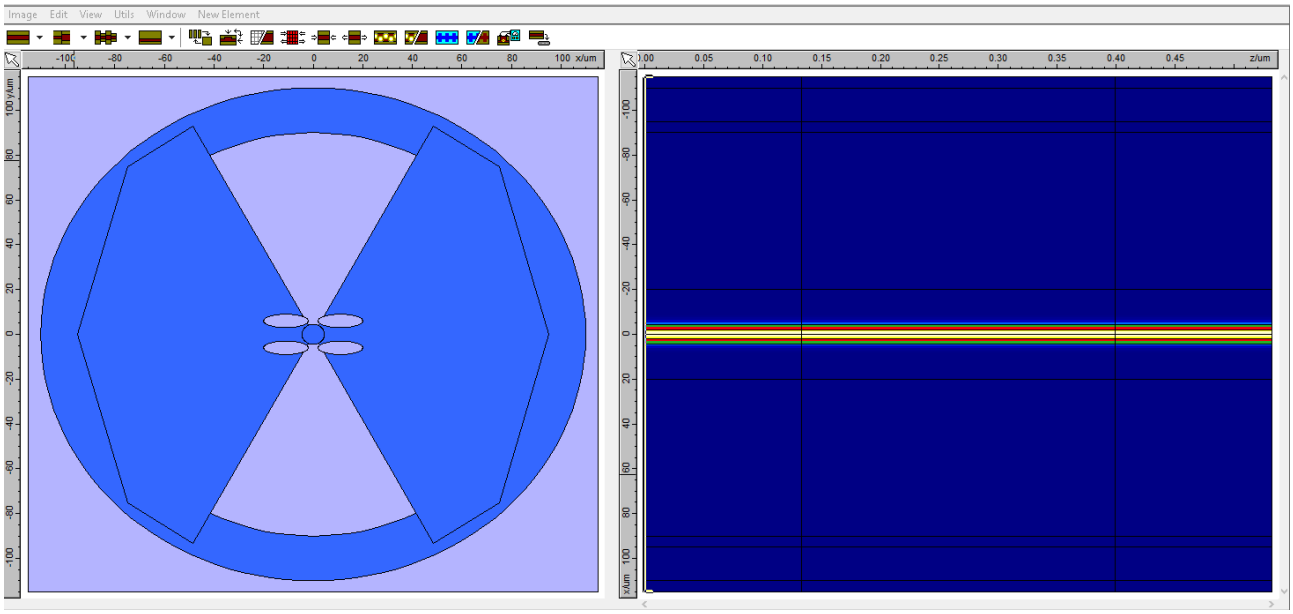


Figure 3.7: Use of the eigenmode expansion method in FIMMPROP to calculate light propagation in microstructured fibres. The specific microstructured fibre geometry shown here is included as an illustrative example of the modelling workflow and is explored in detail in Section 3.3.

By contrast, EME is well suited to periodic structures such as FBGs. The fibre can be partitioned into a sequence of identical unit cells, within which the forward- and backward-propagating eigenmodes are computed to construct a scattering matrix. These matrices can then be reused for all

subsequent cells, dramatically reducing both simulation time and memory consumption. The eigenmodes of each unit cell are calculated with a finite-difference mode solver (FDM). Specifically, a two-dimensional mesh is generated over the fibre cross section, and Maxwell's equations in each grid cell are recast as an eigenvalue problem. This strategy is far simpler and faster than solving the entire device on a three-dimensional mesh. Figure 3.7 demonstrates the calculation of light propagation in a microstructured fibre using the eigenmode expansion method within FIMMPROP.

This study employs the EME solver in FIMMPROP to model the fibre Bragg grating. Because the refractive index distribution is first generated in COMSOL, where the sampling points are defined by COMSOL's meshing scheme, the data must be fitted and resampled before import to conform to FIMMPROP's refractive index grid format. Figures 3.8 and 3.9 present the refractive index distributions obtained directly from COMSOL, while Figures 3.10 and 3.11 present the same data after curve fitting and resampling in MATLAB. The refined data set is then exported in the refractive index matrix format prescribed by the FIMMWAVE user manual (as shown in Figure 3.12), enabling its seamless integration into subsequent simulations.

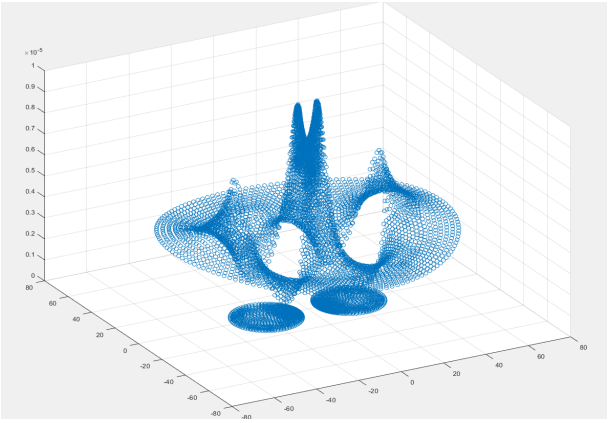


Figure 3.8: Stress-induced change in the refractive-index component along the x-direction, $N_x - N$, obtained directly from the COMSOL stress-optic simulation of the side-hole fibre under applied external pressure. The data are shown before curve fitting and resampling for import into FIMMPROP.

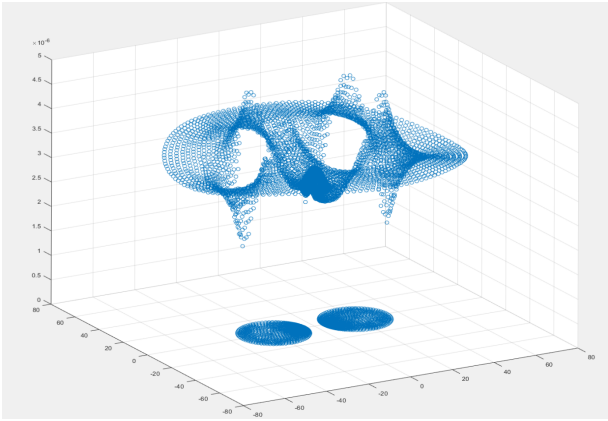


Figure 3.9: Stress-induced change in the refractive-index component along the y-direction, $N_y - N$, obtained directly from the COMSOL stress-optic simulation of the side-hole fibre under applied external pressure. The data are shown before curve fitting and resampling for import into FIMMPROP.

The next step is to simulate the side-hole fibre sensor under external pressure in FIMMPROP and compute its transmission and reflection spectra. The FBG was modelled as a uniform second-order

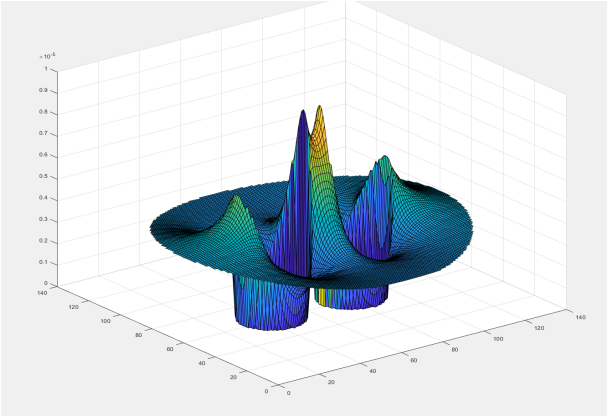


Figure 3.10: Resampled distribution of $N_x - N$ after curve fitting and interpolation in MATLAB. The processed refractive-index data are converted onto the regular grid required for subsequent FIMMPROP simulations.

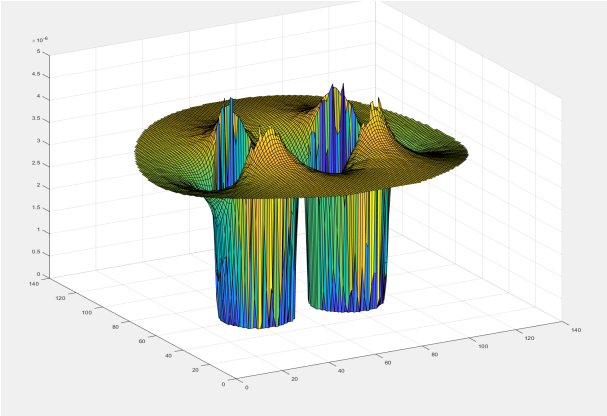


Figure 3.11: Resampled distribution of $N_y - N$ after curve fitting and interpolation in MATLAB. The processed refractive-index data are converted onto the regular grid required for subsequent FIMMPROP simulations.

```
begin <fmwx-rix-profile(2.0)>
0 1 // isRadial isUniform
3  3  3  3  0  0  3  //  nXvals,  nYvals,  width,  height,  interpolateFlag,
nAlphaElts, nRixElts
[1.0,1.0,1.0]          [1.1,1.15,1.5]         [1.0,1.0,1.0]
[1.1,1.15,1.1]         [1.2,1.5,1.2]          [1.1,1.15,1.1]
[1.0,1.0,1.0]          [1.1,1.15,1.5]         [1.0,1.0,1.0]
end
```

Figure 3.12: Anisotropic refractive index profile example from FIMMWAVE manual.

grating with 1000 periods, a grating pitch of $\Lambda = 1.073\ \mu\mathrm{m}$, and a refractive-index modulation amplitude of $\Delta n = 0.001$. The value of Δn was chosen to represent a realistic femtosecond-laser-inscribed FBG and to provide a clearly resolvable resonance in the numerical spectrum. The reflection and transmission spectra of the two orthogonal modes, transverse electric (TE) and transverse magnetic (TM), were computed for the FBG both before and after the application of external pressure. In Figure 3.13, the curves labeled NTE and NTM correspond to the unpressurised state, whereas TE and TM represent the spectra obtained under an applied pressure of 124 bar. In the absence of external pressure, the silica fibre remains isotropic, and the FBG resonance peaks associated with the orthogonal TE and TM modes coincide. When external pressure is applied, the fibre becomes anisotropic; the effective refractive indices of the two modes diverge, and their corresponding FBG resonance peaks split accordingly. The wavelength separation between the TE and TM resonance peaks in this simulated spectrum closely matches the experimental measurements reported by C. M. Jewart et al.

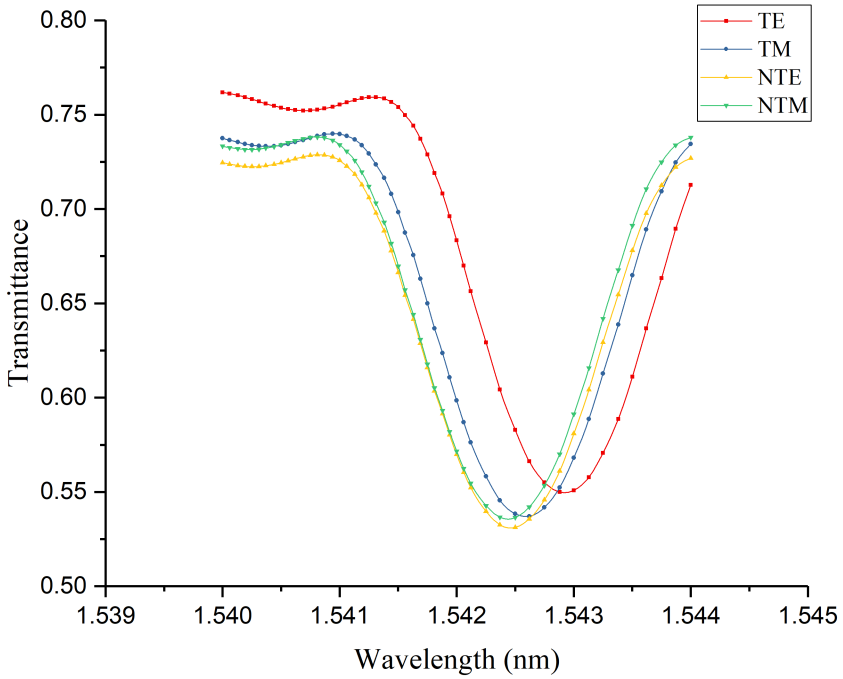


Figure 3.13: Simulated transmission spectra of the side-hole fibre sensor using a 1000-period second-order FBG with a grating pitch of $\Lambda = 1.073\ \mu\mathrm{m}$ and a refractive-index modulation of $\Delta n = 0.001$. The spectra compare the two orthogonal polarisation modes before and after the application of external pressure.

for the same fibre, thus validating the fidelity of the present simulation model [4].

3.3 Sensor Structure Optimization and Parameter Sweep

Pressure sensors based on side hole fibre drawn from conventional preforms are inherently limited in both design flexibility and material composition, since these fibres were never intended specifically for sensing. In practical deployment, the devices must be fusion spliced to standard single mode fibres; air hole collapse and other splice-induced imperfections then generate substantial insertion loss. Using numerical simulations, I have designed and optimized pressure sensors featuring intricate 3D structures that can be selectively fabricated within designated regions of commercial step index single mode fibres, thereby obviating the need for splicing.

Drawing inspiration from bow-tie polarization maintaining fibres, I redesign the air holes as

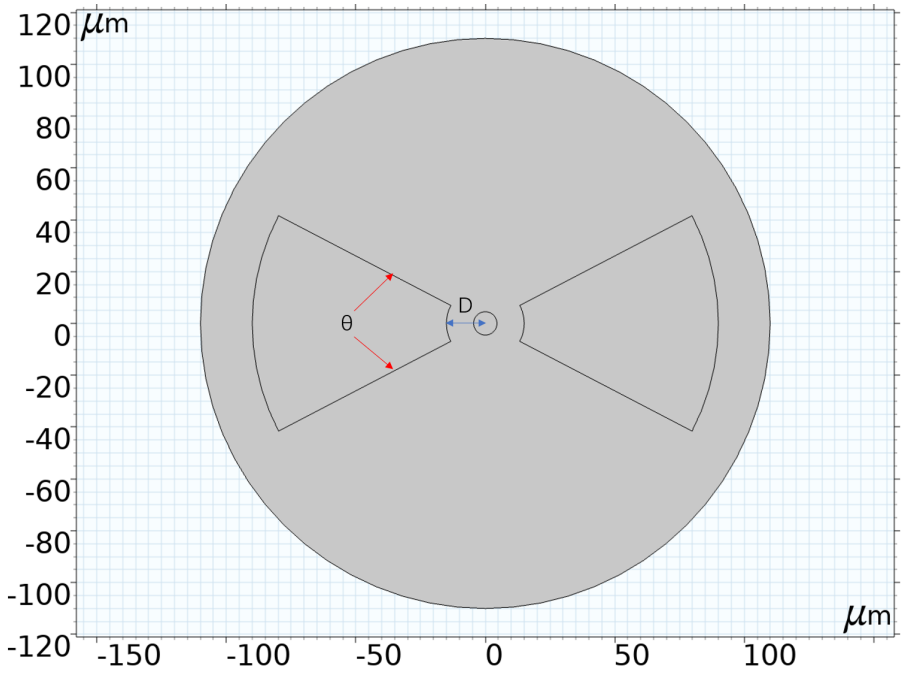


Figure 3.14: Layout of the sector-shaped air holes in a 220 μm diameter silica fibre. The sector regions represent air voids introduced into the cladding, while the remaining cross-section corresponds to the silica step-index fibre.

sector-shaped cavities to enhance stress concentration within the core. Figure 3.14 shows the layout of the holes. To probe the full potential of the sensor, the initial design minimizes the separation D

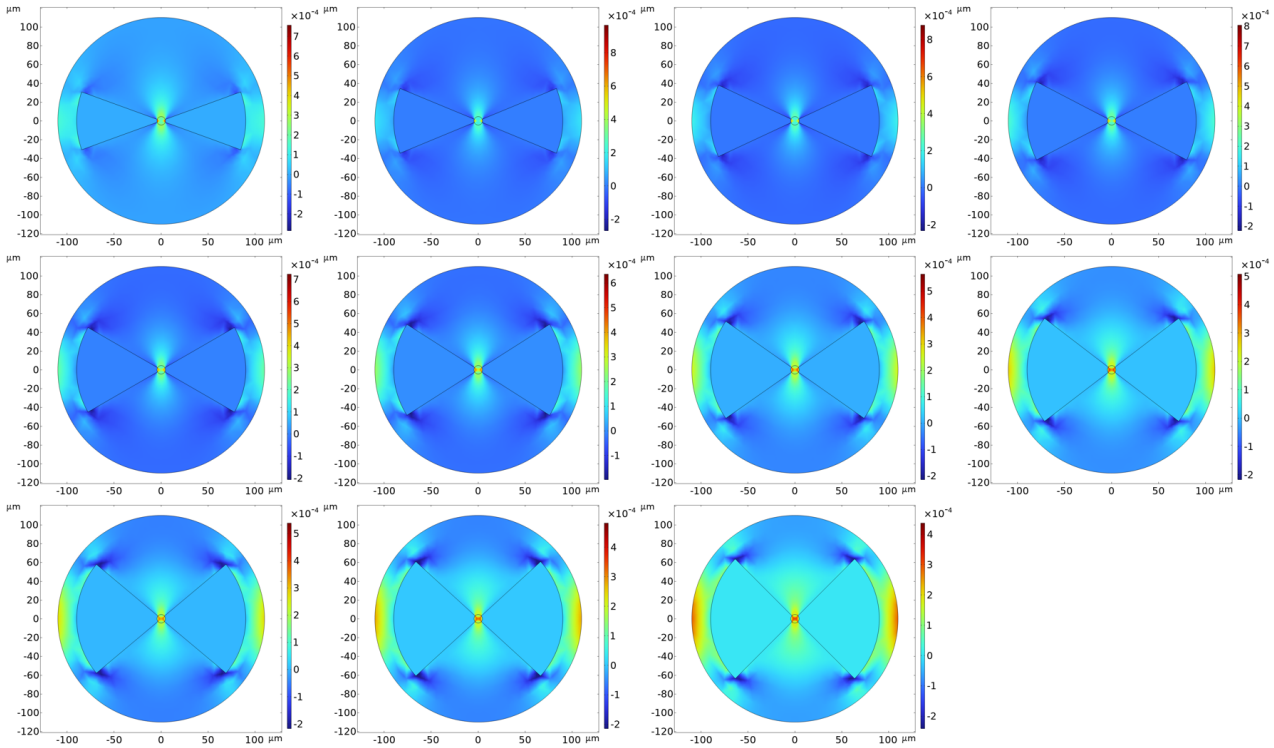


Figure 3.15: Simulated distribution of $N_x - N_y$ for sector-shaped air holes with different opening angles in a 220 μm diameter silica fibre. The sector opening angle was varied from $40°$ to $90°$ in $5°$ increments under an external pressure of 124 bar.

between each sector and the core. Two sectorial hole radiuses of 90 μm were selected, after which the sector opening angle was systematically varied from 40° to 90°. If the angle is too large the hollow area will also become too large and the sensor structure will be unstable. For each angle, I determined the separation between the transmission peak of the two orthogonal modes under a constant external pressure of 124 bar.

Figure 3.15 illustrates the variation in the distribution $N_x - N_y$ for each angle of the sector, while Figure 3.16 shows the relationship between the peak separation of the orthogonal modes and the opening angle of the sector. The wavelength spacing reaches its maximum at an opening angle of 55°. With the opening angle of the sector fixed at 55° and all other conditions kept constant, the radius of the sector was incrementally varied from 10 μm to 90 μm. For each radius, the mean difference between the refractive index components N_x and N_y within the fibre core was calculated to quantify the level of birefringence.

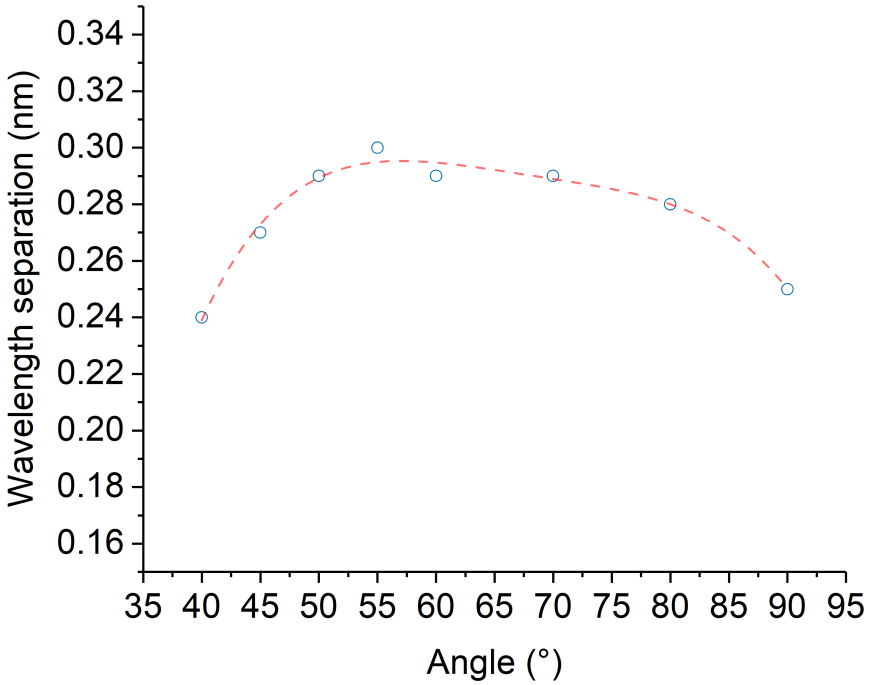


Figure 3.16: Parameter sweep for the sector angle for a 220 μm diameter fibre at an external pressure of 124 bar.

Figure 3.17 maps the distribution of the difference in refractive index components $N_x - N_y$ in

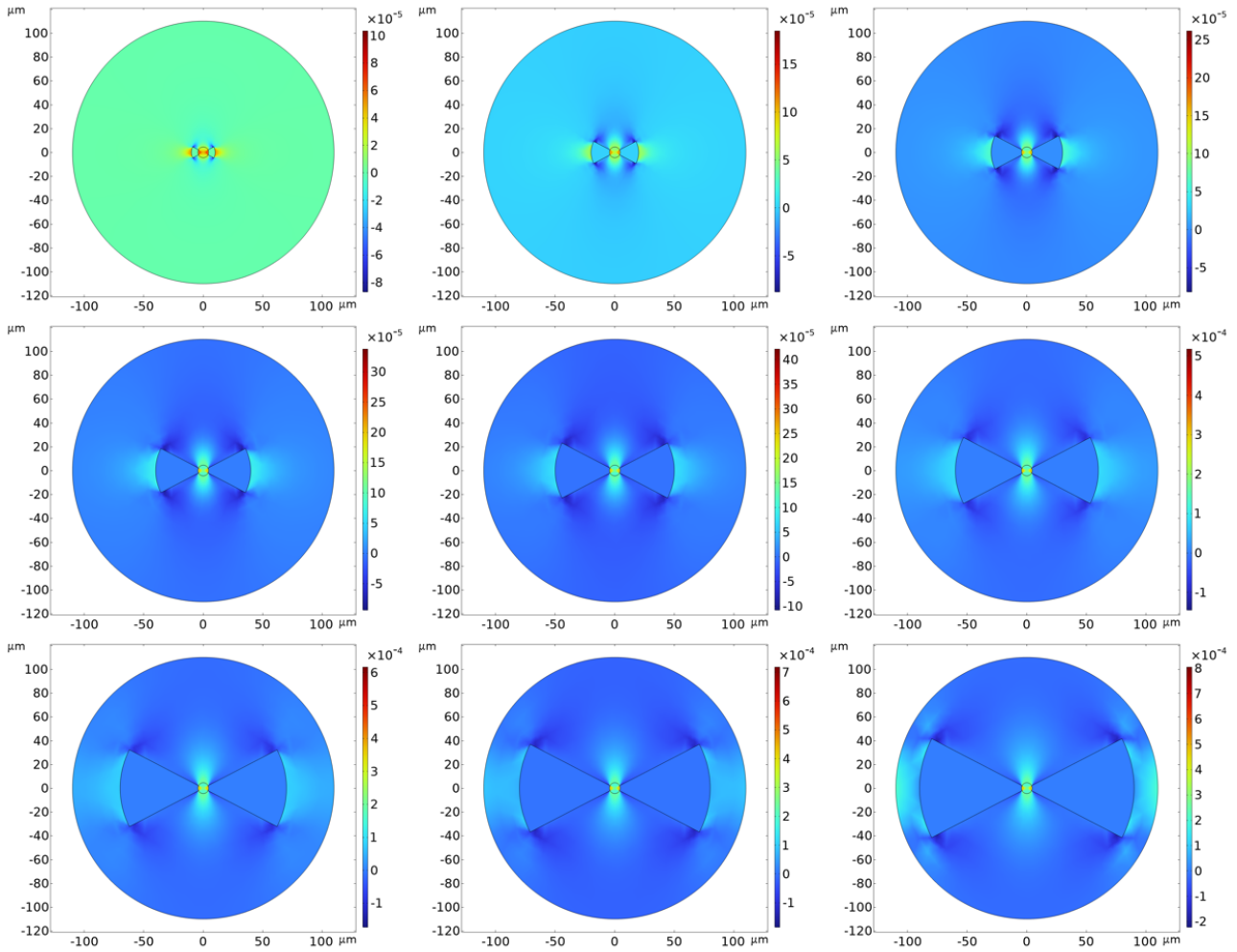


Figure 3.17: $N_x - N_y$ distribution simulation of sector holes with different radius between 10 μm to 90 μm in the 220 μm diameter fibre.

the fibre cross section for a series of sector radiuses, while Figure 3.18 reveals that the mean value of $N_x - N_y$ increases almost linearly with increasing radius. Accordingly, to maximize pressure-induced birefringence one should choose the largest practicable radius, but this should be balanced with structural robustness and manufacturing constraints.

Beyond adjusting the sector radius and opening angle, sensor sensitivity can be further enhanced by introducing more intricate features close to the core region. The preceding parameter sweep shows that increasing the sector radius strengthens the pressure-induced birefringence, but this approach is ultimately limited by structural robustness and fabrication constraints. Therefore, four elliptical micro-holes were introduced near the core to locally enhance the asymmetric stress concentration without further enlarging the main sector-shaped air holes. The elliptical shape was chosen to pref-

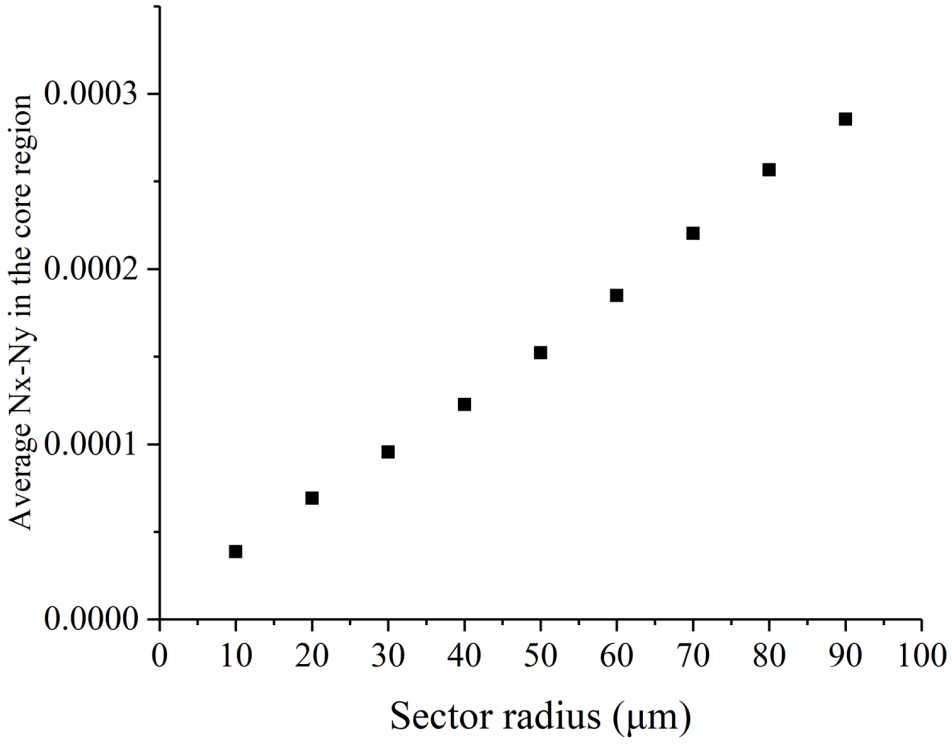


Figure 3.18: Under an external pressure of 124 bar, a sweep of the fibre's inner sector radius was performed to obtain the average $N_x - N_y$ in the core region variation trend.

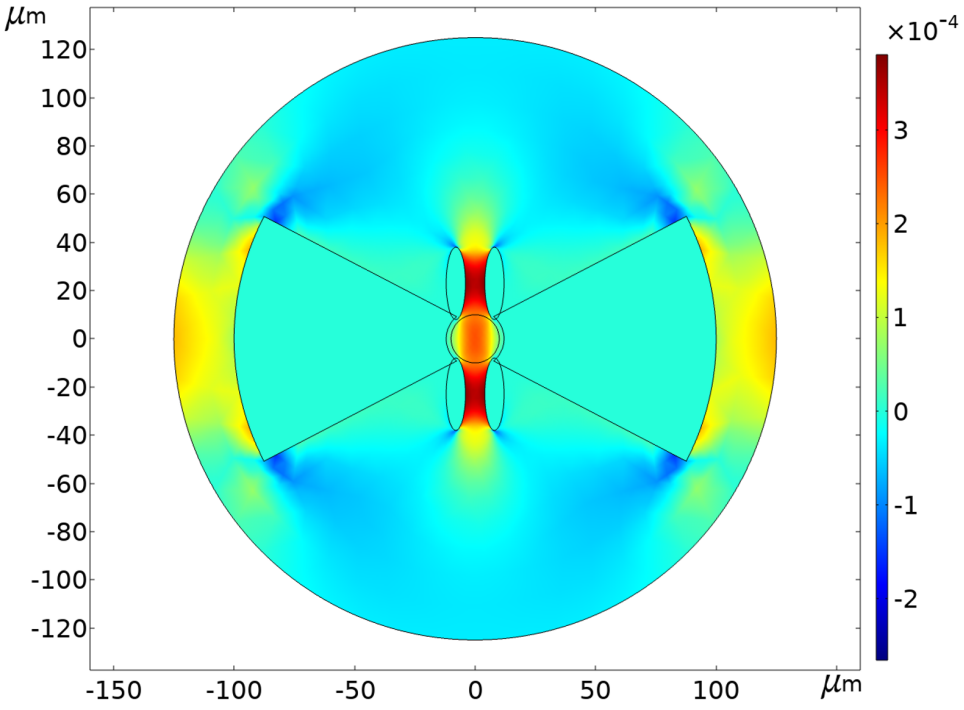


Figure 3.19: simulation of cross-sectional refractive index components difference distribution in sector holes with elliptical micro-holes.

erentially perturb the stress field along one transverse direction, thereby increasing the difference between the refractive-index components N_x and N_y. The simulated cross-sectional refractive-index

component difference under an external pressure of 124 bar is presented in Figure 3.19. The pressure sensitivity of each design was subsequently evaluated, and the resulting values are compiled in Table 3.1. After analysing the influence of the shape of the air holes, it is also important to ensure that the response of the sensor to changes in pressure is linear. For the linear analysis, two sector holes

Table 3.1: Simulation results of sensitivity in different types of optical fibre.

Diameter	Type	Sensitivity
125 μm	Sector hole	1.128 pm/bar
220 μm	Sector hole	2.417 pm/bar
250 μm	Sector hole with elliptical micro-holes	3.304 pm/bar

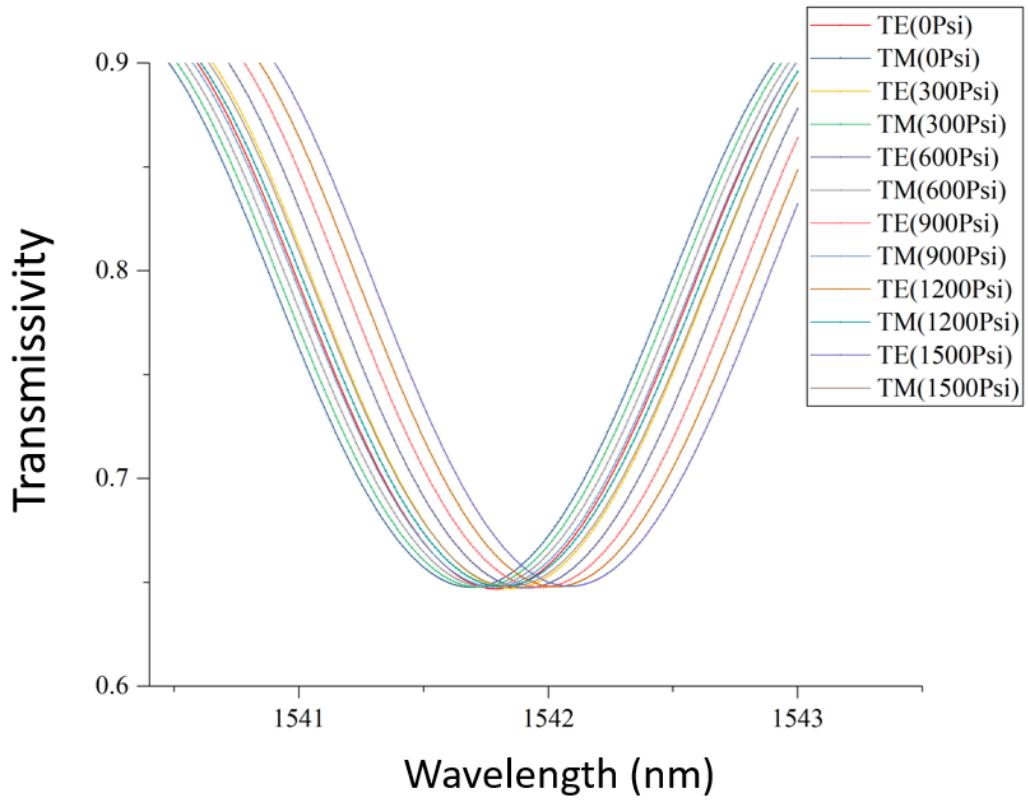


Figure 3.20: Fibre Bragg Grating transmissivity in two polarization directions at different pressure.

with a radius of 90 μm and an opening angle of 55° were adopted, while the temperature and all other conditions were kept constant. The transmission spectra of the FBG were then computed for a series of external pressures. Figure 3.20 displays the resulting spectra for the two orthogonal modes at each pressure level. Figure 3.21 shows that the separation of the peaks between the two orthogonal modes increases linearly with the applied pressure, indicating that this peak separation can serve as a quantitative gauge of pressure variations.

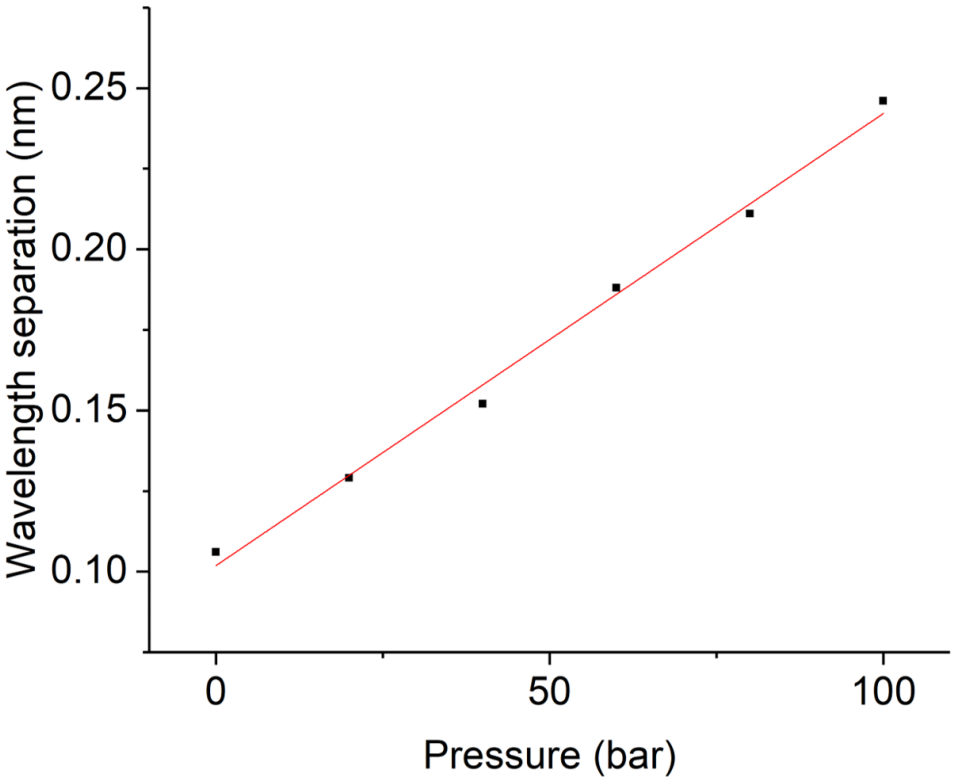


Figure 3.21: Relation between peak wavelength separation and pressure change for a 220 μm diameter fibre.

Beyond characterising the sensor's pressure response, it is crucial to demonstrate that temperature and pressure effects can be decoupled. To this end, both the thermo-optic effect and thermal expansion were incorporated into the simulations. Only the first-order thermo-optic coefficient was considered, higher-order contributions being neglected, and the resulting refractive index changes at material cross-section were computed. Because the thermo-optic effect is isotropic, it does not modify the birefringence. The effect of thermal expansion is mainly reflected in changing the refractive index modulation period length of the FBG.

Figures 3.22 and 3.23 display the transmission peaks of the two orthogonal modes across a range of temperatures when no external pressure is applied. The trend of the separation of the two orthogonal mode transmission peaks as a function of temperature is illustrated in Figure 3.24 for both applied and unapplied pressures. The peak separation remains essentially constant as the temperature varies, yet it changes appreciably in response to pressure, confirming that the sensor effectively decouples thermal and pressure effects. These results show that temperature and pressure data can be acquired

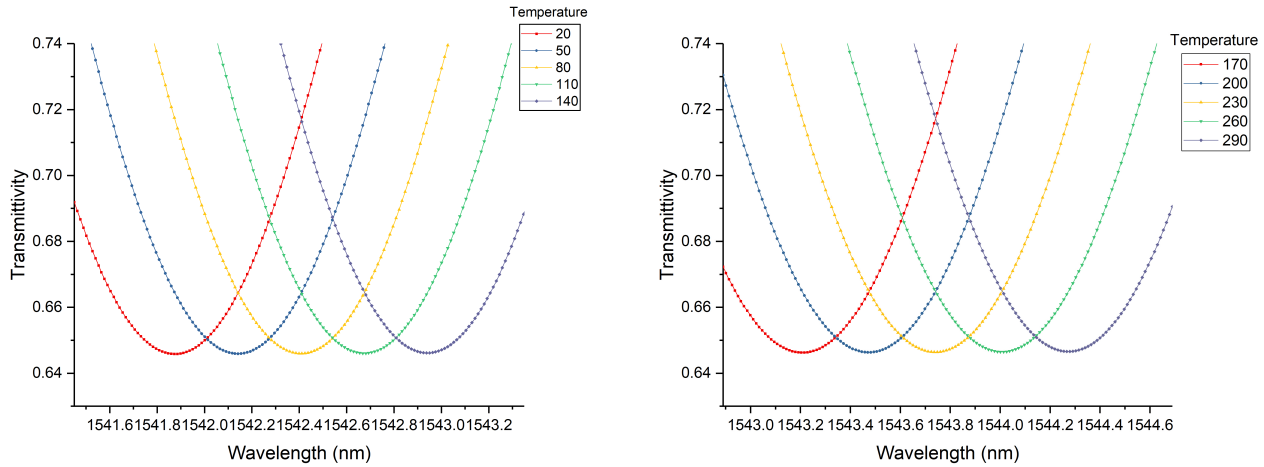


Figure 3.22: Transmission spectrum of TE modes at different temperature.

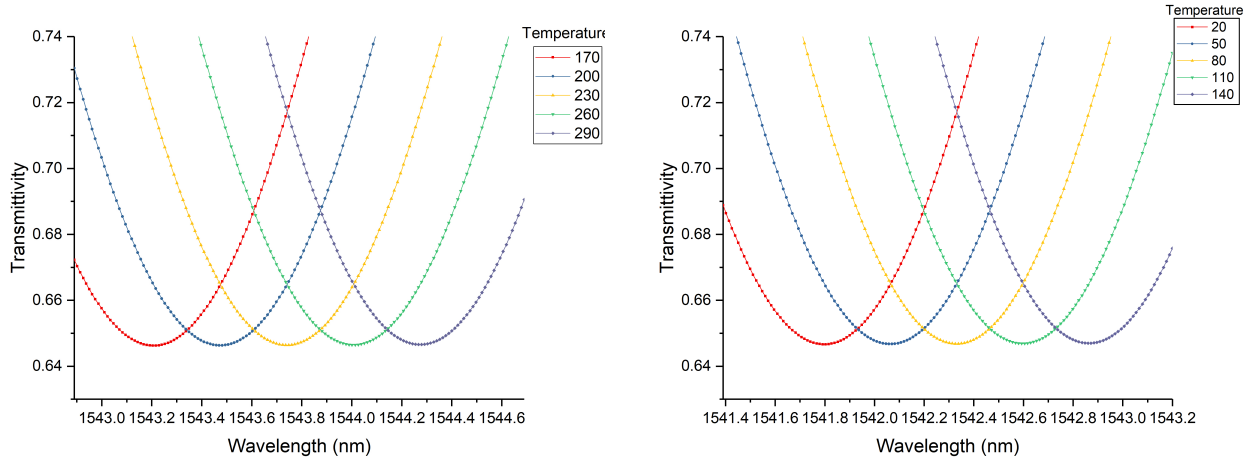


Figure 3.23: Transmission spectrum of TM modes at different temperature.

simultaneously for this type of sensor.

In summary, numerical simulations were employed to investigate how various air hole geometries affect sensor sensitivity, and to quantify the device's responses to pressure and temperature. The simulated results agree with the conclusions drawn from theoretical analysis. Nonetheless, further optimisation is required before laboratory fabrication; practical considerations such as structural robustness, manufacturing techniques, and packaging strategies must be addressed to refine the design.

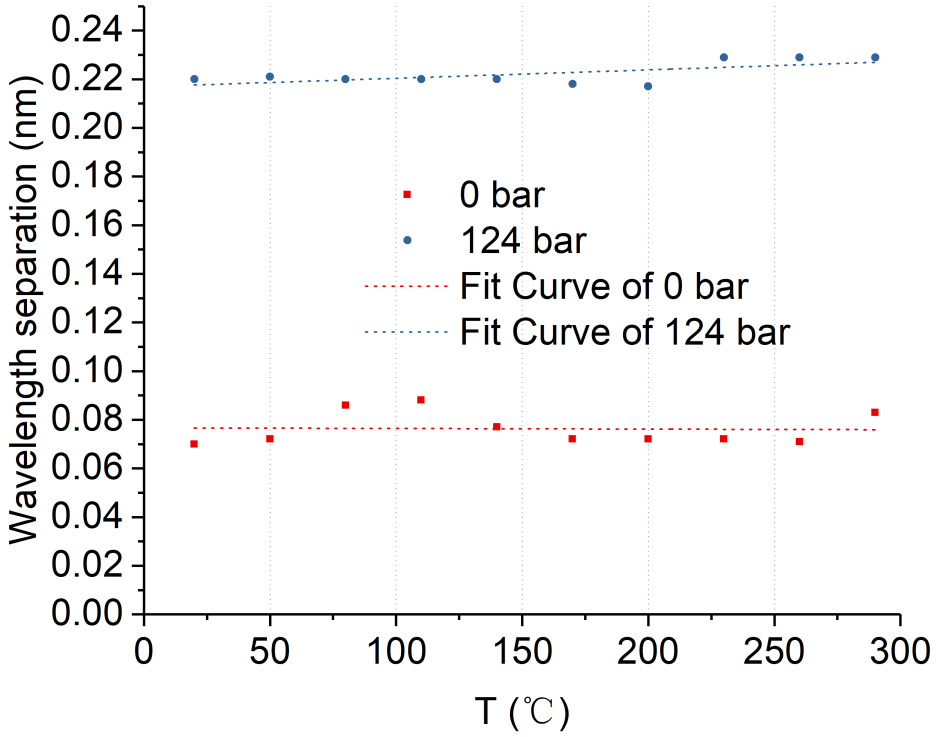


Figure 3.24: Simulation of peak separation at different temperatures and pressures for a 220 μm diameter fibre.

References

[1] HM Xie et al. "Side-hole fibre for fibre-optic pressure sensing". In: *Optics Letters* 11.5 (1986), pp. 333–335.

[2] Alexander Hrennikoff. "Solution of problems of elasticity by the framework method". In: *Journal of Applied Mechanics* (1941), pp. 169–175.

[3] Richard Courant et al. "Variational methods for the solution of problems of equilibrium and vibrations". In: *Lecture notes in pure and applied mathematics* (1994), pp. 1–1.

[4] Charles M Jewart et al. "Ultrafast femtosecond-laser-induced fibre Bragg gratings in air-hole microstructured fibres for high-temperature pressure sensing". In: *Optics letters* 35.9 (2010), pp. 1443–1445.

4 | Fabrication and Characterisation of Sensors

This chapter details a three-stage fabrication route in which tightly focused femtosecond laser pulses first inscribe complex 3D microstructures within the optical fibre; wet chemical etching then selectively removes the laser-modified regions to create hollow cavities; finally, the cavities are hermetically sealed, yielding a fully integrated fibre optic pressure sensor.

4.1 Laser inscription

4.1.1 Laser focusing method

Because an optical fibre acts as a cylindrical lens, the aberrations it introduces must be considered when femtosecond pulses are focused within the glass. Salter et al. have demonstrated that these aberrations can be corrected by adaptive optics techniques [1]. Figures 4.1 and 4.2 present the ray

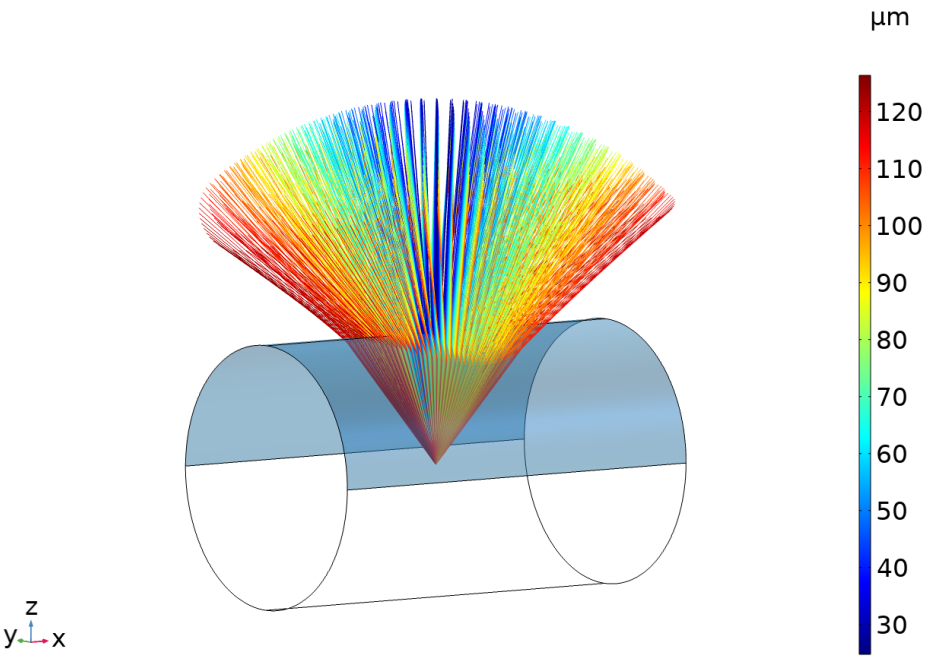


Figure 4.1: Schematic diagram of focusing light exactly on the centre of a fibre.

tracing results and corresponding aberration maps obtained with the Optical Aberration Analysis

module in COMSOL. By applying phase front compensation with either a spatial light modulator or a deformable mirror, the residual aberrations can be minimised, enabling nearly diffraction limited focusing in the core region.

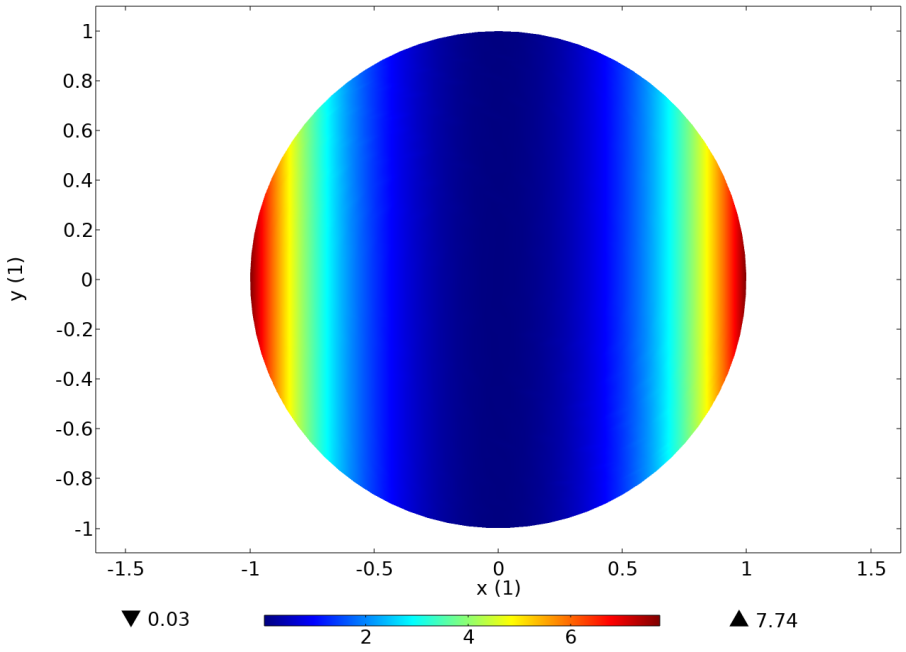


Figure 4.2: Laser focusing aberration at the fibre core.

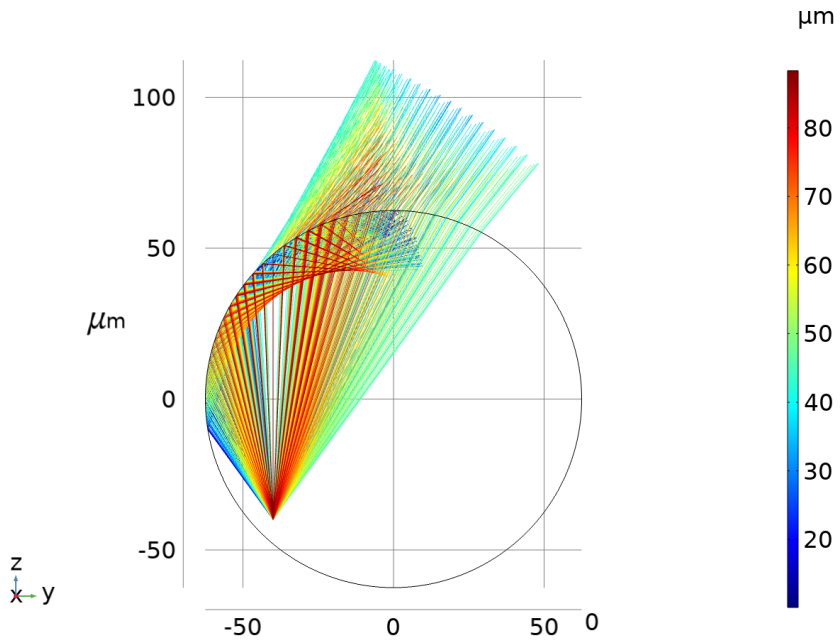


Figure 4.3: Simulation of laser focusing in the fibre periphery.

However, the simulations presented in the previous chapter indicate that achieving higher sensitivity requires fabricating cavities of the largest possible dimensions, which in turn necessitates

focusing the femtosecond laser at the fibre's periphery. Figure 4.3 presents a simulation of such edge focusing: exploiting optical reciprocity, a conical beam emitted from a peripheral point within the fibre shows that nearly half of the rays undergo total internal reflection. Consequently, aberration correction techniques developed for core centred writing are unsuitable for structuring regions far from the core.

I ultimately selected an oil-immersion objective for the laser fabrication of the FBG. By employing an index matching oil whose refractive index closely approximates that of silica, the fibre's intrinsic lensing effect can be neglected. Although focusing too near the cladding surface may locally heat the oil and generate bubbles that impede beam convergence, mechanical integrity considerations likewise require that a sufficient margin be left between the machined features and the fibre's outer boundary.

4.1.2 Principles of laser modified optical materials

When femtosecond pulses are tightly focused inside a transparent medium, they trigger significant non-linear optical absorption. Although a rigorous physical model is still lacking, the phenomenon is conventionally divided into three sequential stages: (i) the initial formation of a free electron plasma, (ii) subsequent energy relaxation, and (iii) the ensuing material modification [2].

Multiphoton absorption is one of the non-linear photo-ionisation mechanisms that occur during femtosecond laser irradiation. In essence, valence band electrons simultaneously absorb several photons whose combined energy exceeds the band gap energy. At moderate intensities and high optical frequencies, multiphoton absorption dominates [2, 4]. Conversely, at very high intensities and lower frequencies, non-linear ionisation proceeds mainly through tunnelling: the strong electric field distorts the band structure, lowering the potential barrier between the valence and conduction bands, so that electrons can undergo a direct interband transition via quantum tunnelling. In most practical situations, the ionisation dynamics reflect a combination of these two processes [2, 5]. Figure 4.4

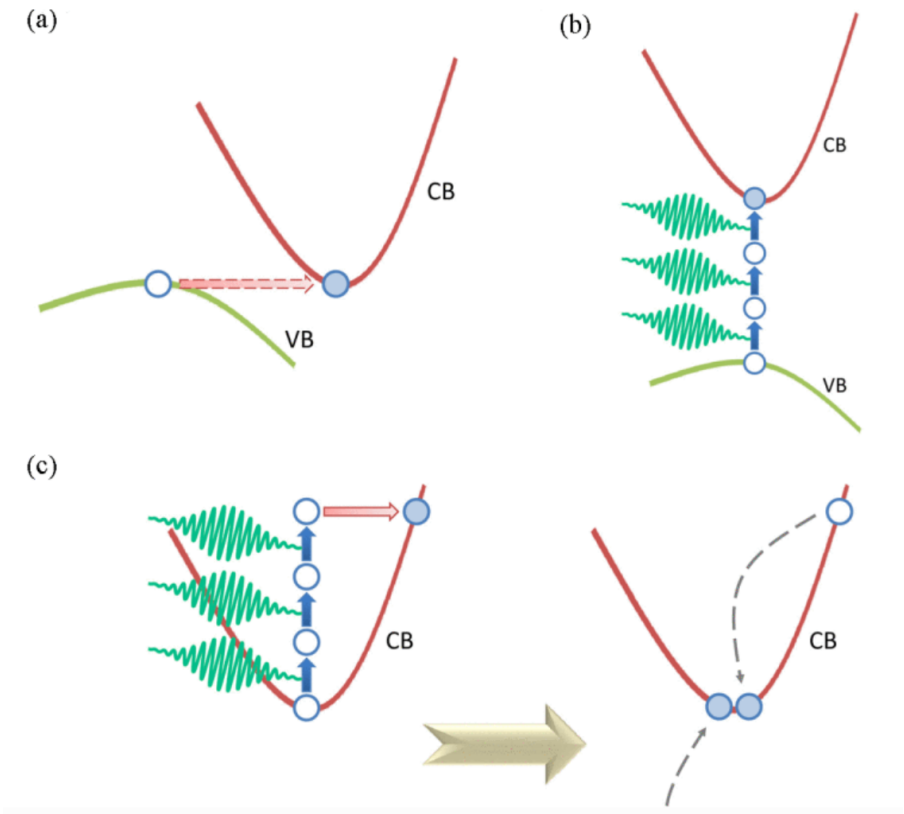


Figure 4.4: Non-linear optical absorption. (a) Quantum tunnelling (b) Multiphoton absorption (c) Avalanche ionization [3].

presents schematic illustrations of several kinds of nonlinear optical absorption.

Furthermore, conduction band free electrons can themselves absorb additional photons; after successive absorptions, their energies may surpass the band gap threshold. These highly energetic carriers then collide with bound electrons in the valence band, promoting them into the conduction band. The newly liberated electrons repeat the same absorption-collision cycle, initiating a cascading multiplication process known as avalanche photo-ionisation [4]. The free electron plasma produced by non-linear or avalanche ionisation transfers its energy to the lattice, thereby initiating permanent material modifications. Although the underlying mechanisms are not yet fully elucidated, well-documented outcomes include changes in refractive index, alterations in birefringence, and the formation of micro-cracks [6, 7, 8].

At relatively low pulse energies, laser exposure produces a smooth refractive index change, plausibly because the material in the focal volume melts and then rapidly solidifies; this quenching step

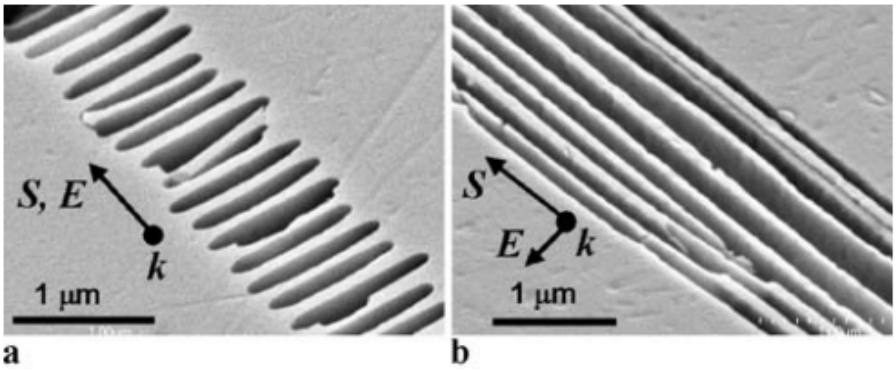


Figure 4.5: SEM images of nano-gratings parallel and perpendicular to the laser direct writing direction [9].

modifies both the local density and the refractive index [10, 11]. Higher pulse energies induce a birefringent refractive index change marked by the emergence of periodically arranged nanoscopic fissures (nano-gratings) within the focal region [7, 9]. The orientation of these nano-gratings depends on the polarisation of the writing laser, so the laser polarisation can influence the anisotropy, birefringence, and etching behaviour of the modified region. The SEM micrograph in Figure 4.5 shows the morphology of the nano-gratings produced by laser direct writing. Owing to their altered microstructure, these modified zones are considerably more susceptible to chemical etching than the surrounding, unexposed glass. When the pulse energy is increased still further, a conspicuous region of reduced density, or even a fully voided cavity, is left at the focus [12]. The SEM image in Figure 4.6 shows a void (hollow cavity) formed by laser direct writing.

This image has been removed from the dissemination version for copyright reasons. For the original figure, please see: EN Glezer et al. "Three-dimensional optical storage inside transparent materials". In: Optics letters 21.24 (1996), pp. 2023–2025.

Figure 4.6: SEM images of the laser direct writing voided cavity [12].

4.1.3 Laser fabrication systems

Figure 4.7 presents a simplified schematic of the laser fabrication system used to fabricate the pressure sensor sample. The laser source is a regenerative femtosecond system (Pharos SP06-1000-PP)

operating at its second harmonic (wavelength = 515 nm) with a pulse duration of 170 fs. The pulse energy is adjusted externally by rotating a motorised half-wave plate positioned upstream of a polarising beam splitter, while an external photodiode continuously monitors the output power. The beam is projected onto a spatial light modulator (Hamamatsu X10468) and then focused inside the optical fibre by a 20× oil-immersion objective (Olympus UPlanApo, NA 0.8). The fibre itself is mounted on a three-axis nano-precision translation stage (X: Aerotech ABL10100 LN; Y: Aerotech ABL10100 LN; Z: ANT95V-3). A red LED provides transmitted illumination through the fibre, enabling real-time observation of the fabrication process via a CCD camera.

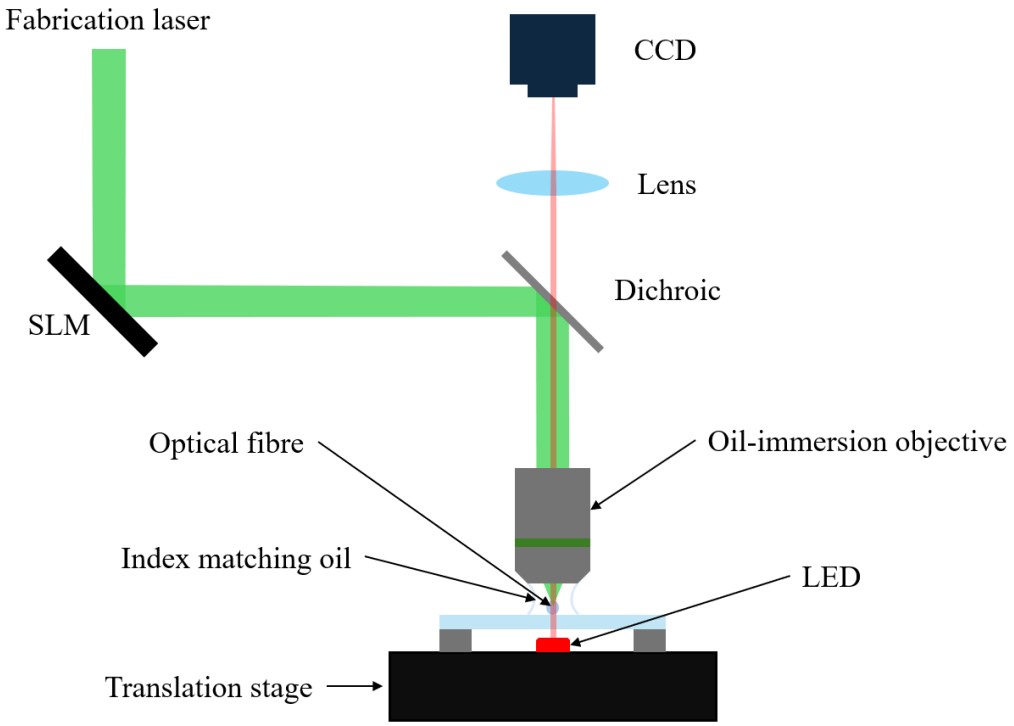


Figure 4.7: A simplified schematic diagram of the femtosecond laser fabrication system.

4.1.4 Fabrication process

First, the COMSOL meshing module was used to discretise the cavity geometry into elements comparable in size to the laser focal spot (2-3 μm). The mesh node coordinates were then exported and fed to the motion-control system, which guided the fibre along its axis while the laser wrote successive

lines. Writing was carried out at 0.5 mm/s with a pulse energy corresponding to an average power of 130 mW and a repetition rate of 100 kHz. Figure 4.8 depicts the COMSOL generated mesh and the representative cross-section of the fabricated structure.

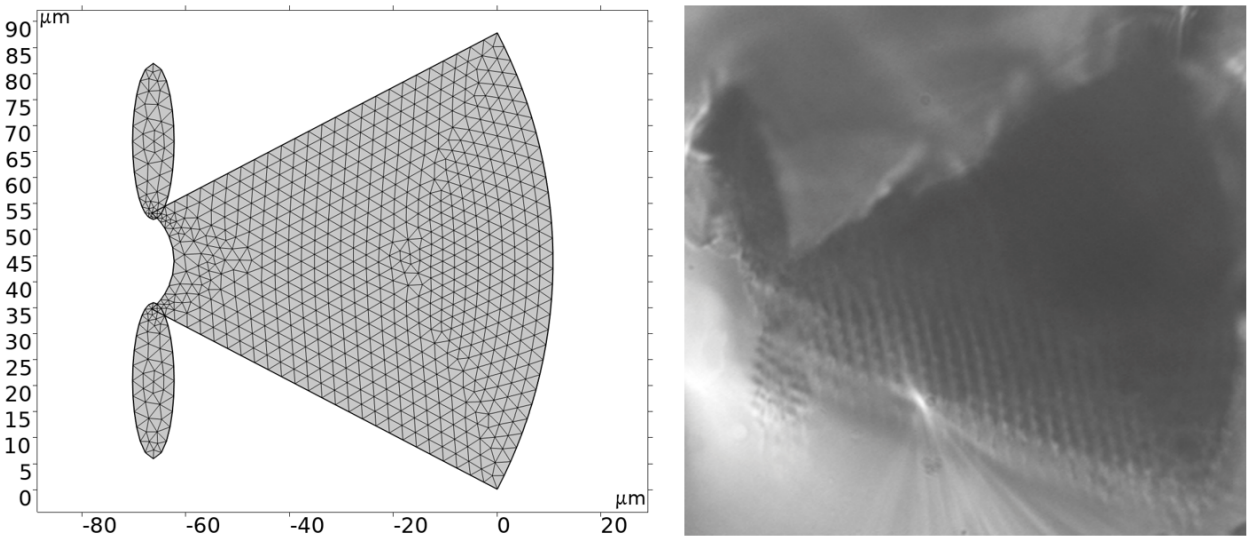


Figure 4.8: Meshing diagram of holes in COMSOL and micrograph of a sample cross section.

4.1.4.1 Fibre Bragg grating inscription

A second-order fibre Bragg grating was selected so that the required grating pitch was compatible with point-by-point femtosecond-laser inscription. To place the Bragg resonance close to 1550 nm, the grating period was calculated from the second-order Bragg condition,

$$\lambda_{\mathrm{B}} = n_{\mathrm{eff}}\Lambda, \tag{4.1}$$

where λ_{B} is the Bragg wavelength, n_{eff} is the effective refractive index of the guided mode, and Λ is the grating pitch. Using the effective refractive index of silica fibre, the required pitch was estimated to be $\Lambda = 1.073\ \mu\mathrm{m}$.

The grating was inscribed using a point-by-point method. The femtosecond laser repetition rate was reduced to 100 Hz, and the fibre was translated along its axis at 0.1073 mm/s. This gives a pulse-to-pulse spacing of approximately 1.073 µm, so each grating plane was produced by a single

laser pulse. The average writing power was 15 µW, corresponding to a pulse energy of 0.15 µJ. This single-pulse point-by-point approach directly defines the grating pitch through the stage speed and laser repetition rate, avoiding the need for a phase mask.

4.2 Wet etching of fused silica

Because femtosecond irradiation induces strong non-linear absorption, the focal volume undergoes micro-explosion and densification, accompanied by significant rearrangement of the local bonding network [13, 14]. The modified glass therefore reacts far more readily with certain acids and bases than unexposed silica. In particular, regions processed by the laser etch much faster in hydrofluoric acid, potassium hydroxide, or sodium hydroxide solutions [15, 16]. This differential reactivity enables the selective removal of the laser-modified zones through wet chemical etching.

Although both hydrofluoric acid and potassium hydroxide enable selective etching of silica, the high toxicity of HF makes KOH the preferred choice. According to the work of Calum A. Ross and colleagues, an 8 mol/L KOH solution at 85 °C exhibits markedly superior performance: its maximum etch selectivity is roughly fourteen times that of HF, and its etch rate 363 μm/h slightly exceeds the 320 μm/h achieved with hydrofluoric acid [17]. Figure 4.9 demonstrates a comparison of etch selectivity in the two solutions.

This image has been removed from the dissemination version for copyright reasons. For the original figure, please see: Calum A Ross et al. "Optimisation of ultrafast laser assisted etching in fused silica". In: Optics express 26.19 (2018), pp. 24343–24356.

Figure 4.9: Heatmaps of the etching selectivity of laser-modified silica in 8 mol/L KOH and 5% HF solution [17].

I first use femtosecond laser irradiation to drill two minute side channels that link the internal

cavities to the external environment, thereby allowing the KOH solution to access and etch the laser modified regions. Because these entry channels are exceedingly small, they can be hermetically sealed with relative ease once the etching step is complete. Such sealing is essential: the optical fibre pressure sensor functions only when its internal cavities are completely isolated. Any leakage would equilibrate the internal and external pressures, eliminate the non-uniform stress distribution, and thus suppress the stress-induced birefringence on which the sensing mechanism relies.

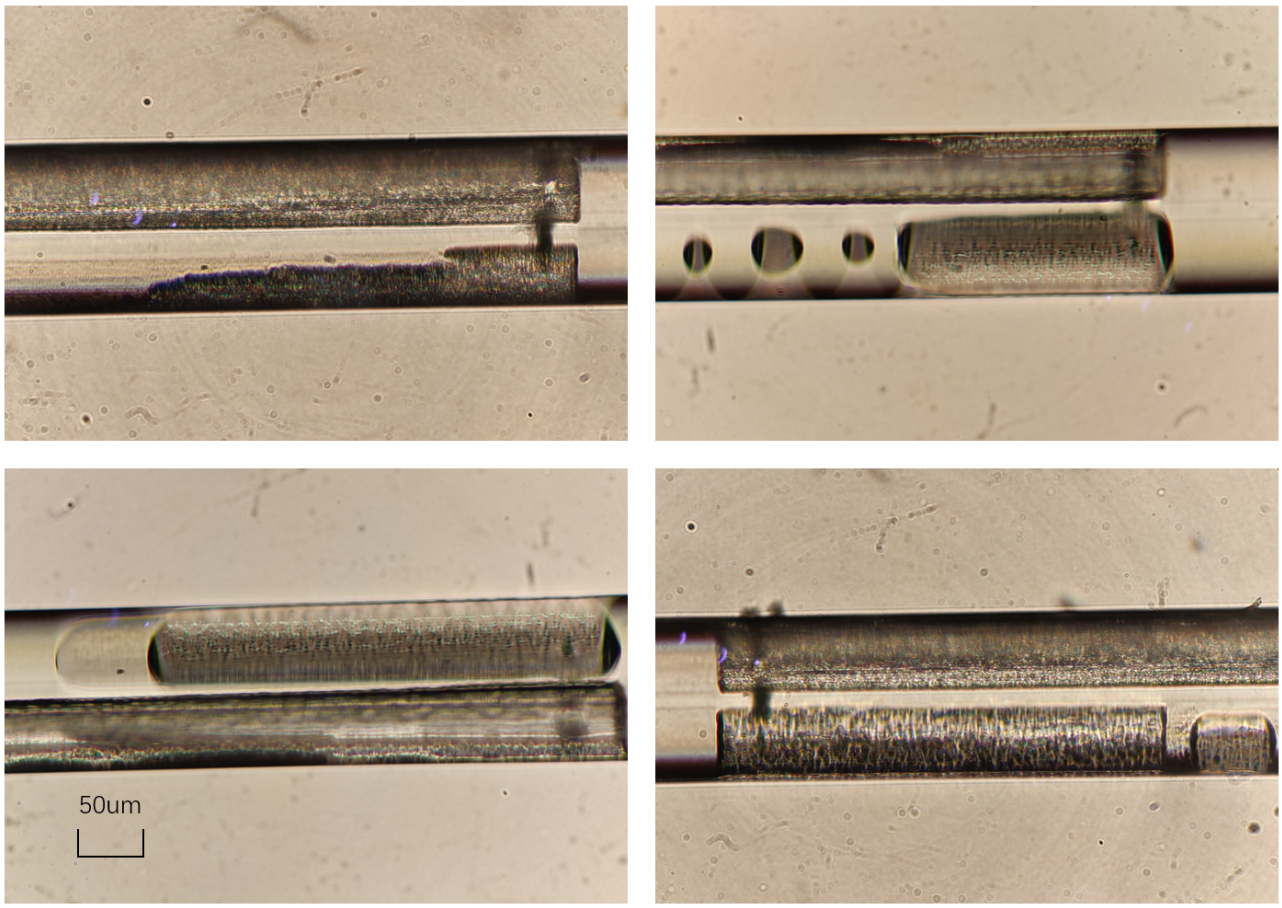


Figure 4.10: Micrographs of samples etched using the entry channel.

Figure 4.10 presents microscope images of several samples after wet etching, revealing that one cavity consistently opens more rapidly than its counterpart. This asymmetry originates from the two-step laser writing protocol. The main cavity is inscribed with an oil-immersion objective, whereas the access channels cannot be fabricated with the same objective: focusing near the cladding surface would heat the immersion oil, generate bubbles, and prevent the beam from reaching the final segment that connects to the exterior. Accordingly, once the cavity is completed, the system is

switched to an air objective to write the access channels, employing the adaptive-optics correction procedure proposed by Patrick Salter and ZiPei Song to compensate for fibre-induced aberrations[1]. Inevitably, however, changing objectives and removing the index-matching oil introduce slight torsion of the sample. As illustrated in Figure 4.11, this results in unequal access-channel lengths, which in turn accounts for the disparity in the etch rates of the two cavities.

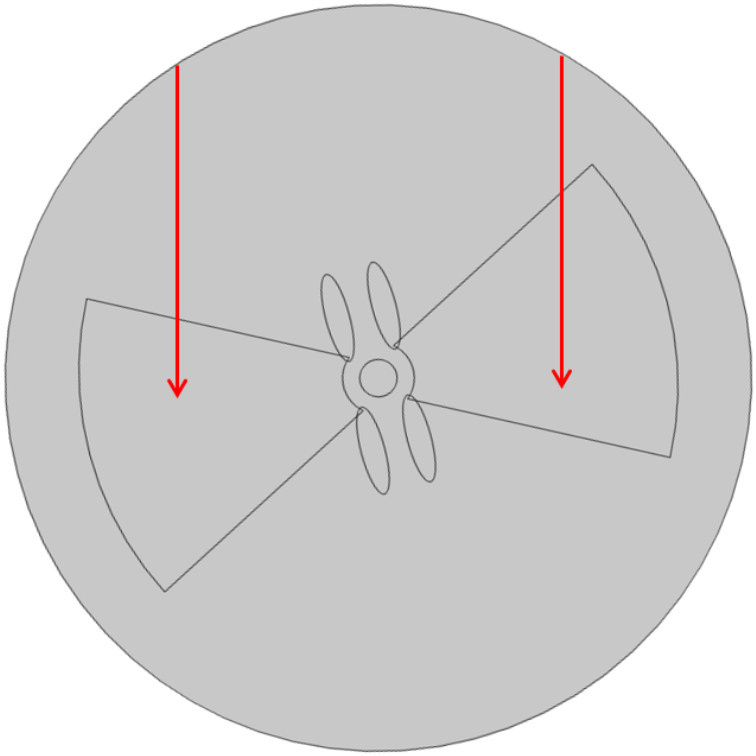


Figure 4.11: Schematic diagram of the access channel.

Repeated attempts confirmed that the disparity in etch rates between the two access channels was difficult to eliminate. Because each cavity lies in close proximity to the fibre core, the side that finishes etching first also begins to erode the core itself. To circumvent this issue, I adopted an alternative approach: the fibre was cleaved at one end to expose the laser-modified region directly, after which the wet-etching step was performed. Each laser-written cavity had an axial length of approximately 5 mm along the fibre.

Figure 4.12 presents side-view micrographs of a standard single mode fibre with a 125 μm outer

diameter and a large cladding fibre (LCF LIEKKI Passive-12/250 DC) with a 250 μm outer diameter, shown both before and after selective etching. The post-etch images reveal cavities with crisp, well-defined edges, attesting to the high precision of the selective-etching technique. Although the etched region appears to extend through the cladding, this impression is purely an artefact produced by optical distortion at the curved fibre surface; the cladding itself remains intact.

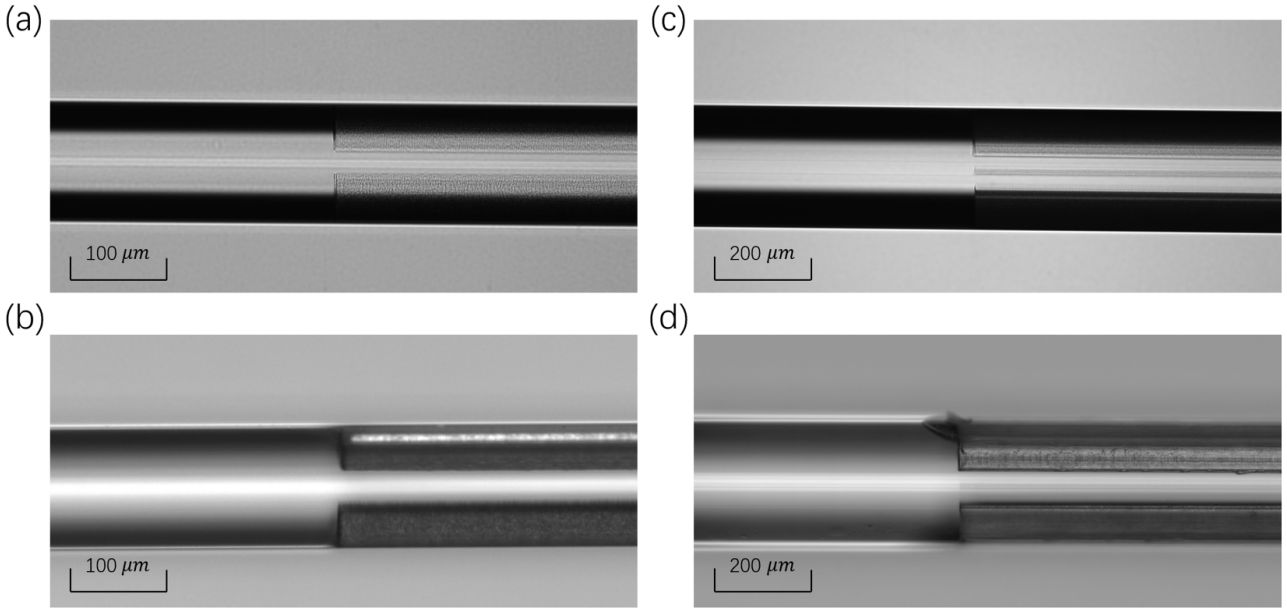


Figure 4.12: Microscope image of the samples. (a),(b) Side views of the inscribed and uninscribed areas of the 125 μm SMF before and after etching. (c),(d) Side views of the inscribed and uninscribed areas of the 250 μm large diameter fibre before and after etching.

Figure 4.13 presents a cross-sectional view of the fibre after etching. The cladding edge is visibly over-etched, a consequence of the laser-modified segment at the cleaved end being the first and longest exposed to the KOH solution. While some unmodified glass near the end face is removed during this prolonged contact, the overall profile shows that the extent of over-etching remains limited. This issue can be mitigated by incorporating a short sacrificial section during laser writing; moreover, the subsequent end-face sealing step will isolate the affected region, so the over-etching has little practical consequence.

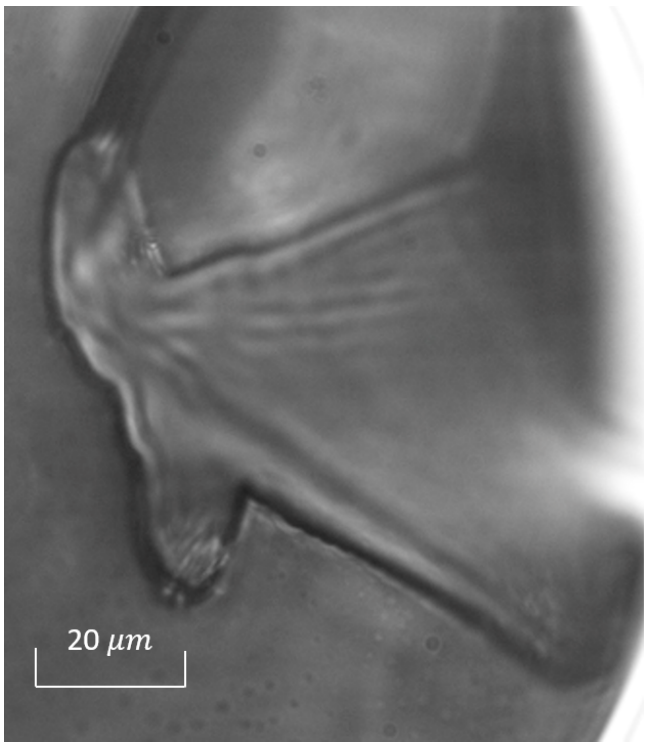


Figure 4.13: Cross-sectional view of the 250 μm fibre inscription area.

4.3 Sensor Sealing

Once etching is complete, the openings must be hermetically sealed. Any residual liquid in the cavities is first removed by placing the sensor in a furnace at 120°C for two hours, thereby ensuring complete evaporation. Two sealing strategies were investigated. In the first, the apertures were capped with Resbond 903HP, an alumina-based ceramic adhesive rated for temperatures up to 1 650 °C and capable of withstanding compressive loads of 483 bar. The adhesive was applied to the cavity mouths and cured at 120 °C for two hours to accelerate hardening. Figure 4.14 illustrates a representative sealed sample.

A second sealing method utilises a fusion splicer (Fujikura 70R) to melt the fibre tip locally. Figure 4.15 shows a micrograph of the end facet after re-solidification. This technique eliminates any concern about thermal-expansion mismatch between an adhesive and silica and benefits from silica's inherent high-temperature stability. Its chief limitation, however, is that melting can induce partial collapse of the cavities, thereby reducing sensor sensitivity.

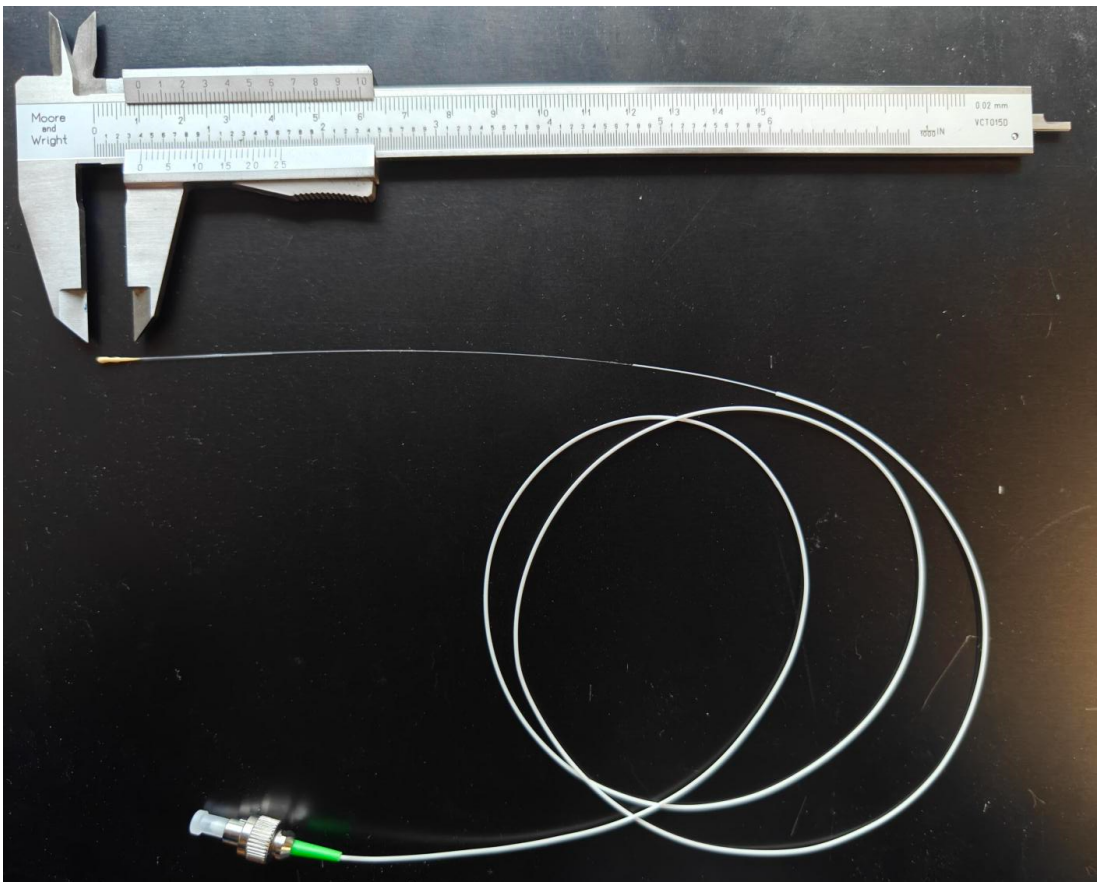


Figure 4.14: The sample was sealed using the adhesive.

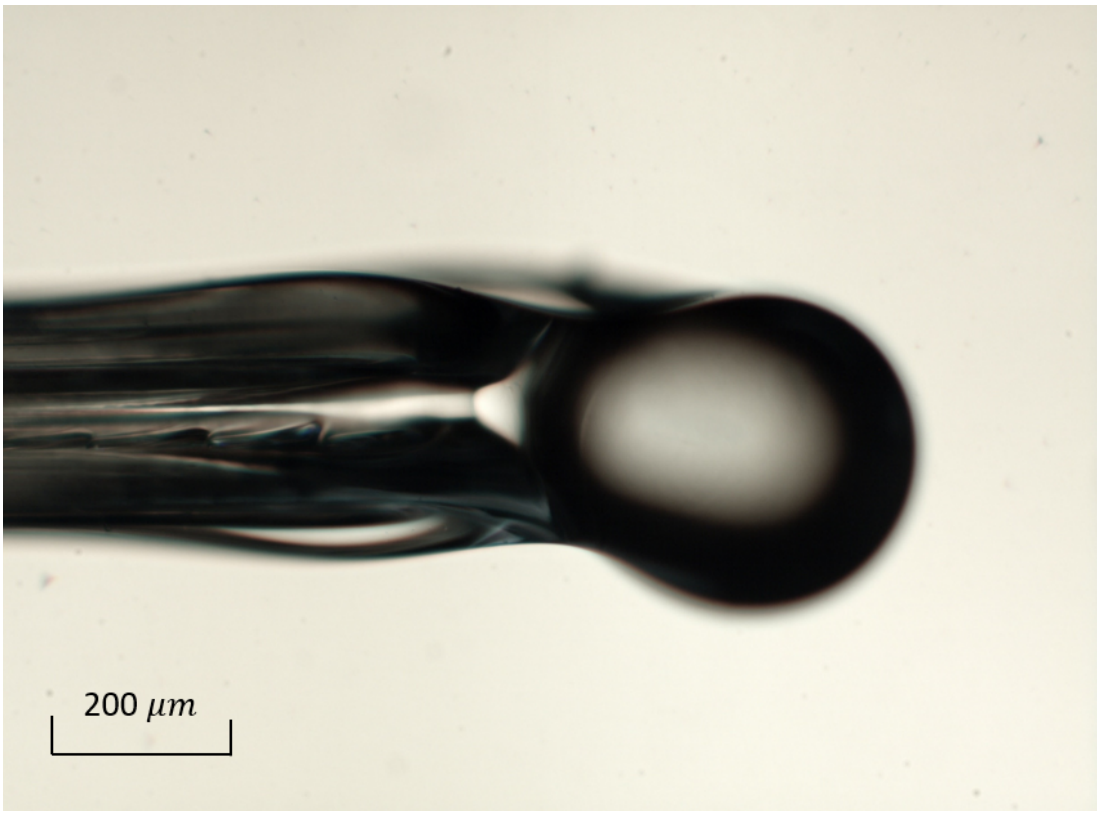


Figure 4.15: The sample was sealed by fusion splicer.

In summary, this chapter has detailed the fabrication of intricate three-dimensional structures inside optical fibres using femtosecond-laser inscription, the subsequent removal of the modified regions by wet chemical etching, and the methods employed to hermetically seal the resulting cavities. The next stage entails subjecting the sensors to pressure and thermal-stability tests to assess their performance under extreme operating conditions.

References

[1] Patrick S Salter et al. "Femtosecond fibre Bragg grating fabrication with adaptive optics aberration compensation". In: *Optics Letters* 43.24 (2018), pp. 5993–5996.

[2] Shane M. Eaton, Giulio Cerullo, and Roberto Osellame. "Fundamentals of Femtosecond Laser Modification of Bulk Dielectrics". In: *Femtosecond Laser Micromachining: Photonic and Microfluidic Devices in Transparent Materials*. Ed. by Roberto Osellame, Giulio Cerullo, and Roberta Ramponi. Berlin, Heidelberg: Springer Berlin Heidelberg, 2012, pp. 3–18. ISBN: 978-3-642-23366-1.

[3] Martin Ams et al. "Investigation of ultrafast laser–photonic material interactions: challenges for directly written glass photonics". In: *IEEE journal of selected topics in quantum electronics* 14.5 (2008), pp. 1370–1381.

[4] Chris B Schaffer, Andre Brodeur, and Eric Mazur. "Laser-induced breakdown and damage in bulktransparent materials induced by tightly focused femtosecond laserpulses". In: *Measurement Science and Technology* 12.11 (2001), p. 1784.

[5] LV Keldysh. "A similar phenomenology pertains to multiphoton ionization in atomic physics". In: *Soviet Physics-JETP* 20.4 (1965), pp. 1037–1037.

[6] K Miura et al. "Photowritten optical waveguides in various glasses with ultrashort pulse laser". In: *Applied Physics Letters* 71.23 (1997), pp. 3329–3331.

[7] Yasuhiko Shimotsuma et al. "Self-organized nanogratings in glass irradiated by ultrashort light pulses". In: *Physical review letters* 91.24 (2003), p. 247405.

[8] S. Juodkazis et al. "Laser-Induced Microexplosion Confined in the Bulk of a Sapphire Crystal: Evidence of Multimegabar Pressures". In: *Physical review letters* 96.16 (2006), p. 166101.

[9] Cyril Hnatovsky et al. "Fabrication of microchannels in glass using focused femtosecond laser radiation and selective chemical etching". In: *Applied Physics A* 84 (2006), pp. 47–61.

[10] James W Chan et al. "Structural changes in fused silica after exposure to focused femtosecond laser pulses". In: *Optics letters* 26.21 (2001), pp. 1726–1728.

[11] Masaaki Sakakura et al. "Temperature distribution and modification mechanism inside glass with heat accumulation during 250kHz irradiation of femtosecond laser pulses". In: *Applied Physics Letters* 93.23 (2008).

[12] EN Glezer et al. "Three-dimensional optical storage inside transparent materials". In: *Optics letters* 21.24 (1996), pp. 2023–2025.

[13] RAB Devine et al. "Pressure-induced bond-angle variation in amorphous SiO 2". In: *Physical Review B* 35.5 (1987), p. 2560.

[14] Andrius Marcinkevičius et al. "Femtosecond laser-assisted three-dimensional microfabrication in silica". In: *Optics letters* 26.5 (2001), pp. 277–279.

[15] Satoshi Kiyama et al. "Examination of etching agent and etching mechanism on femotosecond laser microfabrication of channels inside vitreous silica substrates". In: *The Journal of Physical Chemistry C* 113.27 (2009), pp. 11560–11566.

[16] L Wong et al. "The effect of HF/NH4F etching on the morphology of surface fractures on fused silica". In: *Journal of Non-Crystalline Solids* 355.13 (2009), pp. 797–810.

[17] Calum A Ross et al. "Optimisation of ultrafast laser assisted etching in fused silica". In: *Optics express* 26.19 (2018), pp. 24343–24356.

5 | Pressure and Temperature Testing

This chapter describes the procedures used to characterise both the FBGs and the complete sensors. The reflection spectra of a grating were first compared before and after wet etching. The sensors were then subjected to repeated pressure response and thermal stability tests to verify linearity and to determine the full dynamic range of their pressure response.

5.1 Initial FBG testing

First, the reflection spectrum of a sensor sample was tested prior to wet etching. A tunable laser (Keysight Agilent 8164A) acted as the light source; the output beam passed through a polarization controller, and an optical circulator directed the light reflected from the FBG to to the photodetector integrated within the Agilent Lightwave Measurement system. Figure 5.1 presents a schematic of the measurement arrangement.

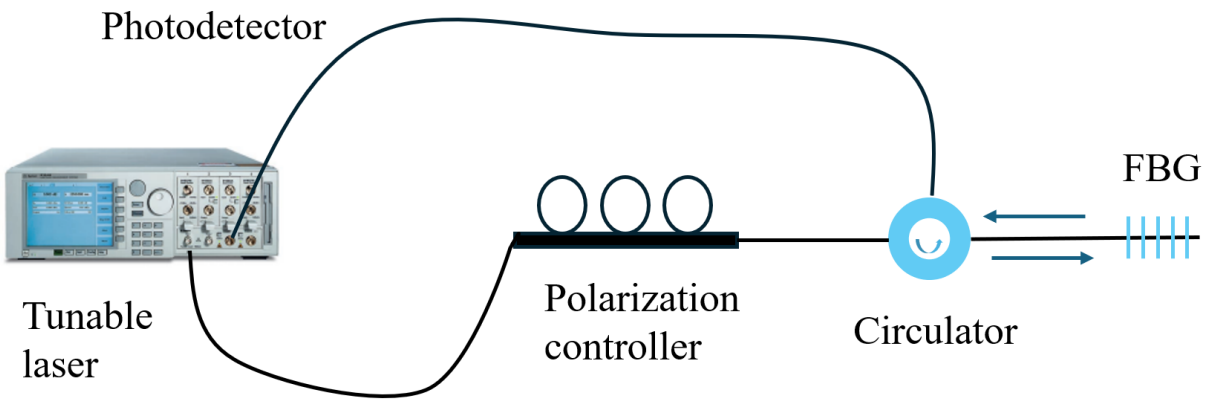


Figure 5.1: Schematic diagram of the measurement system.

The reflection spectrum of a laser-inscribed, unetched sample was measured first. As illustrated in Figure 5.2b, the Bragg resonance of my sample splits into two distinct peaks. This behaviour is

consistent with the stress-induced birefringence reported by Herman and co-workers in femtosecond-laser direct-writing experiments (see Fig. 5.2a) [1]. The laser modified zones impose residual stresses

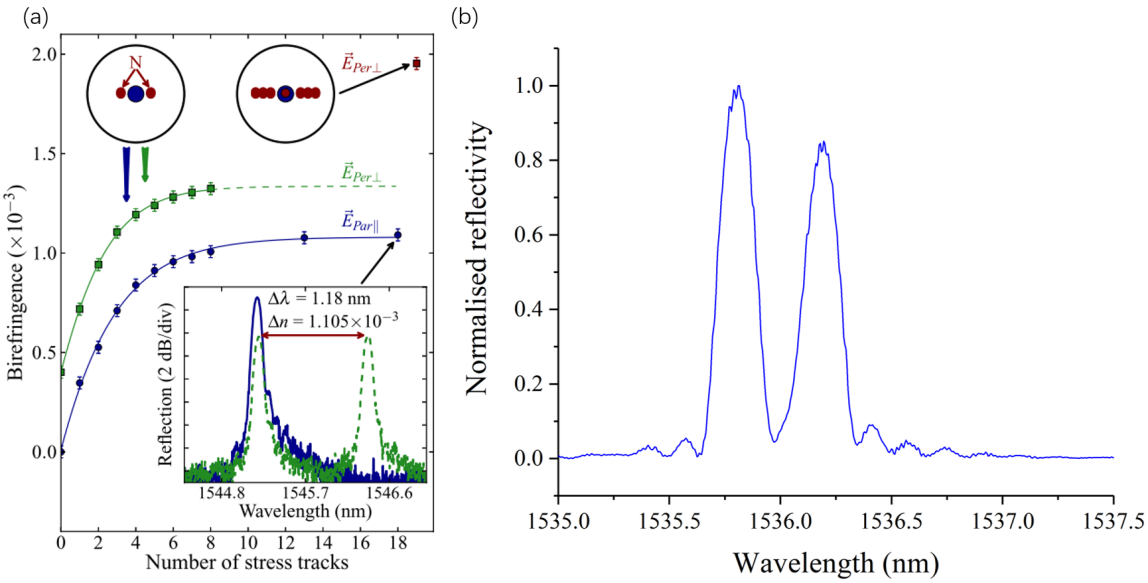


Figure 5.2: (a) Effect of stress introduced by femtosecond laser irradiation on fibre birefringence in the literature[1] (b) Fibre Bragg Grating reflection spectra of my un-etched sample.

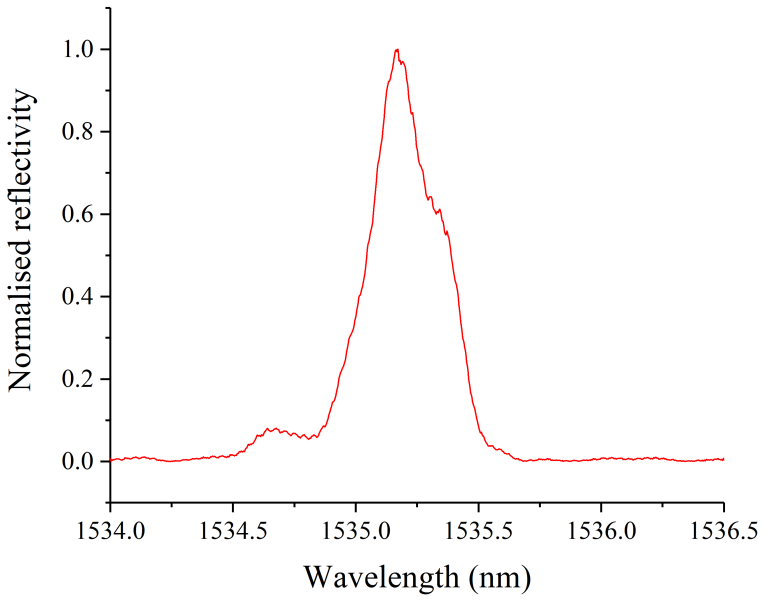


Figure 5.3: Fibre Bragg Grating reflection spectra of the etched sample.

on the surrounding glass, and, via the stress-optic effect, these stresses alter the distribution of the refractive index components in the core, closely resembling the effect of externally applied pressure. Because no cavities are present, however, the internal stress field remains essentially unchanged under

external loading, rendering the un-etched samples unsuitable for pressure sensing. Figure 5.3 presents the reflection spectrum obtained after wet etching. The Bragg resonance now appears as a single, unsplit peak: the peak separation observed previously is absent. The resonance also shifts slightly towards shorter wavelength, most likely because wet etching removes laser-modified material and releases residual laser-induced stress around the grating region. Through the Bragg condition, changes in the effective refractive index and local strain state can shift the Bragg wavelength. Therefore, the observed blue shift is consistent with stress relaxation after etching, while the disappearance of peak splitting indicates that the stress-induced birefringence has largely been removed.

5.2 Hydraulic Testing at Halliburton

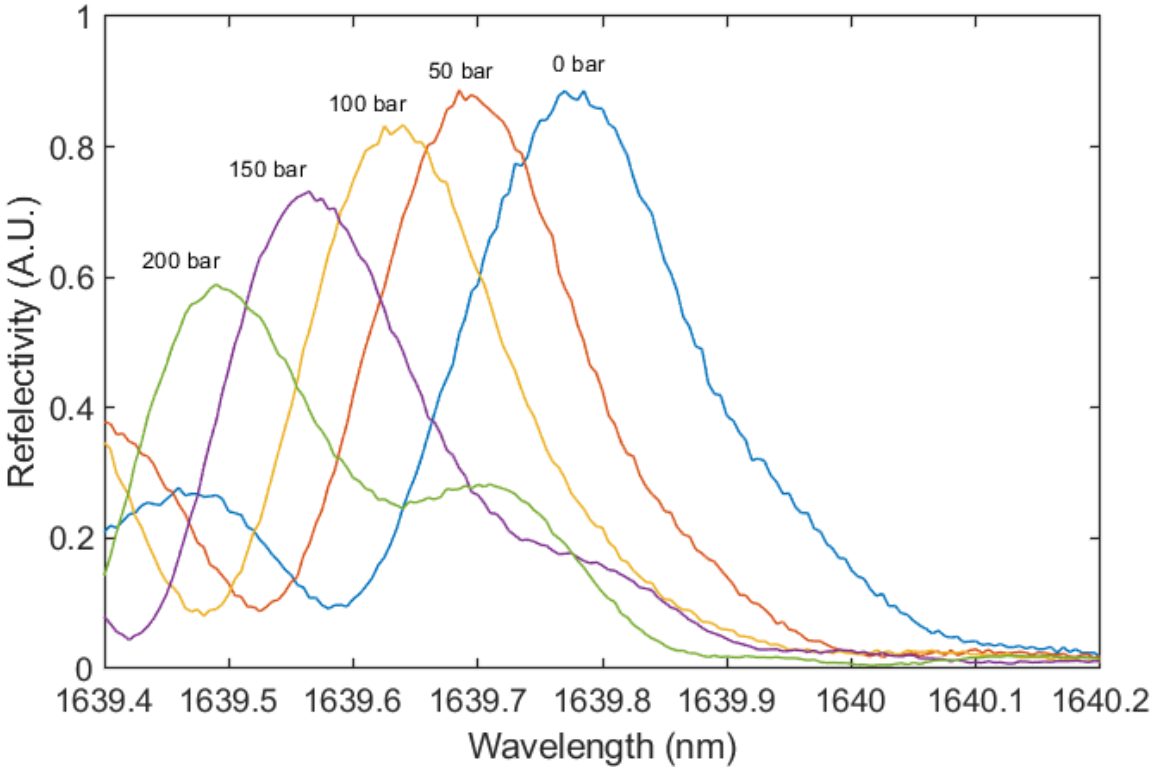


Figure 5.4: Preliminary pressure test result of the sample sealed using the fusion splicer.

Halliburton was an industrial collaborator on this project, providing access to hydraulic pressure-testing facilities and practical guidance on the design and safe operation of a high-pressure test system. In particular, the tests carried out at Halliburton informed the construction of the hydraulic testing

system later built at Oxford. A LCF sensor prototype that incorporates sector cavities with an 80 μm radius and auxiliary micro-holes, smaller than the 90 μm configuration modelled numerically, was pressure tested at Halliburton. The device was fusion spliced to polyimide coated single mode fibre, sealed within stainless-steel tubing of 2 mm internal diameter that was filled with oil. Hydrostatic pressure was increased stepwise to 200 bar using a DHI PPCH automated pressure controller. At each pressure level, the FBG reflection spectrum was recorded by sweeping a tunable laser source (Agilent 8164A). The laser output passed through a polarisation controller, travelled to the grating via an optical circulator, and the reflected signal was detected by the instrument's built in photodetector. The resulting spectra (Fig.5.4) show that the peak splitting begins at 150 bar, with two distinct peaks clearly resolved at 200 bar. At this maximum pressure, the wavelength separation is approximately 240 pm, yielding an estimated pressure sensitivity of 1.2 pm/bar.

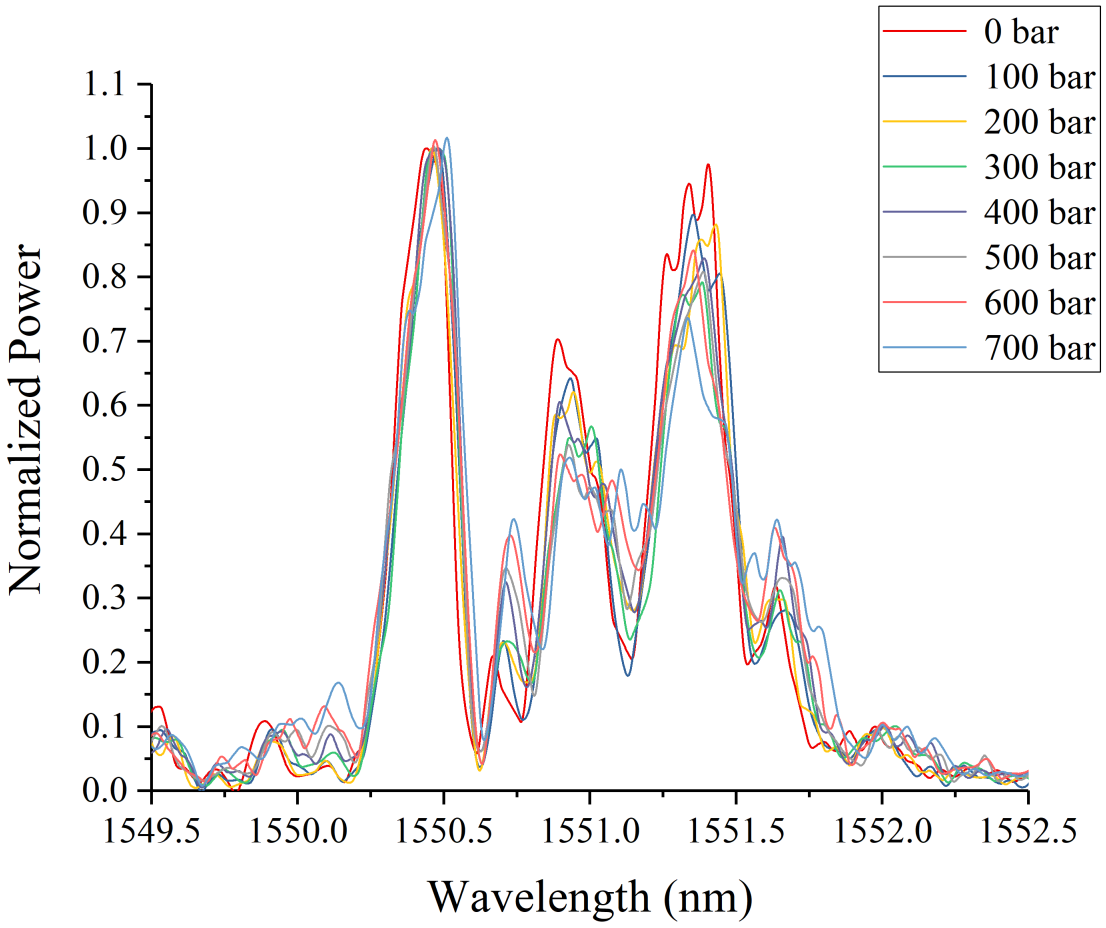


Figure 5.5: Preliminary pressure test result of the sample sealed using the ceramic adhesive.

During this series of tests we observed that samples sealed with the ceramic adhesive exhibited multiple reflection peaks even before any pressure was applied. The most plausible explanation is that the adhesive shrinks during curing, compressing the encapsulated fibre sensor. As shown in Figure 5.5, because the layer of adhesive was not perfectly uniform, the resulting stresses were likewise non-uniform, which caused the FBG reflection to split into several peaks. These additional peaks complicate pressure measurement and may also indicate cracking that could disable the sensor. For these reasons, the ceramic adhesive packaging method was abandoned.

The tests carried out at Halliburton enabled us to evaluate the advantages and disadvantages of the two sealing approaches while yielding the first observation of peak splitting in the sensor spectrum. The collaboration also furnished invaluable guidance on assembling a hydraulic test system. Drawing on this experience, we built our own hydraulic testing system to conduct further pressure measurements and obtain a more complete characterisation of the sensor's pressure response.

5.3 Build of a Hydraulic Test System

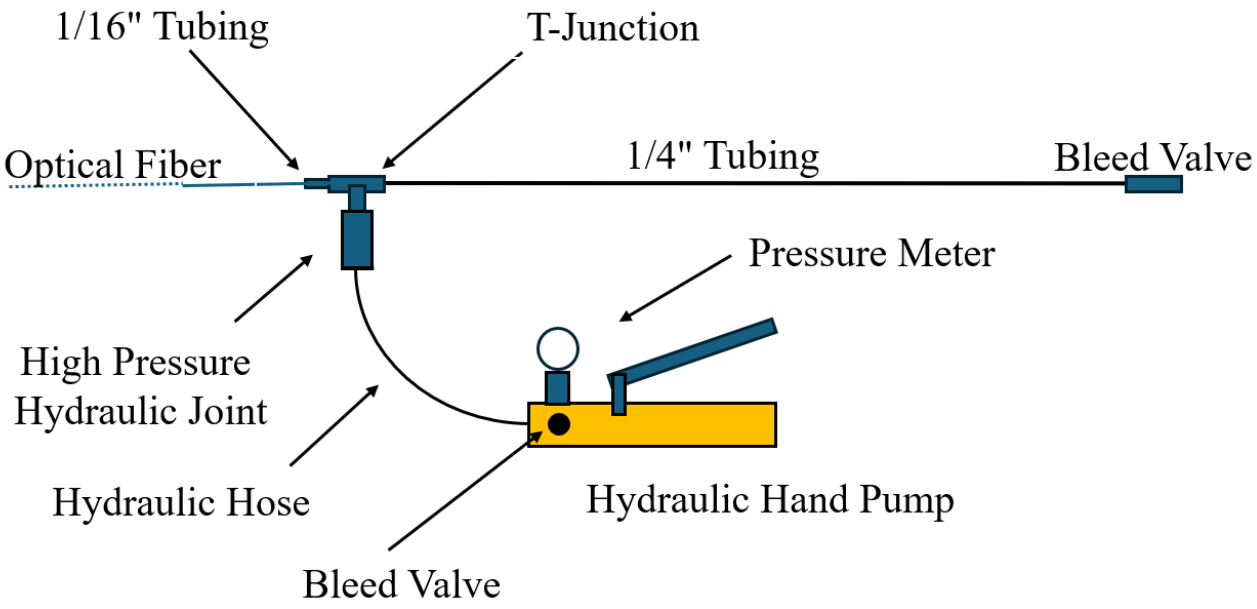


Figure 5.6: Schematic diagram of the hydraulic pressure-testing system for FBG sensors.

Figure 5.6 demonstrates the hydraulic pressure system constructed at Oxford. The FBG sensor

was fusion spliced to polyimide-coated single mode fibre and inserted into stainless-steel tubing with an internal diameter of 1/4 inch. This tube led to a T-connector through which the fibre continued into 1/16 inch tubing; the annular gap around the fibre was sealed with epoxy. The opposite end of the sensor housing terminated at a bleed valve that was opened at the start of each experiment to vent air and ensure complete filling of the system with hydraulic oil. A hand operated Enerpac hydraulic pump was attached to the third arm of the T-connector and supplied pressures up to 600 bar. All tubing and fittings were supplied by Swagelok and carried a rated working pressure of 700 bar. Figure 5.7 provides a photograph of the experimental setup. During pressurisation, all components except the hydraulic pump are enclosed within a housing fabricated from composite plywood to guard against accidental rupture or fluid ejection.

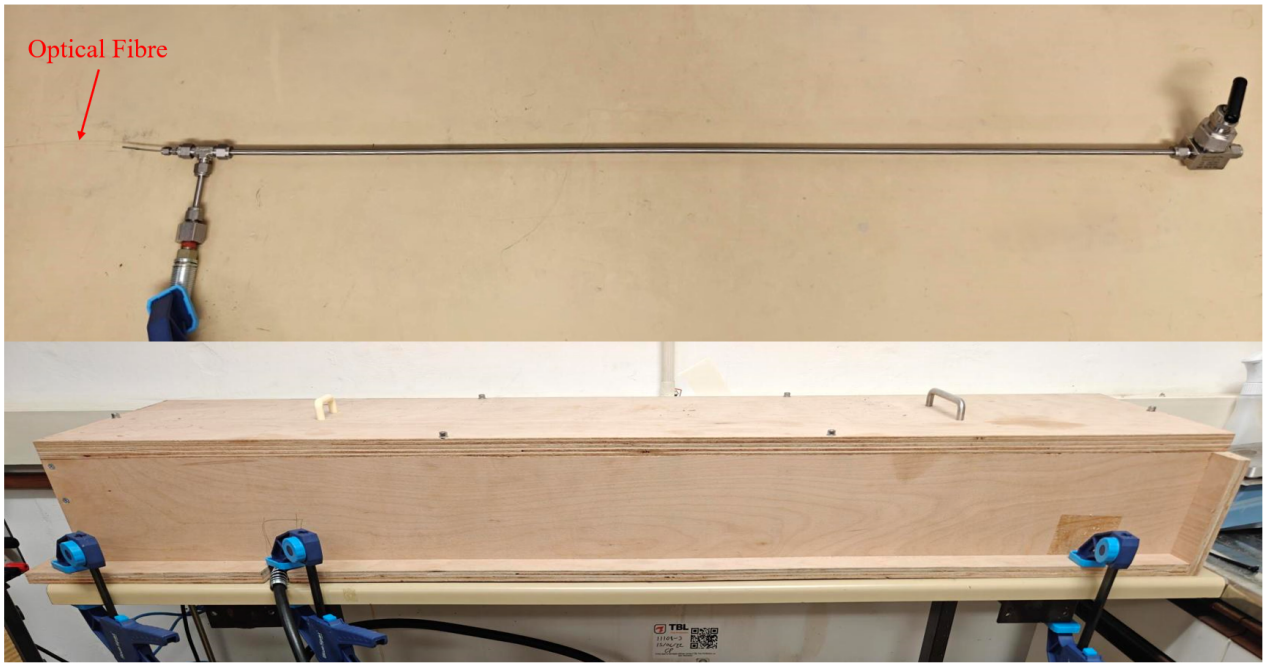


Figure 5.7: Photograph of the hydraulic pressure-testing system for FBG sensors.

5.4 Hydraulic Pressure Testing

A LCF sample featuring a sector radius of 95 μm and auxiliary micro-holes was tested in the hydraulic system. At each pressure step, the FBG reflection spectrum was recorded with an interrogator

(Halliburton SmartFibres SmartScan SBI). Four pressure cycles were conducted, ranging from 300 bar to 600 bar in 50 bar increments. At each pressure, an averaged spectrum from the interrogator was taken. Because the standard interrogator configuration has a polarization scrambler to measure the spectra of both polarization modes simultaneously, whereas our unit lacked this component, we introduced a manual polarisation controller and adjusted it to launch light into both orthogonal modes.

After the first pressure cycle, a temperature stability test was performed, heating the sample to 450°C. Figure 5.8 shows spectra at different pressures for the second test cycle. As the peaks separate their relative power decreases due to the lower overlap. For clarity, each trace has been normalised to the intensity of the short-wavelength peak. Below 300 bar, the spectra of the two polarisations largely coincide, making pressure discrimination difficult. Peak splitting becomes discernible at 300 bar and increases monotonically with pressure, reaching a separation of approximately 174.4 pm at 600 bar.

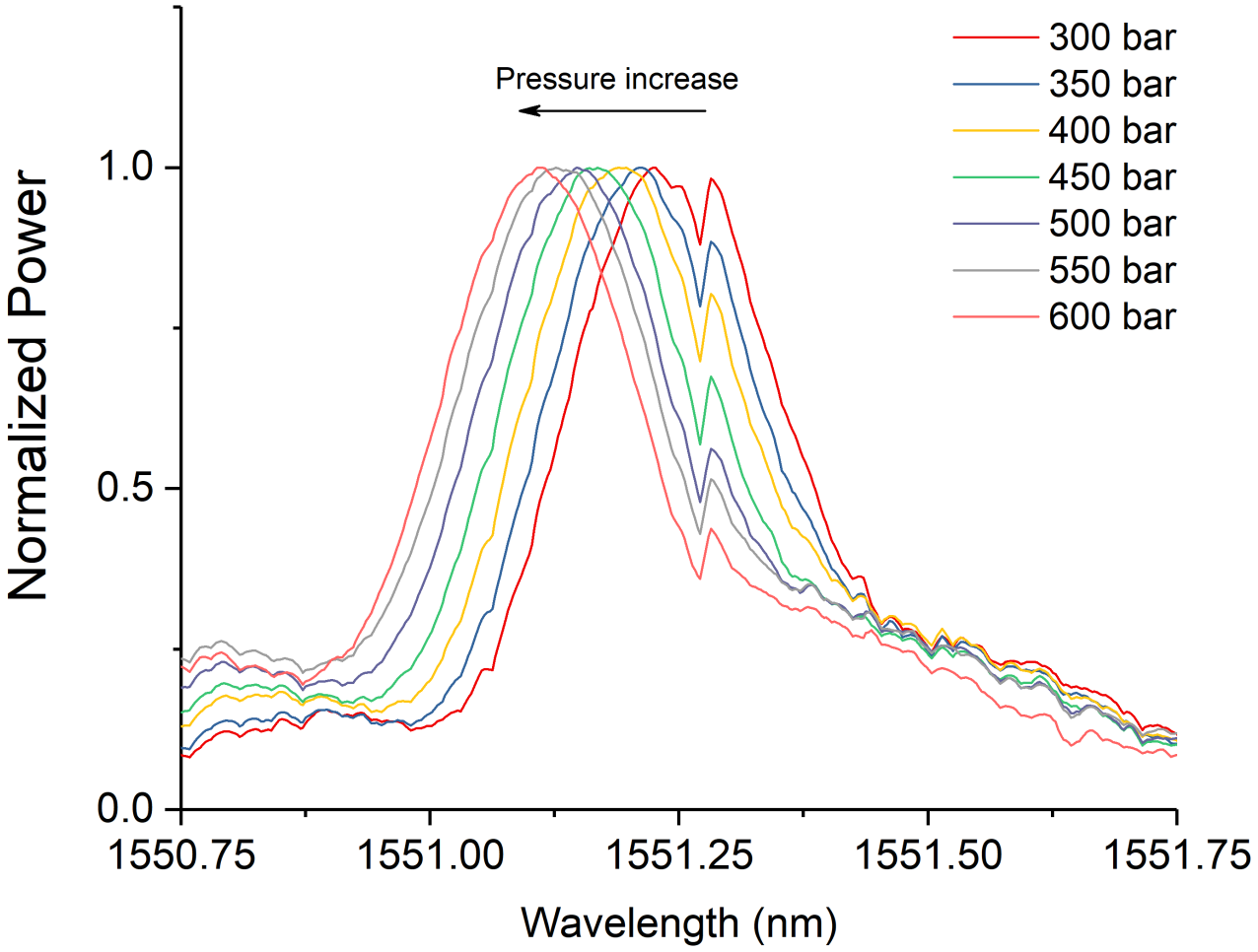


Figure 5.8: Normalised pressure test results of the sector holes with elliptical micro-holes sample.

Figure 5.9 plots the wavelength separation of the two reflection peaks as a function of pressure and confirms a linear dependence across all four test cycles. The first test cycle, which was taken before the sample was taken up to 450°C, has a constant offset in the measurement results compared to the other test cycles. The three cycles obtained after the high temperature exposure display excellent agreement and repeatability, indicating that heating induced a thermal anneal. Annealing did not alter the sensor's pressure sensitivity, but it increased the baseline peak separation by relieving residual stresses introduced during laser fabrication and thereby modifying the fibre's intrinsic birefringence. From the slope of the curves in Figure 5.9, the pressure sensitivity is approximately 0.41 pm/bar. The dominant uncertainty in these measurements arises from the limited accuracy and stability of the hand operated hydraulic pump.

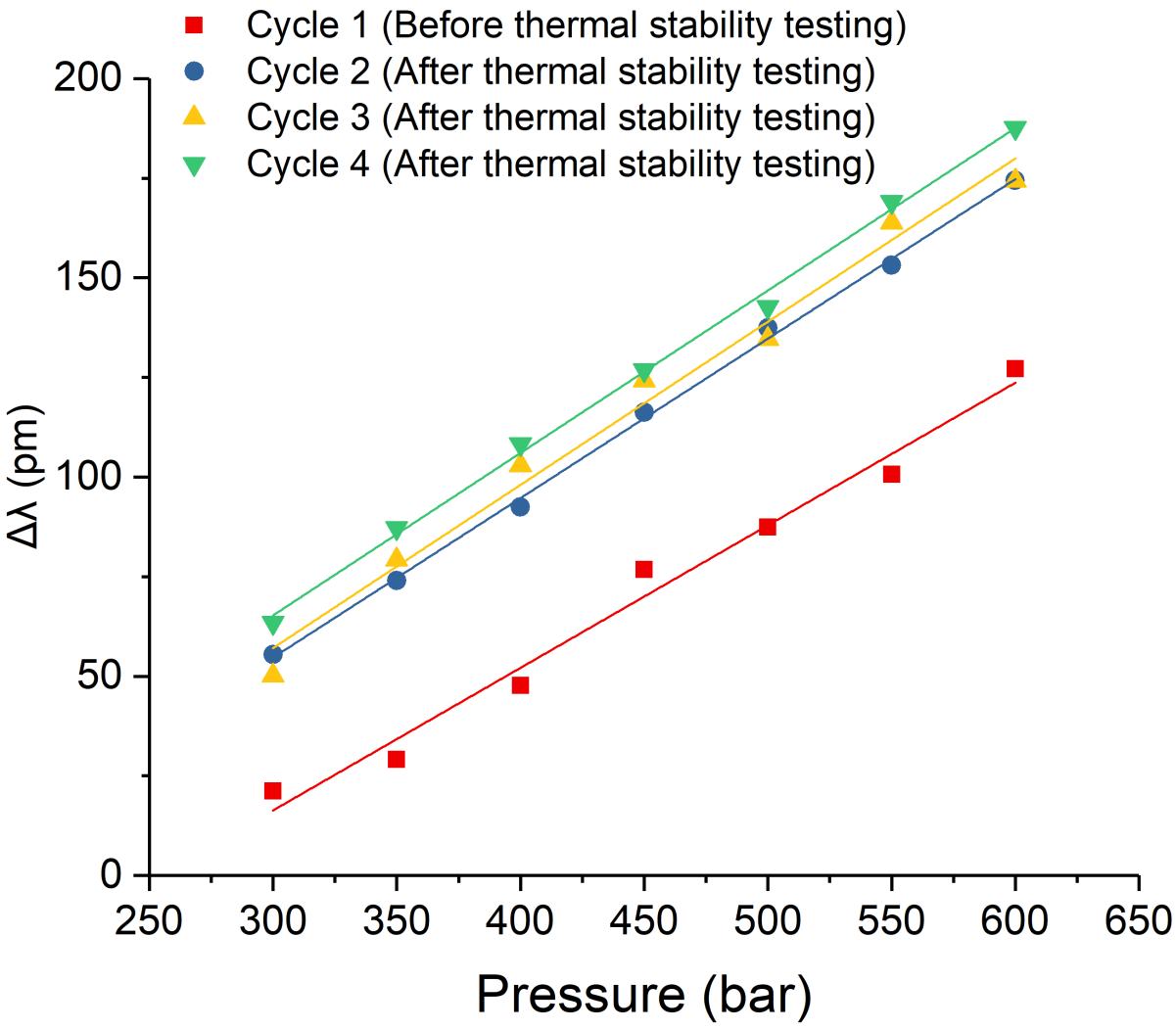


Figure 5.9: Pressure test results before and after thermal stability test, with a linear fit.

5.5 Thermal Stability Testing

The samples were placed in a furnace for thermal stability testing. Figure 5.10 presents the resulting data. At atmospheric pressure the sensor was heated from room temperature to 450°C in 50°C increments. Throughout this range the FBG reflection spectrum displayed no peak splitting, corroborating the simulation prediction that the device decouples temperature from pressure. In addition, the reflection peaks shifted uniformly with temperature, demonstrating the sensor's capability to measure both temperature and pressure simultaneously.

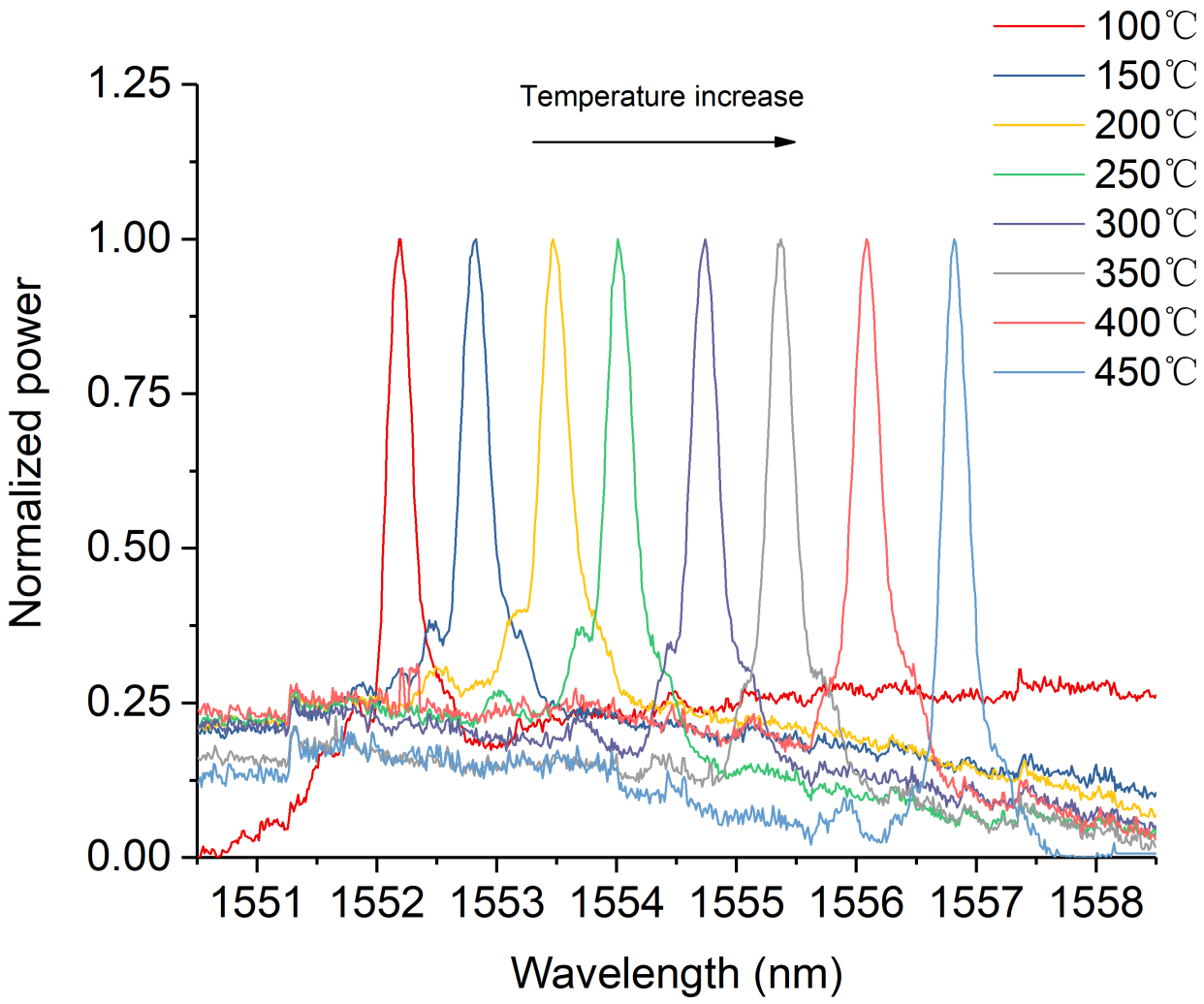


Figure 5.10: Thermal stability test results for the sector holes with elliptical micro-holes sample.

5.6 Analysis of the results

Two principal factors account for the disparity between the experimental and simulated pressure sensitivities. First, to prevent excessive etching of the core during fabrication, a larger separation had to be maintained between the cavity and the core. Consequently, although the nominal sector radius was 95 μm, the effective radial dimension of the cavity was only 83 μm. Second, sealing with a fusion splicer caused partial collapse of the channel as the fibre tip melted, thereby reducing the actual cavity size. Sensitivity could be enhanced through tighter process control that permits etching nearer to the core and by investigating alternative sealing techniques that avoid cavity deformation.

Below 300 bar, the separation between the two reflection peaks is too small to be useful, but this limitation can be addressed by fabricating the sensor in a highly birefringent, polarization maintaining fibre. In such fibres, the intrinsic birefringence produces a substantial peak separation even in the absence of external pressure, allowing low pressure to be resolved with ease. The principal drawback is mechanical fragility: PM fibres possess significant internal stress, and inscribing large structures with femtosecond pulses under these conditions may cause the fibre to fracture. Consequently, both the fabrication process and the structural design must be optimized, with particular emphasis on scaling the cavities to smaller dimensions.

As an alternative to fabricating sensors in polarization maintaining fibre, another strategy is to employ femtosecond laser direct writing to generate high birefringence within the fibre itself, thereby replicating the effect of a PM fibre. As shown in Figs. 5.12 and 5.13, Lei Yuan and colleagues have demonstrated that this technique can produce long period gratings with exceptionally large induced birefringence [2]. I propose to adapt the same approach for fabricating FBGs rather than long period gratings. Integrating the birefringence inducing structures with the air cavities will, however, demand exceptional fabrication accuracy: any portion of the written pattern that encroaches upon the core could introduce substantial loss or even compromise the integrity of the grating. Employing a rota-

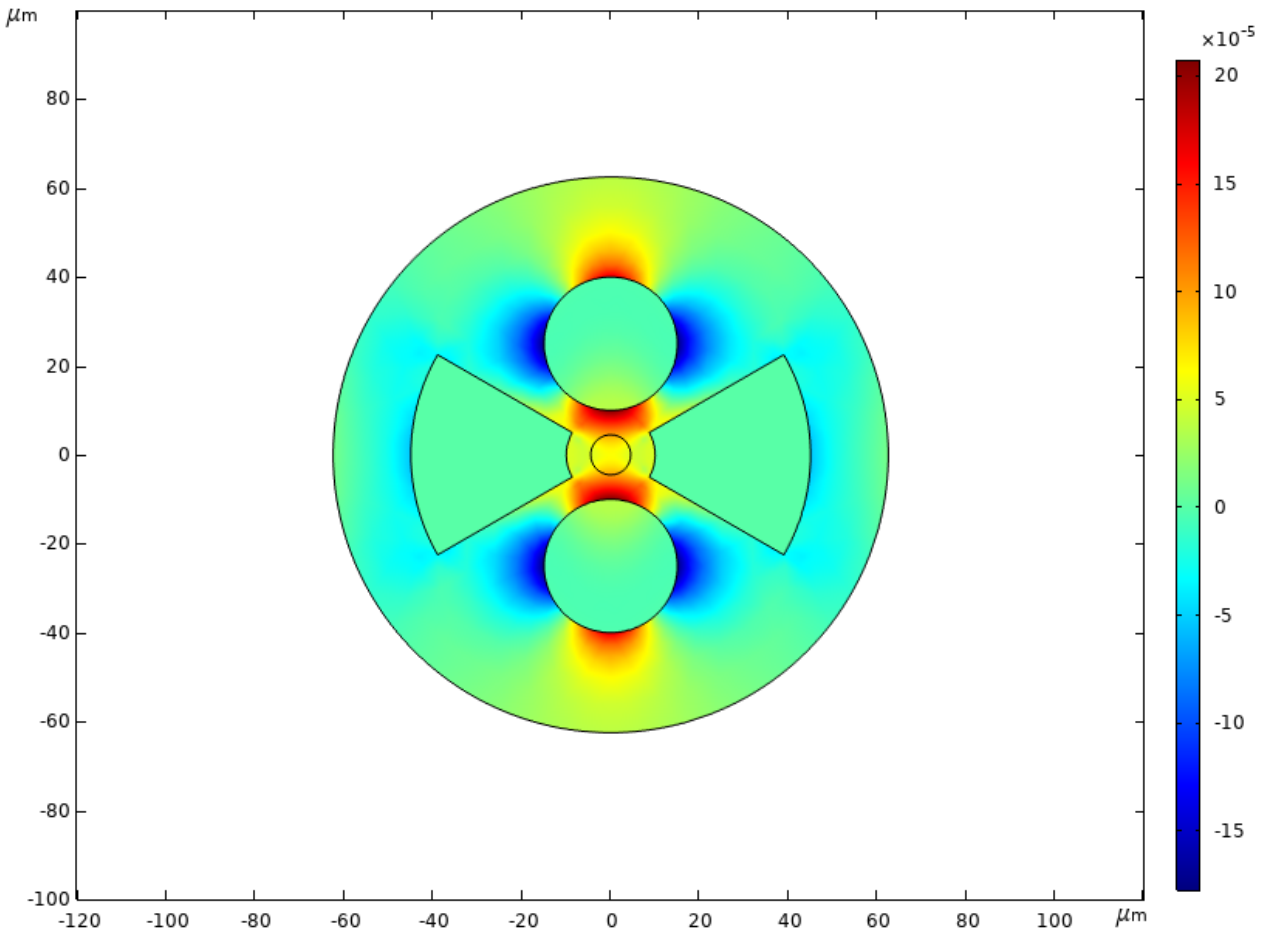


Figure 5.11: Simulation of refractive index change of micro-structured sensors in PM fibres.

tional stage to build up the complex geometry in sequential steps offers a practical means of meeting these stringent tolerances.

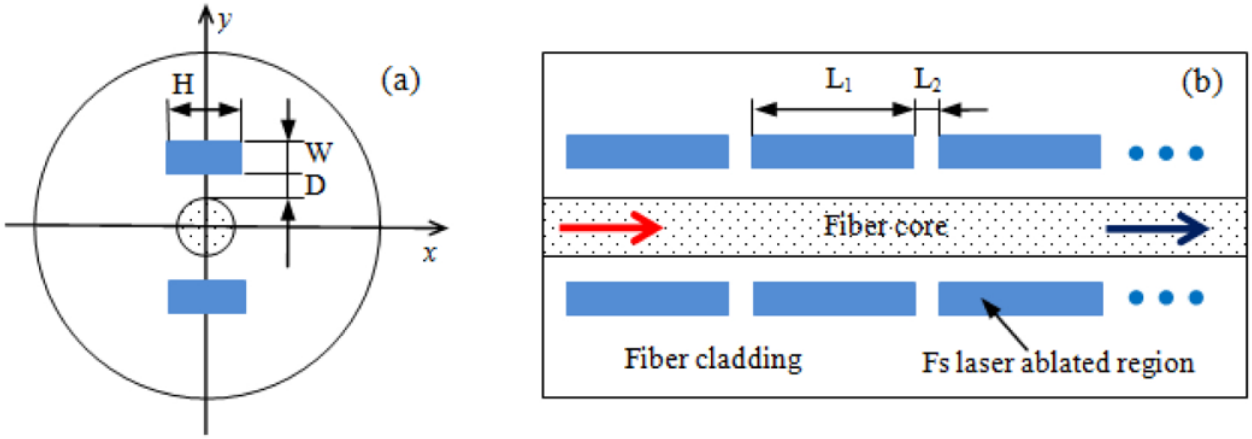


Figure 5.12: Schematic of induced birefringence created by femtosecond laser inside an optical fibre [2].

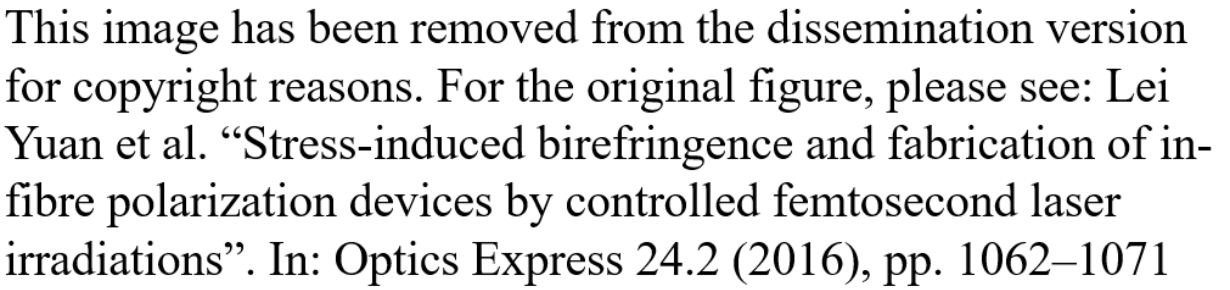


Figure 5.13: Micro graphs of stress rod created by femtosecond laser [2].

5.7 Summary

A fabrication approach combining femtosecond laser inscription with selective wet etching was demonstrated to create fully 3D voids within optical fibres, thereby enabling the production of high-sensitivity pressure sensors without the significant splice losses typically associated with side-hole devices. Numerical modelling predicts pressure sensitivities of up to 3.3 pm/bar in fibres with an outer diameter of 250 μm. Three-dimensional sensors were realised in both standard single-mode silica fibre and in a large-diameter fibre, and hydraulic testing established a pressure sensitivity of 0.41 pm/bar across a dynamic range of 300–600 bar. Although this range is not intended for low-pressure sensing, it is relevant to high-pressure environments such as hydraulic systems, subsurface energy applications, and other extreme-environment monitoring scenarios where pressures of several hundred bar may be encountered. The present device should therefore be viewed as a proof-of-concept high-pressure sensor, while further optimisation of the fibre geometry and birefringence would be required to extend its useful range towards lower pressures. Given its versatility, the technique is readily transferable to a broad array of high-performance fibres, including sapphire fibre, for operation in ultra-extreme environments.

References

[1] Luís A Fernandes et al. "Strong birefringence tuning of optical waveguides with femtosecond laser irradiation of bulk fused silica and single mode fibres". In: *Journal of lightwave technology* 31.22 (2013), pp. 3563–3569.

[2] Lei Yuan et al. "Stress-induced birefringence and fabrication of in-fibre polarization devices by controlled femtosecond laser irradiations". In: *Optics Express* 24.2 (2016), pp. 1062–1071.

6 | Photonic crystal tip temperature sensor based on sapphire optical fibre

This chapter presents a preliminary investigation of a sapphire-fibre-tip temperature sensor based on a photonic crystal resonance. Whereas the previous chapters focused on microstructured silica fibre pressure sensors, this chapter explores an alternative route towards extreme-environment temperature sensing by integrating a resonant photonic crystal structure onto the end face of a sapphire optical fibre. The motivation was to combine the high-temperature capability of sapphire with the sharp spectral response of a photonic crystal resonance, potentially enabling compact fibre-tip sensing at elevated temperatures. The chapter first introduces the Fano-resonance mechanism and reviews relevant photonic-crystal fibre-tip sensors. It then presents the numerical design of a silicon-on-sapphire photonic crystal tip sensor and evaluates its expected temperature response using FDTD simulations. Finally, an initial fabrication attempt using focused ion beam milling is described. Although this route was not pursued further because of the practical difficulty of fabricating a high-quality nanoscale photonic crystal directly on a sapphire fibre tip, the study helped define the fabrication constraints and motivated the subsequent shift towards laser-written sapphire photonic crystal fibre sensors in Chapters 7 and 8.

6.1 Background

During the 1930s, Ugo Fano investigated the puzzling asymmetries appearing in the absorption spectra of rare gases and formulated the concept that now bears his name; he published the definitive exposition of this theory in 1961 [1]. In essence, the theory explains that when two oscillatory channels coexist, one arising from a discrete energy level and the other from a continuum, their mutual coupling creates interference effects that reshape an otherwise symmetric spectral line into a sharply

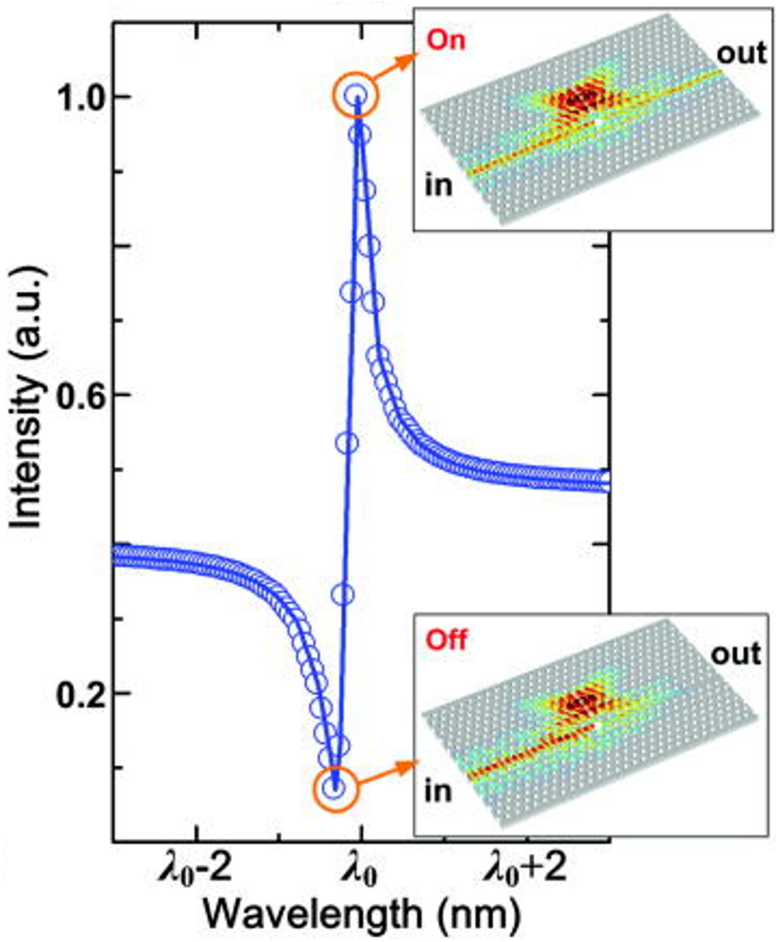


Figure 6.1: FDTD simulation of Fano resonance spectra in photonic crystal structure [2].

asymmetric profile that rises to a maximum on one side of the resonance energy and falls to a minimum on the other. Figure 6.1 presents a representative Fano-resonance spectral shape from a photonic crystal switch [2]. Fano resonances arise in a wide array of physical systems; to illustrate the underlying formalism, I consider a pair of coupled, externally driven oscillators and present the matrix equation that governs their dynamics [3, 4, 5].

$$\begin{pmatrix} \omega_1 - \omega - \mathrm{i}\gamma_1 & g \\ g & \omega_2 - \omega - \mathrm{i}\gamma_2 \end{pmatrix} \begin{pmatrix} X_1 \\ X_2 \end{pmatrix} = \begin{pmatrix} F_1 \\ F_2 \end{pmatrix} \tag{6.1}$$

In this matrix equation, X_1 and X_2 represent the complex amplitudes of the two oscillators; ω_1 and ω_2 denote their natural resonance frequencies. The parameters γ_1 and γ_2 are the associated damping coefficients. The terms F_1 and F_2 correspond to the amplitudes of the periodic driving forces, which oscillate at a common angular frequency ω. Finally, g is the coupling constant that quantifies the

interaction between the two oscillators.

A Fano resonance can be realised only in the weak-coupling limit, where the interaction constant g is sufficiently small [6]. In this case, only the oscillator with the larger damping is driven, meaning that among F_1 and F_2 only one is non-zero; this arrangement ensures the coupling of a discrete spectrum with a continuum [7]. Suppose oscillator 1 has the larger damping($F_1 \neq 0, F_2 = 0$); then, in the spectral region near the resonance of oscillator 2, the amplitude of the driven oscillator 1 is given by:

$$|X_1(\Omega)|^2 \approx |F_1|^2 \frac{\gamma_1^2}{(\omega_1 - \omega_2)^2 + \gamma_1^2} \frac{(q + \Omega)^2}{(1 + \Omega)^2}, \tag{6.2}$$

where the dimensionless frequency Ω is

$$\Omega = \left[\omega - \omega_2 + (\frac{g^2}{\gamma_1}) \frac{(\omega_1 - \omega_2)}{1 + q^2} \right] \frac{\gamma_1 (1 + q^2)}{g^2}, \tag{6.3}$$

and q is the Fano parameter determining the spectral shape.

In photonics, Fano resonances may be generated in a wide range of systems, extending from one dimensional alternating layered stacks, through two dimensional meta surfaces, to three dimensional photonic crystals [8]. Figure 6.2 presents a meta surface produced by depositing polycrystalline silicon on a quartz glass substrate, together with its corresponding Fano resonance spectrum [3].

Figure 6.3 depicts a Fano resonance in a photonic crystal structure. Yichen Shuai and colleagues fabricated a bilayer photonic crystal for optical filtering by employing electron-beam lithography, reactive-ion etching, and low-pressure chemical-vapor deposition, and they subsequently measured the resulting Fano resonance peak [9].

In addition to their filtering function, photonic crystals that support Fano resonances can be engineered as membrane reflectors, membrane lasers, and infrared detectors [10, 11, 12]. These structures

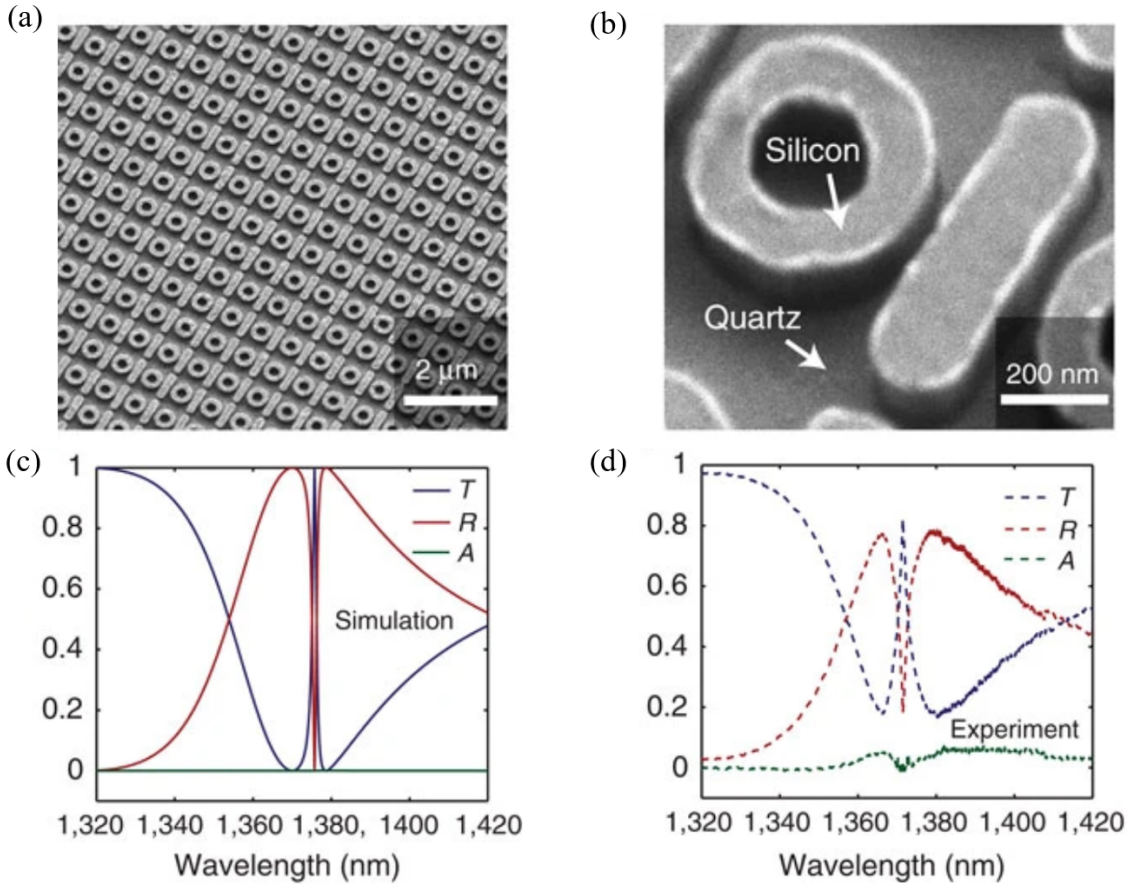


Figure 6.2: (a), (b) Scanning electron micrograph of the meta surface (c) Simulation of transmission and reflection spectra of the meta surface (d) Experimentally measured transmission and reflection spectra of the meta surface [3].

This image has been removed from the dissemination version for copyright reasons. For the original figure, please see: Yichen Shuai et al. "Double-layer Fano resonance photonic crystal filters". In: Optics Express 21.21 (2013), pp. 24582–24589.

Figure 6.3: (a), (b) Scanning electron micrograph of the bilayer photonic crystal (c) Simulated and measured reflection spectra of the bilayer photonic crystal (d) Partial zoom in view of the spectra [9].

also offer valuable sensing capabilities. Variations in ambient temperature shift the Fano-resonance spectrum because the thermo-optic effect alters the refractive index of the constituent material, while thermal expansion changes the lattice constant of the crystal; the resulting spectral displacement provides a basis for temperature sensing. Likewise, immersing the photonic crystal in different liquids modifies the refractive index within its pores, producing a comparable spectral shift that can be exploited for refractive index sensing.

Because a sensing-grade photonic crystal typically measures only a few tens of micrometres across, it can be mounted directly on the tip of an optical fibre, allowing the device to operate in otherwise inaccessible or hostile environments. Woong Jung and co-workers first patterned a photonic crystal membrane on a standard silicon wafer by conventional photolithography, then used focused ion beam milling to cut a square chip with a lateral dimension of 30 μm. Employing an Omniprobe micromanipulator, they transferred the chip onto the fibre end face so that it covered the core region, and finally deposited a thin rim of platinum along the membrane edge to bond it securely to the fibre tip [13].

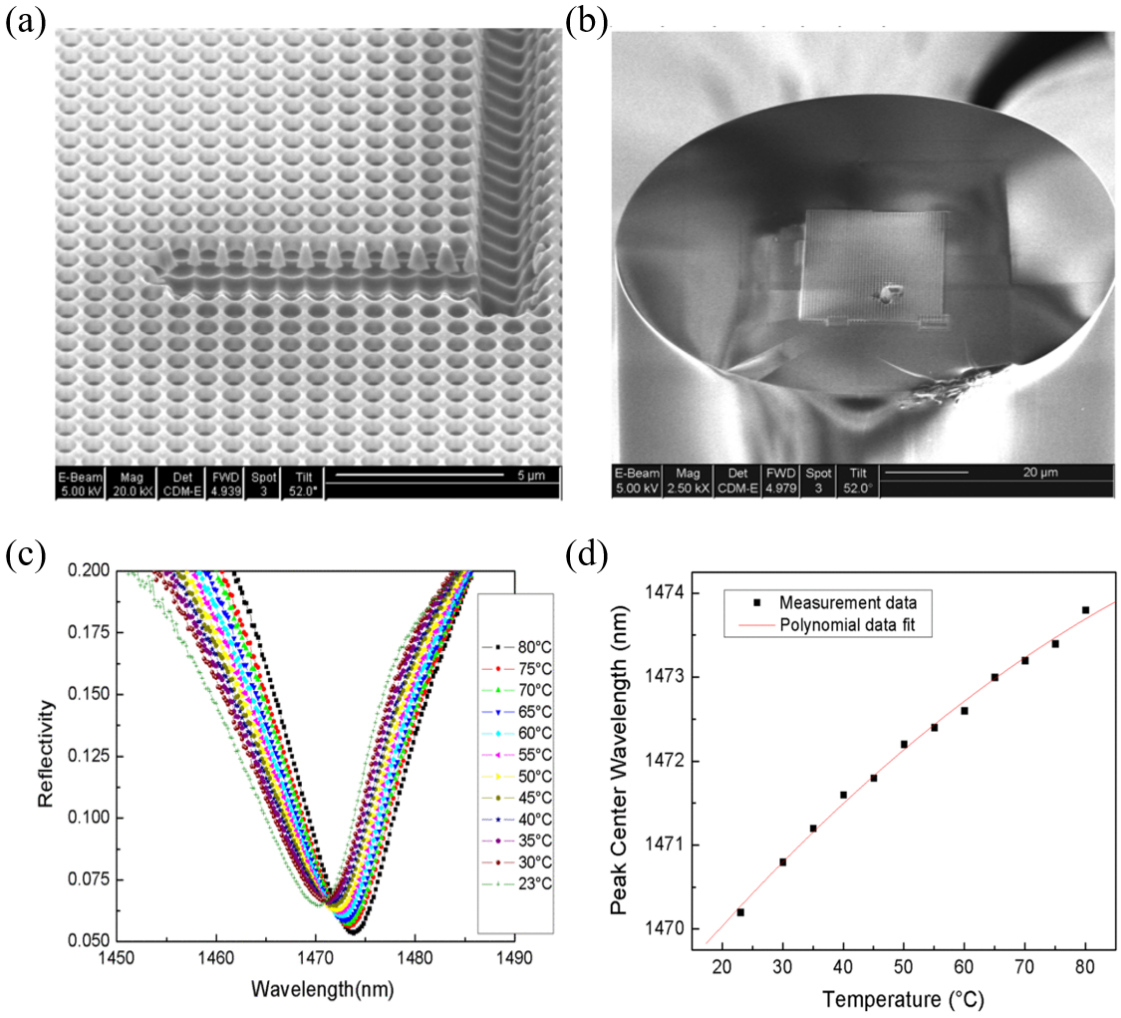


Figure 6.4: (a) Scanning electron micrograph of the photonic crystal slab (b) Scanning electron micrograph of the fibre tip sensor (c) Measured reflection spectra of the fibre tip sensor (d) Peak wavelength shift of the fibre tip sensor [13].

Figure 6.4 presents a scanning electron micrograph (SEM) of the fibre-mounted sensor together

with its temperature sensing performance. Within the range 20 - 80 °C the device delivered high resolution, and its temperature response remained nearly linear. In a separate study the same group extended the tests to 700 °C, repeating five thermal cycles to demonstrate the sensor's durability and reproducibility [14].

Beyond temperature monitoring, a fibre tip photonic crystal can also serve as a refractive index sensor. Mildred S. C. and co-workers fabricated a hexagonally patterned photonic crystal in an InP membrane by electron beam lithography and then transferred the membrane mechanically onto the cleaved end face of an optical fibre to form the sensing element [15]. Immersing this device in different liquids changes the refractive index within the crystal pores, thereby shifting its spectral response. Figure 6.5 displays a SEM of the assembled sensor together with its reflection spectrum.

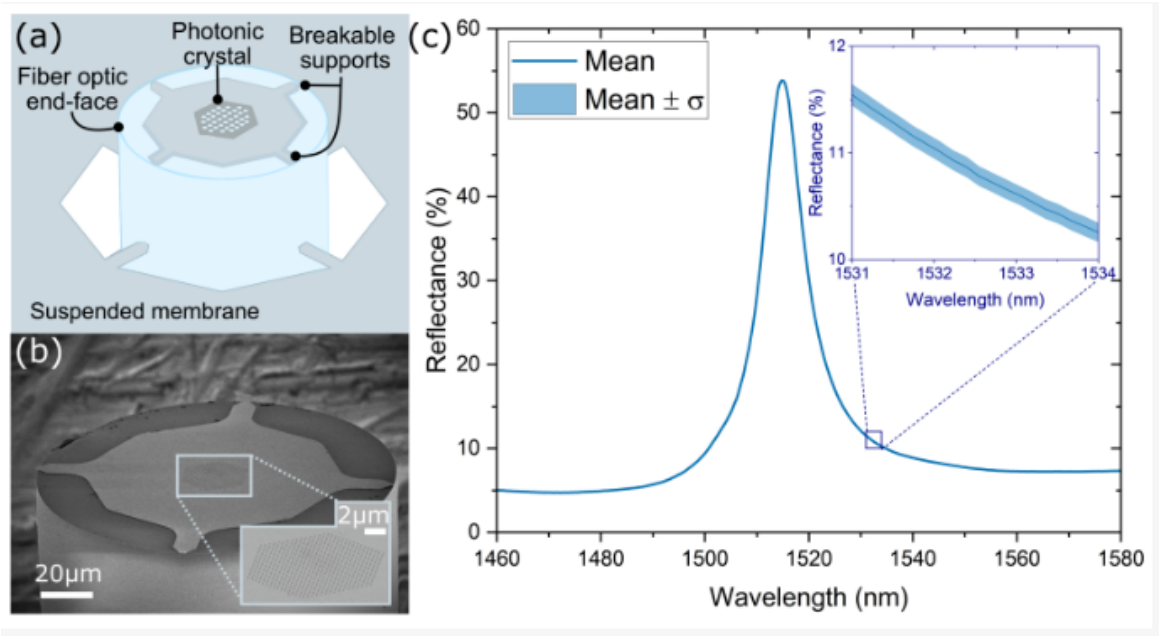


Figure 6.5: (a) Schematic diagram of the fibre tip sensor (b) SEM of the fibre tip sensor (c) Average reflection spectra of the fibre tip sensor [15].

The foregoing techniques fabricate the photonic crystal membrane as a separate component and subsequently transfer it mechanically to the fibre end face, a configuration that fails to remain stable at temperatures exceeding 1000°C. To overcome this limitation I propose an alternative methodology: silicon is first deposited directly onto the fibre tip by vacuum chemical vapour deposition, and the photonic crystal lattice is then sculpted by focused ion beam. This approach enlarges the contact area

between the silicon layer and the fibre substrate, yields a stronger mechanical bond, and simplifies the overall fabrication sequence.

6.2 Sensor Simulation

As shown in Fig. 6.6, a photonic crystal comprising a 30 × 30 array of cylindrical air holes within a square footprint of approximately 24 μm per side was designed. Each hole is 500 nm deep with a radius of 200 nm, and the lattice period is 800 nm. FDTD simulations were subsequently performed to calculate the transmission and reflection spectra, and the results are presented in Fig. 6.7.

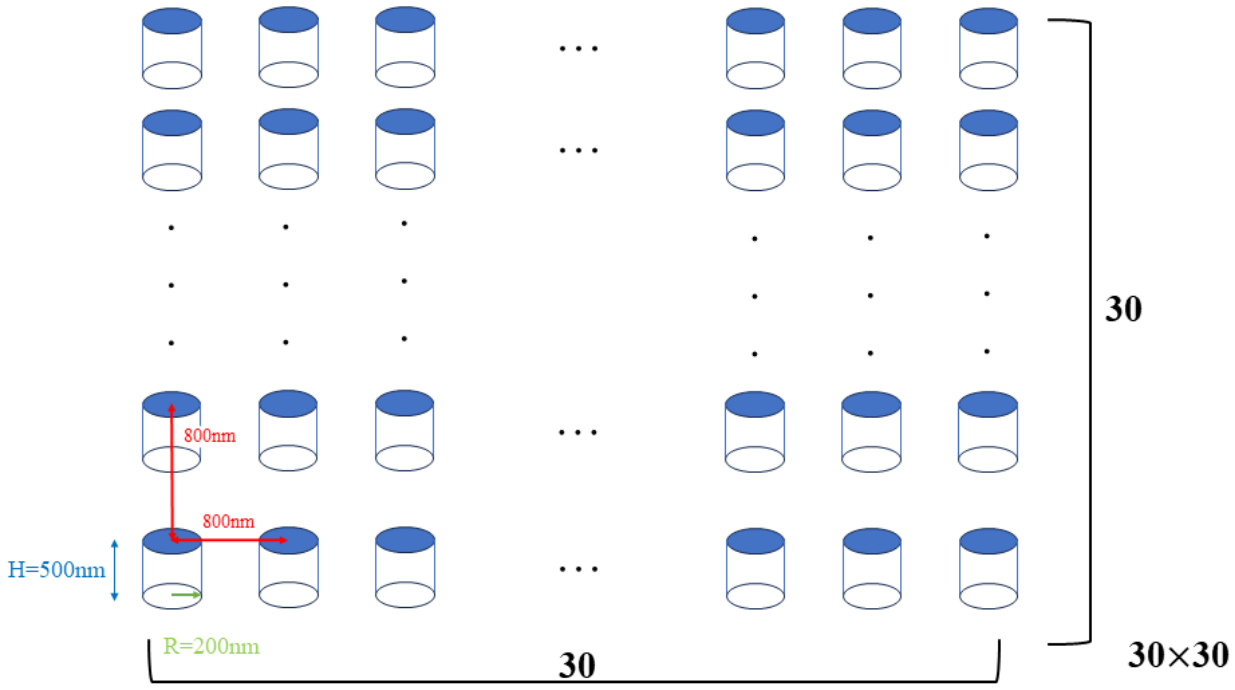


Figure 6.6: Schematic diagram of the photonic crystal fibre tip.

Figure 6.7 displays a characteristic Fano resonance spectrum. To ensure compatibility with standard laser sources, I selected the resonance peak centred near 1550 nm as the temperature sensing signal. I then incorporated both thermal expansion, which alters the photonic crystal dimensions, and the thermo-optic effect, which modifies the refractive index, to calculate the spectral response as a function of temperature. The resulting shift is presented in Figure 6.8.

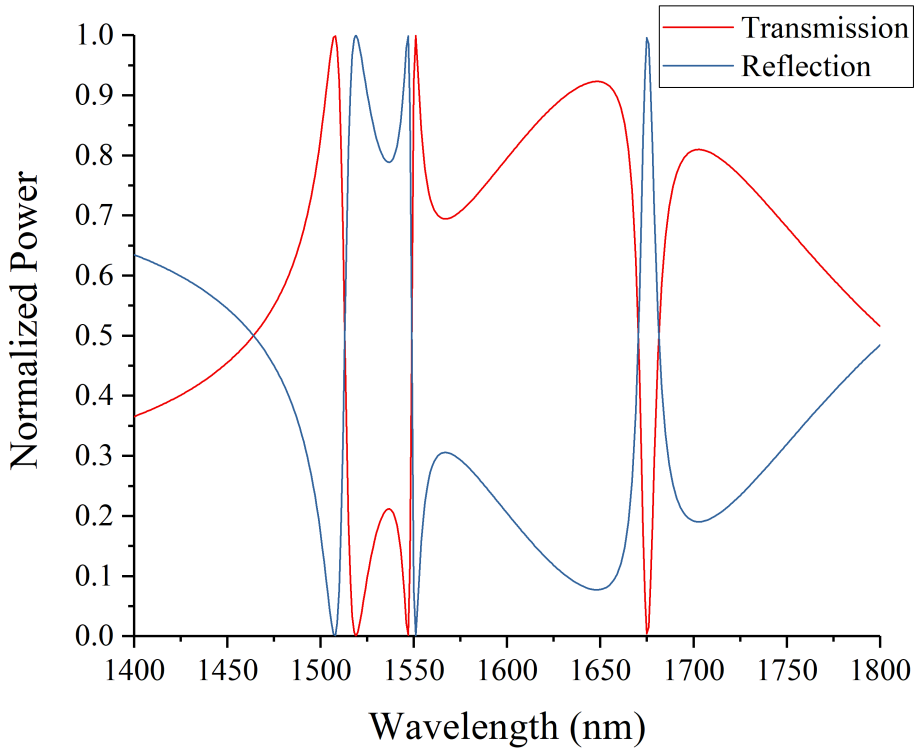


Figure 6.7: Simulated reflection and transmission spectra of the photonic crystal fibre tip.

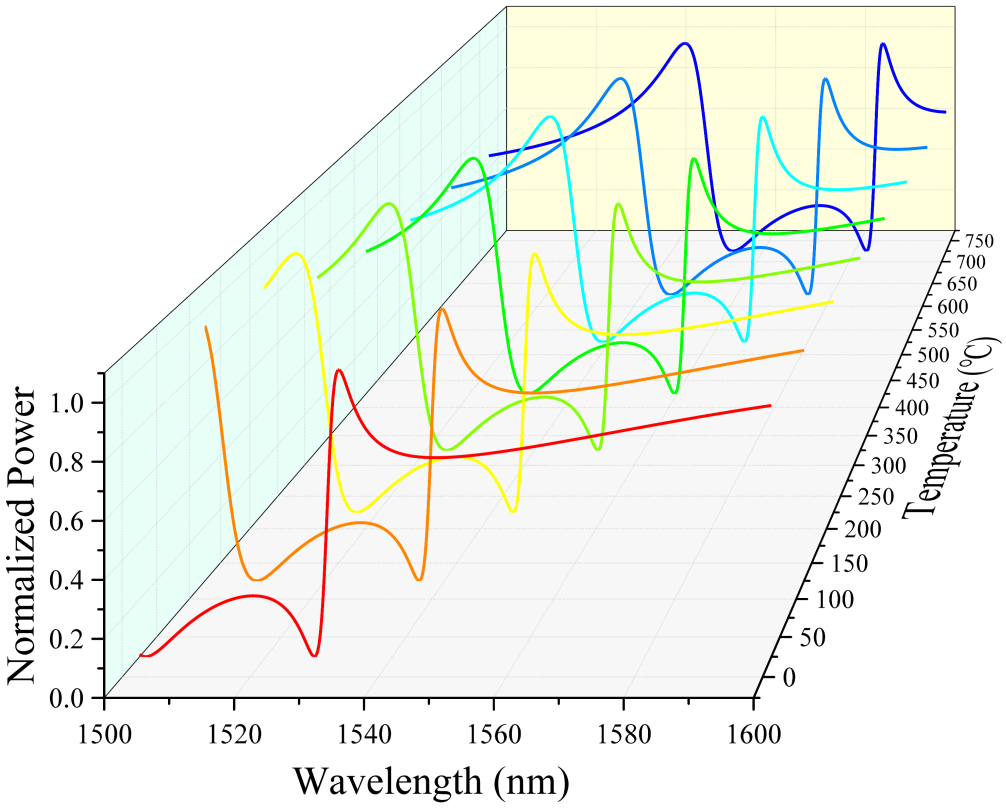


Figure 6.8: Simulated temperature response of the photonic crystal fibre tip.

The simulation result shows that temperature variations induce a uniform spectral shift in the photonic crystal fibre tip, making it an excellent candidate for temperature sensing; the remaining challenge lies in translating the design into a fabricated device.

6.3 Sensor fabrication

To verify the feasibility of the design, I first fabricated an identical photonic crystal structure on a wafer. A silicon on sapphire wafer supplied by Inseto, 76 mm in diameter and 430 μm in total thickness, was chosen. The silicon layer thickness of the wafer is exactly 500 nm as designed in the simulation. Using a focused ion beam, I patterned the 30 $\times$ 30 photonic crystal array described in Fig. 6.6 onto the wafer surface. A SEM of the resulting sample is shown in Fig. 6.9.

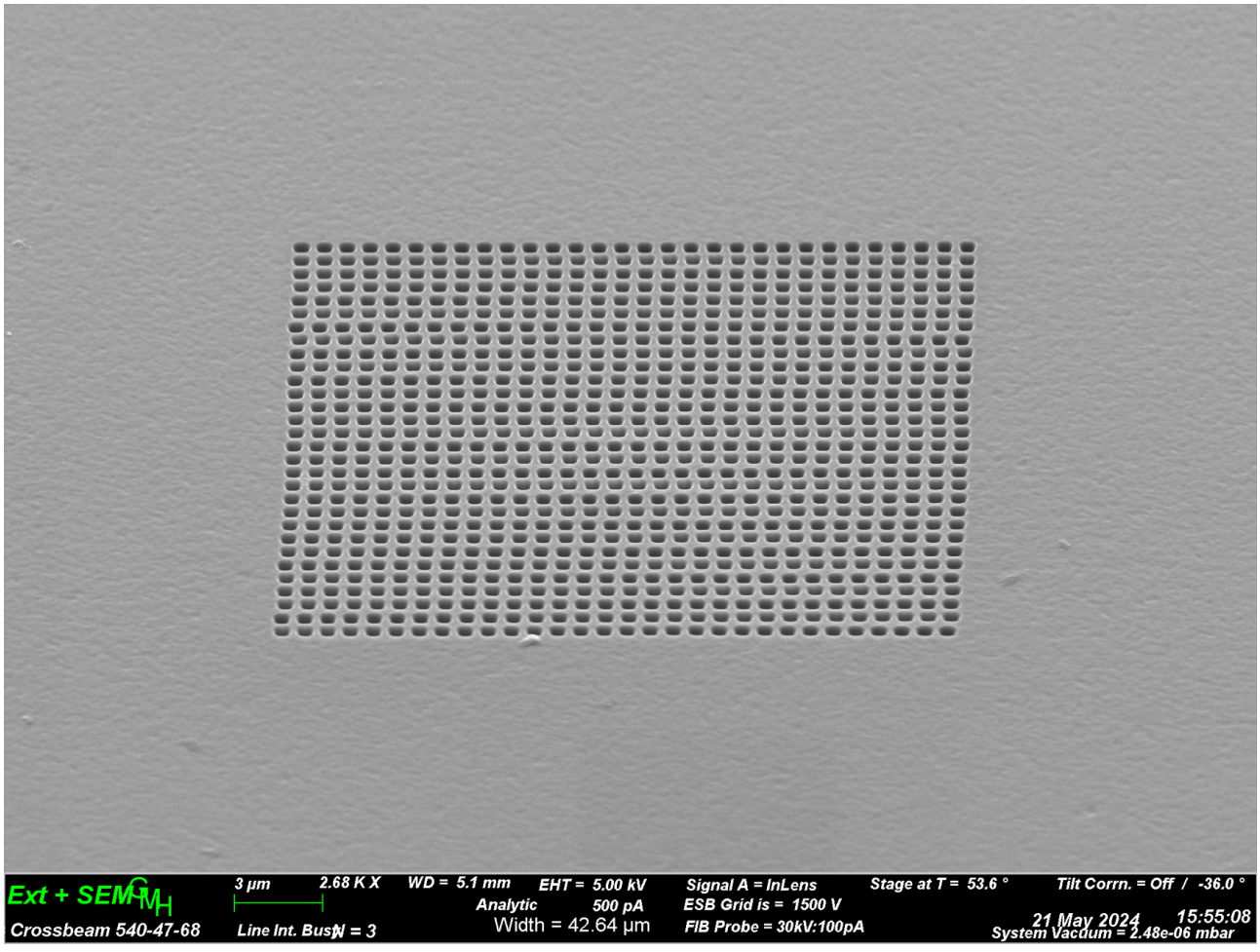


Figure 6.9: SEM of the photonic crystal on a silicon on sapphire wafer.

Because the air holes are milled individually with a focused ion beam, slight positional errors accumulate across the array, so the resulting precision is lower than that obtainable with photolithography, and about three hours are needed to produce a single sample. The next step would require depositing a silicon layer on the fibre tip by plasma enhanced chemical vapour deposition or electron beam physical vapour deposition; yet both systems are optimised for wafer-like substrates, and achieving a uniform, well aligned coating on a sapphire fibre tip is technically demanding.

6.4 Summary and transition

This chapter investigated a photonic-crystal fibre-tip sensor as an alternative route towards high-temperature sensing in sapphire optical fibre. The simulation results showed that a silicon photonic crystal on a sapphire substrate could provide a sharp resonance near 1550 nm and a measurable temperature-dependent spectral shift, indicating that the sensing mechanism is feasible in principle. An initial focused-ion-beam fabrication trial on a silicon-on-sapphire wafer also demonstrated that the designed photonic crystal geometry could be physically patterned.

However, translating this approach from a planar wafer to a sapphire fibre tip introduced substantial fabrication challenges. In particular, depositing a uniform and well-aligned silicon layer onto the small fibre end face, followed by nanoscale focused-ion-beam milling of a large photonic crystal array, would be time-consuming, low-yield, and difficult to scale. The resulting device would also rely on a thin deposited layer at the fibre tip, which may limit its mechanical robustness during handling and high-temperature cycling. For these reasons, this route was not pursued further within the present thesis. Nevertheless, this investigation was useful because it clarified the limitations of fibre-tip photonic-crystal sensing for the intended extreme-environment application. It suggested that a more robust strategy would be to form the guiding and sensing structure within the sapphire fibre itself, rather than adding a delicate nanostructured layer to the end face. This conclusion motivated the work in the following chapters, where sapphire photonic crystal fibre sensors are designed, fabricated,

and tested using femtosecond-laser-induced refractive-index modification.

References

[1] Ugo Fano. "Effects of configuration interaction on intensities and phase shifts". In: *Physical review* 124.6 (1961), p. 1866.

[2] Yi Yu et al. "Fano resonance control in a photonic crystal structure and its application to ultrafast switching". In: *Applied physics letters* 105.6 (2014).

[3] Yuanmu Yang et al. "All-dielectric metasurface analogue of electromagnetically induced transparency". In: *Nature communications* 5.1 (2014), p. 5753.

[4] Yong S Joe, Arkady M Satanin, and Chang Sub Kim. "Classical analogy of Fano resonances". In: *Physica Scripta* 74.2 (2006), p. 259.

[5] Lieven Verslegers et al. "From Electromagnetically Induced Transparency to Superscattering with a Single<? format?> Structure: A Coupled-Mode Theory for Doubly Resonant Structures". In: *Physical review letters* 108.8 (2012), p. 083902.

[6] Alexander B Khanikaev, Chihhui Wu, and Gennady Shvets. "Fano-resonant metamaterials and their applications". In: *Nanophotonics* 2.4 (2013), pp. 247–264.

[7] Mikhail F Limonov. "Fano resonance for applications". In: *Advances in optics and photonics* 13.3 (2021), pp. 703–771.

[8] Mikhail F Limonov et al. "Fano resonances in photonics". In: *Nature photonics* 11.9 (2017), pp. 543–554.

[9] Yichen Shuai et al. "Double-layer Fano resonance photonic crystal filters". In: *Optics Express* 21.21 (2013), pp. 24582–24589.

[10] Weidong Zhou et al. "Progress in 2D photonic crystal Fano resonance photonics". In: *Progress in Quantum Electronics* 38.1 (2014), pp. 1–74.

[11] Robert Magnusson and Mehrdad Shokooh-Saremi. "Physical basis for wideband resonant reflectors". In: *Optics express* 16.5 (2008), pp. 3456–3462.

[12] Hongjun Yang et al. "Transfer-printed stacked nanomembrane lasers on silicon". In: *Nature Photonics* 6.9 (2012), pp. 615–620.

[13] Il Woong Jung et al. "Highly sensitive monolithic silicon photonic crystal fiber tip sensor for simultaneous measurement of refractive index and temperature". In: *Journal of Lightwave Technology* 29.9 (2011), pp. 1367–1374.

[14] Bryan Park et al. "Photonic crystal fiber tip sensor for high-temperature measurement". In: *IEEE Sensors Journal* 11.11 (2011), pp. 2643–2648.

[15] Mildred S Cano-Velázquez et al. "Temperature-compensated solution concentration measurements using photonic crystal fiber-tip sensors". In: *Sensors* 23.18 (2023), p. 7703.

7 | Sapphire Photonic Crystal Fibre Sensors

This chapter first surveys recent progress on photonic crystal fibres (PCFs) for sensing, then evaluates the feasibility of femtosecond-laser direct writing for sapphire PCFs. I compute the guided modes of sapphire PCFs and analyze how the number of cladding rings influences the confinement loss, as well as how the lattice pitch affects splice-induced loss when coupling to standard single-mode silica fibre. The simulation results provide practical guidance for the subsequent fabrication of sapphire PCFs.

7.1 Background

Photonic crystal fibres (PCF) fall into two principal categories. The first relies on the index guiding mechanism. A periodic array of hollow channels or regions with a deliberately modified refractive index is embedded in the cladding, lowering its average refractive index relative to that of the core. Light is confined within the core by a process akin to total internal reflection in conventional fibres, and the necessary index contrast is realised without the introduction of dopant elements.

The second category employs photonic band gap guiding. Photonic crystals possess spectral ranges, or band gaps, in which electromagnetic waves cannot propagate. When the cladding is formed from such a band gap material, wavelengths lying inside the gap are unable to escape, thereby trapping light in the core. Unlike in conventional fibres, this mechanism does not require the core to exhibit a higher refractive index than the cladding; effective guidance is attainable even when the core is an air channel.

In 1996, P. St. J. Russell and colleagues drilled a periodic array of holes into a silica preform and then drew the preform at a temperature of about 2000 °C into a hexagonal fibre with an outer dimension of approximately 38 μm [1]. As shown in Figure 7.1, the resulting structure guided light with stable, low loss across the spectral interval from 458 nm to 1550 nm. Subsequent work demonstrated

that the holey preform need not be created by drilling alone; it can also be fabricated by stacking silica capillaries or by extruding molten glass through a die to produce a preform containing the requisite voids before fibre drawing [2]. Figure 7.2 shows several photonic crystal fibres fabricated at the University of Bath.

This image has been removed from the dissemination version for copyright reasons. For the original figure, please see: JC Knight et al. "All-silica single-mode optical fiber with photonic crystal cladding". In: Optics letters 21.19 (1996), pp. 1547–1549.

Figure 7.1: SEM of the first photonic crystal fibre [1].

Because the architecture of photonic crystal fibres is highly adaptable, their transmission window can be tuned, unwanted wavelengths can be suppressed, and the effective mode area can be engineered simply by modifying the structural parameters [3]. With appropriate lattice designs, it is possible to achieve very large birefringence while still maintaining single mode guidance [4]. Hollow core variants offer additional benefits for high power delivery and can be filled with gases or liquids to investigate non-linear optical phenomena or to serve as refractive index and gas sensors [5, 6, 7].

Research into temperature sensing with photonic crystal fibres has chiefly aimed at reducing cross-sensitivity between temperature and strain and at enhancing responsivity by infiltrating the air holes with functional materials. Yinian Zhu and collaborators produced long period fibre gratings by periodically collapsing the air holes in a photonic crystal fibre with a carbon-dioxide laser (Figure 7.3), thereby imposing a periodic modulation of the cladding diameter [8, 9]. The resulting sensor operates reliably over the range from 24 to 992 °C and exhibits only minimal sensitivity to strain. T. R. Wolinski and colleagues fabricated a sensor by infiltrating the air holes of a PCF with a nematic liquid crystal [10]. As shown in Figure 7.4, the refractive index of the liquid crystal changes with temperature, and an applied electric field alters the spatial orientation of the anisotropic molecules, modifying their refractive index components. As a result, the optical contrast between core and cladding can be

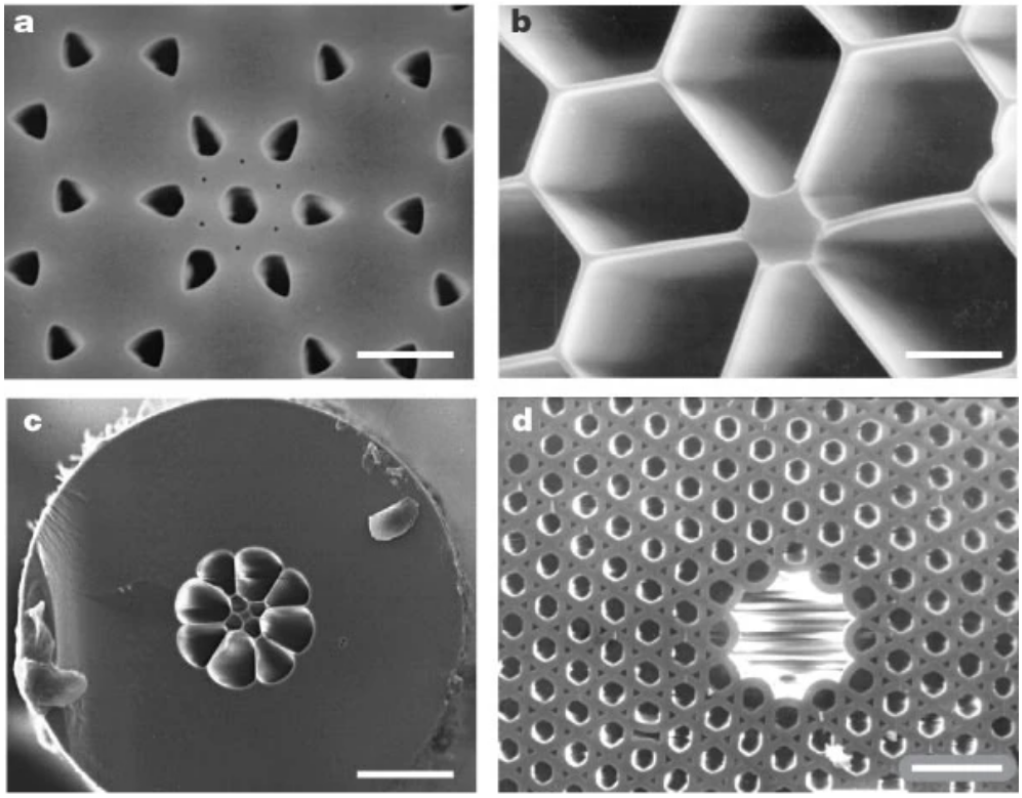


Figure 7.2: Various photonic crystal fibres made at the University of Bath. [2].

dynamically tuned, enabling the waveguide to switch between distinct guiding mechanisms.

This image has been removed from the dissemination version for copyright reasons. For the original figure, please see: Yinian Zhu et al. "Strain-insensitive and high-temperature long-period gratings inscribed in photonic crystal fiber". In: Optics Letters 30.4 (2005), pp. 367–369.

Figure 7.3: SEM of the PCF cross section before and after laser irradiation [8].

This image has been removed from the dissemination version for copyright reasons. For the original figure, please see: TR Wolinski et al. "Influence of temperature and electrical fields on propagation properties of photonic liquid-crystal fibres". In: Measurement Science and Technology 17.5 (2006), p. 985.

Figure 7.4: Three patterns of liquid crystal molecule arrangement in PCF cavities. [10].

Fibre Bragg Grating temperature sensors, which are routinely implemented in conventional optical fibres, have seldom been realised in photonic crystal fibres. The difficulty arises from the many

air voids and regions of modified refractive index that surround the PCF core, complicating grating inscription. When a sapphire PCF is fabricated by laser direct writing, the grating can be written simultaneously with the fibre, so the micro-structured cladding no longer interferes with FBG fabrication.

In 2010, Neal Pfeiffenberger and colleagues investigated the fabrication of sapphire photonic crystal fibres by arranging six segments of single-crystal sapphire fibre (outer diameter 70 μm) at the vertices of a regular hexagon with an additional segment at the centre (Figure 7.5), and then sintering the bundle at 1600 °C for 12 h to form a integrated structure [11]. Because single-crystal sapphire

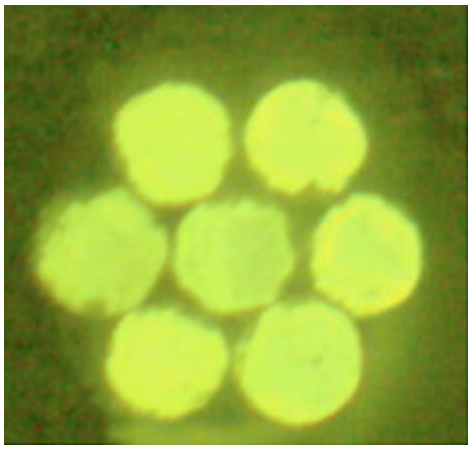


Figure 7.5: The end face of the sintered sapphire photonic crystal fibre [11].

cannot be micro-structured by the conventional stack-and-draw process used for silica, such fibres are typically grown individually via laser-heated pedestal growth (LHPG) [12]; as a result, the as-grown fibre diameter imposes a practical constraint on the lattice geometry attainable in the sintered PCF.

Additionally, Gleb M. Katyba and co-workers employed the edge-defined film-fed growth (EFG) technique to fabricate hollow sapphire photonic crystal waveguides for terahertz sensing. The EFG process yields rigid multichannel sapphire "shaped crystals"; in their demonstrations the waveguides had lengths of 100 and 150 mm and millimeter-scale cross-sections, so they are more appropriately described as hollow waveguides than as optical fibres [13]. Figure 7.6 illustrates the process of fabricating photonic crystal waveguides using the EFG method.

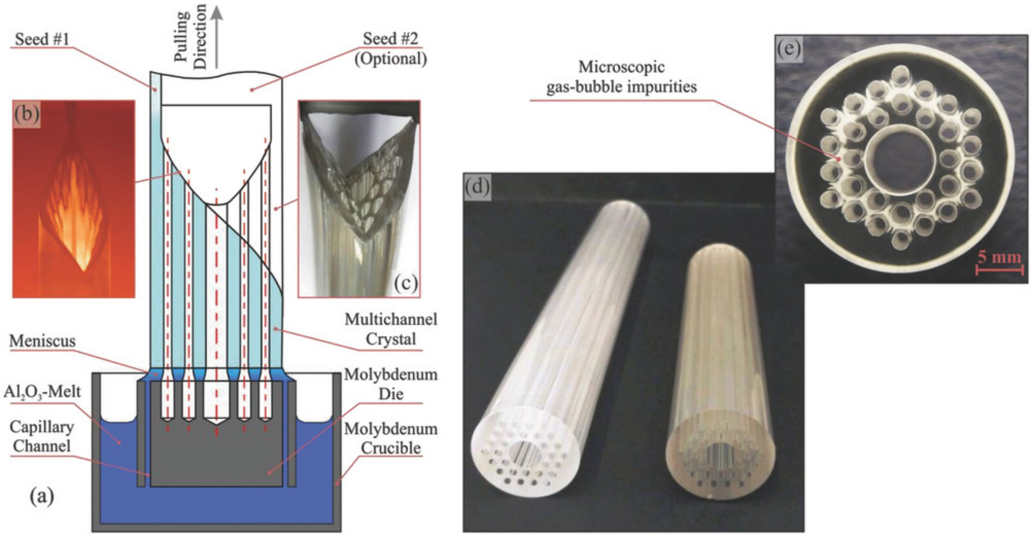


Figure 7.6: Photonic crystal waveguides fabricated using the EFG method [13].

More recently, progress on sapphire photonic crystal waveguides at telecom wavelengths has been reported by Stefan Kefer et al., who inscribed a hexagonal lattice of femtosecond laser inscription in planar bulk sapphire, integrated Bragg-grating structures, and demonstrated single-mode guidance at 1550 nm [14]. Figure 7.7 shows top-view and cross-sectional images of the sapphire photonic crystal waveguides they fabricated. However, planar-bulk-based sapphire waveguides lack the slender, flexible form factor of fibres and are challenging to splice to standard silica fibres, which complicates deployment in extreme high temperature fibre-sensor systems.

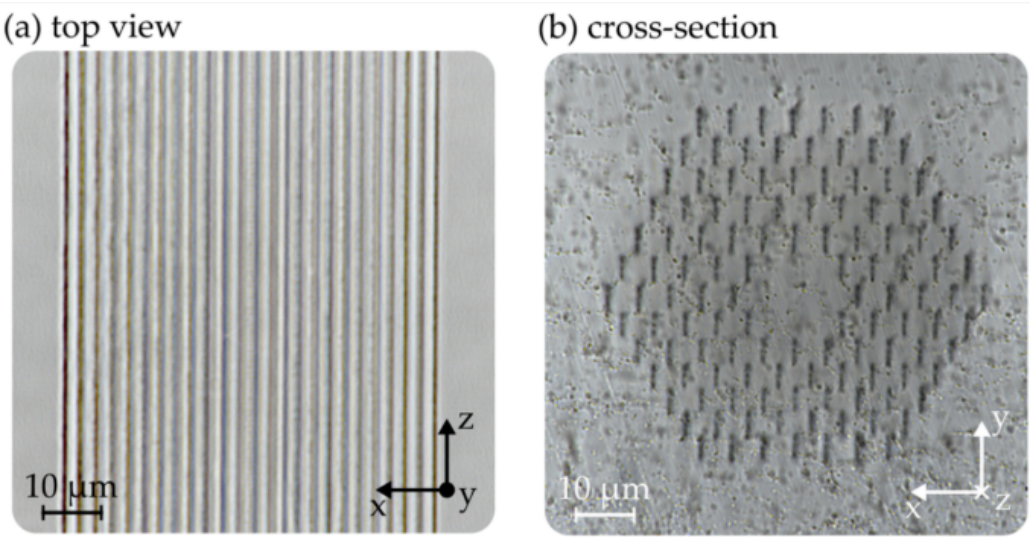


Figure 7.7: Top view and cross-section microscopy images of the sapphire photonic crystal waveguide [14].

In summary, building on prior studies of sapphire photonic crystal waveguides, we aim to lever-

age adaptive optics assisted femtosecond-laser micro machining to develop single-mode sapphire photonic-crystal fibres that are splice-compatible with silica fibres, thereby enabling deployment in high temperature sensing.

7.2 Simulation Design

For the design and fabrication of sapphire photonic-crystal fibres, I first adopt the most representative hexagonal (honeycomb) hole lattice. Using the Wave Optics Module in COMSOL Multiphysics, I construct a two-dimensional eigenmode model and compute the guided modes at 1550 nm; representative results are shown in Fig. 7.8. In the model, the air-hole diameter is set to 4 μm and the

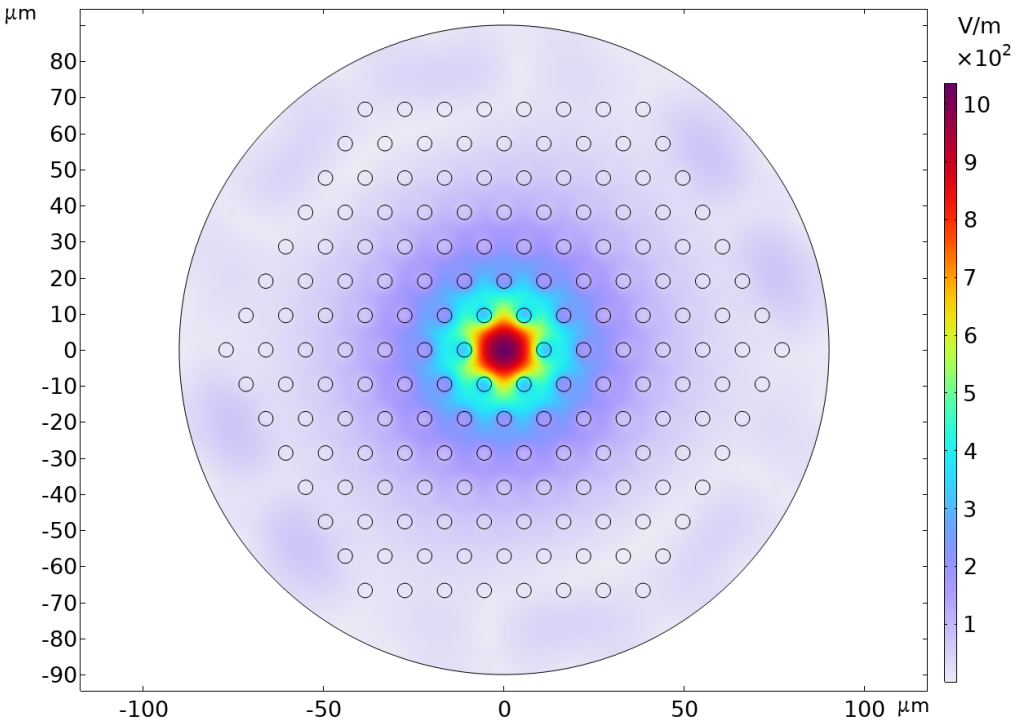


Figure 7.8: Finite element simulation of the air-hole sapphire photonic crystal fibre mode.

photonic-crystal lattice period to 11 μm. The holes are filled with air, while the remaining region is sapphire with a refractive index n = 1.746 at 1550 nm. Because fabricating sapphire PCFs with true air holes generally requires wet-etching steps and a comparatively elaborate process flow, I also simulated an alternative design in which the holes are replaced by a mixture of femtosecond laser modified amorphous sapphire and nano-scale microcracks. Based on previous work on laser-written

depressed-cladding sapphire waveguides, the femtosecond-laser-modified region was assigned a refractive index of 1.742 at 1550 nm for mode analysis [15]. This value represents a local reduction in refractive index relative to unmodified sapphire and is consistent with depressed-cladding guidance in sapphire. Furthermore, due to residual focusing aberrations, the laser modified area in sapphire assumes an ellipsoidal shape; accordingly, in the simulations for Fig. 7.9 I modelled each laser-modified region as an ellipse with a semi-major axis of 3.5 μm and a semi-minor axis of 1 μm.

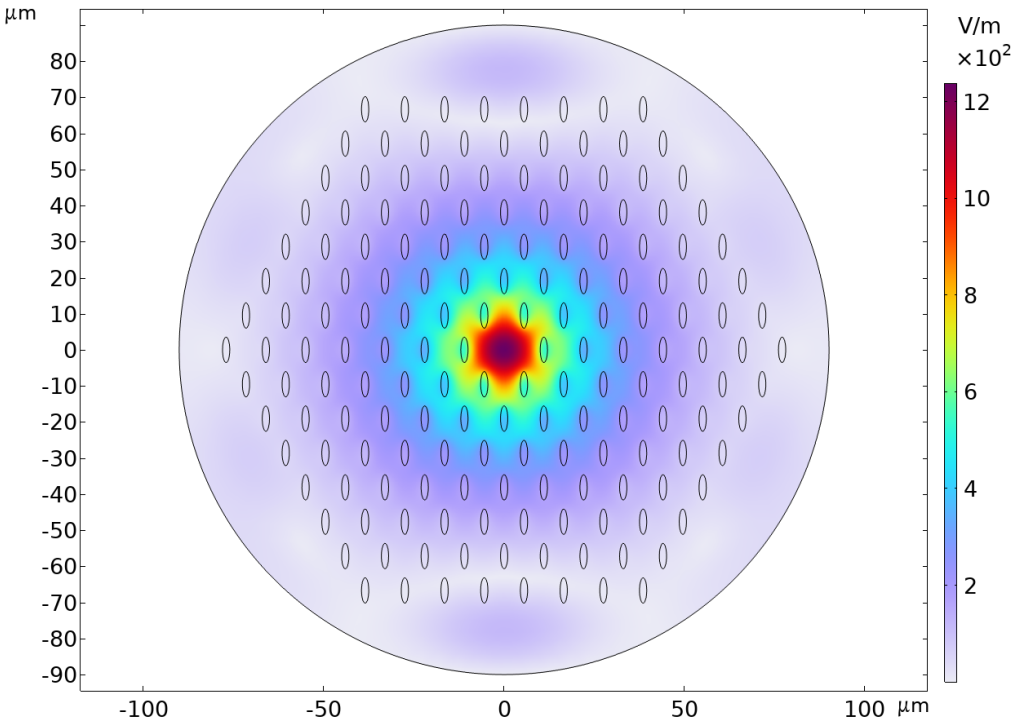


Figure 7.9: Finite element simulation of the solid-hole sapphire photonic crystal fibre mode.

To implement the photonic-crystal structure within a fibre, the feature size must be carefully controlled. Two parameters predominantly set the structural scale: the number of rings and the lattice pitch. I therefore begin by examining how varying the ring count influences the properties of the photonic crystal fibre. Because a PCF has a finite micro-structured cladding, the guided mode is intrinsically leaky: even in the absence of material absorption, part of the field radiates into the cladding and escapes. I refer to this radiation-induced attenuation as the confinement loss [16, 17, 18]. Starting from the propagation equation for the waveguide eigenmodes, we obtain the following

expression:

$$E(x,y,z,t) = E_0(x,y,t)e^{i\beta z} = E_0(x,y,t)e^{iRe(\beta)z}e^{-Im(\beta)z}, \tag{7.1}$$

where $\beta = k_0 n_{eff}$, $k_0 = \dfrac{2\pi}{\lambda}$; accordingly, the loss can be written as:

$$loss(dB) = 10log_{10}\frac{P_0}{P_z} = \frac{20k_0 Im(n_{eff})z}{ln10}, \tag{7.2}$$

and the loss per unit length can be written as:

$$Loss(dB/m) = \frac{20k_0 Im(n_{eff})}{ln10} = 8.686k_0 Im(n_{eff}). \tag{7.3}$$

From equation 7.3, we need only compute the imaginary part of the effective refractive index to obtain the confinement loss of the corresponding structure. Accordingly, I used COMSOL to simulate PCFs with different ring counts and calculate the effective index, selecting a perfectly matched layer (PML) as the boundary layer to absorb all leaked electromagnetic waves without producing reflections at the boundary. In each simulation, the PML thickness and the mesh resolution were gradually increased to ensure convergence.

Figure 7.10 shows the guided modes obtained while varying the number of rings, with the hole diameter and lattice constant held fixed. The imaginary part of the simulated effective index was then substituted into the confinement loss expression to produce the results in Fig. 7.11 (a). An exponential function provides an excellent fit to the dependence of confinement loss on ring count, and plotting the same data on a logarithmic scale in Fig. 7.11 (b) further reveals the exponential decay of confinement loss with increasing number of rings. In conclusion, at a wavelength of 1550 nm, the influence of confinement loss becomes negligible once the cladding consists of four rings.

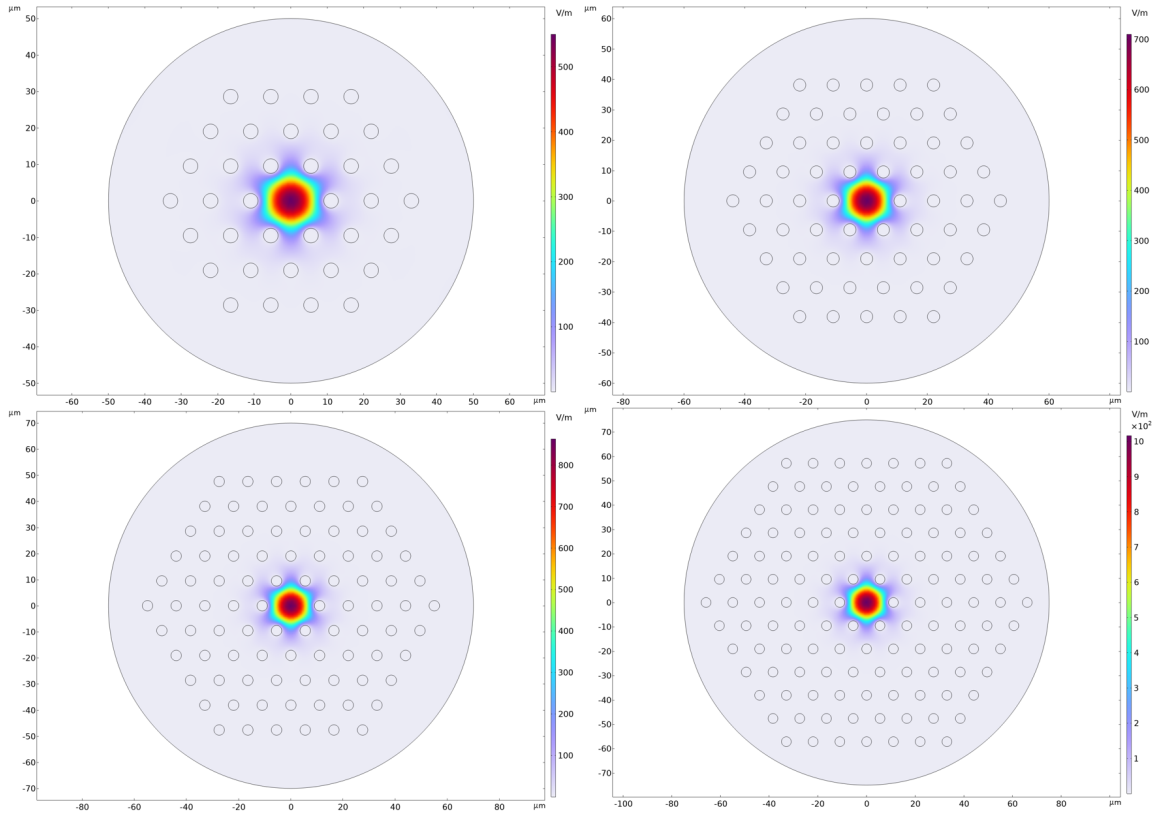


Figure 7.10: Finite element simulation of the PCF modes at different layers.

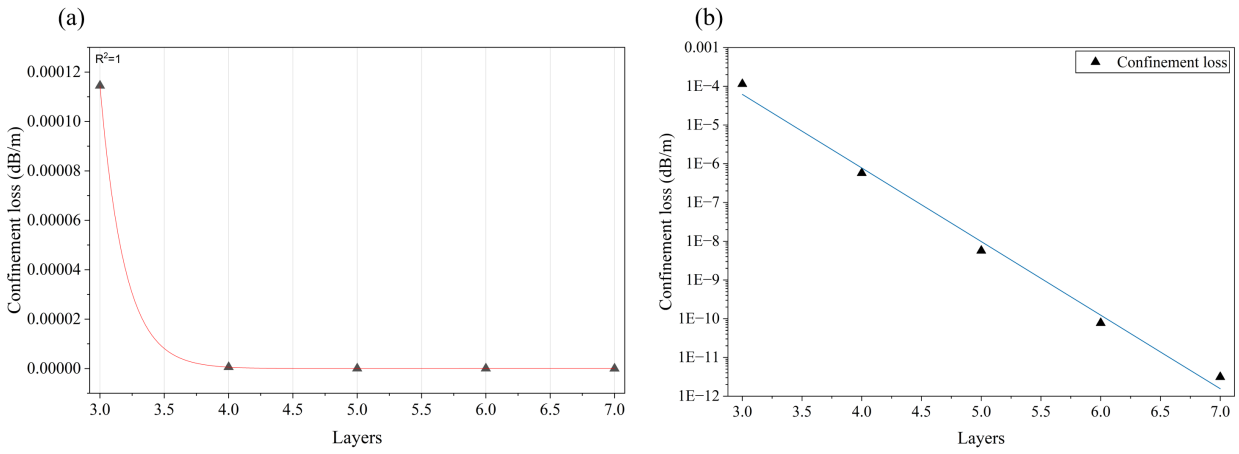


Figure 7.11: (a) Confinement loss for different PCF layers (b) Confinement loss using a logarithmic coordinate axis.

Since PCF-based sensors ultimately need to be spliced to standard single mode silica fibre to interface with the laser source, the coupling efficiency between the two fibres is critical for reliable signal transmission. We can compute the power-coupling coefficient numerically, expressing the

transmitted power at the interface between the two fibres in terms of the Poynting vector:

$$P = \frac{1}{2} Re[\int (E \times H^*) \cdot dS]. \tag{7.4}$$

The output modal field can be expressed as a superposition over an orthogonal modal basis.

$$\begin{gathered} E = \sum_m a_m e_m, H = \sum_m b_m h_m \\ \int (e_m \times h_n^*) \cdot dS = \delta_{mn} \int (e_m \times h_m^*) \cdot dS \end{gathered} \tag{7.5}$$

Assuming reflections are negligible, we impose the boundary condition $E_{in} = E_{out}, H_{in} = H_{out}$ at the interface; the corresponding expansion coefficients can then be written as:

$$\begin{aligned} a_m &= \frac{\int (E_{in} \times h_m^*) \cdot dS}{\int (e_m \times h_m^*) \cdot dS} \\ b_m &= \frac{\int (e_m \times H_{in}^*) \cdot dS}{\int (e_m \times h_m^*) \cdot dS} \end{aligned} \tag{7.6}$$

Substituting these coefficients into the power equation yields the coupling ratio for the m-th mode.

$$\begin{aligned} \frac{P_m}{P_{in}} &= \frac{Re[a_m b_m^* \int (e_m \times h_m^*) \cdot dS]}{Re[\int (E_{in} \times H_{in}^*) \cdot dS]} \\ &= Re[\frac{(\int E_{in} \times h_m^* \cdot dS)(\int e_m \times H_{in}^* \cdot dS)}{\int (e_m \times h_m^*) \cdot dS}] \frac{1}{Re[\int (E_{in} \times H_{in}^*) \cdot dS]} \end{aligned} \tag{7.7}$$

Based on equation 7.7, I compute in simulation the coupling efficiency between the PCF and a standard single-mode fibre. Holding all other parameters fixed while varying only the photonic crystal lattice pitch, the resulting mode area and power coupling efficiency are summarized in Table 7.1. Figure 7.12 displays the simulated modal profiles for different lattice pitches. As the lattice pitch decreases, the mode area shrinks and the coupling efficiency increases. Because the PFC's mode

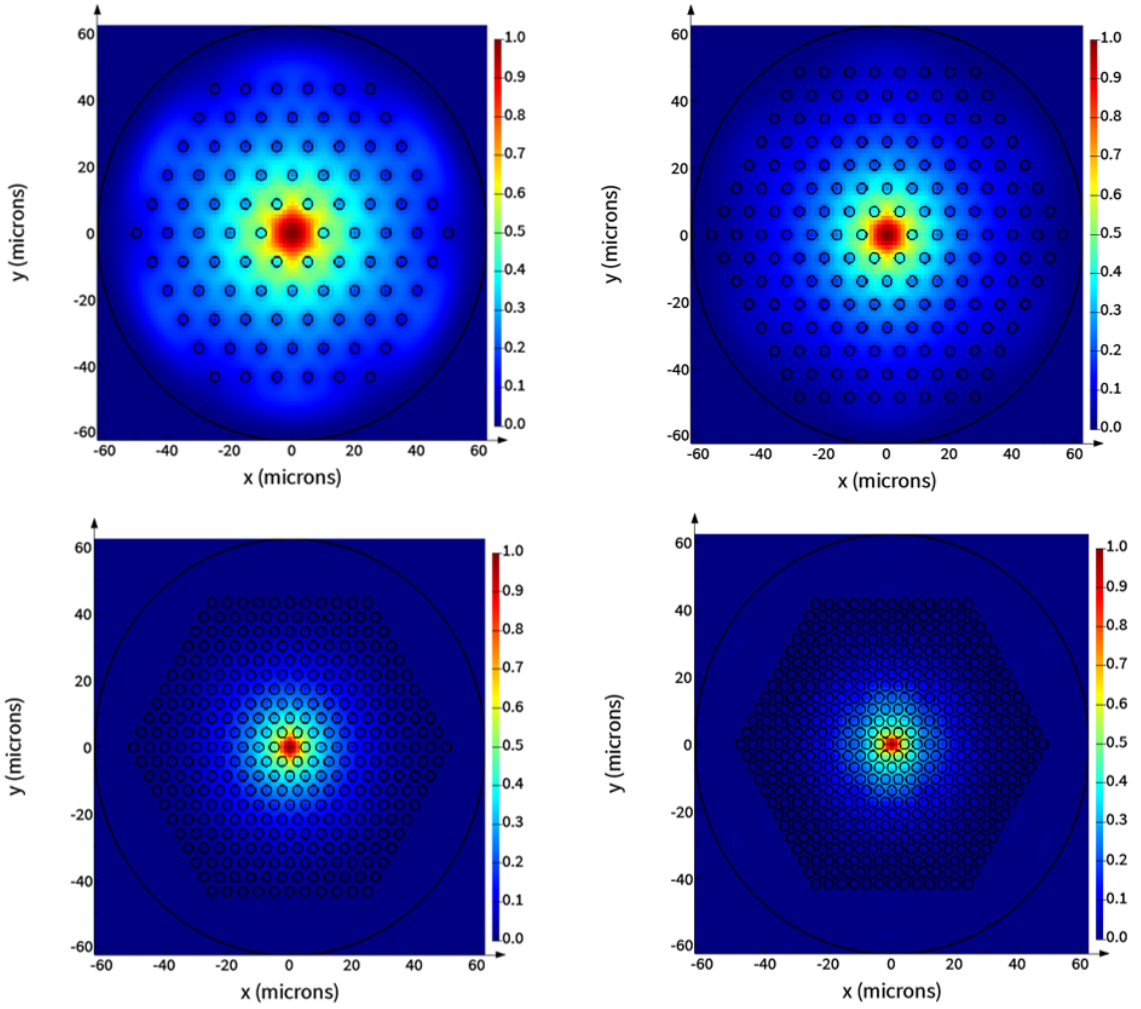


Figure 7.12: Finite element simulation of the PCF modes in different lattice pitches.

area remains larger than that of a standard single-mode fibre, minimizing the lattice constant during fabrication can reduce interface loss.

Table 7.1: Simulation results of power coupling efficiency in different PCF lattice pitches.

Photonic crystal lattice pitch	Mode area	Power coupling efficiency
10 μm	7241.94 μm^2	6.749%
8 μm	5339.85 μm^2	9.393%
5 μm	2436.21 μm^2	18.019%
4 μm	2011.52 μm^2	20.659%

References

[1] JC Knight et al. "All-silica single-mode optical fiber with photonic crystal cladding". In: *Optics letters* 21.19 (1996), pp. 1547–1549.

[2] Jonathan C Knight. "Photonic crystal fibres". In: *nature* 424.6950 (2003), pp. 847–851.

[3] Ana MR Pinto and Manuel Lopez-Amo. "Photonic crystal fibers for sensing applications". In: *Journal of Sensors* 2012.1 (2012), p. 598178.

[4] Peter John Roberts et al. "Design of low-loss and highly birefringent hollow-core photonic crystal fiber". In: *Optics Express* 14.16 (2006), pp. 7329–7341.

[5] Dimitre G Ouzounov et al. "Generation of megawatt optical solitons in hollow-core photonic band-gap fibers". In: *Science* 301.5640 (2003), pp. 1702–1704.

[6] Fetah Benabid et al. "Stimulated Raman scattering in hydrogen-filled hollow-core photonic crystal fiber". In: *Science* 298.5592 (2002), pp. 399–402.

[7] YL Hoo et al. "Evanescent wave gas sensing using microstructure fibre". In: *Technical Digest. CLEO/Pacific Rim 2001. 4th Pacific Rim Conference on Lasers and Electro-Optics (Cat. No. 01TH8557)*. IEEE. 2001, pp. 8–9.

[8] Yinian Zhu et al. "Strain-insensitive and high-temperature long-period gratings inscribed in photonic crystal fiber". In: *Optics Letters* 30.4 (2005), pp. 367–369.

[9] Yinian Zhu et al. "Deep-notch, ultracompact long-period grating in a large-mode-area photonic crystal fiber". In: *Optics Letters* 28.24 (2003), pp. 2467–2469.

[10] TR Wolinski et al. "Influence of temperature and electrical fields on propagation properties of photonic liquid-crystal fibres". In: *Measurement Science and Technology* 17.5 (2006), p. 985.

[11] Neal Pfeiffenberger et al. "Sapphire photonic crystal fibers". In: *Optical Engineering* 49.9 (2010), pp. 090501–090501.

[12] DH Jundt, MM Fejer, and RL Byer. "Characterization of single-crystal sapphire fibers for optical power delivery systems". In: *Applied Physics Letters* 55.21 (1989), pp. 2170–2172.

[13] Gleb M Katyba et al. "Sapphire photonic crystal waveguides for terahertz sensing in aggressive environments". In: *Advanced Optical Materials* 6.22 (2018), p. 1800573.

[14] Stefan Kefer et al. "Sapphire photonic crystal waveguides with integrated bragg grating structure". In: *Photonics*. Vol. 9. 4. MDPI. 2022, p. 234.

[15] Mohan Wang et al. "Optimization of single-mode sapphire waveguide Bragg gratings". In: *Journal of Lightwave Technology* 42.16 (2024), pp. 5629–5638.

[16] TP White et al. "Confinement losses in microstructured optical fibers". In: *Optics Letters* 26.21 (2001), pp. 1660–1662.

[17] Jui-Ming Hsu, Che-Wei Yao, and Jian-Zhi Chen. "Wavelength-tunable dispersion compensating photonic crystal fibers suitable for conventional/coarse wavelength division multiplexing systems". In: *Journal of Lightwave Technology* 33.11 (2015), pp. 2240–2245.

[18] Jian Ju, Wei Jin, and M Suleyman Demokan. "Design of single-polarization single-mode photonic crystal fiber at 1.30 and 1.55/spl mu/m". In: *Journal of lightwave technology* 24.2 (2006), pp. 825–830.

8 | Fabrication and Test of Sapphire Photonic Crystal Fibre Sensors

This chapter presents research on the fabrication of photonic crystal waveguides in sapphire slabs and sapphire fibres using femtosecond laser direct writing. I analyse the impact of optical aberrations on the machining process and describe adaptive optics strategies to mitigate these effects. I further discuss methods for reducing waveguide loss and optimizing the reflection response of fibre Bragg gratings embedded in the guides. Finally, sapphire PCFs incorporating FBGs are subjected to high temperature testing to evaluate their viability for extreme temperature sensing applications.

8.1 Sensor fabrication

I employed the femtosecond laser fabrication system described in Chapter 4 to fabricate photonic crystal waveguides in sapphire. As a first step, I validated and optimized our design on a 1 cm bulk sapphire (PI-KEM Limited 10 $\times$ 10 $\times$ 1 mm). Figure 8.1 presents an optical micrograph of the photonic crystal cross section. The sample was fabricated using a femtosecond laser with a 515 nm wavelength, 100 kHz repetition rate, and 102.8 mW average power. During inscription, the translation stage moved at 8 mm/s. A 63×/1.25 NA oil-immersion objective (ZEISS Plan-Apochromat) was employed, together with refractive index matching oil (Cargille Labs, n=1.7450).

From Fig. 8.1, the laser modified region is clearly axially elongated; the SEM image in Fig. 8.2 likewise shows a slender, bead-like geometry. Two factors account for this behaviour. First, the oil immersion objective employed was designed for silica (refractive index 1.45-1.56); in the absence of objectives specifically corrected for sapphire's refractive index, spherical aberration cannot be completely eliminated [1]. Second, non-linear optical effects, notably self-focusing, axially extend

the laser energy absorption region [2].

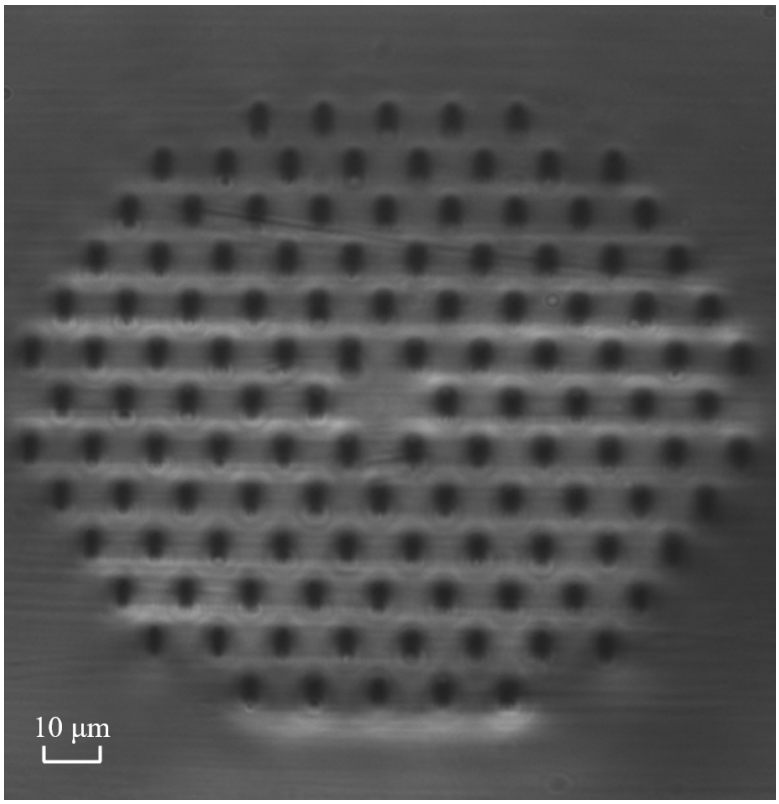


Figure 8.1: Optical micrograph of the sapphire photonic crystal structure cross section in slab.

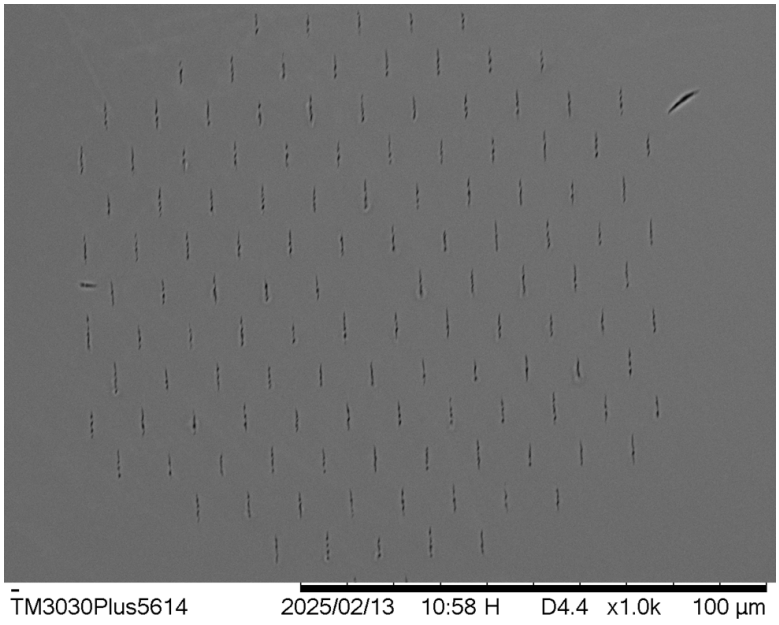


Figure 8.2: SEM of the sapphire photonic crystal structure cross section in slab.

Because fabricating photonic-crystal structures in either sapphire slabs or sapphire fibres requires an oil-immersion objective, I propose an adaptive optics aberration correction strategy to compensate

for the mismatch between the available objectives and a refractive index matching oil with refractive index 1.745. The central idea is to treat the sample, whether a fibre or a slab immersed in the 1.745-index oil, as an effectively planar window directly contacting the objective, and to pre-compensate the residual spherical aberration by comparing and correcting the optical path length calculated for conventional immersion (refractive index 1.56) versus the high-index immersion (refractive index 1.745). With assistance from Dr. Mohan Wang, we implemented this AO-based correction in practice.

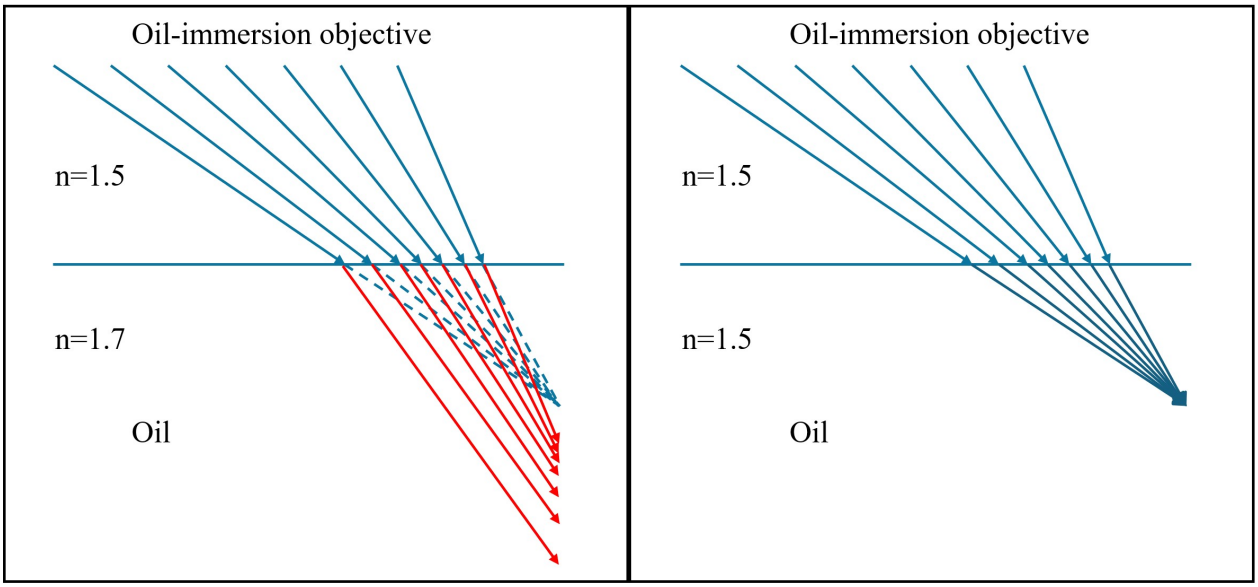


Figure 8.3: Schematic diagram of the focal positions of two different refractive index matching oils.

The optical path difference can be calculated using the following formula:

$$\begin{aligned} \Delta L &= n_2 L_2 - n_1 L_1 \\ L_1 &= L_2 \cos(\phi_2 - \phi_1). \end{aligned} \tag{8.1}$$

Based on the geometric relations shown in Fig. 8.4 and Snell's law $n_1 \sin\phi_1 = n_2 \sin\phi_2$, the focal

depth D can be expressed as a function:

$$\begin{aligned} L_2 &= D/\cos\phi_2 \\ \Delta L &= D(n_2\cos\phi_2 - n_1\cos\phi_1) \end{aligned} \tag{8.2}$$

By substituting the numerical aperture $NA = n\sin\alpha$ and the normalized radius $\rho = \sin\phi_1/\sin\alpha$ where α is is half the maximum cone angle when light enters or exits the lens [3, 4], we obtain:

$$\psi_R(\rho) = -k\Delta L = kD(\sqrt{n_2^2 - (NA\rho)^2} - \sqrt{n_1^2 - (NA\rho)^2}) \tag{8.3}$$

where $\psi_R(\rho)$ denotes the pupil-plane phase that the objective must apply to cancel the aberration induced by the refractive-index mismatch at the interface, k is the wave vector, and D is the ideal focal depth in the absence of any index mismatch.

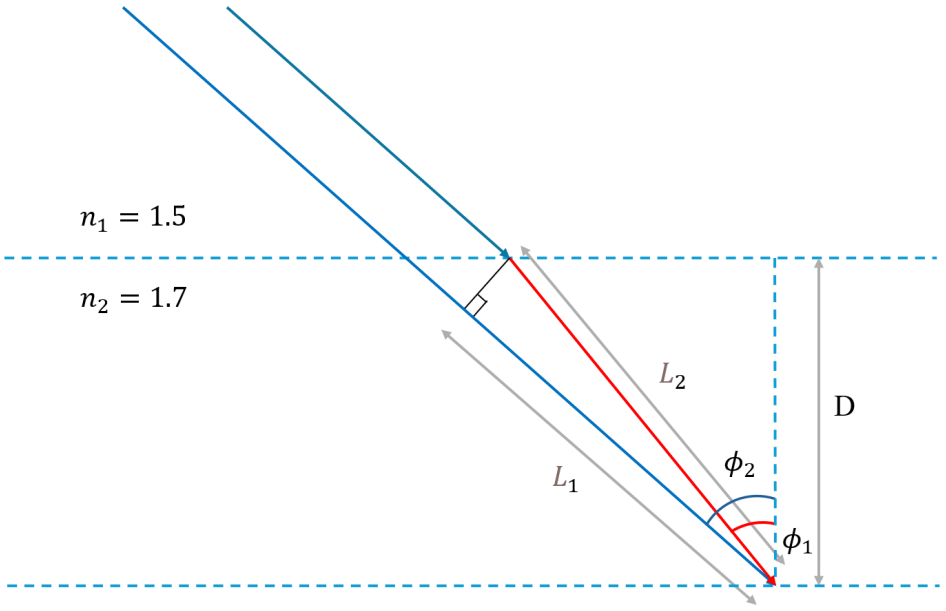


Figure 8.4: Schematic Diagram of Optical Path Difference.

Next, we seek a spherical defocus term that repositions the focal point from its actual location to the desired target, while minimizing the peak-to-peak phase modulation applied to the spatial light

modulator (SLM) [5]. The actual focal depth D_A and the target focal depth D_T can be expressed by the following relation:

$$\begin{aligned} D_T &= sD_A \\ 0 &< s < 1 \end{aligned} \tag{8.4}$$

To shift the focus from D_A to D_T , the focal point must be advanced by a distance $\Delta Z = D_A - D_T$ toward the n_2 medium. The corresponding pupil-plane defocus phase is given by

$$\psi_{DP}(\rho) = k\Delta Z(n_2 \cos\phi_2) = kD_A(1-s)\sqrt{n_2^2 - (NA\rho)^2} \tag{8.5}$$

By substituting equation 8.4 into the expression for $\psi_R(\rho)$ and then taking the difference $\psi'_R(\rho) = \psi_R(\rho) - \psi_{DP}(\rho)$, we obtain the refractive index mismatch aberration compensation with the defocus component decoupled.

$$\psi'_R(\rho) = kD_A[s\sqrt{n_1^2 - (NA\rho)^2} - \sqrt{n_2^2 - (NA\rho)^2}] \tag{8.6}$$

By decoupling the defocus term from the spherical aberration, the defocus can be compensated via simple mechanical axial translation, while the residual aberrations are corrected using the SLM. Since this residual term remains linearly proportional to the writing depth D_A, the phase maps for different depths can be obtained by linearly scaling with D_A, which greatly simplifies dynamic compensation.

Optimizing s minimizes the phase gradient across the SLM, yielding a smoother compensation pattern and higher SLM efficiency. Two approaches can be employed to determine the optimal s: (i) a one-dimensional grid search implemented in code, or (ii) an analytical solution obtained by enforcing phase equality at the pupil centre and edge, which minimizes the phase gradient. The

resulting expression can be written as:

$$s = \frac{n_2 - \sqrt{n_2^2 - NA^2}}{n_1 - \sqrt{n_1^2 - NA^2}}. \tag{8.7}$$

Using MATLAB, I computed the three phase maps ($\psi_R(\rho), \psi_{DP}(\rho), \psi'_R(\rho)$) arising from the refractive-index mismatch between a sapphire index-matching oil and a conventional oil-immersion objective, as well as the SLM phase mask required for the final compensation; the results are shown in Fig. 8.5 and Fig. 8.6.

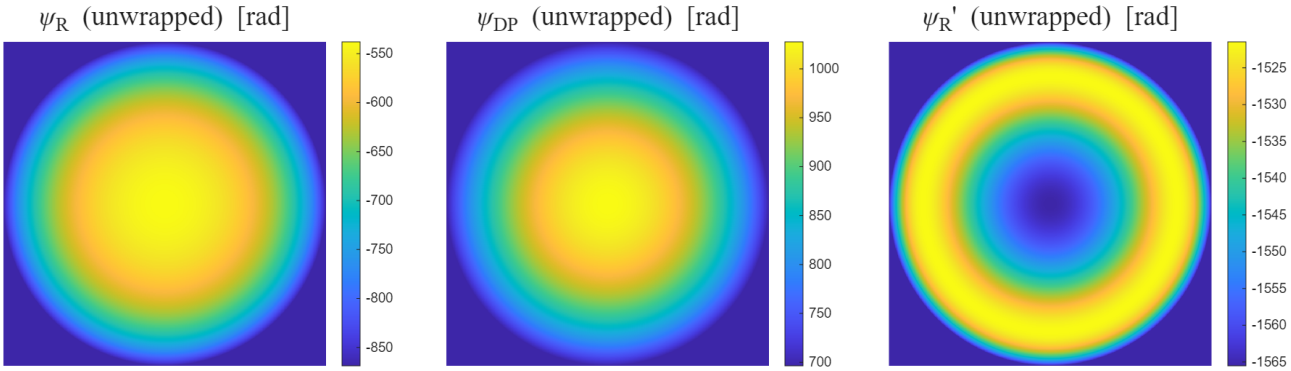


Figure 8.5: Phase maps of $\psi_R(\rho), \psi_{DP}(\rho), \psi'_R(\rho)$.

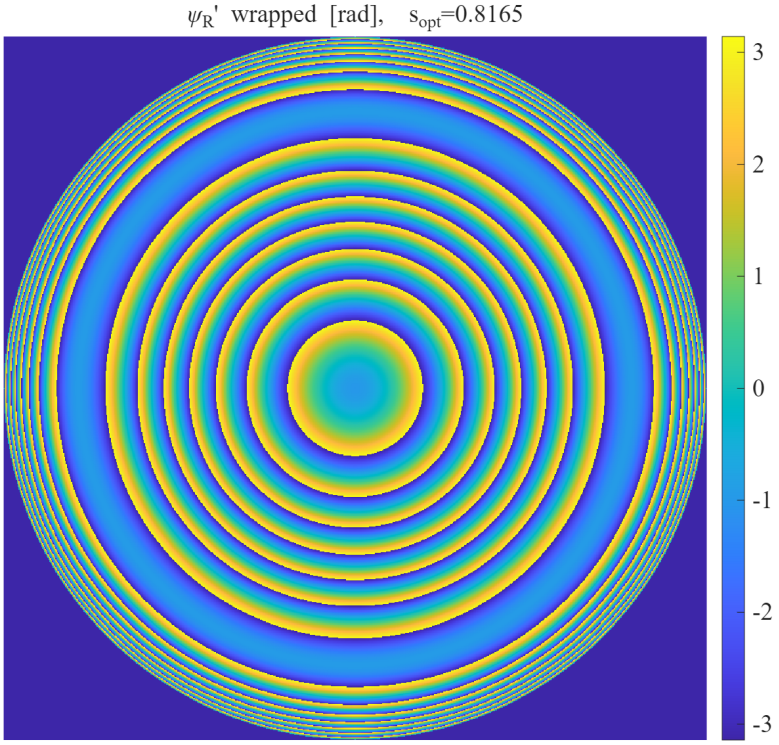


Figure 8.6: SLM phase mask required for the final compensation.

Figure 8.7 compares the geometry of the laser-modified region, with and without adaptive-optics correction, over a range of incident powers. At high power, axial elongation is markedly suppressed after correction. At lower power (e.g., 50.1 mW), however, the modified region exhibits little improvement. This behaviour is attributed to the fact that aberration correction concentrates the focal energy, more readily exceeding the threshold required for material modification, whereas the uncorrected focus is axially extended and its energy more dispersed. As the power decreases, parts of the elongated uncorrected focal volume fall below the modification threshold, resulting in only minor morphological differences between the corrected and uncorrected cases at low power.

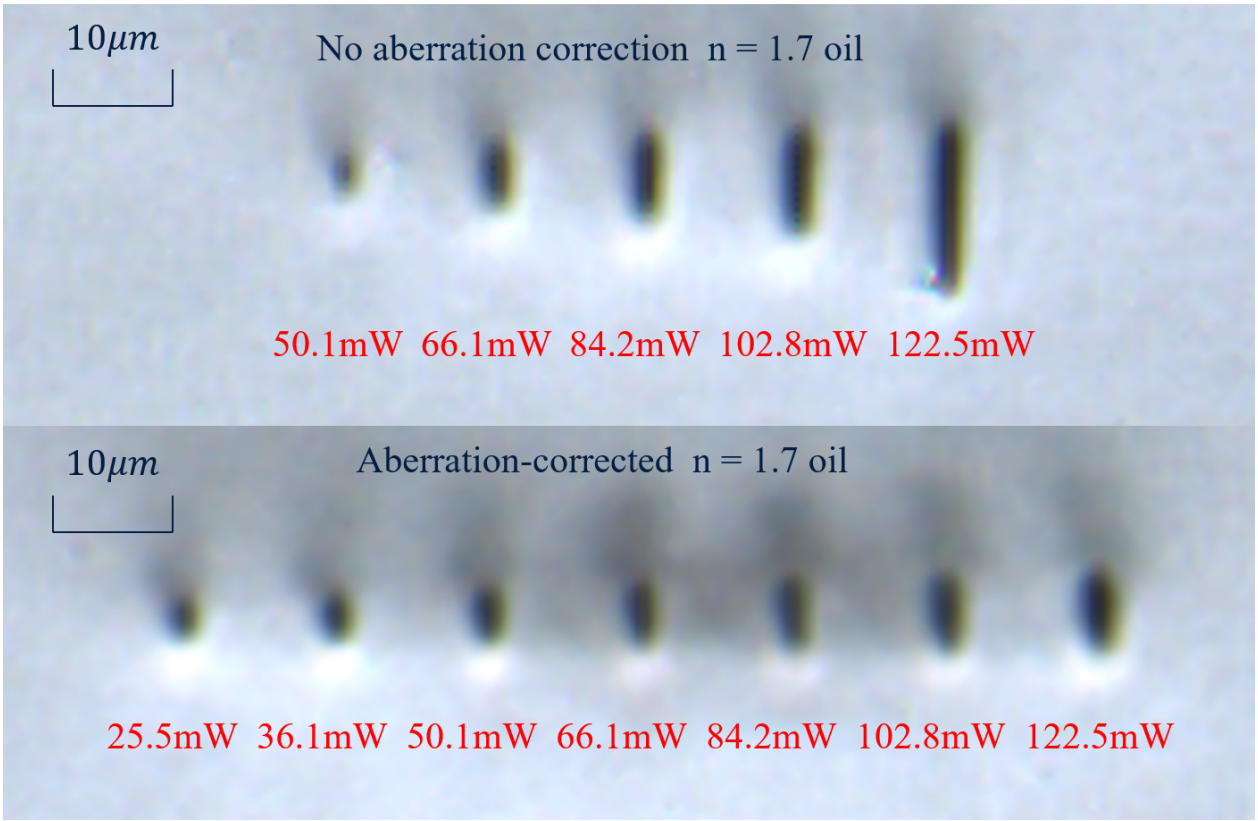


Figure 8.7: Corrected and uncorrected cross sectional micrographs of laser-modified regions.

Figure 8.8 shows photographs of photonic crystal structures laser written on a sapphire slab with AO assistance. The axial elongation of the laser-modified region is markedly suppressed. This reduction enables a further decrease in the photonic crystal lattice constant. Based on the simulations in the previous chapter, a smaller lattice constant yields a smaller effective mode area, thereby improving the coupling efficiency between the photonic crystal fibre and a standard single mode fibre.

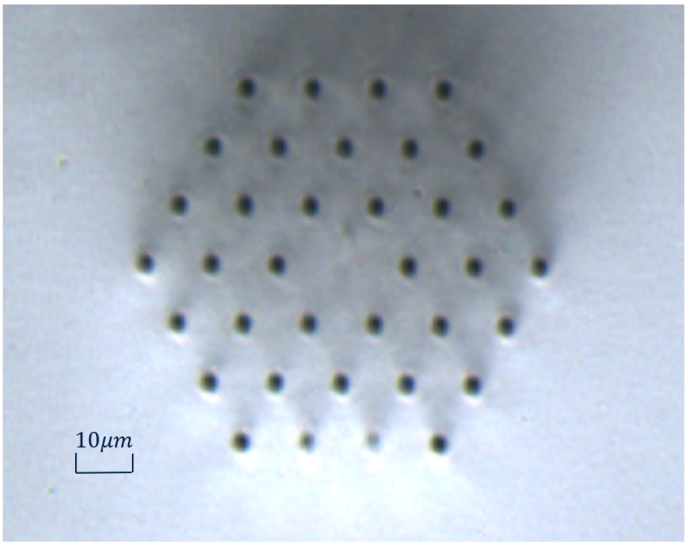


Figure 8.8: AO corrected cross sectional micrographs of photonic crystal structure in sapphire slab.

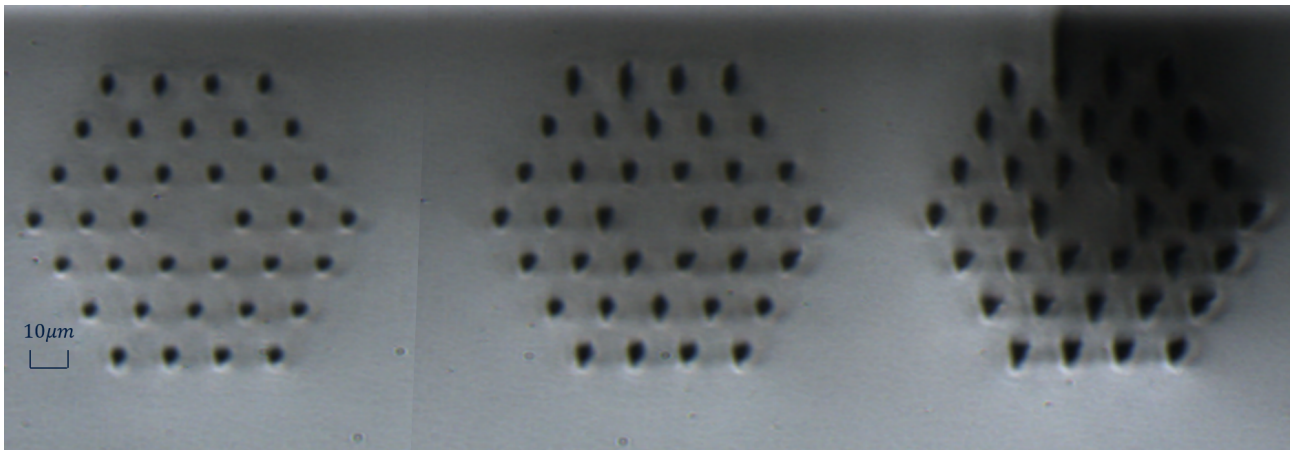


Figure 8.9: Micrographs of cracks in the laser-modified region as power increases in sapphire slab.

While AO correction concentrates the focal energy, it introduces a further concern: at higher laser powers the modified region becomes more susceptible to crack initiation. Consequently, when employing AO correction, lower laser powers should be selected to mitigate crack formation.

Beyond aberration correction based fabrication, an approach omitting AO was also investigated, using an enlarged laser-modified volume as the photonic crystal unit cell. To make the lateral and axial extents of each cell comparable, we performed three adjacent inscription tracks per cell, yielding a cross-section-comprising three slender modified tracks—that approximates a square. Cross sectional images are shown in Figures. 8.10 and 8.11.

This design also presents several notable drawbacks. First, the three tracks within a single cell

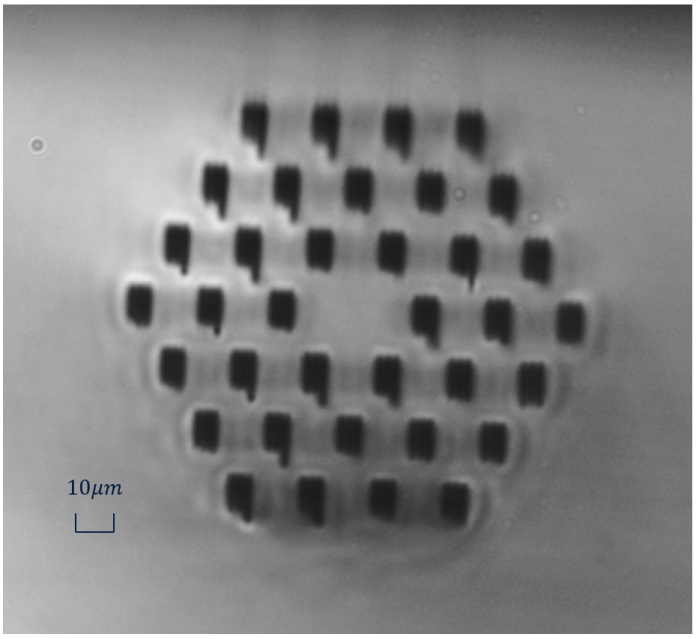


Figure 8.10: Micrographs of the 3 tracks per cell photonic crystal laser-modified region in sapphire slab.

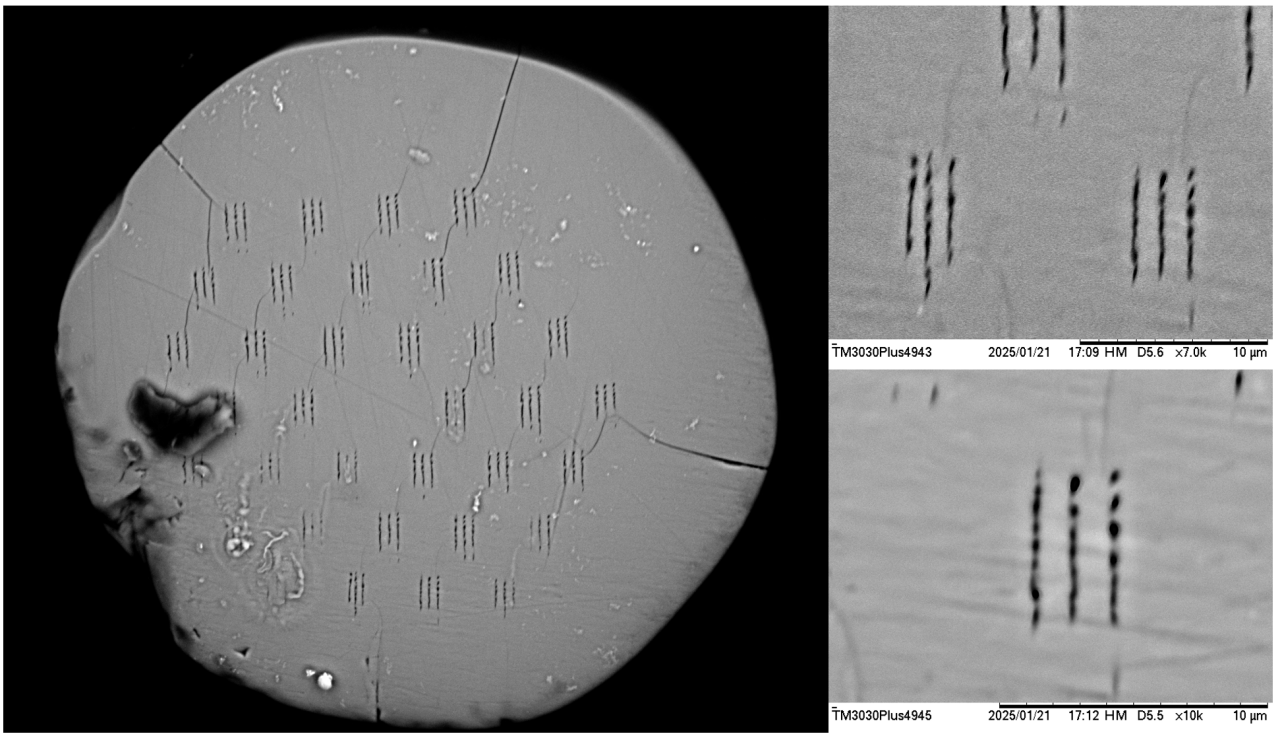


Figure 8.11: SEM of the 3 tracks per cell photonic crystal laser-modified region in sapphire fibre.

cannot be brought sufficiently close to merge into a unified modified area. Empirically, reducing the spacing between adjacent tracks below approximately 1.5 μm during laser processing induces severe cracking. As evidenced by the SEM images, even at an inter-track spacing of exactly 1.5 μm, fine cracks persist in the surrounding unmodified regions, although the photonic-crystal region itself

remains crack-free. Furthermore, because the three tracks fail to merge, each cell occupies a larger cross-sectional area, necessitating a larger lattice constant. The structures shown in Figures. 8.10 and 8.11 employ a lattice constant of 13 μm. Under comparable laser powers and while avoiding widespread cracking, a single-track design fabricated without AO can achieve a lattice constant of 10 μm, whereas employing AO permits a further reduction to 6 or 7 μm. Therefore, this design is at a disadvantage in terms of reducing the mode field area.

8.2 Sensor Testing

I first evaluated the impact of the number of rings in the photonic-crystal lattice on transmission loss, since loss is presently a key bottleneck for sapphire-fibre sensors. As shown in Figure 8.12, using identical scan speeds and laser-processing parameters, I inscribed photonic crystal waveguides with three, four, five, and six rings (layers) in a 1-cm-long bulk sapphire sample (PI-KEM Limited 10 $\times$ 10 $\times$ 1 mm), and then measured their propagation losses.

Measurements were conducted using the setup shown in Fig. 8.13. A CoBrite DX tunable laser source was operated at 1550 nm with an output power of 8.8 dBm. The beam was coupled into the sample via SMF-28e single mode fibre, then focused onto the sensor using an objective and relay optics, and the transmitted power was recorded with a Newport 843-R optical power meter. Because an air gap between the fibre and sample and additional losses from the objective and lenses introduce unknown insertion loss, I did not attempt to extract the intrinsic loss of the photonic crystal waveguides. Instead, I compared the measured output powers to infer their relative losses.

Table 8.1 reports the measured output powers. In principle, the dependence of output power on the number of rings should follow an exponentially saturating model. This arises because the evanescent field in the PCF cladding decays exponentially from ring to ring, leading to an exponential reduction in confinement loss and, consequently, a monotonic increase in output power that

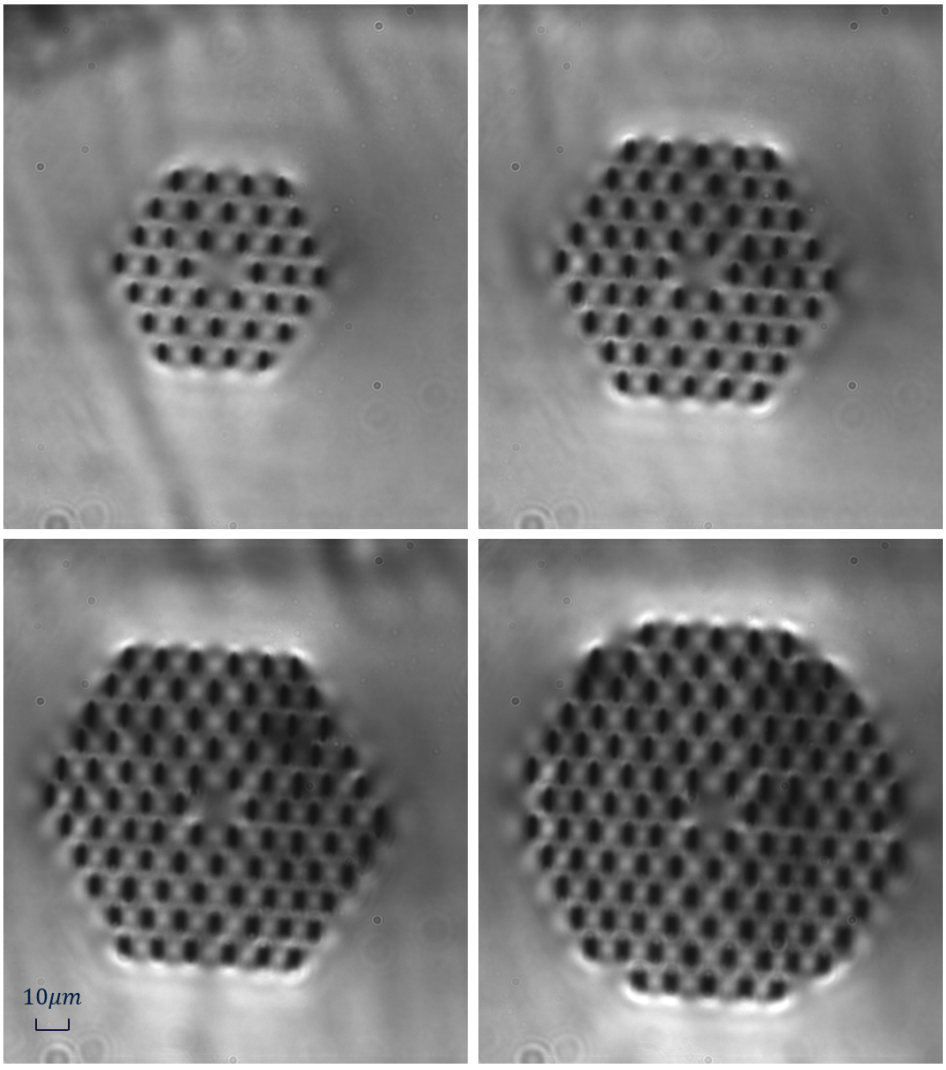


Figure 8.12: Micrographs of the photonic crystal waveguide with different rings in sapphire slab.

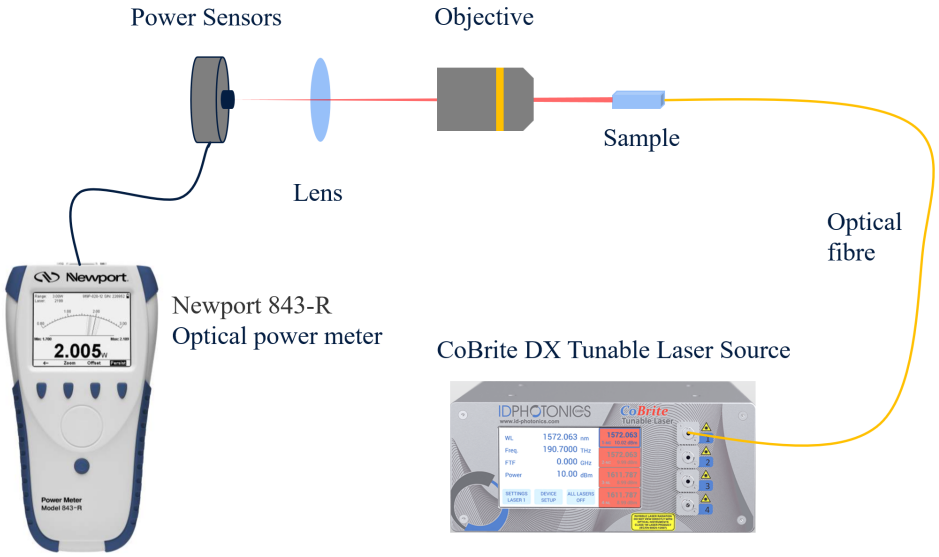


Figure 8.13: Micrographs of the photonic crystal waveguide with different rings.

approaches saturation. The data likewise indicate diminishing returns: as the ring count increases, the incremental improvement in loss continues to decrease. This is consistent with the simulation results I presented in the previous chapter.

Table 8.1: Measurement Results for Output Power at Different Ring Numbers.

Number of rings	Output power
3 rings	14.57 μW
4 rings	29.53 μW
5 rings	34.00 μW
6 rings	41.20 μW

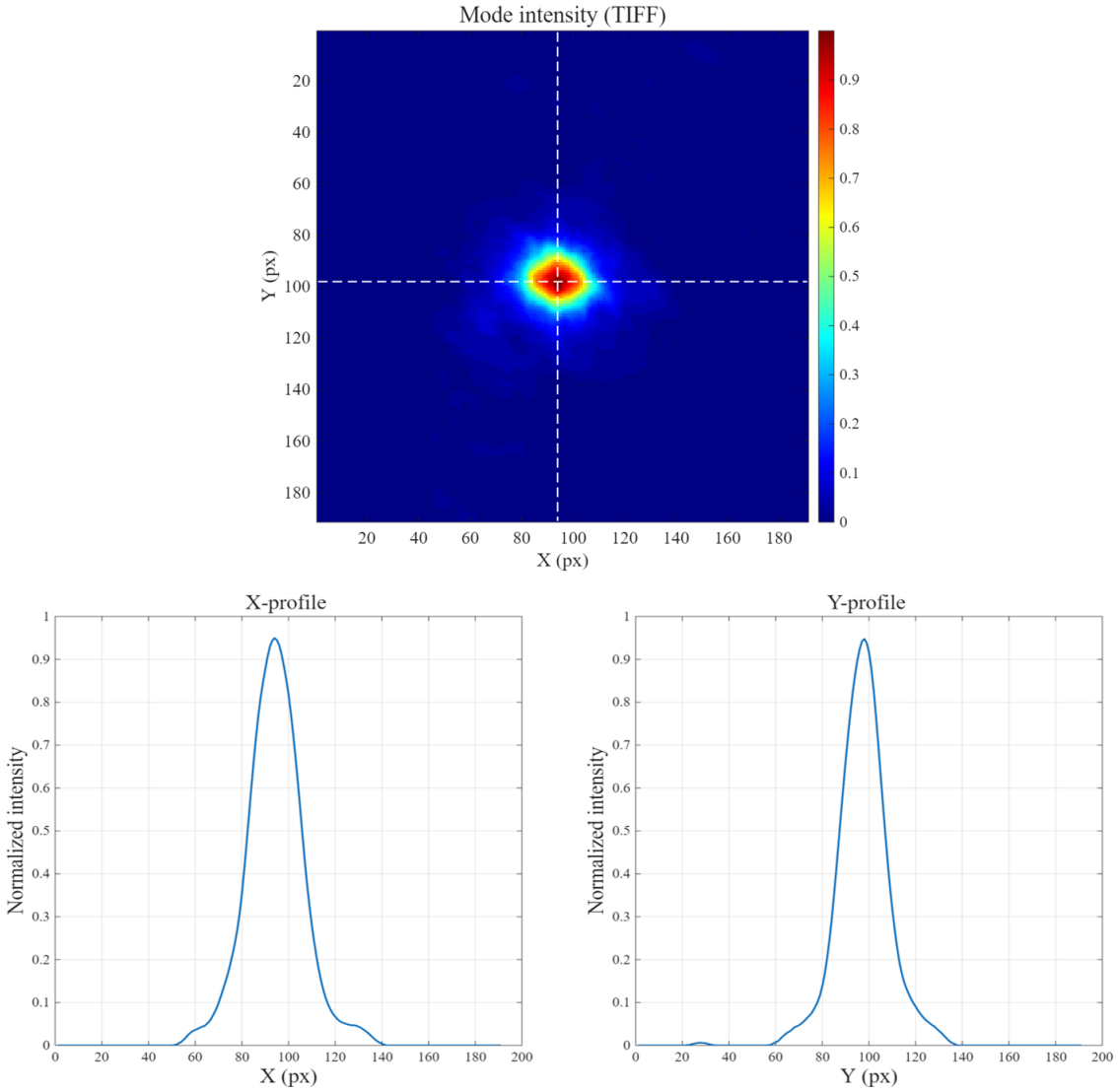


Figure 8.14: Mode field of the waveguide and X Y cross-sectional profiles (the image has been noise-reduced and smoothed).

By replacing the power meter with an infrared camera (Hamamatsu C14041-10U), the mode field

of the waveguide can be recorded. The measured intensity distribution and cross-sectional profiles are shown in Fig. 8.14. The intensity decreases approximately monotonically from the centre outward, with no discernible secondary lobes or pronounced oscillations. Both the horizontal and vertical cuts exhibit a single, symmetric peak that is well approximated by a near-Gaussian profile. Although a slight diamond-shaped distortion arises from the hexagonal hole lattice (common in PCF) the overall morphology remains consistent with single mode LP_{01} guidance.

Next, using the same parameters, I inscribed the identical photonic-crystal pattern in a custom sapphire fibre of 150 μm diameter grown by laser-heated pedestal growth (LHPG) [6, 7]. I first tested samples written without AO using an oil-immersion objective. Constrained by the fibre's cross-section, a six-ring lattice brought the outer ring too close to the perimeter: when focusing on the outermost ring, the immersion oil generated copious bubbles, preventing inscription; consequently, the design was limited to five rings. I further observed that, even under identical power and scan speed conditions, the fibre is more prone to cracking than the slab, likely because the fibre's much smaller volume concentrates the stress introduced by femtosecond laser writing.

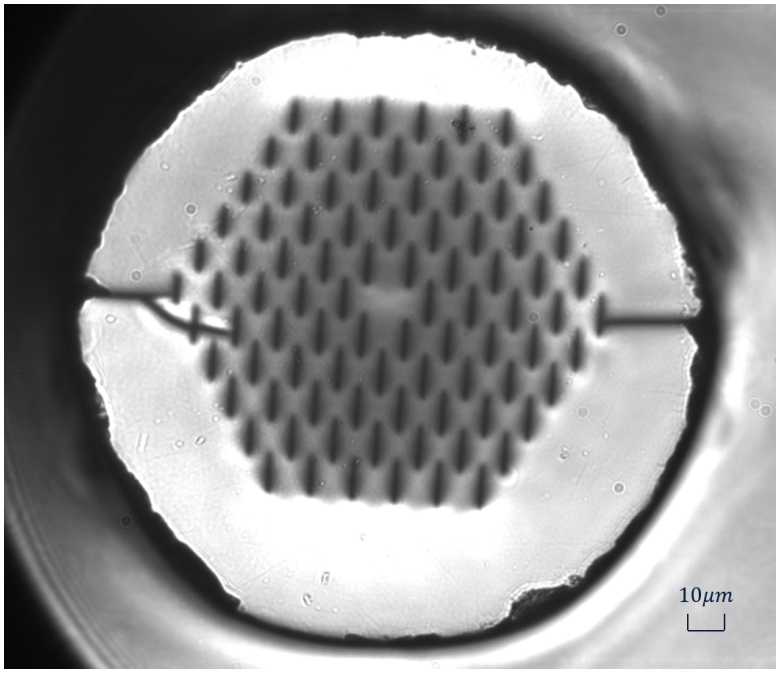


Figure 8.15: Micrographs of the sapphire photonic-crystal fibre cross section.

Figures 8.15 and 8.16 show, respectively, the cross-section and mode field of the sapphire PCF.

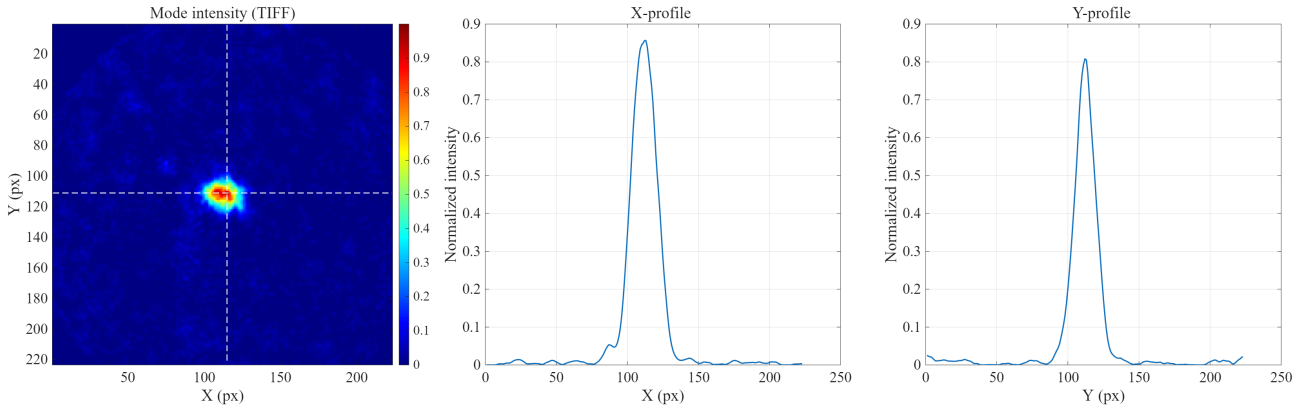


Figure 8.16: Mode field of the sapphire photonic-crystal fibre and X Y cross-sectional profiles (the image has been noise-reduced and smoothed).

From these results, I confirm that I have fabricated- to the best of my knowledge- the first single mode sapphire photonic crystal fibre, with a length of 4.15 cm. I subsequently produced a second fibre of identical design, 7.30 cm in length, to measure the transmission loss of this sapphire PCF. The propagation loss of the sapphire PCF is evaluated as follows:

$$Loss\ [dB/cm] = \frac{10log_{10}(P_1/P_2)}{L_2 - L_1} = \frac{10log_{10}(46.10/17.45)}{7.30 - 4.15} \approx 1.34\ dB/cm. \tag{8.8}$$

I then invert the transmission loss model to back calculate the propagation losses of the two samples, obtaining respectively:

$$\begin{aligned} 4.15cm &: 1.34 \times 4.15 \approx 5.56\ dB \\ 7.30cm &: 1.34 \times 7.30 \approx 9.78\ dB \end{aligned} \tag{8.9}$$

Subsequently, using the same setup, I measured the output power of a 4-cm SMF-28e fibre to be 157.00 μW. This value was used as a reference to evaluate whether the fibre sample coupling remained consistent across measurements.

$$\begin{aligned} 4.15cm &: 10log_{10}(157.00/46.10) \approx 5.32\ dB \\ 7.30cm &: 10log_{10}(157.00/17.45) \approx 9.54\ dB \end{aligned} \tag{8.10}$$

Relative to the reference single mode fibre, the measured losses of both samples deviate by approximately 0.24 dB from the transmission losses computed via Eq. (8.9). This indicates that, when measured on the same setup, the end face coupling for the two samples of different lengths is effectively consistent, thereby lending confidence to the inferred loss values. Relative to the previously reported single mode sapphire fibres with depressed-cladding structures (propagation loss ≈ 1.5 dB/cm), the sapphire PCF achieves an 10% reduction in loss [8]. Moreover, its usable length is increased by 82.5% compared with the 4 cm benchmark (to 7.30 cm). Another significant advantage is that far fewer laser-written modification tracks are required to fabricate the PCF than in the depressed-cladding approach, which substantially shortens manufacturing time and reduces production cost. These advances are significant for extending the operational range and practical applicability of sapphire fibre temperature sensors.

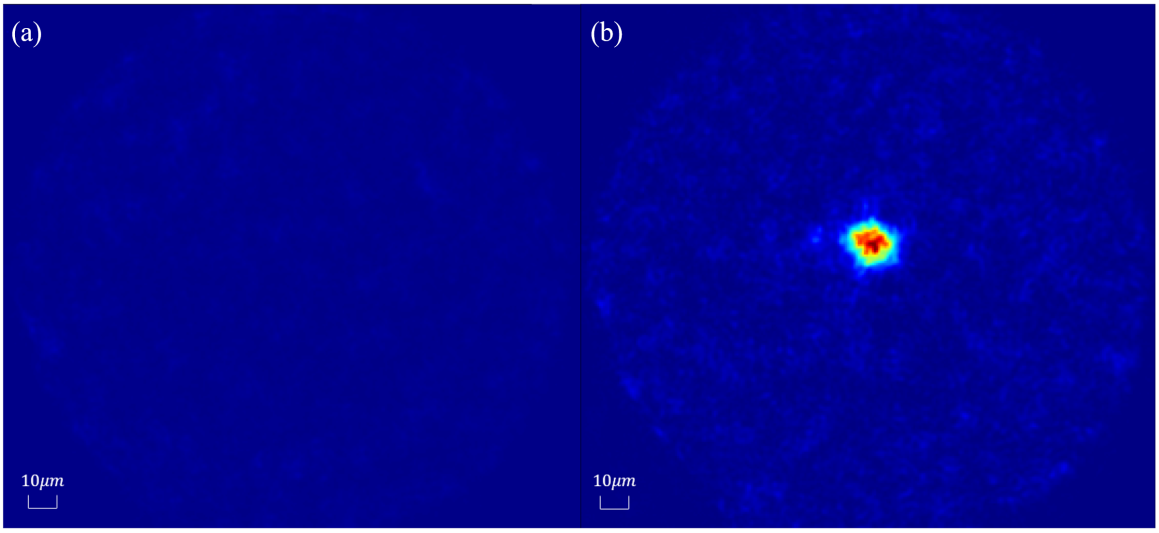


Figure 8.17: Micrographs of the two orthogonal polarisation modes input after propagation in sapphire PCF. (a) adjust the polarisation to minimise the mode field (b) adjust the polarisation to maximise the mode field.

During characterization, I also observed single polarization behaviour in the sapphire PCF. Figure 8.17 shows the output mode field for two orthogonal input polarisations corresponding to the measured maximum- and minimum-transmission axes of the fabricated sapphire PCF. One polarisation transmits normally, whereas the orthogonal polarisation suffers such high attenuation that no output spot is identifiable. A possible origin is the aberration introduced by the mismatch between

the objective and the high-index index-matching oil in the absence of AO correction, which renders the written tracks within the lattice anisotropic with elongated elliptical cross-sections, thereby imparting polarization maintaining and high birefringence characteristics [9, 10]. Whether this effect leads to genuine polarization suppression (i.e., true single-polarization operation) requires further measurements and modelling. In any case, this behaviour has no significant impact on the intended temperature sensing application.

Next, I examined the incorporation of a Bragg grating into the photonic crystal structure. As an initial step, I fabricated a sample on a 1 cm sapphire slab featuring a second-order Bragg grating, written at a scan speed of 1 mm/s, 10% duty cycle, 500 kHz repetition rate, and 102.8 mW average power. Figure 8.18 presents cross-sectional micrographs of two photonic crystal waveguides incorporating Bragg gratings. Figure 8.19 shows the corresponding reflectivity spectra acquired while interfacing with an interrogator (Halliburton SmartFibres SmartScan SBI).

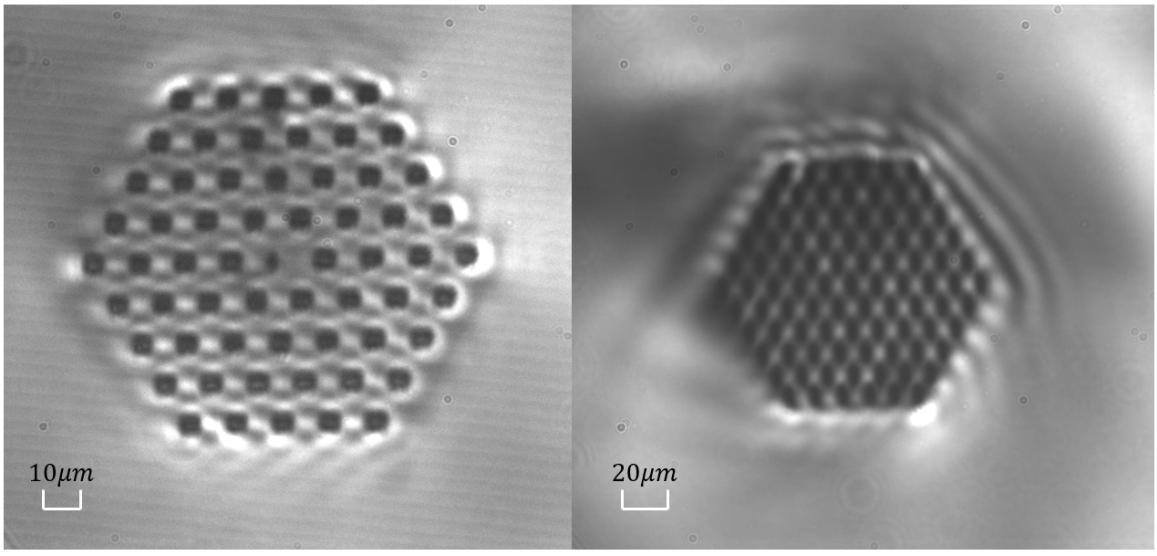


Figure 8.18: Cross-sectional micrographs of sapphire-slab photonic crystal waveguides incorporating Bragg gratings. The two structures compare PCW unit cells formed from a single laser-written track and from three adjacent laser-written tracks, respectively. The Bragg grating was written along the waveguide propagation direction by periodically modulating the femtosecond-laser exposure.

During reflection spectrum measurements of the two waveguides, the gap between the fibre and the sapphire slab was filled with index-matching oil to suppress interfacial reflections and minimize Fabry-Perot resonances. As Figure 8.19 demonstrates, I observed that only photonic crystal waveg-

uides (PCWs) whose unit cell comprises three adjacent laser-written tracks exhibited a clear Bragg reflection peak, whereas PCWs with a single track unit cell showed little or no Bragg response; this result was reproduced across multiple samples, ruling out chance. Notably, prior trials confirmed that single track PCWs can guide light. A plausible explanation is that the Bragg grating inscription region and the single track unit entail similar material modifications; writing the Bragg grating within such a single track unit locally reduces the core-cladding index contrast that underpins guidance, thereby weakening the waveguide and suppressing the grating reflectivity. By contrast, in a three track unit the cladding perturbation is stronger and more distinct from the Bragg grating region, so the grating can be inscribed without excessively degrading guidance, yielding a pronounced Bragg peak.

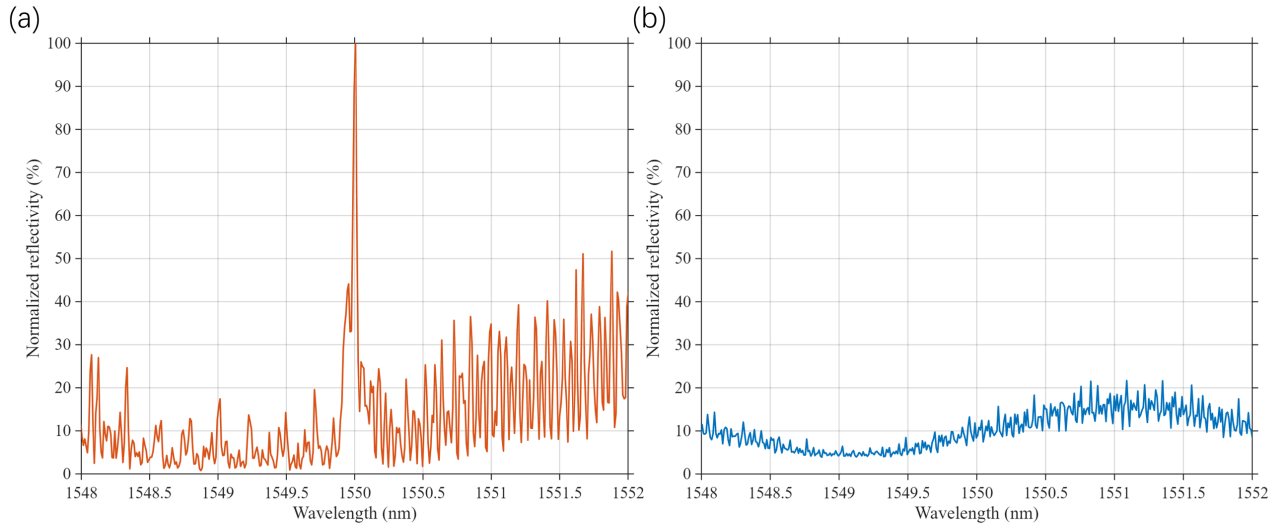


Figure 8.19: (a) Reflectivity spectrum of 3 tracks per cell PCW (b) Reflectivity spectrum of 1 track per cell PCW.

Subsequently, I attempted to fabricate, on a 4 cm sapphire slab, a PCW whose unit cell comprised three tracks, with a 1 cm long Bragg grating written at one end. However, no Bragg reflection peak was observed, most likely due to excessive propagation loss. In 2022, Kefer and co-workers reported a 4 cm PCW on a sapphire slab incorporating a 5 mm Bragg grating and observed a pronounced reflection peak. Unlike the three track scheme, their design employed a single track PCW while removing the innermost ring of tracks to mitigate grating induced weakening of the waveguide [11, 12, 13]. Adopting this architecture, and combining it with aberration correction under an oil-immersion

objective, I fabricated PCWs on a 4 cm sapphire slab and on a 7 cm long, 150 μm diameter sapphire fibre, each incorporating a 1 cm Bragg grating at one end. These two samples were both fabricated using a femtosecond laser with a 515 nm wavelength, 500 kHz repetition rate, and 75.1 mW average power. During inscription, the translation stage moved at 4 mm/s. Figure 8.20 presents cross section photos of these two samples.

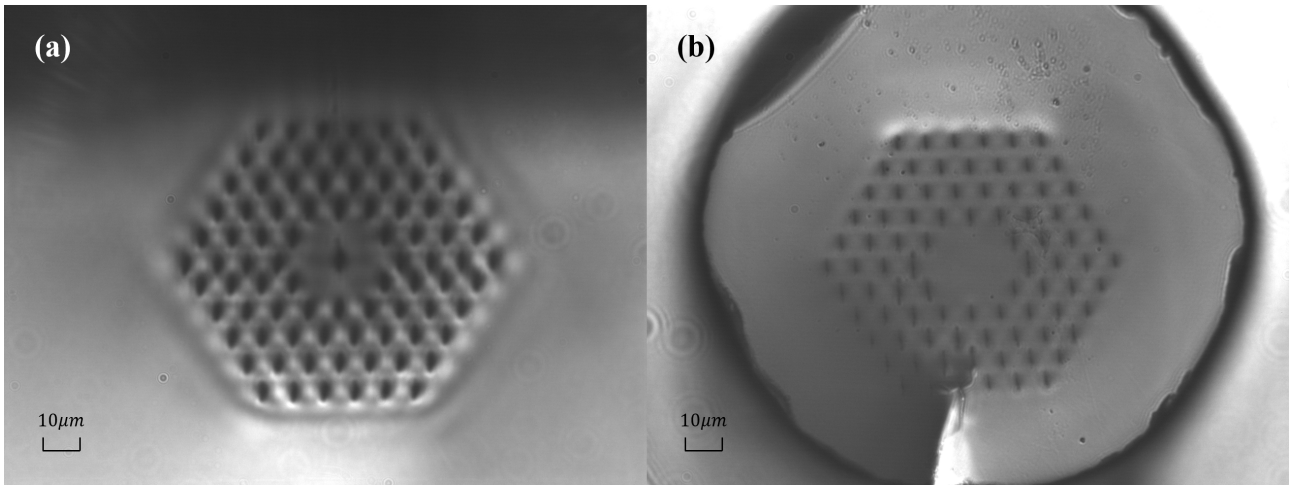


Figure 8.20: (a) PCW in the sapphire slab (b) PCW in the sapphire fibre.

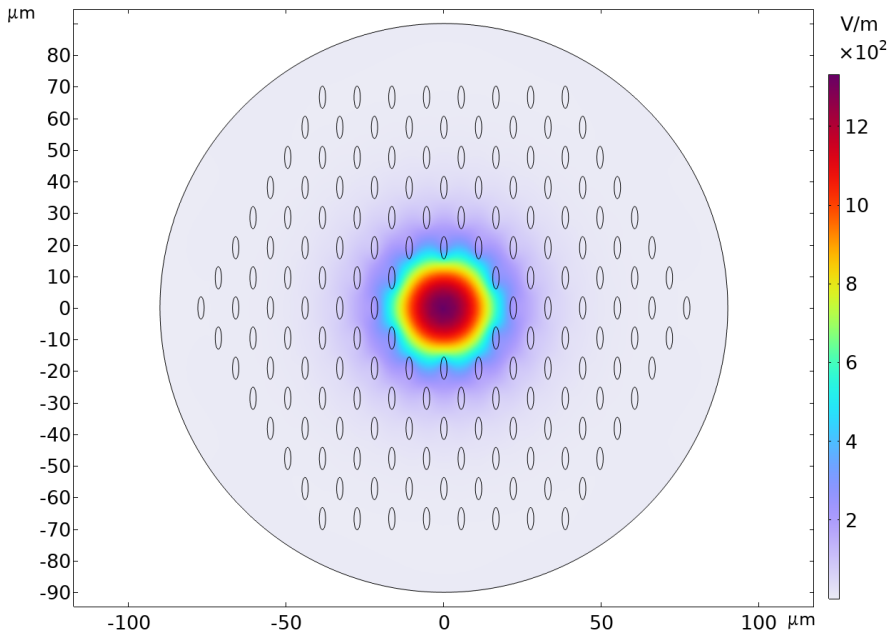


Figure 8.21: Simulation of the mode field for a PCW with the innermost ring removed.

In addition, COMSOL simulations confirmed that this PCW design supports single mode guidance, as shown in Fig. 8.21. Subsequently, I measured the reflection spectrum of the 7 cm sapphire fibre sample and observed clear FBG reflection peaks. Owing to birefringence, two distinct peaks

appeared upon rotating the input polarization; the spectra are presented in Fig. 8.22. To suppress Fabry-Perot fringes arising from reflections at the silica and sapphire interfaces, the raw data were processed with a low-pass filter, yielding a smoother spectrum.

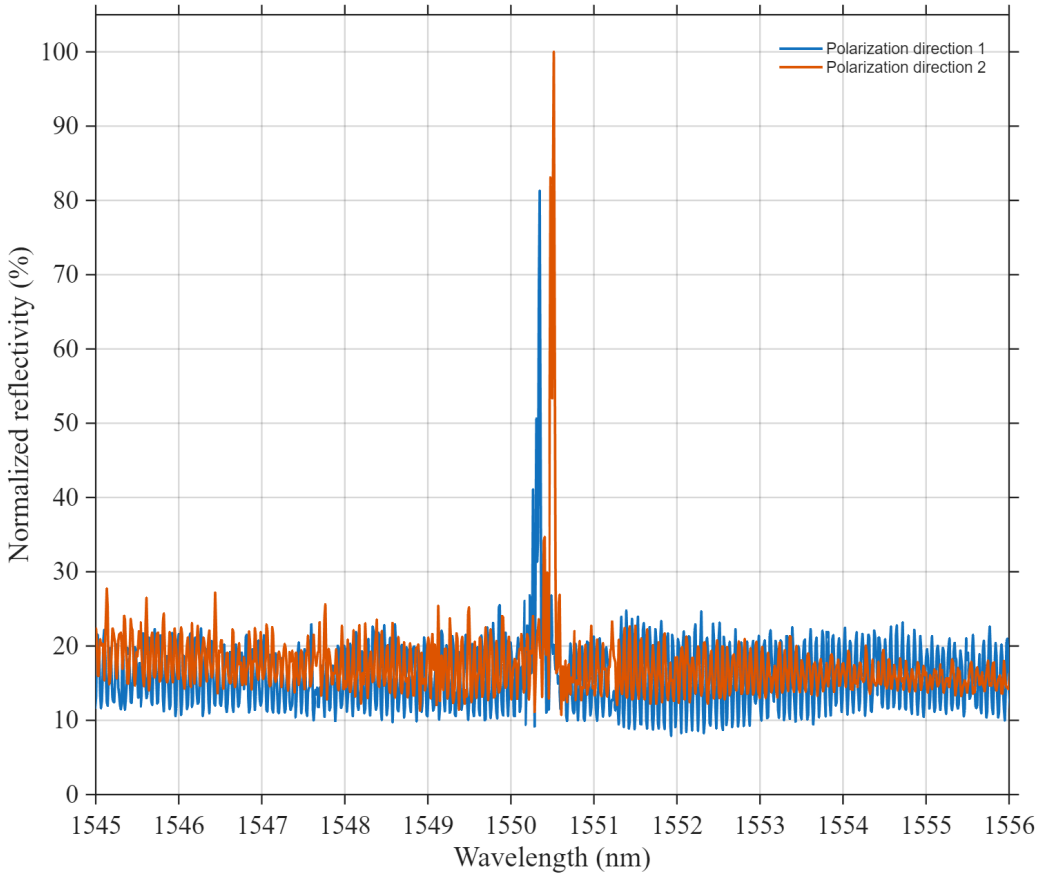


Figure 8.22: Normalised reflectivity spectra of the 7 cm sapphire photonic-crystal fibre Bragg grating sample for two orthogonal polarisation states before fusion splicing to SMF-28e.

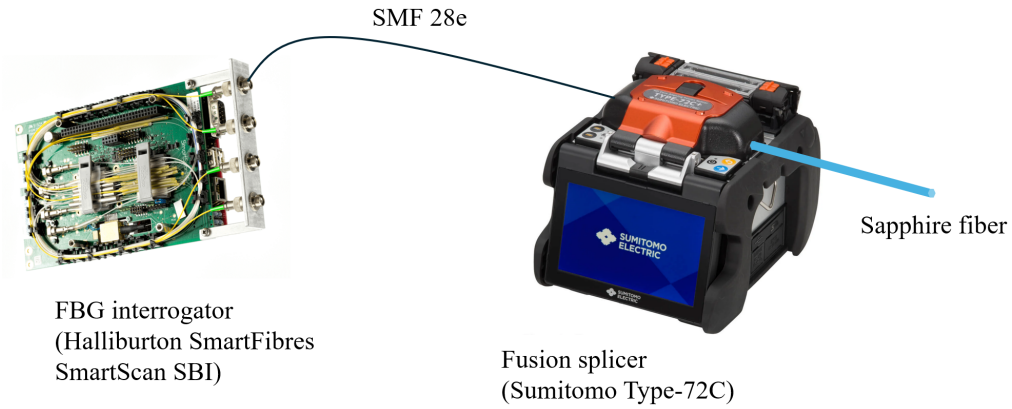


Figure 8.23: Schematic of the sapphire photonic crystal FBG temperature sensor fusion splicing setup.

To realize the first practically deployable sapphire photonic crystal FBG temperature sensor, I

fusion spliced the sapphire fibre to a standard single mode silica fibre. Because the sapphire fibre has a hexagonal prism outer profile and a diameter of 150 μm (slightly larger than the 125 μm cladding of SMF 28e) I employed the manual alignment mode of a Sumitomo Type-72C splicer. During alignment, I monitored the interrogator's real-time reflection spectrum to locate the position yielding the strongest Bragg peak, thereby achieving near core to core registration before initiating the splice. The complete splicing setup is shown in Fig. 8.23.

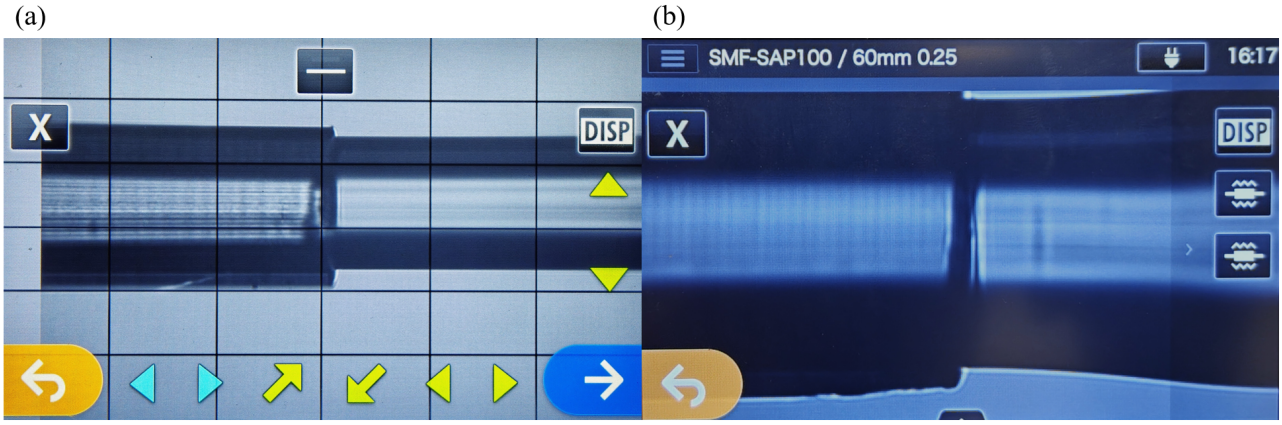


Figure 8.24: (a) The alignment screen for the two fibres before fusion splicing (b) Photo of the joint after fusion splicing.

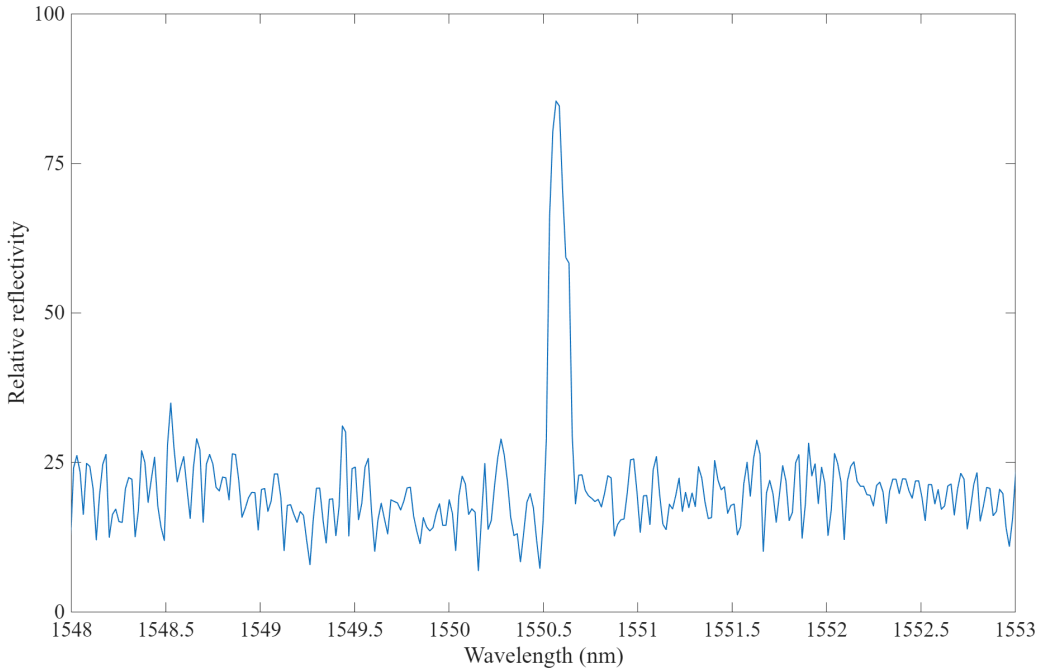


Figure 8.25: Reflectivity spectrum of the 7 cm sapphire FBG sample after fusion splicing.

Despite the mismatch in diameter and cross sectional geometry, the fusion joint passed the

splicer's automatic proof (tensile) test. Photographs of the fibres before and after splicing are shown in Fig. 8.24. We then measured the FBG reflection spectrum of the spliced assembly; the Bragg peak intensity was reduced relative to the pre-splice level. A slow-motion review of the splicing video indicates that the splicer momentarily separates the fibre ends prior to arc discharge and then retracts them, introducing a slight positional shift that degrades core alignment at the moment of fusion. The post splice FBG spectrum is presented in Fig. 8.25.

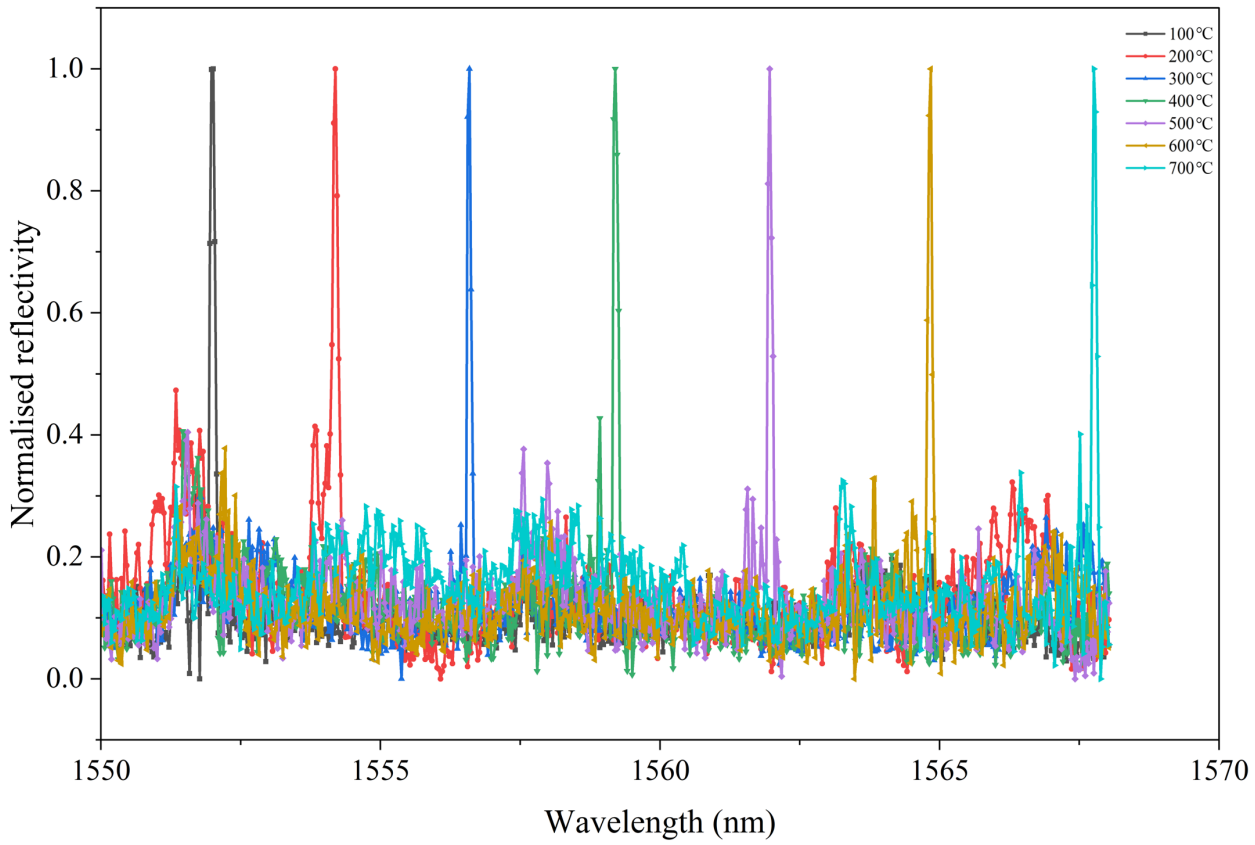


Figure 8.26: Spectra of the 7 cm sapphire FBG sensor at different temperatures between 100 °C to 700 °C.

The 7 cm sensor was placed in a box furnace and heated to 700 °C in 100 °C increments, while an interrogator recorded the FBG reflection spectrum. At each temperature setpoint, multiple spectra were acquired and averaged to suppress jitter. The normalized results are shown in Fig. 8.26, revealing a non linear dependence of the Bragg wavelength on temperature. I subsequently fitted the data with a polynomial model to obtain the temperature response curve shown in Fig. 8.27.

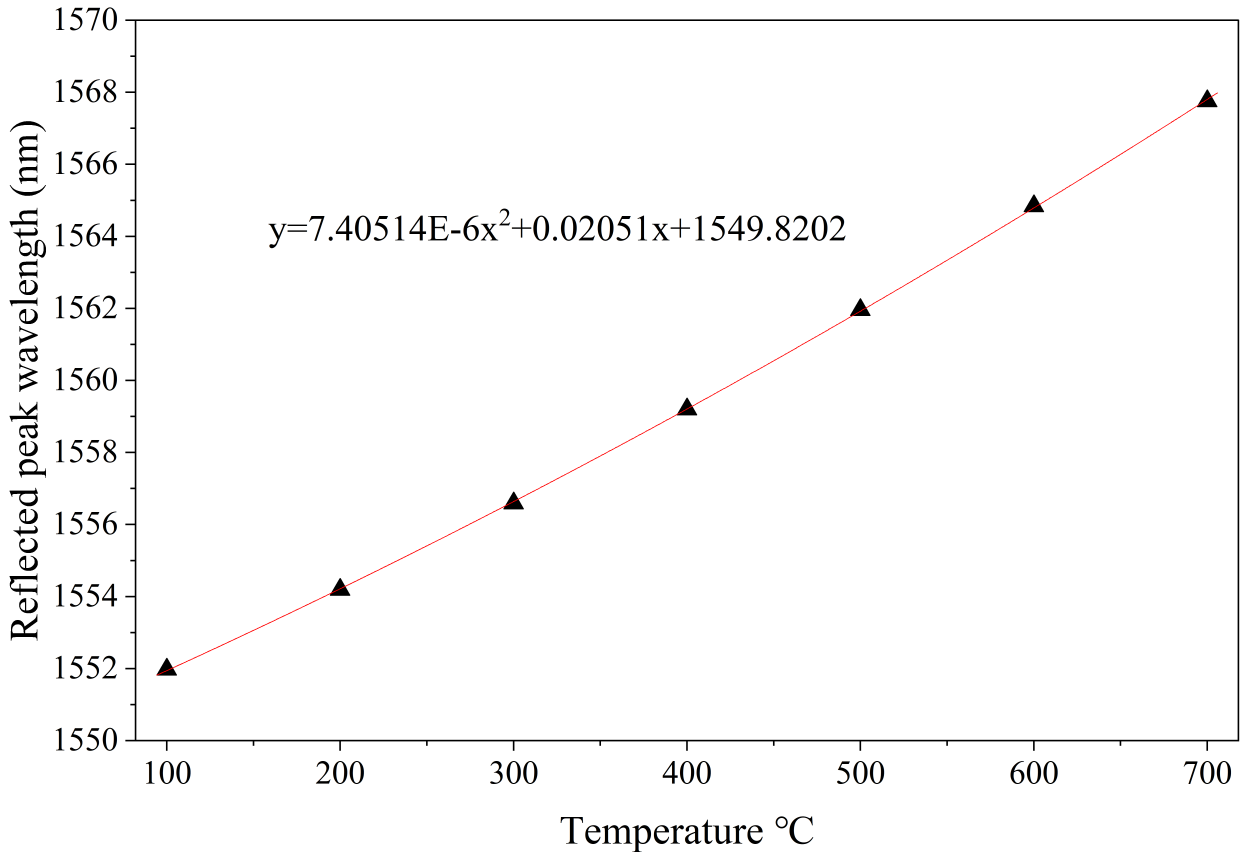


Figure 8.27: Characterization curve of the 7 cm sapphire FBG sensor at different temperatures.

Because the fabrication yield of the 7 cm devices was limited, additional 4 cm sapphire PCF-FBG samples were fabricated to obtain sufficient experimental data over a wider temperature range. These shorter samples were tested from 25 °C to 1200 °C. The normalised reflection spectra over this temperature range are shown in Fig. 8.28, where the Bragg resonance remains observable throughout the heating cycle. Figure 8.29 shows the corresponding peak wavelength as a function of temperature. The response was fitted using a polynomial model, and the temperature sensitivity, defined as the local gradient of the fitted curve, increased from 19.0 pm/°C at 25 °C to 32.3 pm/°C at 1200 °C.

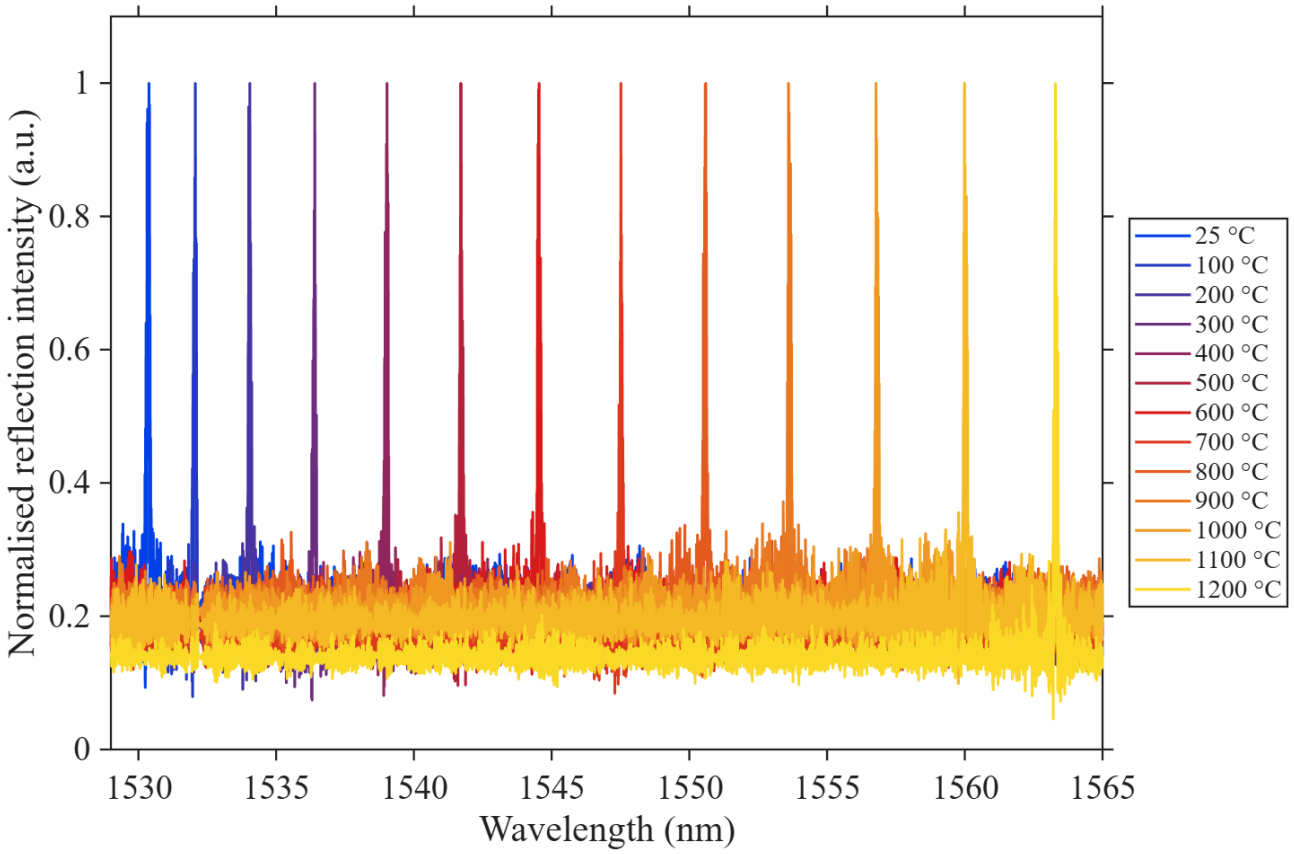


Figure 8.28: Spectra of the 4 cm sapphire FBG sensor at different temperatures between 25 °C to 1200 °C.

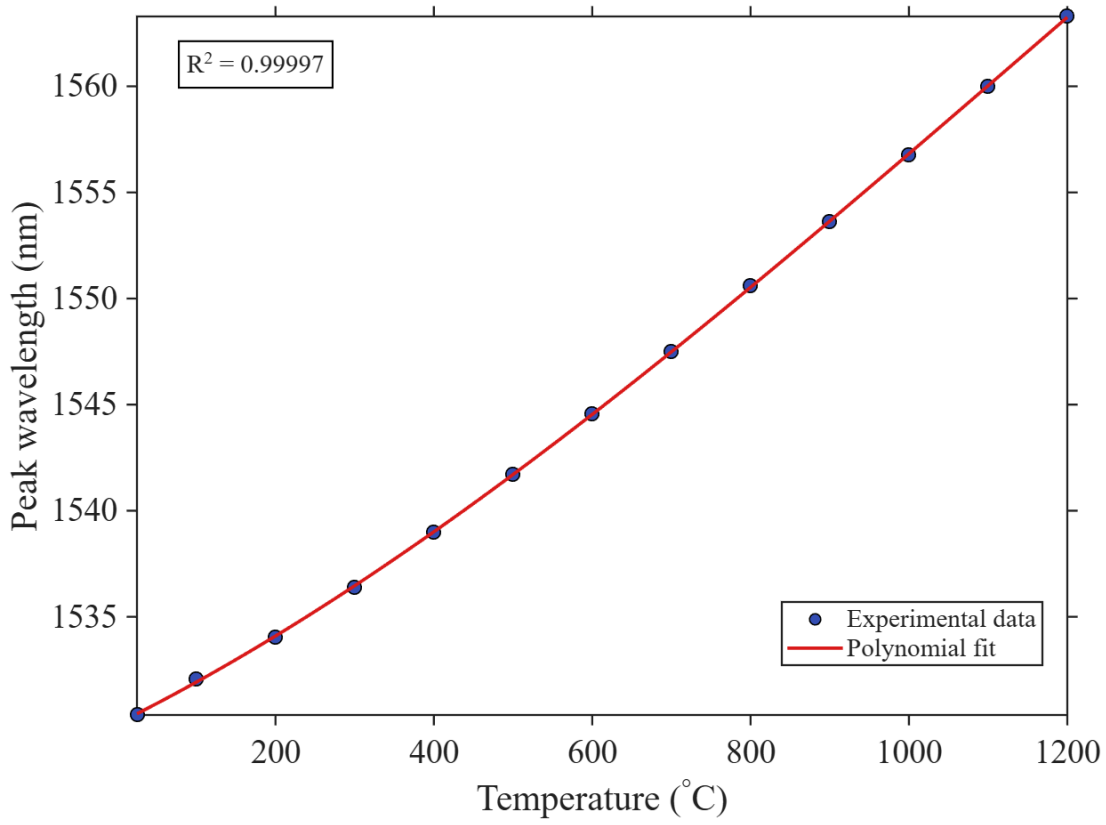


Figure 8.29: Characterization curve of the 4 cm sapphire FBG sensor at different temperatures.

8.3 Summary

By employing adaptive optics to compensate refractive-index-mismatch aberrations and analytically decoupling the spherical-defocus term to minimize the SLM phase excursion, we achieved a markedly shorter focal volume and (at appropriate powers) reduced the risk of crack formation in sapphire slab and fibre. On 1 cm sapphire slabs, we quantified transmission as a function of ring count, observing an exponentially saturating increase in throughput concurrent with a progressive reduction in confinement loss; infrared imaging confirmed near-Gaussian, single-mode profiles. Translating these designs to custom 150 μm LHPG sapphire fibres, we realized a single mode PCF (4.15 cm) and a second device (7.30 cm) for loss extraction; relative to reported depressed cladding sapphire fibres (1.5 dB/cm), our PCF exhibited 10% lower loss. We further integrated femtosecond written FBGs and developed and tested the first sapphire photonic crystal fibre temperature sensor, revealing birefringence induced dual reflection peaks. Furnace measurements from ambient to 700 °C in 100 °C increments yielded a non-linear Bragg wavelength response; Because of the limited fabrication yield of the 7.30 cm devices, supplementary 4 cm sapphire PCF-FBG samples were fabricated and tested from 25 °C to 1200 °C, showing a non-linear temperature response with the local sensitivity increasing from 19.0 pm/°C at 25 °C to 32.3 pm/°C at 1200 °C. compared with published single-mode depressed cladding sapphire sensors, our device nearly doubled the sensor length while requiring a substantially smaller laser modified volume. These advances significantly broaden the application space of sapphire fibre temperature sensing.

References

[1] Nicolas Huot et al. "Analysis of the effects of spherical aberration on ultrafast laser-induced refractive index variation in glass". In: *Optics express* 15.19 (2007), pp. 12395–12408.

[2] Arnaud Couairon et al. "Filamentation and damage in fused silica induced by tightly focused femtosecond laser pulses". In: *Physical Review B—Condensed Matter and Materials Physics* 71.12 (2005), p. 125435.

[3] PS Salter et al. "Exploring the depth range for three-dimensional laser machining with aberration correction". In: *Optics express* 22.15 (2014), pp. 17644–17656.

[4] Martin J Booth, Mark AA Neil, and Tony Wilson. "Aberration correction for confocal imaging in refractive-index-mismatched media". In: *Journal of microscopy* 192.2 (1998), pp. 90–98.

[5] Benjamin P Cumming et al. "Adaptive optics enhanced direct laser writing of high refractive index gyroid photonic crystals in chalcogenide glass". In: *Optics express* 22.1 (2014), pp. 689–698.

[6] Tao Wang et al. "Anisotropic growth and characterizations of large length-diameter ratio sapphire fibers via laser-heated pedestal growth technique". In: *Journal of Crystal Growth* 620 (2023), p. 127363.

[7] Tao Wang et al. "Single crystal fibers: diversified functional crystal material". In: *Advanced Fiber Materials* 1.3 (2019), pp. 163–187.

[8] Mohan Wang et al. "Single-mode sapphire fiber temperature sensor". In: *Journal of Lightwave Technology* (2024).

[9] MJ Steel and RM Osgood. "Polarization and dispersive properties of elliptical-hole photonic crystal fibers". In: *Journal of lightwave technology* 19.4 (2001), p. 495.

[10] MJ Steel and RM Osgood Jr. "Elliptical-hole photonic crystal fibers". In: *Optics Letters* 26.4 (2001), pp. 229–231.

[11] Stefan Kefer et al. "Sapphire photonic crystal waveguides with integrated bragg grating structure". In: *Photonics*. Vol. 9. 4. MDPI. 2022, p. 234.

[12] Yuechen Jia et al. "Monolithic crystalline cladding microstructures for efficient light guiding and beam manipulation in passive and active regimes". In: *Scientific reports* 4.1 (2014), p. 5988.

[13] Gian-Luca Roth et al. "Polymer photonic crystal waveguides generated by femtosecond laser". In: *Laser & Photonics Reviews* 15.11 (2021), p. 2100215.

9 | Conclusions and Outlook

This thesis summarized my research on fibre optic pressure sensors and sapphire based high temperature fibre Bragg grating sensors. It highlighted simulation guided design, the fabrication of micro structured fibre sensors via femtosecond laser direct writing, and the subsequent testing and characterization of device performance. I then discussed the principal limitations of the present study and concluded by outlining directions for future research.

Chapter 1 introduced the broad application landscape of fibre Bragg grating sensors, the motivation for this study, and a concise review of their history and current state of the art. Chapter 2 focused on the sensing principle of pressure fibre sensors based on the stress-optic effect and presented the theoretical framework for decoupling temperature from pressure. In light of the limitations of preform-drawn side-hole fibres for pressure sensing (most notably hole collapse and high insertion loss when fusion spliced to standard single mode fibre), Chapter 3 proposed inscribing three dimensional structures inside commercial step-index fibres and employing wet etching to form micro-holes. Structural simulations in COMSOL (stress distributions under applied pressure) were combined with the stress-optic tensor to compute refractive index perturbations, which were then imported into FIMMWAVE to model the two polarization modes and their Bragg-grating reflection spectra. This modelling pipeline enabled simulation-based performance evaluation and design optimization. Starting from a sector-shaped air hole layout, parametric sweeps were carried out to identify optimal geometries; notably, adding micro-holes near the core further enhanced sensitivity beyond what is achievable through geometric adjustment alone. Finally, simulations were used to compute the sensor's pressure response curve and to verify its capability to decouple temperature from pressure.

Chapter 4 detailed the practical fabrication of the proposed sensor. I first described the use of femtosecond laser direct writing to delineate three dimensional architectures within the fibre, thereby defining the regions to be subsequently developed. The laser-modified zones were then selectively

opened by KOH wet etching, yielding the intended micro features. I concluded the chapter by comparing alternative sealing strategies and their trade off in terms of hermeticity, thermal tolerance, insertion loss, and mechanical robustness and by reporting the final process flow that successfully completed device assembly. Chapter 5 presented the construction of a hydraulic pressure test system and the ensuing measurements. I recorded the sensor's pressure response and temperature response curves and benchmarked them against the simulation results. The experimentally obtained transfer characteristics exhibited close agreement with the modelled predictions, thereby validating both the sensing concept and the design methodology.

Chapter 6 presented my preliminary exploration of a photonic crystal tip temperature sensor. I first validated the sensing mechanism through numerical simulations and then fabricated an initial prototype using focused ion beam milling. However, the nanoscale machining required at the sapphire-fibre end face proved prohibitively challenging and low-yield, which led me to discontinue this route. I therefore pivoted to photonic-crystal fibre sensors fabricated within bare (undeveloped) sapphire fibres instead.

Chapter 7 surveyed the current state of sapphire fibre sensors and, through numerical modelling, verified a sapphire photonic crystal fibre design capable of single mode guidance. The simulations further quantified how confinement loss scales with the number of cladding rings in the PCF lattice, and elucidated how the lattice constant governs coupling efficiency and hence insertion loss when interfacing the PCF with dissimilar fibres (e.g., standard silica SMF) via its impact on effective index and mode field diameter. These results provided practical design guidelines that informed subsequent device fabrication.

Chapter 8 addressed the focusing challenges encountered during femtosecond laser fabrication of sapphire photonic crystal fibres. I developed a compensation model for refractive index mismatch aberrations tailored to direct writing, deriving a pupil-plane phase pre-compensation that explicitly decouples the defocus term. Both an analytic formulation and numerical validation were provided, and

the resulting phase maps were used to guide adaptive-optics correction, compress the focal volume, and mitigate crack initiation. Building on this framework, I fabricated two sapphire PCF waveguides with distinct geometries and analysed their respective advantages and trade-off. During the FBG integration, I observed that a photonic crystal employing a single-track-per-cell lattice suffered appreciable perturbation from the grating inscription, rendering the waveguide's reflection peak difficult to resolve. To minimize grating-induced loading, I adopted a modified architecture that removes the innermost track, thereby preserving the guided mode and spectral contrast. Using this approach, I realised the world's first sapphire photonic-crystal fibre Bragg-grating sensor, with a length nearly twice that of the best published benchmark for other device types to date; it was successfully fusion-spliced to SMF-28, and temperature-response measurements were performed to verify the device's performance.

Notwithstanding the progress achieved, several avenues remain for further improvement. First, the current fabrication route is constrained by the selectivity and rate of KOH etching, which necessitates an end face cut-and-etch process in which material is removed from a single side of the fibre. Future work should explore faster and more selective etchants or processes that eliminate the need to open the end face, instead leveraging side-access microchannels to deliver wet etchants into the fibre interior. Such an approach could enable the serial inscription and development of multiple pressure sensors on a single fibre, paving the way for quasi-distributed pressure sensing. For the sapphire PCF temperature sensor, the dominant challenges remain propagation loss and resultant device length. Reducing transmission loss would allow substantially longer structures, thereby relocating the sapphire-silica splice well outside the hot zone to enhance both the operational envelope and mechanical robustness. In parallel, coupling femtosecond laser direct writing with wet etching offers a promising route to more advanced architectures-such as hollow sapphire PCFs and perforated sapphire fibre pressure sensors which could deliver lower loss, stronger modal control, and broader functionality in extreme-environment sensing.